



Research@**ARL**

Energy & Energetics

Dr. Betsy M. Rice and Dr. T. Richard Jow
Editors-in-Chief

U.S. Army Research Laboratory

Report Documentation Page				Form Approved OMB No. 0704-0188	
Public reporting burden for the collection of information is estimated to average 1 hour per response, including the time for reviewing instructions, searching existing data sources, gathering and maintaining the data needed, and completing and reviewing the collection of information. Send comments regarding this burden estimate or any other aspect of this collection of information, including suggestions for reducing this burden, to Washington Headquarters Services, Directorate for Information Operations and Reports, 1215 Jefferson Davis Highway, Suite 1204, Arlington VA 22202-4302. Respondents should be aware that notwithstanding any other provision of law, no person shall be subject to a penalty for failing to comply with a collection of information if it does not display a currently valid OMB control number.					
1. REPORT DATE JUN 2012		2. REPORT TYPE		3. DATES COVERED 00-00-2012 to 00-00-2012	
4. TITLE AND SUBTITLE Energy & Energetics				5a. CONTRACT NUMBER	
				5b. GRANT NUMBER	
				5c. PROGRAM ELEMENT NUMBER	
6. AUTHOR(S)				5d. PROJECT NUMBER	
				5e. TASK NUMBER	
				5f. WORK UNIT NUMBER	
7. PERFORMING ORGANIZATION NAME(S) AND ADDRESS(ES) U. S. Army Research Laboratory,Aberdeen Proving Ground,MD,21005				8. PERFORMING ORGANIZATION REPORT NUMBER	
9. SPONSORING/MONITORING AGENCY NAME(S) AND ADDRESS(ES)				10. SPONSOR/MONITOR'S ACRONYM(S)	
				11. SPONSOR/MONITOR'S REPORT NUMBER(S)	
12. DISTRIBUTION/AVAILABILITY STATEMENT Approved for public release; distribution unlimited					
13. SUPPLEMENTARY NOTES Research@ARL, Jun 2012					
14. ABSTRACT					
15. SUBJECT TERMS					
16. SECURITY CLASSIFICATION OF:			17. LIMITATION OF ABSTRACT Same as Report (SAR)	18. NUMBER OF PAGES 157	19a. NAME OF RESPONSIBLE PERSON
a. REPORT unclassified	b. ABSTRACT unclassified	c. THIS PAGE unclassified			

Editorial Board



Dr. T. Richard Jow
Editor-in-Chief



Dr. Betsy M. Rice
Editor-in-Chief



Dr. Brad E. Forch



Dr. Joseph N. Mait



Dr. James W. McCauley

Advisory Board

Dr. Kwong K. Choi

Dr. Brad E. Forch

Dr. Piotr J. Franaszczuk

Dr. Shashi P. Karna

Dr. Stephen J. Lee

Dr. Tomasz R. Letowski

Dr. Joseph N. Mait

Dr. James W. McCauley

Dr. Nasser M. Nasrabadi

Dr. Peter J. Reynolds

Dr. Paul H. Shen

Dr. Ananthram Swami

Dr. Bruce J. West

Research@**ARL** can be accessed electronically at www.arl.army.mil/ResearchARL

Introduction to ARL	2
Foreword.....	3
<i>John M. Miller, Director</i>	
Introduction to ARL Research in Energy and Energetics	4
<i>Betsy M. Rice and T. Richard Jow, Editors-in-Chief</i>	
Improved Cycle Life of Fe-Substituted LiCoPO_4	9
<i>Jan L. Allen, T. Richard Jow, and Jeffrey Wolfenstine</i>	
Electrolyte Additive in Support of 5 V Li Ion Chemistry	17
<i>Arthur von Cresce and Kang Xu</i>	
Interfacing Electrolytes with Electrodes in Li Ion Batteries	25
<i>Kang Xu and Arthur von Cresce</i>	
Distinguishing Li^+ Charge Transfer Kinetics at NCA/Electrolyte and Graphite/Electrolyte Interfaces, and NCA/ Electrolyte and LFP/Electrolyte Interfaces in Li-Ion Cells.....	43
<i>T. Richard Jow, Michelle B. Marx, and Jan L. Allen</i>	
A New Direction for the Performance Improvement of Rechargeable Lithium/Sulfur Batteries.....	53
<i>Sheng S. Zhang and Jeffrey A. Read</i>	
Oxygen Reduction Reaction Catalyst on Lithium/Air Battery Discharge Performance.....	61
<i>Xiaoming Ren, Sheng S. Zhang, Dat T. Tran, and Jeffrey A. Read</i>	
Effect of Substitution (Ta, Al, Ga) on the Conductivity of $\text{Li}_7\text{La}_3\text{Zr}_2\text{O}_{12}$.....	71
<i>Jan L. Allen, Jeffrey Wolfenstine, Ezhiylmurugan Rangasamy, and Jeff Sakamoto</i>	
Shock-Induced Behavior of Cubic Gauche Polymeric Nitrogen	77
<i>William D. Mattson and Radhakrishnan Balu</i>	
Optical Cell for In Situ Vibrational Spectroscopic Measurements at High Pressures and Shear	85
<i>Jennifer A. Ciezak and Timothy A. Jenkins</i>	
The First Launch of an Autonomous Thrust-Driven Microrobot Using Nanoporous Energetic Silicon.....	91
<i>Wayne A. Churaman, Luke J. Currano, Christopher J. Morris, Jessica E. Rajkowski, and Sarah Bergbreiter</i>	
Simulations of High-Pressure Phases in RDX.....	101
<i>Lynn B. Munday, Peter W. Chung, Betsy M. Rice, and Santiago D. Solares</i>	
Elastic-Plastic Behavior of Cyclotrimethylene Trinitramine Single Crystals Under Spherical Indentation: Modeling and Simulation.....	111
<i>J. D. Clayton and R. Becker</i>	
Particle-Based Multiscale Coarse Graining with Density-Dependent Potentials: Application to Molecular Crystals (hexahydro-1,3,5-trinitro-s-triazine)	121
<i>Sergei Izvekov, Peter W. Chung, and Betsy M. Rice</i>	
Laser-Induced Plasma Chemistry of the Explosive RDX with Various Metallic Nanoparticles	139
<i>Jennifer L. Gottfried</i>	
Biographies of ARL Authors	149

Introduction to ARL

The Army Research Laboratory of the U.S. Army Research, Development and Engineering Command (RDECOM) is the Army's corporate laboratory. ARL's research continuum focuses on basic and applied research (6.1 and 6.2) and survivability/lethality and human factors analysis (6.6). ARL also applies the extensive research and analysis tools developed in its direct mission program to support ongoing development and acquisition programs in the Army Research, Development, and Engineering Centers (RDECs), Program Executive Offices (PEOs)/Program Manager (PM) Offices, and Industry. ARL has consistently provided the enabling technologies in many of the Army's most important weapons systems.

The Soldiers of today and tomorrow depend on us to deliver the scientific discoveries, technological advances, and the analyses that provide Warfighters with the capabilities with which to execute full-spectrum operations. ARL has Collaborative Technology Alliances in Micro Autonomous Systems and Technology, Robotics, Cognition and Neuroergonomics, and Network Science, an International Technology Alliance, and new Collaborative Research Alliances in Multiscale Multidisciplinary Modeling of Electronic Materials and Materials in Extreme Dynamic Environments. ARL's diverse assortment of unique facilities and dedicated workforce of government and private sector partners make up the largest source of world class integrated research and analysis in the Army.

ARL Mission

The mission of ARL is to "Provide the underpinning science, technology, and analysis that enable full-spectrum operations."

Our Vision

America's Laboratory for the Army: Many Minds, Many Capabilities, Single Focus on the Soldier

ARL's Organization

- Army Research Office (ARO) - Initiates the scientific and far reaching technological discoveries in extramural organizations: educational institutions, nonprofit organizations, and private industry.
- Computational and Information Sciences Directorate (CISD) - Scientific research and technology focused on information processing, network and communication sciences, information assurance, and battlespace environments, and advanced computing that create, exploit and harvest innovative technologies to enable knowledge superiority for the Warfighter.
- Human Research and Engineering Directorate (HRED) - Scientific research and technology directed toward optimizing Soldier performance and Soldier-machine interactions to maximize battlefield effectiveness, and to ensure that Soldier performance requirements are adequately considered in technology development and system design.
- Sensors and Electron Devices Directorate (SEDD) - Scientific research and technology in electro-optic smart sensors, multifunction radio frequency (RF), autonomous sensing, power and energy, and signature management for reconnaissance, intelligence, surveillance, and target acquisition (RISTA), fire control, guidance, fuzing, survivability, mobility and lethality.
- Survivability/Lethality Analysis Directorate (SLAD) - Integrated survivability and lethality analysis of Army systems and technologies across the full spectrum of battlefield threats and environments as well as analysis tools, techniques, and methodologies.
- Vehicle Technology Directorate (VTD) - Scientific research and technology addressing propulsion, transmission, aeromechanics, structural engineering, and robotics technologies for both air and ground vehicles.
- Weapons and Materials Research Directorate (WMRD) - Scientific research and technology in the areas of weapons, protection, and materials to enhance the lethality and survivability of the Nation's ground forces.

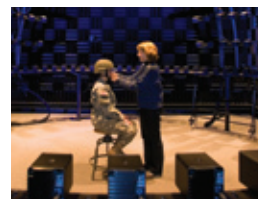
ARL Workforce in 2012

- 2013 Civilians - 33 Military
- 1399 S&Es
- 541 (39%) S&Es hold PhDs
- 13 STs / 26 ARL Fellows

ARL's Primary Sites

- Aberdeen Proving Ground, MD
- Adelphi Laboratory Center, MD
- White Sands Missile Range, NM
- Raleigh-Durham, NC
- Orlando, FL

Visit ARL's web site at www.arl.army.mil



Unique ARL facilities provide our scientists and engineers access to world-class research centers.

FOREWORD

As we complete two decades of excellence as the Army's Corporate Research Laboratory, we look forward to creating even more innovative capabilities for the Army, the Department of Defense and our Nation. Without the dedication to both basic and applied research, it would be impossible for us to effectively focus on the future. Our dynamic workforce, in collaboration with our national and international partners in industry, national laboratories and academia, ensure that we are well positioned to take an active role in anticipating and fulfilling the changing needs of our military and Nation. Visionary ARL scientists and engineers will provide revolutionary technology through novel and innovative research, analysis, design, development and evaluation. We are committed to scientific excellence as we boldly pursue new opportunities. While we cannot predict the exact situations and threats we will face, we focus our research creatively by addressing a full spectrum of potential combat, counterinsurgency and humanitarian scenarios.



In this, our inaugural issue of Research@ARL monograph series, we endeavor to share with you the excitement of our scientists and engineers as they investigate cutting-edge science within the Energy and Energetics research areas through advanced experimentation, computational chemistry and physics.

Motivated by the intense need for lightweight portable power, ARL has led the development of higher voltage cathode materials and high voltage electrolytes. ARL is gaining significant insight into understanding the interfacial chemistry and kinetics in Li-ion batteries, which is vital to enable leap-ahead technology to meet future needs. In the energetics arena, ultrafast spectroscopic and imaging methods are enabling us to probe chemical, mechanical and structural failure and decomposition in ultra-fast time regimes. Our research teams are exploring novel ways to convert mechanical energy to thermal energy by examining initiation mechanisms, multi-phase combustion, detonation and the mechanisms that lead to the release of energy. Advances in science are facilitating the integration of nanoenergetics and electronics to provide integrated chip-level devices for high-power, precision initiation and ignition effects for specialized weapons applications, as well as to enable the controlled mobility of millimeter-scale robotic platforms.

As the Army's underpinning science organization, ARL is uniquely positioned to advance its leadership with a portfolio of science and technology that has been built over the years in survivability, lethality and vulnerability assessment and analysis, materials sciences, information sciences, ballistics and aeromechanic sciences, and human sciences.

In the future issues of Research@ARL, we look forward to sharing with you further highlights from our interdisciplinary strategic focus areas where our scientists and engineers are leading with a single focus on the Soldier.

A stylized, handwritten signature of John M. Miller in black ink.

John M. Miller
Director, U.S. Army Research Laboratory

INTRODUCTION

The discovery of novel materials and methods to store more energy and release energy faster is a crucial area of research to address Army needs in both weapons development and lightweight compact power for individual Soldiers, combat vehicles and munitions. The U.S. Army Research Laboratory (ARL), the Army's corporate research laboratory, is breaking existing paradigms in these areas by developing a rigorous science-based understanding of diverse multidisciplinary domains, integrating theoretical, computational and experimental research. Recently, ARL announced the establishment of Enterprise for Multiscale Research of Materials to create a unique capability for the design of materials that are suitable for extreme dynamic environments and novel electronic and electromagnetic devices. Cognizant of new research initiatives during the past five years, powered by breakthroughs in advanced experimentation and computational chemistry, physics, and materials science, ARL is boldly creating and enhancing the essential computational tools and capabilities to advance these rapidly evolving fields.

The select papers included in this monograph are representative of the high level of theoretical and experimental research, discoveries and achievements of ARL scientists and engineers in energetics science and technology, and in energy storage-electrochemical power, focusing on lithium-ion, lithium-air and lithium-sulfur batteries.

ENERGY STORAGE:

Current lithium-ion battery technology is an outgrowth of early space-race research. The success of using pure lithium as the anode in primary cells stimulated efforts to employ this material for rechargeable and direct power applications, as well as to develop cathode materials and compatible electrolytes that could also endure cycling. The particular difficulty encountered in attempts to cycle lithium pertained to the poor morphology of lithium electrodeposits produced during cell recharge in the organic solvent based electrolytes of the time. This poor morphology (i.e., dendritic with poor adhesion) invariably led to very limited cycle life and the very serious safety problem relating to short-circuiting of cells due to cell separator penetration by lithium dendrites. After decades of such experimentation with pure lithium and some practical success by the Sony Corporation in 1991 using a lithium/graphitic carbon alloy, a consensus developed that the most promising route was to retreat from the use of pure lithium. Instead lithium-ion batteries employ lithium as the intercalated element in graphitic carbon.

Finding better lithium anode intercalates and compatible electrolytes and cathode materials is the central thrust of lithium-ion battery development today. Current Li-ion batteries based on lithium cobalt oxide (LiCoO_2) with an energy density of 200 Wh/kg supply compact power for commercial (e.g., smartphones, laptops, cameras and power tools) and military applications. Li-ion batteries stand on the brink of solving many societal power needs, e.g., affordable energy storage for hybrid and electric vehicles and alternative energy applications (e.g., wind, solar), and extremely high power for electric weapons. Only dedicated, focused research will enable the identification of new materials and technology that will increase energy and power density, lengthen service life, enhance user safety, lower cost, and provide the all-weather service needed by rechargeable batteries.

In this monograph, we present a representative collection of articles that reveal ARL's cutting-edge advances in the area of electrochemical energy storage on lithium and lithium-ion batteries. Particular attention is given to work on developing higher voltage cathode materials and high voltage electrolytes; understanding interfacial chemistry and kinetics in Li-ion batteries, and fabricating and testing emerging lithium batteries and the computational efforts that support such research.

Advanced Li-ion Batteries

The present state-of-the-art cathode material for Li-ion batteries is LiCoO_2 , which has a theoretical energy density of 518 Wh/kg when paired with a Li/carbon anode. To increase energy density, cathode materials that can provide a higher charge storage capacity, higher voltage or both (energy is the product of both voltage and capacity) are needed. Among the three cathode materials that have higher theoretical energy density than LiCoO_2 , we decided to investigate lithium cobalt phosphate (LiCoPO_4),

which has a potential of 4.8 V vs. a reference Li/Li⁺ electrode and has a theoretical energy density of 800 Wh/kg. Lithium cobalt phosphate has the same atomic structure (olivine) as the 3.4 V lithium iron phosphate (LiFePO₄) cathode material that is presently regarded as providing the highest user safety in a Li-ion battery. Potentially, this should result in a Li-ion battery with both higher energy density and good user safety. However, there are several challenges to overcome to develop this cathode for Li-ion batteries. It has been known since the year 2000 that it is difficult to cycle LiCoPO₄ with good capacity retention. It was not understood whether the difficulty in cycling this cathode material with good capacity retention was due to the structural instability of the electrode material itself or the instability of the experimental electrolytes at high voltage. While the lack of electrolytes that would allow stable and prolonged operation at voltages over 4.5 V was often cited as the main cause of that difficulty, the structural stability of the lithium depleted phases of a LiCoPO₄ cathode including CoPO₄, has also not been given much attention in the past when considering cathode life limitations. Two main approaches were taken at ARL to tackle these challenges. Allen et al. (*J. Power Sources*, **2011**, 196, 8656) proceeded with substituting part of Co with other transition metals such as Fe to see if this can stabilize the structure. Cresce et al. (*J. Electrochem. Soc.*, **2011**, 158, A337) engaged in exploring solvents and additives that would allow the operation of the cathodes at voltages approaching 5 V.

ARL has made great advances on both fronts. With Fe doping, Allen et al. succeeded in increasing the structural stability of the LiCoPO₄ cathode. Cresce et al. succeeded in identifying tris(hexafluoro) isopropyl phosphate (HFIP) as an effective additive in the baseline electrolyte allowing the operation of 5 V class of cathode materials by stopping further oxidation electrolyte components on the high voltage cathode surfaces. The structural stability of the cathode is a necessary requirement of a long cycle life with sustained capacity retention. The pristine LiCoPO₄ lost 50% of its charge capacity in 10 cycles even in the ARL-developed high voltage electrolyte, while the stabilized LiCoPO₄ can maintain good capacity retention even in standard baseline electrolyte. Thus, the capacity fade is mainly a result of LiCoPO₄/CoPO₄ structural decomposition and, to a lesser degree, a result of electrolyte decomposition. Nonetheless, the high voltage electrolyte was still needed for long-term cycling. In short, ARL has had success in achieving a stabilized cathode and a compatible electrolyte for a safe Li-ion battery with a cathode that can provide both high energy density and good cycle and storage life. The understanding of the mechanisms of structural stability by doping Fe in LiCoPO₄ and effectiveness of HFIP in stopping further oxidation of electrolytes are being actively pursued.

Interfacial Chemistry and Interfacial Kinetics of Li-ion Battery Electrodes

While the energy density of an electrochemical couple is determined by the electrochemical potential difference and the charge capacity of the electrodes chosen, all of the electrochemical reactions occur at the electrode/electrolyte interfaces and the electrolyte is needed to perform its function of delivering the needed Li⁺ to the electrodes and for completing the electrochemical reactions by accepting the electron transfer from the external circuit. For Li-ion batteries to achieve long storage and cycle life with a high charge/discharge rate, it is essential that the electrolyte is able to perform its functions with low impedance and without undesirable parasitic reactions. This is a very challenging requirement due to the extreme electrochemical potentials of the anode and the cathode materials used in this chemistry. The electrochemical potential of the lithiated graphite anode, which is close to Li potential, is about 3 V negative of standard hydrogen potential, is reductively very active and lies outside the stability window of the state-of-the-art nonaqueous electrolytes. The electrochemical potential of the lithium transition metal oxides is near the oxygen evolution potential in aqueous systems. State-of-the-art Li-ion batteries rely on the ability of the electrolyte to form protective layers (referred to as solid electrolyte interfaces [SEIs]) on the surfaces of the electrodes during initial charging. SEIs prevent undesirable reactions. During charge, the solvated Li ion needs to be de-solvated before entering the SEI, diffused into SEI, and then intercalated into graphite completing the electron transfer process. The charge of the Li ion is balanced by the electron coming from the external circuit near or at the electrode/electrolyte interface. The same process happens at the cathode during discharge. These processes involve the steps of solvated Li-ion transport in the bulk, desolvation of solvents before entering the SEI, transport through the SEI and intercalation into the electrode, and the electron charge transfer. However, the SEI can impede the electrode processes if it is too thick, poorly conducting or unstable. The properties of the SEI for any particular electrode material are determined by the composition of the electrolyte and electrolyte additives, and this important issue has generally been treated in a very difficult, time-consuming and imperfect manner in the past. At ARL, we believe that future progress requires an in-depth understanding of the mechanism of the SEI formation. Accordingly, the SEI has been investigated using surface analysis methods including X-ray photoelectron spectroscopy, Nuclear Magnetic Resonance spectroscopy (NMR), and Fourier Transform Infrared spectroscopy (FTIR). Such studies and our results are described in a featured article by Xu et al. (*J. Mater. Chem.*, **2011**, 21, 9849). Jow et al. (*J. Electrochem. Soc.*, **2012**, 59(5), A604) studied the Li⁺ charge transfer kinetics at graphite anode/electrolyte and LiFePO₄ cathode/electrolyte or LiNi_{1-y-z}Co_yAl_zO₂ cathode/electrolyte interfaces at the same time in full cells. They found that the activation energy of the Li⁺ charge transfer kinetics varied with the electrode materials. This clearly suggests that the different electrodes create different interphases in the same electrolyte and result in different Li⁺ charge transfer kinetics. The understanding of how the electrode surface reacts with the electrolyte is critical in advancing the Li-ion energy storage technology.

Emerging Lithium Battery Systems and Novel Solid Electrolytes

The energy density of Li-ion batteries based on intercalation reactions has its limitations. What is beyond Li-ion? At ARL and other laboratories, researchers are once again exploring the use of pure Li as a negative electrode, pairing it with an air or sulfur cathode that has a higher theoretical energy density than Li-ion. The fact that dissolved sulfur eliminates Li dendrites may overcome the usual safety problem. The use of a ceramic electrolyte in a Li/air battery may similarly overcome the lithium safety problem.

A key issue in the development of a Li-S cell has been the excessive reaction of soluble polysulfide (formed during cell discharge) with the Li anode. Most prior work in this area has involved the attempt to reduce polysulfide solubility. Zhang et al. (*J. Power Sources*, **2012**, 200, 77) were successful in pursuing a completely different approach to this problem. Instead of resolving the solubility issue of the polysulfide, they treated the soluble product as a soluble cathode and discovered an additive that could protect the Li anode from reacting with the dissolved sulfur compounds. Further research is required to refine this approach. In the area of Li-air batteries, there are many challenges to making the air electrode operate properly. Ren et al. (*J. Mater. Chem.*, **2011**, 21, 10118) demonstrated that the catalyst causes a shift in the discharge reaction pathway, making the discharge capacity more effectively utilized.

To utilize pure Li metal as an anode for Li-S and Li-air batteries, there is a critical need for a solid electrolyte membrane that is compatible with Li, has high Li⁺ conductivity ($>10^{-4}$ S/cm), and is thin and mechanically strong. The Li⁺ solid electrolyte based on the garnet atomic structure (Li₇La₃Zr₂O₁₂) [LLZO] can potentially meet the needs. However, the challenge is to stabilize the LLZO cubic structure, to provide higher Li⁺ conductivity, at room temperature. Presently, a lower conductivity tetragonal phase is more stable at room temperature. Allen and Wolfenstine et al. (*J. Power Sources*, **2012**, 206, 315–319) succeeded in achieving the stabilization of LLZO in the cubic phase and achieved the highest known conductivity for a Li⁺ solid conductor by Ta substitution. The value achieved, 8.9×10^{-4} S/cm, is close to values for liquid electrolytes. They also showed that Ta substitution in the Li sublattice is preferred over the previously reported Al, which substitutes for Li. Through hot pressing, a near-100% dense material can also be achieved. Thus, Ta doping is very promising. Future work will focus on chemical stability, mechanical properties and making test cells of the Ta-doped material.

Computational Exploration of Electrolytes and Electrodes

Despite the progress ARL has made in materials development, there are still many materials issues that need to be understood to assist in the advancement of higher energy density and better performance energy storage devices. In particular, a basic theoretical understanding of factors controlling stability of electrolytes and their reactivity pathway with electrode materials for guiding future materials development is urgently needed. Borodin as a primary author and his coauthors (Xing et al., , Density Functional Theory Study of the Role of Anions on the Oxidative Decomposition Reaction of Propylene Carbonate, *J. Phys. Chem. A*, **2011**, 115, 13896–13905) demonstrated that the presence of anions such as PF₆⁻ or ClO₄⁻ not only significantly reduces the oxidative stability of the carbonate electrolyte solvents but also stabilizes the solvent-anion oxidation decomposition products and changes the order of the oxidation decomposition paths. The primary oxidative decomposition products of PC-PF₆⁻ and PC-ClO₄⁻ were CO₂ and acetone radical, which is in good agreement with available experimental data. Density Function theory (DFT) calculations also explained why toxic fluoro-organics were experimentally observed at elevated temperatures in a carbonate-LiPF₆ electrolyte in the presence of a cathode material and were not observed during electrolyte oxidation at room temperature. The ARL-initiated Collaborative Research Alliance (CRA) on Multiscale Multidisciplinary Electronic (MSME) Materials will further enhance and expand our efforts for enhancing the basic understanding of factors controlling stability of electrolytes and electrode materials and providing materials predictive and design capability for achieving over 300 Wh/kg energy density goals for electrochemical energy storage devices.

ENERGETICS

ARL has an overarching objective to develop a science-based understanding of novel ways to store and release chemical and structural energy for use in explosive and propellant applications that may lead to leap-ahead weapons capabilities. The fundamental research initiative is capitalizing on recent breakthroughs in advanced experimentation and computational chemistry and physics to identify, understand and characterize processes and mechanisms that control energy storage and release. ARL, as a recognized leader in theoretical chemistry research, is directing its resources and expertise into a rigorous and innovative program that will lead to a new generation of energetics whose development is computationally guided. One example of ARL's paradigm-breaking research is the quest to store large quantities of structural energy in simple molecular systems,

which are inert under ambient conditions but can be compelled to form extended solids by compressing them under extreme pressure. Of interest are high pressure forms of polymerized nitrogen, theorized for decades through quantum mechanical prediction but only recently synthesized by compressing it in a diamond anvil cell at temperatures and pressures exceeding 2000 K and 110 GPa, respectively. The energy content of this polymerized nitrogen material is expected to significantly exceed any existing conventional explosive, thus ARL has initiated efforts to overcome the substantial scientific and technical challenges to create this material under less extreme conditions and stabilize it to an ambient state. New agile synthetic methods are being designed and developed to fabricate recoverable highly energetic metastable states of matter using combinations of extreme pressure, mechanochemistry, mechanophysics and laser photochemical processes.

The exciting potential of the nanoscale also forms a large part of ARL's novel energetics thrust. Based on recent advances in nanoscale materials and nanofabrication, ARL is investigating ways of engineering energetic materials with fundamentally new and technologically useful characteristics. Over the past decade considerable evidence has accumulated showing that energetic nanoparticulates may react to produce enhanced power compared to their more conventional counterparts of the same chemical composition.

Extended Solids: A new class of energetic materials

Extended solids are emerging as a novel new class of energetic materials. Large-scale quantum molecular dynamics (QMD) calculations are being used to identify and characterize candidate extended solid structures and determine what factors affect stability. Polymeric nitrogen is the current frontrunner due to its unusually large energy content (its energy release and rapid conversion to molecular form), which could be classed as "superexplosive." Mattson and Balu (*Physical Rev. B*, **2011**, 83, 174105) are using QMD simulations to study the shock response of the cubic gauche form of nitrogen, the only crystalline polymeric form of nitrogen synthesized to date. Their findings revealed that this cubic gauche nitrogen exhibits unusual mechanical properties, which produce an extremely complex shock behavior, far different from that seen in conventional energetic materials. Rather than initiating chemical reaction behind the compression front, the shock impact induced phase transitions and material defects that resulted in unusual energy dispersion mechanisms that slowed the shock wave. To foster the rapid release of the stored structural energy in this material, we must develop new methods to trigger high-rate chemical reactions. One method being pursued at ARL is the imposition of mechanical stresses through a process known to accelerate solid-state reaction rates.

Another new approach is introducing shear into the fabrication process to lower the transition pressures needed to form novel high-pressure-phase materials when compressed. The goal is to enable the scale-up synthesis of these new materials for further test and evaluation. As such, ARL researchers Ciezak and Jenkins (*Rev. of Scientific Instruments*, **2011**, 82, 073905) have designed a special rotational diamond anvil cell for generating high pressure and shear simultaneously. Preliminary studies using this cell indicate that both amorphous and crystalline polymeric nitrogen can be synthesized at room temperature and pressures of ~ 40 GPa when shear is introduced.

ARL is also developing novel energetic materials for fuel cells, solar cells and actuators in microrobots. We have made great strides in these areas building upon the development of a new type of energetic material based on nanoporous silicon (PS). When silicon oxidizes it produces a significantly greater energy release than conventional energetic materials. Of course, the rate of energy release depends on intimate mixing of the oxidant with the silicon-based fuel. Capitalizing on the high reactivity (oxidation potential) of PS, Becker et al. (Galvanic Porous Silicon Composites for High-Velocity Nanoenergetics, *Nano Letters*, **2011**, 11, 803–807) have successfully engineered highly explosive composite materials composed of PS infused with an oxidizer that can produce very high combustion velocities (~3 km/s). Churaman et al. (*J. Microelectromechanical Systems*, **February 2012**, 21(1)) used this novel material for thrust actuation of an autonomous jumping microelectromechanical system (MEMS) microbot. The actuation pulse lasted several microseconds allowing the robot to reach a vertical height of approximately 8 cm.

Multiscale Response of Energetic Materials

A key challenge facing energetic material design and development is to understand the response of an energetic material within a munition to unexpected initiation. Given the multi-scale nature of the response of the energetic material in a munition (i.e., decomposition and energy release occur at the molecular scale where material response is manifested at the macroscale), considerable technology gaps exist in both the measuring and modeling processes.

ARL is spearheading a research program to explore the multiscale response of energetic materials, with a goal to develop methods and models to predict response of energetic materials, with all models validated by advanced experimentation at scales

ranging from molecular to continuum. Although in its infancy, this program has yielded notable theoretical and experimental advances. As a demonstration of this multiscale approach, ARL has targeted a simple explosive formulation for quantum-based multiscale modeling. This formulation, composed of cyclotrimethylene trinitramine (RDX, a commonly used energetic material) and polyethylene, has been subjected to extensive quantum mechanical calculations and the results have been homogenized into atomistic models for molecular dynamics (MD) simulations. To allow the atomistic simulation results to subsequently be upscaled to continuum-level descriptions, Munday et al. (*J. Phys. Chem. B*, **2011**, 115, 4378–4386) have performed a series of comprehensive MD simulations using this model to provide information about its atomic-level dynamic response, properties, localized heating and mechanical deformation, looking specifically at the various conditions this material will experience under extreme compression. Their results demonstrated that molecular deformation is coupled with material phase transitions and could activate new slip systems while blocking slip systems of other phases. Such information about deformation mechanisms is crucial for the emerging plasticity models for RDX that are being developed at ARL. Clayton and Becker (*J. Applied Physics*, **2012**, 111, 063512) recently described the elastic-plastic behavior of single crystals of RDX under spherical indentation using this new model. Their results will be used in the continuum simulations of macroscale response to mechanical stresses.

At present, system size and simulation constraints prevent the representation of microstructural features inherent in a composite energetic formulation in atomistic simulations. To overcome this challenge, ARL has developed a mesoscale modeling methodology, similar in spirit to a MD simulation, but that can bridge the system sizes and simulation times necessary to explore the dynamic response and evolution of microstructural features. This methodology, Dissipative Particle Dynamics (DPD), uses coarse-grain (CG) representations of the materials, and has been shown to work well in describing dynamic and rheological properties of soft matter such as liquids or polymers using very simple models of the interparticle interactions. ARL has made tremendous advances in the state of the art with the development of density-dependent CG models of a condensed phase explosive that properly depict structure and shock properties of RDX for use within the DPD method. Izvekova et al. (*J. Chem. Phys.*, **2011**, 135, 044112) have produced accurate particle-based CG models directly from atomistic-level interactions for RDX through force matching to quantum-based MD simulations. The development of this model is a notable step forward to bridging the scales by providing a model that allows for the dynamic response of a realistic composite energetic material at the microscale level.

Direct experimental observation of the key phenomena at the various scales also presents a formidable challenge due to the numerous processes occurring at the same time, at extremely rapid rates, and under conditions of extreme temperatures and pressures. To tackle these obstacles, ARL has invested in advanced experimental tools and systems to unravel the details of the fundamental chemical and physical steps involved in the combustion or detonation of an energetic material. Gottfried's (*Applied Optics*, **2012**, 51(7), b13–b21) recent work using laser-induced breakdown spectroscopy to monitor the time-resolved chemical reactions of metallic nanoparticles with RDX at high temperatures is a prime example. In this study, Gottfried showed that the plasma chemistry of RDX in the presence of metallic nanoparticles is substantially different from that of the pure material, suggesting that introducing aluminum into explosive formulations not only produces extra heat due to aluminum oxidation, but also affects the chemical reactions that are occurring.

In addition to interrogating the subscale chemistry in energetic material response, ARL is addressing the challenges inherent in characterizing macroscale material response within extreme dynamic environments by developing novel experimental capabilities, as typified in the study by Densmore et al (High-speed two-camera imaging pyrometer for mapping fireball temperatures, *Applied Optics*, **2011**, 50(33), 6267–6271). In this work, ultrafast imaging methods were created to monitor temperature in explosive events using a specially designed high-speed imaging pyrometer that allows direct imaging and determination of temperature profiles within fireballs produced by explosions. Incorporation of this information into experimentally validated multiscale modeling and simulation schemes will provide a true predictive capability of energetic material response based on fundamental physics and chemistry parameters linked to engineering/continuum models.

The examples highlighted in this monograph are but a small sample of the numerous cutting-edge research initiatives within ARL that have the potential to revolutionize the design, manufacture and implementation of novel, advanced energetic materials, all at substantially reduced risk, time and cost.

Improved Cycle Life of Fe-Substituted LiCoPO_4

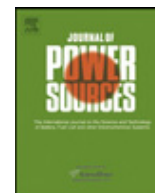
Jan L. Allen, T. Richard Jow, and Jeffrey Wolfenstine

U.S. Army Research Laboratory, Adelphi, MD

ABSTRACT

Fe-substituted LiCoPO_4 exhibits greatly improved cycle life relative to LiCoPO_4 . Whereas, pure LiCoPO_4 loses more than half of its discharge capacity at the 10th cycle, the Fe-substituted LiCoPO_4 retains about 100% of its discharge capacity at the 10th cycle and about 80% of its capacity at the 500th cycle. It is suggested that improved cycle life results from Fe^{3+} substitution on the Li and Co sites. The partial substitution of Li^+ by Fe^{3+} and Co^{2+} by Fe^{2+} and Fe^{3+} was evidenced from Rietveld analysis of X-ray powder diffraction data, infrared spectroscopy, X-ray photoelectron spectroscopy and Mossbauer spectroscopy. The majority of the Fe^{3+} substitutes at the Co^{2+} site. The composition of Fe-substituted LiCoPO_4 is $\text{Li}_{0.92}\text{Co}_{0.8}\text{Fe}^{2+}_{0.12}\text{Fe}^{3+}_{0.08}\text{PO}_4$ for a sample of starting composition $\text{LiCo}_{0.8}\text{Fe}_{0.2}\text{PO}_4$.

Journal of Power Sources, Volume 196, Pages 8656-8661 (2011)



Improved cycle life of Fe-substituted LiCoPO₄

J.L. Allen*, T.R. Jow, J. Wolfenstine

U.S. Army Research Laboratory, 2800 Powder Mill Road, Adelphi, MD 20783-1197, USA

ARTICLE INFO

Article history:

Received 17 May 2011

Received in revised form 14 June 2011

Accepted 15 June 2011

Available online 22 June 2011

Keywords:

Li-ion battery

High voltage

XRD

Mössbauer

Cathode

LiCoPO₄

ABSTRACT

Fe-substituted LiCoPO₄ exhibits greatly improved cycle life relative to LiCoPO₄. Whereas, pure LiCoPO₄ loses more than half of its discharge capacity at the 10th cycle, the Fe-substituted LiCoPO₄ retains about 100% of its discharge capacity at the 10th cycle and about 80% of its capacity at the 500th cycle. It is suggested that improved cycle life results from Fe³⁺ substitution on the Li and Co sites. The partial substitution of Li⁺ by Fe³⁺ and Co²⁺ by Fe²⁺ and Fe³⁺ was evidenced from Rietveld analysis of X-ray powder diffraction data, infrared spectroscopy, X-ray photoelectron spectroscopy and Mössbauer spectroscopy. The majority of the Fe³⁺ substitutes at the Co²⁺ site. The composition of Fe-substituted LiCoPO₄ is Li_{0.92}Co_{0.8}Fe_{0.12}Fe_{0.08}PO₄ for a sample of starting composition LiCo_{0.8}Fe_{0.2}PO₄.

Published by Elsevier B.V.

1. Introduction

LiMPO₄ compounds, where M=Fe, Mn, Co or Ni, have been the focus of intense study both for scientific and practical reasons as Li-ion battery energy storage materials since the pioneering work of Padhi et al. [1]. The voltage of the redox couple varies with transition metal from 3.4 V for Fe [1], 4.1 V for Mn [1], 4.8 V for Co [2] and 5.1 V for Ni [3]. High voltage batteries are desirable because the stored energy is proportional to the voltage and the power is proportional to the square of the voltage. For example, LiFePO₄ has potentially an energy storage capability of 578 Wh kg⁻¹ (3.4 V × 170 Ah kg⁻¹) and LiCoPO₄ about 802 Wh kg⁻¹ (4.8 V × 167 Ah kg⁻¹). Hence, there is a keen interest to move beyond already commercialized LiFePO₄ to the other transition metals. As LiCoPO₄ in particular has the potential to increase energy ~40% compared to LiFePO₄, we have focused our work on this material. Initial work on LiCoPO₄ led to improved rate capability but capacity fade soon emerged as an impediment to further progress [4–6]. The initial discharge capacity and rate capability of LiCoPO₄ were improved by varying the oxygen partial pressure during synthesis [6], carbon coating [7] and substitution on the Co site [8]. However, until now, LiCoPO₄ has shown a severe loss of discharge capacity upon charge–discharge cycling. For example, Tadanga et al. [4] observed a 10th cycle discharge capacity of ~52% of the initial capacity, Bramnik et al. [5] reported a 10th cycle dis-

charge of ~59% of the initial capacity and Wolfenstine et al. [6] reported ~53% capacity retention at the 10th cycle. This capacity fade has been attributed to irreversible structural changes such as amorphization [5,6] of the material and/or electrolyte degradation [4]. In this paper, we will show that a substitution of Li⁺ by Fe³⁺ and Co²⁺ by Fe³⁺ and Fe²⁺ improves not only rate capability but also dramatically reduces capacity fade. In addition, even further reduction in capacity fade is observed when the Fe-substituted LiCoPO₄ was used with electrolyte containing tris(hexafluoroisopropyl) phosphate (HFIP) [9].

2. Experimental

LiCoPO₄ samples were prepared via a citrate complexation route. Co(OH)₂, LiH₂PO₄, and citric acid, 1, 1.01, 1.02, molar ratio, respectively, were mixed into deionized water until all solids were dissolved. The resulting solution was evaporated to dryness via a microwave oven. The resulting dried mass was removed, ground lightly with mortar and pestle and heated in air at a rate of 10 °C min⁻¹ to 600 °C and the reactant mixture was held at this temperature for 12 h.

In order get Fe substitution on both the Li and Co sites, Co(OH)₂, LiH₂PO₄ and FeC₂O₄·2H₂O with a nominal stoichiometry of LiCo_{1-x}Fe_xPO₄, x = 0.05, 0.1, 0.2 were weighed and then dissolved in 1 M HNO₃ (aq). The resulting nitrate solution was evaporated to dryness via a microwave oven in a fume hood and then heated under N₂ at a rate of 10 °C min⁻¹ to 600 °C and held at this temperature for 12 h. During the decomposition of the co-precipitated nitrates, the decomposition of the nitrate ion provided an oxidizing

* Corresponding author. Tel.: +1 301 394 0291; fax: +1 301 394 0273.

E-mail addresses: jan.l.allen8.civ@mail.mil, jallen@arl.army.mil (J.L. Allen).

component to the N_2 atmosphere which transformed a portion of the Fe^{2+} to Fe^{3+} .

Carbon coating to improve electronic conductivity was done by ball milling the samples of $LiCoPO_4$ and Fe-substituted $LiCoPO_4$ for 30 min with 5% by mass acetylene black followed by heating for 1 h at $600^\circ C$ under N_2 . The improvements of the activity of $LiCoPO_4$ after carbon coating [5] and after a short ball milling (<1 h) have been previously reported [10].

Phase purity was evaluated using X-ray powder diffraction. Data were collected using a Rigaku Ultima III diffractometer. Lattice constants were calculated from peak positions using Rietveld refinement of the pattern collected in a parallel beam geometry or with the use of a NIST certified silicon standard for collection in a Bragg–Brentano geometry using Riqas software (Materials Data Inc.). Samples were further evaluated spectroscopically using Attenuated Total Reflectance Fourier-Transform Infrared (ATR-FTIR) Spectroscopy, X-ray Photoelectron Spectroscopy (XPS) to evaluate site occupancy and oxidation states, respectively. Additional information about the oxidation state of Fe was obtained from Mössbauer spectroscopy (collected at SEE Company, Edina, Mn) and elemental analysis via inductively coupled plasma optical emission spectroscopy (ICP-OES, data collected at Galbraith Laboratories, Inc.).

For electrochemical testing, a composite electrode was fabricated by a slurry coating method. Using N-methylpyrrolidone (NMP) as solvent, a slurry was used to coat an Al foil substrate to produce a composite electrode of 80 wt.% active, 10 wt.% polyvinylidene fluoride (PVDF) and 8 wt.% super-P carbon and 2 wt.% conductive carbon nanotube composite (CheapTubes.com). The electrode film was cut into small discs with an area of 0.97 cm^2 , dried under an infrared lamp in air before use and thereafter in a heated vacuum oven ($\sim 100^\circ C$). In a dry room (dew point $< -80^\circ C$), Li/active coin cells (Hohsen Al-clad CR2032) were assembled using Celgard® 3501 as the separator and a 1.0 molal $LiPF_6$ solution in a 3:7 (wt.%) mixture of ethylene carbonate (EC) and ethyl methyl carbonate (EMC) electrolyte with and without 1 wt.% HFIP. Electrochemical testing was performed using a Maccor Series 4000 tester. For calculation of C-rate, a capacity of $\sim 170\text{ mA h g}^{-1}$ was assumed.

3. Results and discussion

The partial substitution of Co^{2+} by Fe^{2+} was explored because it is known that substitution with Fe^{2+} can improve the rate capability of the other olivines [1]. For example, Padhi et al. [1] showed that Fe substitution for Mn^{2+} in $LiMnPO_4$ enabled it to be cycled whereas pure $LiMnPO_4$ was found to be essentially electrochemically inert. At the time, Padhi et al. proposed that the Fe^{3+} –O– Mn^{2+} interactions destabilize the Mn^{2+} level and stabilize the Fe^{3+} level so as to make the Mn^{3+}/Mn^{2+} energy accessible. Thus, we report here on the substitution of Co^{2+} by Fe^{2+} as a means to improve the rate capability in an analogous fashion. However, there is no reported improvement in capacity fade owing to the substitution of Co^{2+} by Fe^{2+} .

The partial substitution of Li^+ and Co^{2+} by Fe^{3+} was explored to address capacity fade through improved structural stability of $LiCoPO_4/CoPO_4$ during cycling. This substitutional strategy is based upon the speculation that decomposition of $LiCoPO_4$ or $CoPO_4$ may result from a loss of oxygen during charging–discharging as shown below.

For the case of $CoPO_4$, the proposed decomposition reaction is:



This reaction results in the release of O_2 during the discharge. This potential mechanism is proposed based on the reported

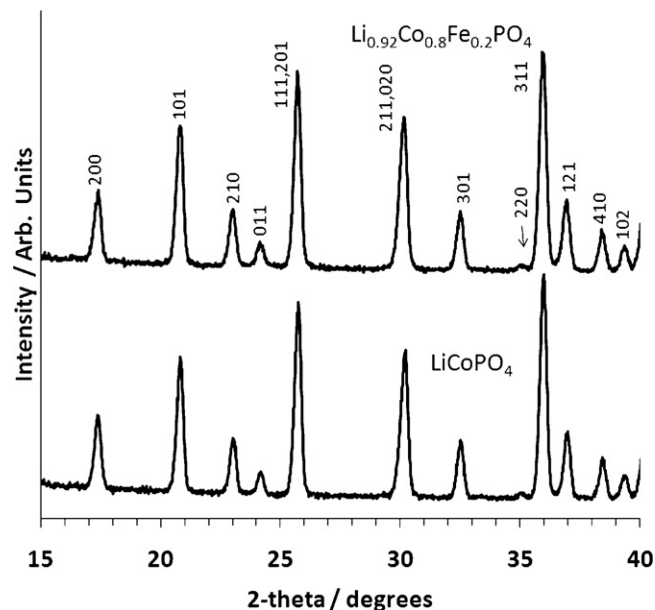


Fig. 1. X-ray powder diffraction pattern of $LiCoPO_4$ prepared via citrate aqueous precursor route, bottom, and the X-ray powder diffraction pattern of $Li_{0.92}Co_{0.8}Fe_{0.2}PO_4$, top. The peaks are labeled with the Miller indices of the phospho-olivine structure, $Pnma$ spacegroup.

decomposition of $CoPO_4$ to $Co_2P_2O_7$ and O_2 during heating under reducing conditions [11].

For the case of $LiCoPO_4$, the proposed decomposition reaction is:



A similar mechanism leading to the electrochemical formation of Li_2O was reported by Armstrong et al. [12] during the electrochemical charge of Li_2MnO_3 :



We believe that Fe^{3+} substitution on the Li^+ and Co^{2+} sites might be a means to slow these types of reactions owing to the higher affinity of Fe^{3+} to oxygen relative to Co^{2+} [13] and/or owing to changes in the underlying electronic structure of Fe^{3+} substituted $LiCoPO_4$ (or substituted $CoPO_4$) relative to pristine $LiCoPO_4$ (or $CoPO_4$).

$LiCoPO_4$ was prepared for comparison to substituted samples. A typical X-ray diffraction pattern is shown as the lower pattern in Fig. 1. The pattern confirms that a single phase $LiCoPO_4$ was prepared. A typical X-ray diffraction pattern is shown as the upper pattern in Fig. 1 for a sample of starting composition $LiCo_{0.8}Fe_{0.2}PO_4$. As with $LiCoPO_4$, there is no evidence of any impurity phases. ICP was used to calculate the amount of Fe^{3+} in the sample of starting composition $LiCo_{0.8}Fe_{0.2}PO_4$ from the assumption that the Fe^{3+} will be compensated by Li^+ ion vacancies. This atomic ratio was measured to be 0.92, which indicate 55% Fe^{2+} and 45% Fe^{3+} . Li^+ is volatilized during the synthesis in order to accommodate the Fe^{3+} . The product for the sample of starting composition $LiCo_{0.8}Fe_{0.2}PO_4$ was thus $Li_{0.92}Co_{0.8}Fe_{0.2}^{2+}Fe_{0.08}^{3+}PO_4$ or $Li_{0.92}Co_{0.8}Fe_{0.2}PO_4$, for short. Table 1 shows the lattice constants for the series of compounds prepared for this study.

Fig. 2 demonstrates the effect of Fe substitution on the capacity fade and the importance of the HFIP electrolyte additive. The $Li_{0.92}Co_{0.8}Fe_{0.2}PO_4$ composition was chosen to examine the cycle life since it had the largest capacity at the higher rate. The rate study will be discussed later in the paper. The cells were cycled between 2.5 and 5.3 V via a constant current method at C/5 rate except for the first two cycles which used a C/10 rate. The time of charge was

Table 1

Lattice constants for the series of Fe-substituted LiCoPO_4 compounds. Numbers in parentheses are the estimated standard deviation of the last significant digit.

Starting composition	a (Å)	b (Å)	c (Å)	Vol. (Å ³)
LiCoPO_4	10.1950(3)	5.9179(1)	4.6972(1)	283.39(1)
$\text{LiCo}_{0.95}\text{Fe}_{0.05}\text{PO}_4$	10.1913(4)	5.9190(2)	4.6983(2)	283.42(2)
$\text{LiCo}_{0.9}\text{Fe}_{0.1}\text{PO}_4$	10.1925(4)	5.9211(2)	4.6991(2)	283.60(2)
$\text{LiCo}_{0.8}\text{Fe}_{0.2}\text{PO}_4$	10.1981(3)	5.9252(1)	4.6986(1)	283.92(1)

also limited to 10 h for C/10 rate and 5 h for C/5 rate so that during the first few cycles the discharge capacity increased after the solid electrolyte interphase (SEI) was formed on the cathode [9].

From Fig. 2, several points can be made. We first, used a standard Li-ion electrolyte (1 m LiPF_6 in 3:7 EC:EMC) to compare LiCoPO_4 (blue open triangles) to the nominal $\text{Li}_{0.92}\text{Co}_{0.8}\text{Fe}_{0.2}\text{PO}_4$ composition (blue open squares). (For interpretation of the references to color in text, the reader is referred to the web version of the article.) For this case, it is clear that the Fe-substituted sample demonstrates considerable improvement in reducing capacity fade. However, capacity fade is still evident. Second, using a high voltage electrolyte (1 m LiPF_6 in 3:7 EC:EMC + 1% HFIP additive) we compare the capacity fade of the $\text{Li}_{0.92}\text{Co}_{0.8}\text{Fe}_{0.2}\text{PO}_4$ composition (orange solid squares) to the same composition with the standard electrolyte (blue open squares). For this comparison, there is additional decrease of the capacity fade with this change in electrolyte. Third, in order to discriminate fully between the effect of the high voltage electrolyte and the substitutional effects, we compare the LiCoPO_4 with standard electrolyte (blue open triangles) to LiCoPO_4 with the high voltage electrolyte (orange solid triangles). In this comparison, there is little discernible difference in the fading. Both samples evidence rapid capacity fade. The electrolyte has little effect. Thus, it is clear that structural decomposition of LiCoPO_4 or CoPO_4 is primarily responsible for the discharge capacity fade of the LiCoPO_4 electrode. In quantitative terms, about a 33% drop in capacity is observed between LiCoPO_4 (blue open triangles) and nominal $\text{Li}_{0.92}\text{Co}_{0.8}\text{Fe}_{0.2}\text{PO}_4$ (blue open circles) at the 10th cycle using a standard electrolyte. The drop in capacity between $\text{LiCo}_{0.8}\text{Fe}_{0.2}\text{PO}_4$ with high voltage electrolyte (orange solid squares) and $\text{Li}_{0.92}\text{Co}_{0.8}\text{Fe}_{0.2}\text{PO}_4$ with standard electrolyte (blue open squares) is 12%. Thus, the capacity fade is mainly a result of

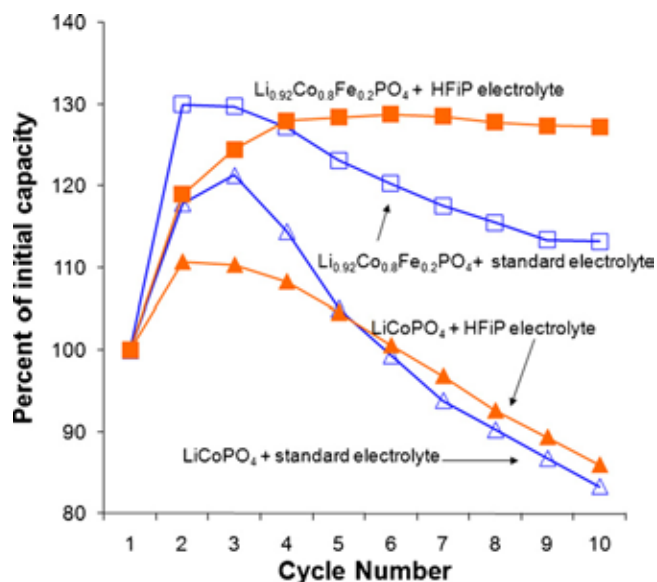


Fig. 2. Effect of LiCoPO_4 modification and HFIP electrolyte additive. The “standard (std.) electrolyte” is 1 m LiPF_6 in EC:EMC, 3:7. The HFIP electrolyte is 1 m LiPF_6 in EC:EMC, 3:7 with 1% HFIP electrolyte additive.

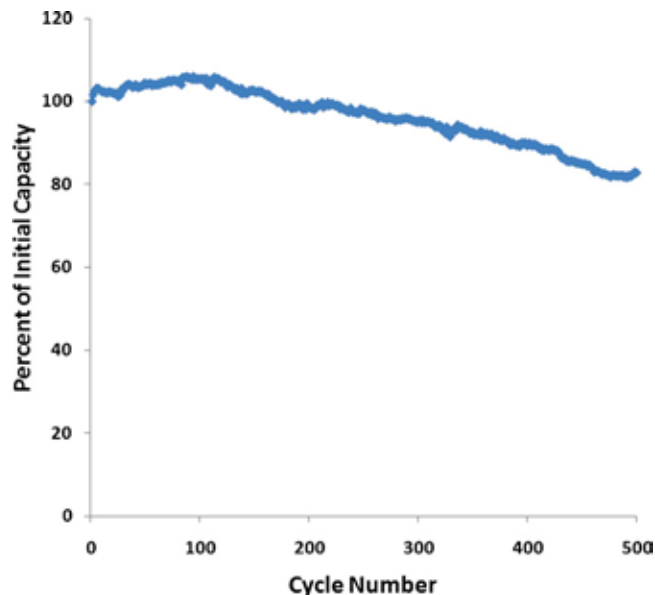


Fig. 3. Long term cycling of composition $\text{Li}_{0.92}\text{Co}_{0.8}\text{Fe}_{0.2}\text{PO}_4$ using 1 m LiPF_6 in EC:EMC, 3:7 with 1% HFIP electrolyte additive.

$\text{LiCoPO}_4/\text{CoPO}_4$ structural decomposition and, to a lesser degree, a result of electrolyte decomposition.

Fig. 3 shows the cycling performance of the $\text{Li}_{0.92}\text{Co}_{0.8}\text{Fe}_{0.2}\text{PO}_4$ composition over 500 cycles in a coin cell with Li metal as the anode. The coulombic efficiency is about 97%. Although, a noticeable fade is still evident it is a vast improvement over prior literature reports [4–6]. To reiterate, Tadanga et al. [4] observed a 10th cycle discharge capacity of ~52% of the initial capacity, Bramnik et al. [5] reported a 10th cycle discharge of ~59% of the initial capacity and Wolfenstine et al. [6] reported ~53% capacity retention at the 10th cycle. We observe approximately, 100% capacity retention at the 10th cycle and about 80% capacity retention at the 500th cycle. Fig. 4 shows the X-ray diffraction pattern of the cycled nominal $\text{Li}_{0.92}\text{Co}_{0.8}\text{Fe}_{0.2}\text{PO}_4$ cathode composite ($\text{Li}_{0.92}\text{Co}_{0.8}\text{Fe}_{0.2}\text{PO}_4$ with carbon and PVDF) on Al foil. All peaks can be assigned to the LiCoPO_4 olivine structure, indicating structural integrity after cycling of

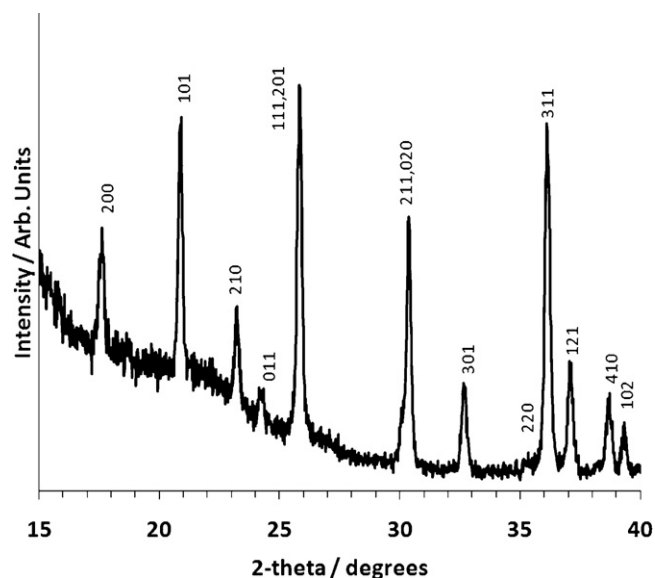


Fig. 4. X-ray diffraction of $\text{Li}_{0.92}\text{Co}_{0.8}\text{Fe}_{0.2}\text{PO}_4$ after electrochemical cycling. The peaks are labeled with the Miller indices of the $Pnma$, phospho-olivine structure.

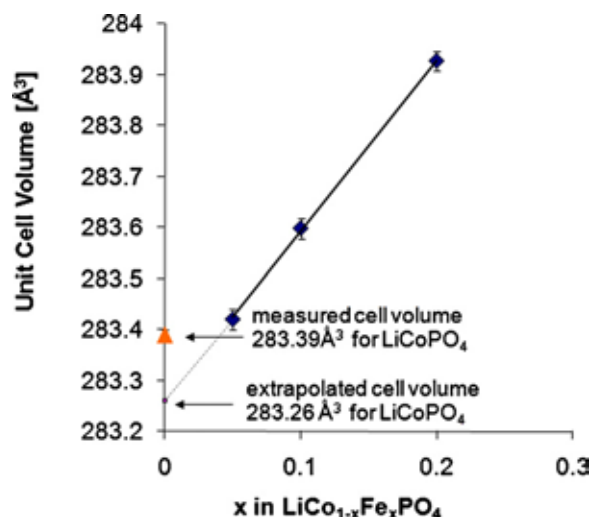


Fig. 5. Unit cell volume as a function of the nominal substitution of Co by Fe in LiCoPO₄.

the Li_{0.92}Co_{0.8}Fe_{0.2}PO₄ strikingly different from the reported amorphization of LiCoPO₄ during cycling [5,6].

Thus, we have shown the improved cycle life of Fe-substituted LiCoPO₄ and we assert that it mainly results from the substitution of Fe³⁺ on the Li and Co sites. In order to more fully characterize this substitution we turn to X-ray diffraction, XPS, FTIR spectroscopy and Mössbauer spectroscopy. First, from Rietveld analysis of the X-ray diffraction data, the unit cell volumes of LiCoPO₄ and Fe-substituted LiCoPO₄ were determined. Fig. 5 shows the effect on unit cell volume by the nominal substitution of Fe for Co²⁺ in LiCoPO₄. The observed linear increase in unit cell volume is consistent with the larger unit cell volume of LiFePO₄ relative to LiCoPO₄. However, the line extrapolated to zero does not intercept at the unit cell volume of Fe free LiCoPO₄ as would be expected for LiCo_{1-x}Fe_xPO₄ where only Fe²⁺ substitution for Co²⁺ is observed. The “extrapolated volume” is 283.26 Å³ and the measure volume is 283.39 Å³. This smaller unit cell volume results from the partial substitution of smaller Fe³⁺ for Li⁺ and Co²⁺.

Rietveld refinements were done to look at the anti-site defects, e.g., Fe³⁺ or Co²⁺ on the Li site. The results are shown in Fig. 6. Hence, this confirms that a small amount of Fe³⁺ is substituting at the Li site ($\sim 1.8 \pm 0.5\%$ for the nominal LiCo_{0.8}Fe_{0.2}PO₄ composition). The difference between the Li anti-site defect disorder concentration as a function of Fe content falls within the measurement error. There is on average for all samples about a $1.5 \pm 0.5\%$ concentration of anti-site defects on the Li site. Pujana et al. [14] previously reported the site preference of Fe³⁺ for the Li site in Li_{1-3x}Fe_xCoPO₄. They did not report Fe³⁺ substitution on the Co site. This difference from our materials is a result of different starting compositions and different reaction conditions.

Pujana et al. [14] also reported that the infrared (IR) spectra of Fe³⁺ substituted samples have broadened peaks owing to an increase of disorder resulting from the substitution of a portion of the lithium ions by Fe³⁺ and the creation of 2 vacancies per Fe³⁺ atom. The IR spectra of Fe-substituted LiCoPO₄ and LiCoPO₄ are shown in Fig. 7. We observed a small broadening upon substitution of Li by Fe³⁺, in agreement with Pujana et al. [14] Furthermore, as additional confirmation of Fe³⁺ in our samples, XPS revealed the presence of both Fe²⁺ and Fe³⁺ in a sample of nominal composition LiCo_{0.8}Fe_{0.2}PO₄. Two peaks were observed in the Fe2p spectra which can be assigned to Fe³⁺ and Fe²⁺.

Mössbauer spectra and analysis were obtained from the SEE Co. (Edina, MN) to corroborate the ICP data with respect to the relative amounts of Fe³⁺ and Fe²⁺ and to learn about the coordination envi-

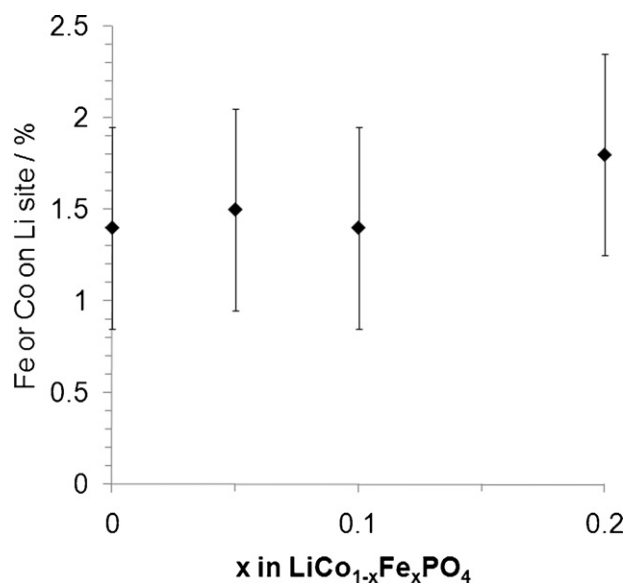


Fig. 6. Percent anti-site disorder on Li site from Rietveld refinement of X-ray diffraction data.

ronment of the Fe²⁺ and Fe³⁺. The room temperature spectrum is shown in Fig. 8. First, we identify the peaks as following: the doublet with the larger splitting (3.0 mm s^{-1}) is typical high spin ($S=2$) Fe²⁺. The doublet with the smaller splitting (0.8 mm s^{-1}) and shift (0.44 mm s^{-1}) is typical high spin ($S=5/2$) Fe³⁺ [14]. Second, the sharpness of the peaks gives information about the local environment. The Fe²⁺ lines are very sharp indicating that Fe²⁺ exclusively sits at one site, the Co site of LiCoPO₄ and locally all Fe²⁺ experiences a similar environment [15]. On the other hand, the lines of the Fe³⁺ doublet are broad. The broadening of the peak results from the differences in next nearest neighbors. The M2 (Co) octahedron shares edges with two M1 (Li) octahedra and corners with four M2 octahedra. Thus, the local environment of the M2 site is mainly controlled by the differences in the occupancy of the edge-sharing M1 sites. An Fe³⁺ sited on the M2 will be adjacent to an M1 site containing in order of likelihood either Li⁺, a vacancy, or Fe³⁺. Furthermore, vacant M1 sites will cluster around the Fe³⁺ therefore

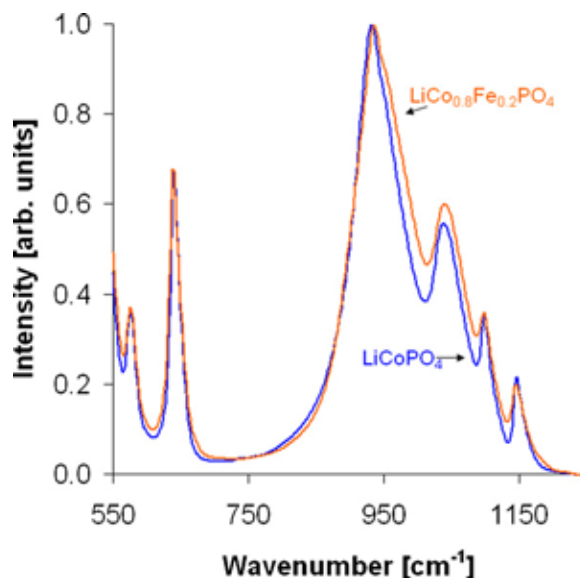


Fig. 7. Comparison of the infrared spectra of samples of nominal composition Li_{0.92}Co_{0.8}Fe_{0.2}PO₄ and LiCoPO₄.

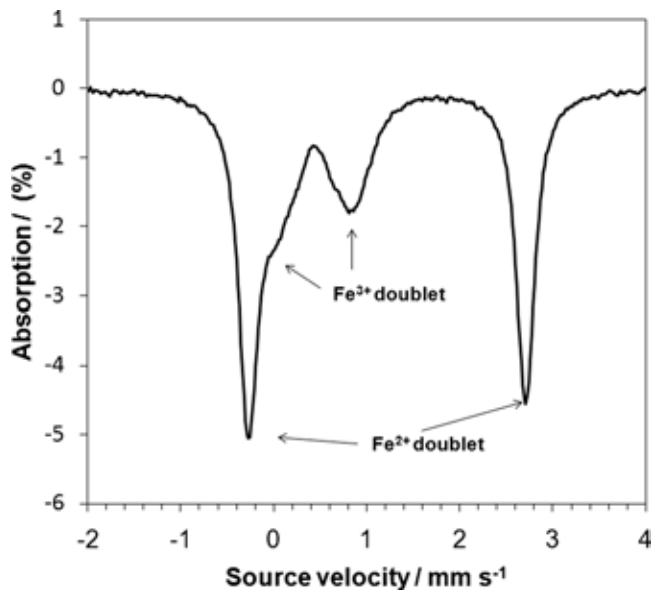


Fig. 8. Mössbauer spectrum of composition $\text{Li}_{0.92}\text{Co}_{0.8}\text{Fe}_{0.2}\text{PO}_4$.

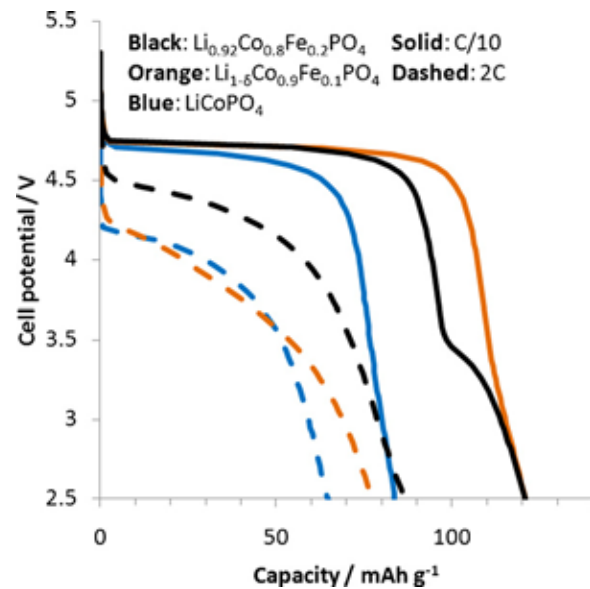


Fig. 9. Discharge curves at different rates for starting compositions, LiCoPO_4 , $\text{Li}_{1-\delta}\text{Co}_{0.9}\text{Fe}_{0.1}\text{PO}_4$, and $\text{Li}_{0.92}\text{Co}_{0.8}\text{Fe}_{0.2}\text{PO}_4$.

creating a more heterogenous environment for Fe^{3+} than for Fe^{2+} . Li and Shinno [15] described this “next nearest neighbor effect” in detail for the mineral ferrisicklerite, $\text{Li}_{1-x}\text{Mn}^{2+}_{1-x}\text{Fe}^{3+}_x\text{PO}_4$, a mineral isotopic with the phospho-olivines. Third, from the area of the peaks we can quantify the relative ratio of $\text{Fe}^{2+}/\text{Fe}^{3+}$. The Mössbauer spectrum yields 60% Fe^{2+} and 40% Fe^{3+} in excellent agreement with the ICP results. The analysis of the $\text{Fe}^{2+}/\text{Fe}^{3+}$ ratio by 2 independent methods and 2 different laboratories is summarized in Table 2. All are in excellent agreement.

Finally, having shown the improvements in capacity fade because of the Fe substitution into LiCoPO_4 , we now show the favorable effects of Fe substitution on capacity as a function of rate in Fig. 9. Typical discharge curves for an electrode of nominal starting composition LiCoPO_4 (blue), $\text{Li}_{1-\delta}\text{Co}_{0.9}\text{Fe}_{0.1}\text{PO}_4$ (orange) where δ is the Li vacancy concentration and $\text{Li}_{0.92}\text{Co}_{0.8}\text{Fe}_{0.2}\text{PO}_4$ (black) are shown. Solid lines represent a C/10 discharge rate and the dashed lines correspond to a 2C discharge rate. Several observations can be noted from Fig. 9. First and foremost, it is clear that Fe-addition improves the capacity at both C/10 and 2C compared to pure LiCoPO_4 . Second, at the C/10 rate we observe that the nominal $\text{Li}_{1-\delta}\text{Co}_{0.9}\text{Fe}_{0.1}\text{PO}_4$ has the longest plateau at 4.8 V. The discharge capacity for the nominal $\text{Li}_{0.92}\text{Co}_{0.8}\text{Fe}_{0.2}\text{PO}_4$ is equal, but a portion of the capacity is observed at around 3.5 V, which corresponds to the $\text{Fe}^{2+}/\text{Fe}^{3+}$ couple. The LiCoPO_4 discharge shows evidence of polarization (lower average discharge voltage) compared to the Fe-substituted LiCoPO_4 . Turning our attention to the 2C discharge curves, we observe that the nominal $\text{Li}_{0.92}\text{Co}_{0.8}\text{Fe}_{0.2}\text{PO}_4$ (black dashed curve) has the highest average discharge voltage and the highest capacity. The nominal $\text{Li}_{1-\delta}\text{Co}_{0.9}\text{Fe}_{0.1}\text{PO}_4$ and LiCoPO_4 have similar discharge voltages though $\text{Li}_{1-\delta}\text{Co}_{0.9}\text{Fe}_{0.1}\text{PO}_4$ has a larger capacity. At 2C, the $\text{Fe}^{3+}/\text{Fe}^{2+}$ plateau is not observed for either Fe containing composition.

Table 2

Analysis of the Fe^{3+} content for sample of starting composition $\text{LiFe}_{0.2}\text{Co}_{0.8}\text{PO}_4$.

Analysis method	Atom % Fe^{2+} of total Fe	Atom % Fe^{3+} of total Fe	Laboratory
Mössbauer	60	40	SEE Co.
ICP-OES (from Li/M)	55	45	Galbraith Laboratories, Inc.
Average	~58	~42	

The high rate performance may seem surprising owing to the presence of anti-site disorder on the Li site. As discussed previously, the nominal $\text{LiCo}_{0.8}\text{Fe}_{0.2}\text{PO}_4$ composition has about $1.8 \pm 0.5\%$ disorder on the Li site. Intuitively, one would expect that the presence of Fe on the Li site would impede the rate performance by blocking the Li ion channels. However, we postulate that anti-site Fe does not impede the rate for the following reasons. First, the anti-site defect concentration in the Fe substituted samples is not much greater than that reported for typical LiCoPO_4 [16]. Second, the anti-site defects will most likely cluster in some fashion. If the defects preferentially occupy certain Li^+ conduction channels they may effectively leave other channels clear to enable Li^+ conduction leading to higher conductivity than if anti-site defects are present in all the channels. The aggregation of defects is a well-known phenomenon. For example, Unger and Perlman [17] showed that divalent impurities in KCl and NaCl form impurity-vacancy dipoles that aggregate in order to form dipolar pairs. The vacancy is a center of excess negative charge and the divalent impurity has an excess positive charge. This creates an electric dipole which will prefer to interact with another dipole in order to collectively lower the energy of the two defects. Similarly, in Fe-substituted LiCoPO_4 the $\text{Fe}^{2+}_{\text{Li}}$ is a center of excess positive and its associated vacancies, V_{Li}^+ , are centers of excess negative charge and a lower energy state may be achieved by clustering of these defect-vacancy complexes into certain channels leaving other channels free to conduct Li and hence higher conductivity than anti-site defects in all channels. Finally, the rate capability is also a function of the electronic structure and so we further postulate that the rate capability of the Fe-substituted LiCoPO_4 is enhanced relative to pristine LiCoPO_4 because of the substitution of Fe for Co.

4. Conclusion

A synthesis method for Fe-substituted LiCoPO_4 electrode material has been reported. The improved rate and dramatically reduced capacity fade is striking. The capacity fade of LiCoPO_4 results mainly from structural decomposition of $\text{LiCoPO}_4/\text{CoPO}_4$ and to a lesser degree results from electrolyte decomposition. Fe^{3+} on the Li and Co sites appears to stabilize the structure. X-ray diffraction, XPS, Mössbauer Spectroscopy, ICP-OES and FTIR spectroscopy confirm the presence of Fe^{3+} on the Li and $\text{Fe}^{3+}/\text{Fe}^{2+}$ on the Co sites. Use of the HFiP containing electrolyte further reduced capacity fade during charge–discharge cycling of the Fe-substituted- LiCoPO_4 . This Fe-substitution in combination with the HFiP containing electrolyte shows dramatically improved discharge capacity retention as well as improved rate capability relative to un-substituted LiCoPO_4 with “standard” Li-ion electrolyte.

Acknowledgements

We thank ARL colleagues Kang Xu and Arthur von Cresce for providing electrolyte, Unchul Lee for XPS measurements and Bruce Poesse for obtaining FT-IR spectra. We thank Thomas Kent (SEE Co.) for obtaining and assisting with the analysis of the Mössbauer spectrum.

References

- [1] A.K. Padhi, K.S. Nanjundaswamy, J.B. Goodenough, *J. Electrochem. Soc.* 144 (1997) 1188.
- [2] K. Amine, H. Yasuda, M. Yamachi, *Electrochem. Solid State Lett.* 3 (2000) 178.
- [3] J. Wolfenstine, J.L. Allen, *J. Power Sources* 142 (2005) 389.
- [4] K. Tadanaga, F. Mizuno, A. Hayashi, T. Minami, M. Tatsumisago, *Electrochemistry* 71 (2003) 1192.
- [5] N.N. Bramnik, K.G. Bramnik, T. Buhrmester, C. Baehtz, H. Ehrenberg, H. Fuess, *J. Solid State Electrochem.* 8 (2004) 558.
- [6] J. Wolfenstine, U. Lee, B. Poesse, J.L. Allen, *J. Power Sources* 144 (2005) 226.
- [7] J. Wolfenstine, J. Read, J.L. Allen, *J. Power Sources* 163 (2007) 1070.
- [8] J. Wolfenstine, J.L. Allen, *J. Power Sources* 136 (2004) 150.
- [9] A.V. Cresce, K. Xu, *J. Electrochem. Soc.* 158 (2011) A337.
- [10] M.E. Rabanal, M.C. Gutierrez, F. Garcia-Alvarado, E.C. Gonzalo, M.E. Arroyo-de Dompablo, *J. Power Sources* 160 (2006) 523.
- [11] N.N. Bramnik, K. Nikolowski, D.M. Trots, H.E. Bramnik, *Electrochem. Solid-State Lett.* 11 (2008) A89.
- [12] A.R. Armstrong, M. Holzapfel, P. Novak, C.S. Johnson, S.H. Kang, M.M. Thackeray, P.G. Bruce, *J. Am. Chem. Soc.* 128 (2006) 8694.
- [13] R.H. Perry, D.W. Green, J.O. Maloney (Eds.), *Perry's Chemical Engineers' Handbook*, sixth ed., McGraw-Hill Book Company, New York, 1984, p. 3-149.
- [14] A. Pujana, J.L. Pizarro, A.A. Goni, T. Rojo, M.I. Arriortua, *Anal. Quim. Int. Ed.* 94 (1998) 383.
- [15] Z. Li, I. Shinnio, *Miner. J.* 19 (1997) 99.
- [16] S. Adams, *J. Solid State Electrochem.* 14 (2010) 1787.
- [17] S. Unger, M.M. Perlman, *Phys. Rev. B* 10 (1974) 3692.

Electrolyte Additive in Support of 5 V Li Ion Chemistry

Arthur von Cresce and Kang Xu

U.S. Army Research Laboratory, Adelphi, MD

ABSTRACT

An electrolyte additive based on highly fluorinated phosphate ester structure was identified as being able to stabilize carbonate-based electrolytes on 5 V class cathode surfaces. The synthesis and structural analysis of the additive are described, and preliminary yet encouraging results from electrochemical characterization showed that this additive participates in forming a protective interphasial chemistry not only on transition metal oxide cathode at high voltage (~ 5 V vs Li) but also on graphitic graphite at low voltage (~ 0 V vs Li), making it possible to formulate an electrolyte supporting reversible Li^+ -intercalation chemistry in the coveted 5 V region.

Journal of The Electrochemical Society, Volume 158, Number 3,
Pages A337-A342 (2011)



Electrolyte Additive in Support of 5 V Li Ion Chemistry

Arthur von Cresce* and Kang Xu*^z

Electrochemistry Branch, Power and Energy Division Sensor and Electron Devices Directorate,
U.S. Army Research Laboratory, Adelphi, Maryland 20783, USA

An electrolyte additive based on highly fluorinated phosphate ester structure was identified as being able to stabilize carbonate-based electrolytes on 5 V class cathode surfaces. The synthesis and structural analysis of the additive are described, and preliminary yet encouraging results from electrochemical characterization showed that this additive participates in forming a protective interphasial chemistry not only on transition metal oxide cathode at high voltage (~ 5 V vs Li) but also on graphitic graphite at low voltage (~ 0 V vs Li), making it possible to formulate an electrolyte supporting reversible Li^+ -intercalation chemistry in the coveted 5 V region.

© 2011 The Electrochemical Society. [DOI: 10.1149/1.3532047] All rights reserved.

Manuscript submitted October 27, 2010; revised manuscript received December 1, 2010. Published January 21, 2011. This was Paper 581 presented at the Las Vegas, Nevada, Meeting of the Society, October 10–15, 2010.

Li-ion chemistry is established upon reversible intercalation/deintercalation of Li^+ into/from host compounds.¹ The voltage of such an electrochemical device is dictated by the chemical natures of anode and cathode, where Li^+ is accommodated or released at low potentials in the former and high potentials in the latter. In the state-of-the-art Li-ion batteries, the operating voltage ranges between 3.5 and 4.2 V, as determined by the potentials of delithiated olivine ironphosphates or transition metal oxides against that of Li^+ -intercalated graphite, providing energy density between 110 and 175 Wh/kg, respectively.² In pursuit of both a higher energy density and a higher potential platform to deliver the energy, there have been persistent attempts in quest of a new cathode chemistry that can operate in the vicinity of 5 V, and various candidates have demonstrated this novelty, including $\text{LiCu}_x\text{Mn}_{2-x}\text{O}_4$ (~ 4.9 V),³ $\text{LiNi}_{0.5}\text{Mn}_{1.5}\text{O}_4$ (~ 4.7 V),⁴ $\text{LiNi}_x\text{Co}_{1-x}\text{PO}_4$ (4.8–5.1 V),⁵ $\text{Li}_2\text{FeCoPO}_4$ (~ 5.1 V),⁶ etc. However, a practical application of any of these 5 V class chemistries is possible only with the removal of a severe hurdle set by the electrolyte: the anodic stability limit of the nonaqueous components, especially solvents, on highly oxidative surfaces of these charged cathodes. In today's market, the majority of Li-ion batteries use organic carbonate esters as electrolyte solvents, whose sustaining decomposition above 4.5 V vs Li sets an intrinsic upper limit to the candidate cathode chemistry.^{7,8}

Efforts were made in the past to seek nonaqueous solvent alternatives to carbonate esters, and anodic stability higher than 5 V was reported for various systems, including asymmetric members from sulfone family,⁹ and ionic liquids based on ammonium, imidazolium, and pyrrolidinium cations and bis(trifluoromethane)sulfonyl imide anion.¹⁰ However, the intrinsic weaknesses of sulfone-based electrolytes, i.e., high viscosity and inability to form a protective solid electrolyte interphase (SEI) on graphitic anode surfaces, have either led to the formulation using low viscosity solvents, such as linear carboxylate ester at the expense of anodic stability,¹¹ or limited their use to applications where no graphitic carbon is used at the expense of both operating voltage and energy density¹²; meanwhile, ionic liquids introduced additional issues such as cathodic stability of these onium-based cations on graphitic carbon, high viscosity, and limited low temperature performance due to the supercooling of the resultant electrolytes. Especially, because most ionic liquids still rely on the use of fluorinated imide anions to ensure their low freezing temperature, there is a frequent concern about corrosion of the cathode substrate at high potentials despite various efforts to achieve passivation, while there is a constant concern about the cost.

In order to formulate an electrolyte composition that supports 5.0 V Li-ion intercalation cathode in combination with the low potential (< 0.20 V) graphitic anode, we have explored various ap-

proaches, including design and synthesis of both new solvents and additives. In the latter, we tried to minimize the disturbance to the bulk composition of the state-of-the-art electrolyte systems by using a trace amount of additives, which were already proven successful on graphitic anode,¹³ with the hope to tailor an interphasial chemistry on the cathode surface that can protect the bulk electrolyte components from oxidative decomposition. In this short communication, we report preliminary yet encouraging results obtained from such an additive based on a phosphate ester with highly fluorinated alkyl moieties.

Experimental

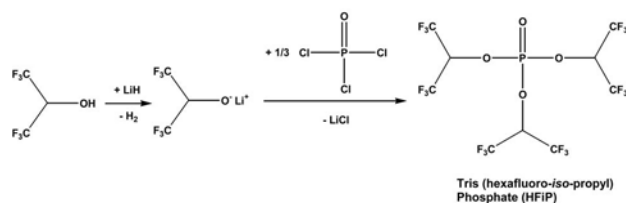
Synthesis of tris(hexafluoro-*iso*-propyl)phosphate ($((\text{C}_3\text{HF}_6\text{O})_3\text{PO}$ or HFiP) was conducted in a glassware setup equipped with water-chilled condenser, addition funnels, and outlets filled with silica drying agents. Thus, 0.45 mol 1,1,1,3,3,3-hexafluoro-2-propanol ($\text{C}_3\text{H}_2\text{F}_6\text{O}$, Fluka) was dissolved in 50 mL diethyl ether (Et_2O) at 0 – 5°C under continuous stirring, followed by the addition of 0.45 mol lithium hydride (LiH, Aldrich) through a solid-addition funnel. Once the generation of hydrogen stopped and the reaction suspension became clear, 0.15 mol phosphorus oxychloride (POCl_3 , Aldrich) was introduced dropwise through an addition funnel. Precipitation of solid lithium chloride (LiCl) was observed immediately and persisted until the end of the reaction. Heat generation at the initial addition of POCl_3 was intense enough to keep the Et_2O refluxing; but near the late stage, the reaction mixture had to be further refluxed by gently heating for 5 h to ensure the completion of phosphorylation of alkoxides. Ether was removed by distillation, and HFiP was purified through repeated distillations. Purified product appeared as a clear needlelike crystal with melting and boiling points of approximately 27°C and 50 – $55^\circ\text{C}/3.0$ mm Hg, respectively. For a higher purity, HFiP can also be sublimed under vacuum at $\sim 30^\circ\text{C}$. Electrospray ionization mass spectrum (EISMS) and NMR spectra of ^1H -, ^{13}C -, and ^{19}F -nuclei were used to confirm its chemical structure.

All procedures involving electrolyte solutions and cell assembly were carried out in dry room, whose dew point is approximately -90°C , or glove box, where moisture level is below 5 ppm. Ethylene carbonate (EC), propylene carbonate (PC), ethyl methyl carbonate (EMC), and methylpropyl carbonate (MPC) were purchased from Ferro, Corp., dried over molecular sieves, and stored in an argon-filled glove box. The moisture level in the dried solvents was below 10 ppm according to Karl–Fischer titration. Lithium hexafluorophosphate (LiPF_6) from Stella Chemifa was used as received; 1.0 M LiPF_6 in EC/EMC (30:70 by weight) was selected as baseline electrolyte, while a high voltage electrolyte was formulated by dissolving 1% (weight) HFiP in the baseline.

CR2032 coin cells with aluminum-clad cap were used as testing hardware, and 0.8 mm lithium foil cut to 12.7 mm diameter

* Electrochemical Society Active Member.

^z E-mail: cxu@arl.army.mil



Scheme 1. Synthesis of HFiP.

(1.27 cm²) was used as the counter electrode/anode. LiNi_{0.5}Mn_{1.5}O₄ cathode material synthesized as reported was coated onto Al foil and punched into 11.1 mm diameter (0.97 cm²) circular electrodes. Celgard 3501 with a hydrophilized surface was used as separator. All test cells were assembled with a Hohsen automatic crimper. Galvanostatic cycling of the assembled cells was conducted on a Maccor Series 4000 Battery Tester, wherein a constant charge/discharge current of 0.5 mA from 3.5 to 4.95 V with no rest in between charge and discharge cycles. All cycling tests were performed at room temperature (21°C).

Results and Discussion

Synthesis and structural identification of HFiP.— Because the bulky fluorinated groups in hexafluoro-*iso*-propanol constitute spatial hindrance to the access of its hydroxyl, conventional approach using trialkyl amine as an organic base catalyst usually lead to a low yield (< 30%) of the title compound HFiP,¹⁴ leaving behind a reaction mixture of corresponding mono- and biesters of phosphoric acid. To ensure that POCl₃ be completely alkylated at maximum yield, we activated the nucleophilicity of the alcohol by converting it into lithium alkoxide, which reacts exothermically with POCl₃ at much improved yields (Scheme 1). The reaction yield of the alkoxide with POCl₃ ranged averagely above 50%, as assessed from the crude products.

HFiP can be purified by repeated distillation or recrystallization in appropriate solvents; if desired, highly purified HFiP can also be obtained by sublimation under high vacuum in a warm water bath.

HFiP exists as a crystalline solid at room temperature; above its melting temperature, it acts as a viscous and weakly polar solvent that shows negligible solubility toward most of the lithium salts, likely due to the presence of high fluorine density in the molecule. However, in most cases, it is miscible with typical nonaqueous electrolytes based on organic carbonate esters, especially when linear carbonate such as EMC or DMC is the dominating cosolvent. A phase separation occurs only when high HFiP concentration (> 10%) is used in a solution where cyclic carbonate such as EC is above 30%.

Purified HFiP was subjected to structural analysis, and Figs. 1a–1c showed the NMR spectra collected on this compound in deuteriated acetonitrile (CD₃CN). In addition to signals arising from the solvent and internal reference (0.00 ppm, singlet, from tetramethylsilane; 1.95 ppm, multiplet, from CD₃CN; and 2.15 ppm, singlet, from trace moisture in CD₃CN), there is only one NMR-anisotropic proton as detected in ¹H spectra, which is represented by a collection of multiplets ranging between 5.6 and 5.9 ppm with complicated structures. Upon closer examination (Fig. 1a, left side inset, above), these multiplets seem to consist of two sets of heptets that partially overlap with each other. We speculated that this split pattern correspond to the substructure as shown in Scheme 2a, where the proton is simultaneously split by six neighboring ¹⁹F nuclei and one ³¹P-nucleus, giving rise to total of 7 × 2 = 14 peaks. An estimation based on the heptet pattern yielded a coupling constant of ~5.19 Hz, typical of a spin-spin coupling between ¹H and ¹⁹F-nuclei in vicinal positions.¹⁵

In order to simplify the spectra and confirm the source of these spin-spin interactions, we decoupled the interaction between ¹H- and ¹⁹F-nuclei by exercising irradiation at the characteristic Larmor frequency of the latter, and the above multiplets turned into a doublet (Fig. 1a, left side inset, below), with a coupling constant of 11.99 Hz, typically observed between ¹H and ³¹P-nuclei.¹⁵ On the other hand, ¹⁹F-spectra collected detected only one NMR-anisotropic ¹⁹F-nucleus that is split into a doublet (Fig. 1a, right side inset, above), with a coupling constant of 5.26 Hz, which is in a good agreement with the reciprocal coupling constant of 5.19 Hz as estimated from the ¹H-spectra. Furthermore, the above doublet merged into a singlet when ¹H-decoupling is conducted (Fig. 1a,

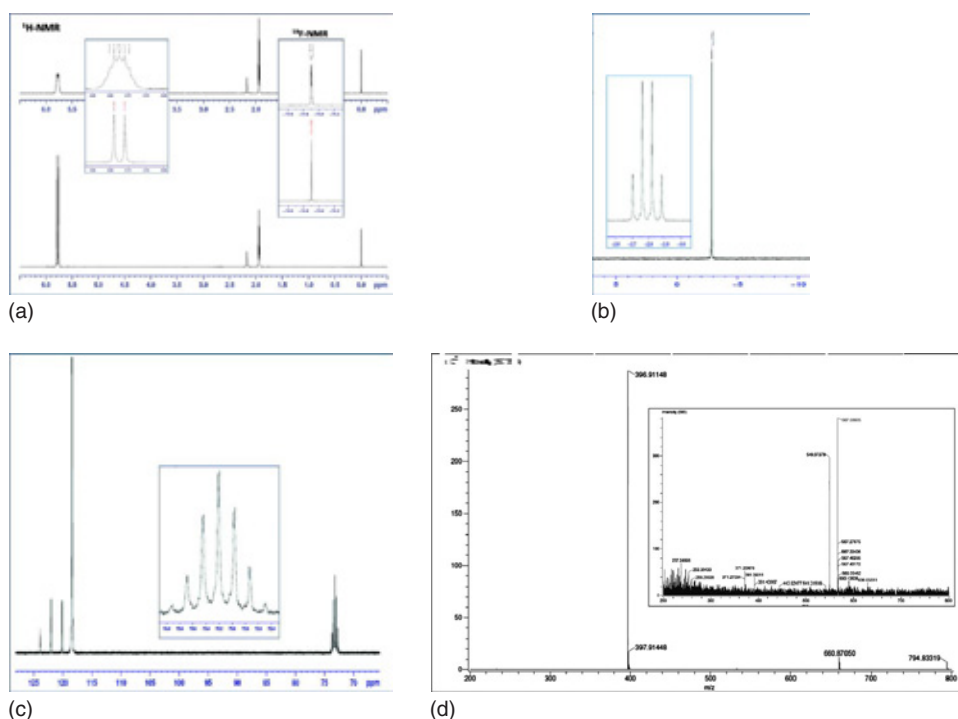
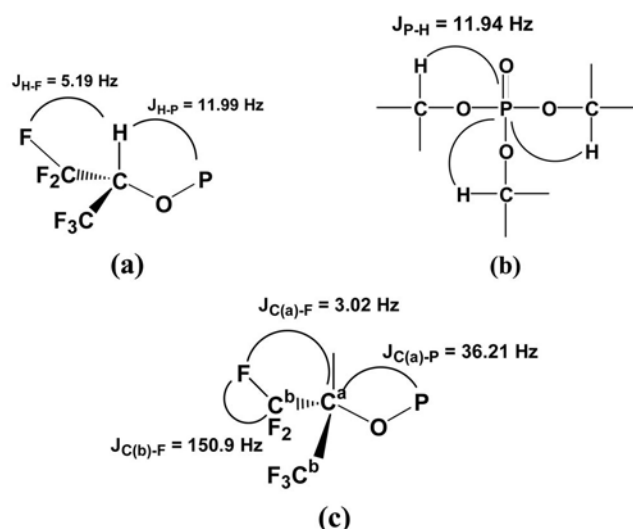


Figure 1. (Color online) (a) ¹H-spectra of HFiP in CD₃CN without ¹⁹F-decoupling; J_{H-F} = 5.19 Hz; left inset, above: two sets of ¹H-heptet due to simultaneous spin-spin couplings with both ¹⁹F- and ³¹P-nuclei; left inset, below: ¹H-spectra with ¹⁹F-decoupling; J_{H-P} = 11.99 Hz; right inset, above: ¹⁹F-spectra without ¹H-decoupling; J_{F-H} = 5.26 Hz; right inset, below: ¹⁹F-spectra with ¹H-decoupling. These spin-spin couplings along with individual coupling constants confirm the substructure shown in Scheme 2a. (b) ³¹P-Spectra of HFiP with ¹H-decoupling in CD₃CN using H₃PO₄ as external reference; inset: ³¹P–¹H spin-spin coupling with J_{P-H} = 11.94 Hz confirming substructure in Scheme 2b. (c) ¹³C-Spectra of HFiP with ¹H-decoupling in CD₃CN; inset: simultaneous ³¹P- and ¹⁹F coupling generate two sets of heptets with J_{C(a)-F} = 3.02 Hz, J_{C(b)-F} = 150.902 Hz, and J_{C(a)-P} = 36.20 Hz, respectively, confirming substructure in Scheme 2c.



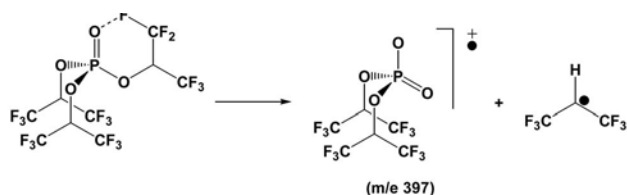
Scheme 2. Substructures derived from the spin-spin couplings as observed in Fig. 1: (a) ^1H -nucleus is split simultaneously by six vicinal ^{19}F -nuclei and one vicinal ^{31}P -nucleus; (b) ^{31}P is split by three vicinal ^1H -nuclei; (c) $^{13}\text{C}^a$ is split simultaneously by six vicinal ^{19}F -nuclei and one ^{31}P -nucleus, while $^{13}\text{C}^b$ by six germinal ^{19}F -nuclei.

right side inset, below). This confirms that (1) there is only one NMR-isotropic fluorine in the molecule, and (2) they are all located at a vicinal position with a single NMR-isotropic ^1H -nucleus. Because of the remote locations of these two atoms in HFiP molecule, there is no spin-spin coupling found between ^{19}F - and ^{31}P -nuclei, which is consistent with the structure of HFiP as illustrated in Scheme 1.

The ^{31}P -spectra (Fig. 1b) also detected only one NMR-anisotropic ^{31}P -nucleus, which was found between 2.7 and 2.9 ppm as a quartet and turned into a singlet at 2.862 ppm upon ^1H -decoupling irradiation. This ^{31}P - ^1H spin-spin interaction has a coupling constant of 11.94 Hz, again in a good agreement with 11.99 Hz of the ^1H - ^{31}P interaction. More importantly, the quartet pattern with ^1H -coupling, which can only arise from a substructure where ^{31}P is surrounded by three NMR-isotropic ^1H -nuclei (Scheme 2b), confirmed that the compound has to be a triester of phosphoric acid, instead of partial alkylation products of phosphoric acid such as mono- or biesters.

^{13}C -spectra were shown in Fig. 1c, where, in addition to the solvent molecules (1.33 ppm, singlet, and 118.20 ppm, multiplet for CD_3CN), two NMR-anisotropic ^{13}C -nuclei were detected, which are represented by a multiplet at 72.50–74.0 ppm for C^a and a quartet between 123.86–118.41 ppm for C^b as shown in the substructure of Scheme 2c. (Note that the rightmost peak of the quartet overlapped with the solvent signal at 118.41 ppm.) The coupling constant between C^b and F is ~ 150.902 Hz, consistent with the germinal spin-spin interaction between a ^{13}C - and ^{19}F -nuclei. Of special interest is the $^{13}\text{C}^a$ -nucleus at 72.50–74.0 ppm, which is obviously composed of two sets of heptets (inset, Fig. 1c). Because these twin heptets were obtained under the condition of ^1H -decoupling, the pattern has to arise from simultaneous splitting by six ^{19}F - and one ^{31}P -nuclei, whose coupling constants are $J_{\text{C-F}} = 3.02$ Hz and $J_{\text{C-P}} = 36.21$ Hz, respectively. This split pattern acts as the structural key that links the F-nuclei in alkyl moiety and P-nucleus in phosphate moiety, thus confirming the substructure represented in Scheme 2c.

Mass spectra were used to further characterize HFiP. As shown in Fig. 1d, initial spectra failed to show the molecular peak (m/e 548), which may indicate the reactivity of its radical cation with a possible connection to its decomposition at the positively charged



Scheme 3. Proposed fragmentation routes of HFiP under ionization state.

electrode surfaces. The major peak at m/e 396.9 is a fragment arising from HFiP losing one of the fluoroalkyl side arms, probably through a McLafferty-like rearrangement mechanism with the generation of a very stable radical (Scheme 3).

On the other hand, there are multiple signals representing larger molecular weight species (m/e 660.8, 794.8, 1192, 1628, etc.), which are apparently the dimeric, trimeric, and even polymeric forms of HFiP or clusters of its fragments with new bonds formed. The exact bonding configurations in these oligomeric species are unclear at the moment and would require analytic tools that can provide more detailed structural connectivity information. However, in a general sense, this propensity of HFiP to polymerize may hint at the preference of the molecule to form a network under oxidative condition and even might be the source of its electrochemical behavior on a 5 V-class cathode surfaces.

Eventually, by employing a mild soft-ionization technique to prevent fragmentation, which is usually used to analyze fragile molecules, we successfully obtained the protonated and hydrated forms of the molecule in high abundance ($\text{M} + \text{H}^+$, m/e 549 and $\text{M} + \text{H}_3\text{O}^+$, m/e 567), which are shown as inset of Fig. 1d.

Based on the structural information summarized above, we have firmly established the chemical identity of the synthesized compound HFiP.

Rationale for tailoring cathode interphasial chemistry.— Since the birth of Li ion chemistry, the central role of the electrode/electrolyte interphase in this device has been recognized. However, the majority of the investigations have hitherto focused on the anode side for various reasons, the most important of which being the need to stabilize the “fragile” graphene structure against a possible solvent intercalation.¹⁶ The understanding of the oxidation mechanism of electrolyte components, especially the carbonate solvents, on the surfaces of cathode materials has been scarce,^{7,17} and there is still an on-going debate regarding whether an interphase such as the one observed on graphitic anode surface also exists on the cathode, despite spectroscopic detection of similar chemical deposits in the latter. However, there is a consensus among researchers that the commonly used nonaqueous electrolyte solvents based on organic carbonate esters are not stable at potentials beyond 4.5 V vs Li,^{7,8,10} thus setting technical challenge to the application of a high voltage Li ion chemistry.

With increasing interests in developing new Li ion chemistries of higher energy density, researchers have resumed in recent years the quest for 5 V class cathode materials, and several approaches have been taken from solid chemistry perspective to mitigate the strongly oxidative nature of these 5 V class cathode surfaces, such as lattice-doping or surface coating,¹⁸ with various degree of success; on the other hand, we believe that the most economical approach based on the consideration of processing cost should be from an electrolyte perspective, whose effectiveness has already been proven with the various electrolyte additives nowadays widely employed by the Li ion battery industry to modify the interphasial chemistry on graphitic anode. Similar to anode, the cathode in a newly assembled Li ion cell is in “discharged state,” whose potential is only gradually brought up to the “charged state” during the initial activation stage of the cell; therefore, we envision that this stepwise potential increase would provide us the opportunity of tailoring the interphasial chemistry on the cathode surface by selecting appropriate chemical

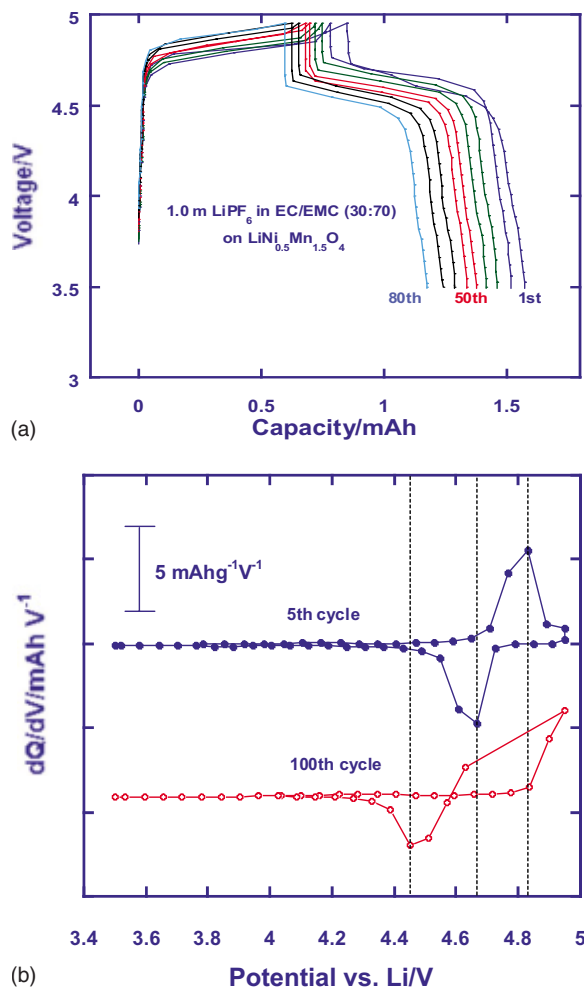


Figure 2. (Color online) (a) Voltage profiles of a 5 V class cathode $\text{LiNi}_{0.5}\text{Mn}_{1.5}\text{O}_4$ in baseline electrolyte $\text{LiPF}_6/\text{EC}/\text{EMC}$ (30:70). Only selected cycles were shown for graphic clarity. (b) Comparison of differential capacity of $\text{LiNi}_{0.5}\text{Mn}_{1.5}\text{O}_4$ in baseline electrolyte for the 5th and the 100th cycles.

species, whose sacrificial oxidation occurs before oxidation of the bulk electrolyte components and whose oxidation products passivate the catalytic sites of the cathode surface. Leveraging knowledge in interphasial chemistry on graphitic anode as well as corrosion-protection science of metal surfaces, we have designed and synthesized several families of chemicals that have the potential to act as protective passivates on transition metal oxide surfaces. In testing the effectiveness of these chemicals on a host of a 5 V class cathode materials, a member of the phosphate ester family, HFIP, stands out conspicuously, reminiscent of the phosphate-treatment techniques adopted for corrosion-prevention in steel industry,¹⁹ the corrosion-inhibitor used to passivate aluminum surfaces in the high voltage electrolytic capacitor,²⁰ and similar modification of transition metal oxide surfaces to modulate catalysis.²¹ Extensive tests on diversified 5 V cathode materials have confirmed the versatility of HFIP under a high voltage constraint, which will be described in future publications. Here we selected to highlight the interphasial novelties of HFIP on the surfaces of a candidate “5 V” cathode $\text{LiNi}_{0.5}\text{Mn}_{1.5}\text{O}_4$ and a graphitic anode.

Electrochemical characterization on a 5 V cathode surface.— Spinel structured $\text{LiNi}_{0.5}\text{Mn}_{1.5}\text{O}_4$ with a redox potential between 4.5 and 4.7 V was selected as the primary testing platform for the high voltage electrolyte formulated in this study. Figure 2a showed its voltage profile in a cathode half cell constructed with baseline electrolyte and Li as counter electrode and cycled galvanostatically

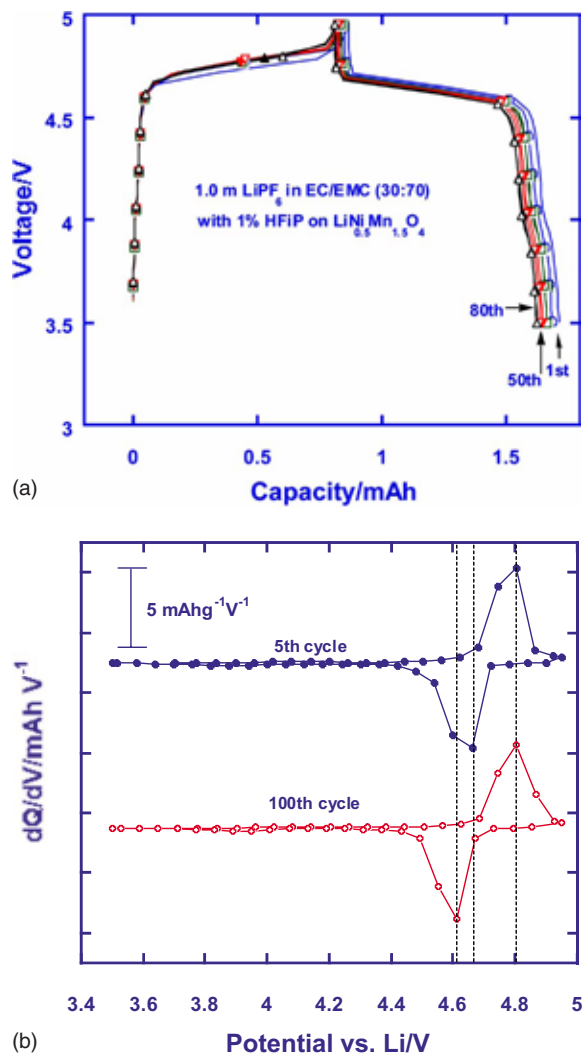


Figure 3. (Color online) (a) Voltage profiles of a 5 V class cathode $\text{LiNi}_{0.5}\text{Mn}_{1.5}\text{O}_4$ in baseline electrolyte with 1% HFIP as additive. Only selected cycles were shown for graphic clarity. (b) Comparison of differential capacity of $\text{LiNi}_{0.5}\text{Mn}_{1.5}\text{O}_4$ in electrolyte with HFIP as additive for the 5th and the 100th cycles.

statically between 3.5 and 4.95 V. Although reversible Li^+ -intercalation/deintercalation was observed in the expected potential range, both the rapidly decreasing capacity utilization and the increasing ohmic drop as characterized by the voltage hysteresis between charging and discharging profiles indicated that there is a severe and sustaining electrolyte decomposition on the cathode surface. The ac impedance spectra measured before and after cycling have confirmed the cell resistance increase with cycling (not shown here), while differential capacity plots made for the 5th and the 100th cycle best represented the worsening irreversibility of the cell chemistry with the widening separation between the lithiation and delithiation peaks (Fig. 2b). As comparison, with only 1% HFIP present in the baseline electrolyte, both capacity fading and the ohmic drop between charging and discharging profiles were minimized as shown in Figs. 3a and 3b. Figure 4 compared the cycle life of $\text{LiNi}_{0.5}\text{Mn}_{1.5}\text{O}_4$ in both baseline and high voltage electrolytes in the span of 200 cycles, which is close to the limit set by the lithium dendrite growth in a half cell. Although the capacity fading still exists with HFIP-presence, there is already a significant improvement as compared with the baseline, and we are expecting that ad-

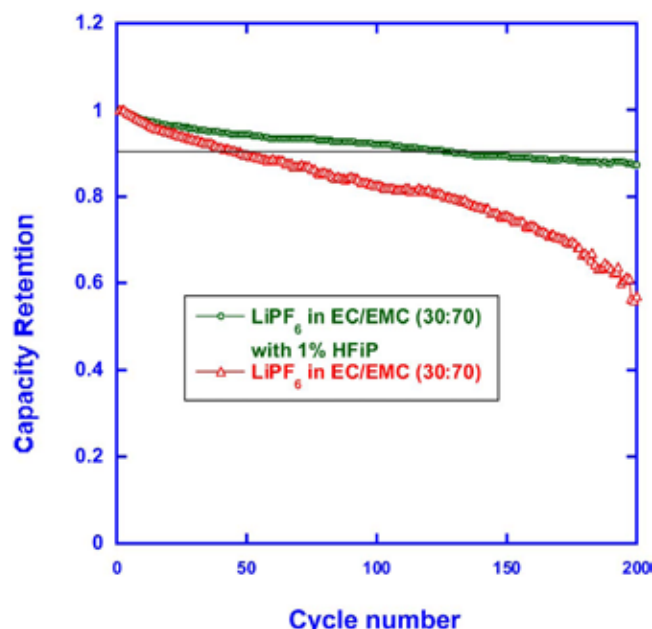


Figure 4. (Color online) Galvanostatic cycling performance of $\text{LiNi}_{0.5}\text{Mn}_{1.5}\text{O}_4$ in baseline and additive-containing electrolytes. Capacity retention was used for convenience of comparison, while the actual utilization of $\text{LiNi}_{0.5}\text{Mn}_{1.5}\text{O}_4$ is 98 mAh/g with baseline electrolyte and 108 mAh/g with HFiP-containing electrolyte.

ditional stabilization is possible with the combination of the current electrolyte approach and the lattice stabilizations/surface modifications from the solid chemistry perspective.¹⁸

To further confirm that it was the presence of HFiP that stabilized the interphase between the 5 V cathode and electrolyte, we took the test of our electrolyte to an extreme condition, where only a linear carbonate MPC was used as the neat solvent and no EC was present. It was well known that most of those linear carbonate are not anodically stable beyond 4.0 V vs Li,^{8,9b} and EC presence is required not only for interphasial chemistry on graphitic anode but also for anodic stability on the 4.0 V class cathode materials currently used in Li ion industry. As shown in Fig. 5, LiPF_6/MPC electrolyte did not survive initial charging to 4.95 V and was never able to support any Li^+ -intercalation/deintercalation chemistry between 4.5 and 4.7 V; instead, the voltage profile behave much like that of a double-layer capacitance due to the high resistance built on the cathode surface and the lack of Faradaic processes (only the first cycle was shown). On the other hand, LiPF_6/MPC with only 1% HFiP not only provided the Li^+ -intercalation/deintercalation chemistry in the range of 4.4–4.90 V but also, surprisingly, survived the prolonged cycling with even a slight improvement in the polarization. While the detailed mechanism of the decreasing resistance is still unclear, it is unequivocal that HFiP must have participated in some interphasial process on spinel $\text{LiNi}_{0.5}\text{Mn}_{1.5}\text{O}_4$. Based on its test on other 5.0 V cathode platforms (to be published), this participation of HFiP at a high potential might be universal.

Effect on graphitic anode.— In order for a new electrolyte additive to be used in Li ion system, its effect on every cell component that it would be in contact with must be taken into consideration. In the current case, the importance of graphitic anode is only second to the cathode because it is known that the stacked graphene layer structure is very sensitive to variation in electrolyte.²² We selected mesocarbon microbead (MCMB) as the representative of the various graphitic anode materials used in commercial Li ion batteries and evaluated the potential impact of HFiP. Figure 6a showed the voltage profile of such an MCMB anode in both baseline and the high voltage electrolytes formulated with 1% HFiP. As we have expected,

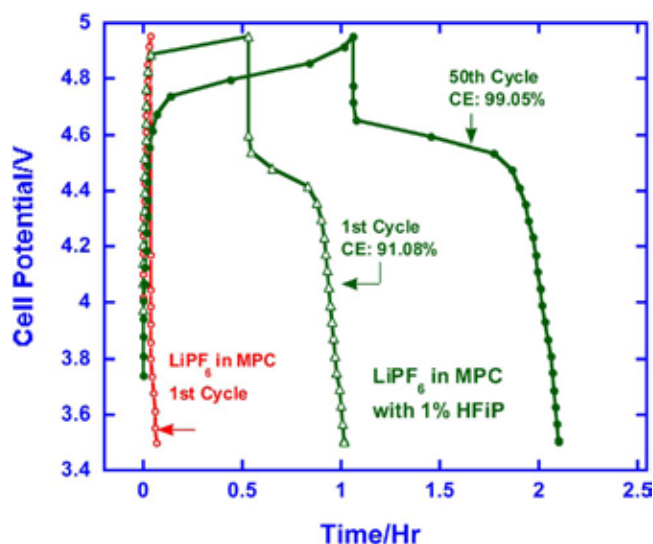


Figure 5. (Color online) Confirming HFiP-induced interphasial chemistry on cathode surface under extreme condition: voltage profiles of $\text{LiNi}_{0.5}\text{Mn}_{1.5}\text{O}_4$ in electrolytes based on a single solvent electrolyte using a linear carbonate (MPC) with or without 1% HFiP. Only the first cycle was shown for LiPF_6/MPC because its subsequent cycles essentially showed no difference from the first.

due to the small presence of additive, the difference between the baseline and the high voltage electrolyte is negligible; if there is any difference, both the capacity utilization and Coulombic efficiency in the first cycle of HFiP-containing electrolyte are slightly better than those of baseline. Upon closer examination, there seems to be an early electrochemical reduction event in HFiP-containing electrolyte at potentials around 1.2 V (inset, Fig. 6a), which we tentatively attribute to the initial reductive decomposition of HFiP; but at the moment, we must caution that a conclusion on the role of this 1.2 V event for a better SEI formed cannot yet be drawn with certainty, as we have learnt in the past from the 1.7 V event of bis(oxalato)borate (BOB) anion.²³ Further studies are needed to understand the nature of this reductive process, and its impact on the performance of graphitic anode materials in electrolytes containing HFiP and related additive materials.

To further reveal the cathodic property of HFiP on graphitic anode, we took it to another extreme condition, where PC was used as the neat solvent. It was well known that graphitic structure is sensitive to solvent cointercalation, and PC is the most typical solvent that fails to form a stable anode SEI to stop extensive graphene-exfoliation due to its cointercalation.^{8,22} The behavior of graphite anode in a PC-dominant electrolyte is thus typically characterized by a flat voltage profile at 0.7–0.8 V, where indefinite solvent decomposition proceeds without any Li^+ -intercalation chemistry involved, as shown in Fig. 6b. However, with only 1% HFiP presence in PC, the above cointercalation/exfoliation process was quickly suppressed by a new interphasial chemistry, and reversible Li^+ -intercalation chemistry was eventually realized after a brief initial decomposition bump that corresponds to PC cointercalation. The subsequent lithiation/delithiation for more than 30 cycles (only the initial four cycles were shown for clarity) proved that this new interphasial chemistry, apparently with chemical signature of HFiP, serves as a protective SEI as one usually formed in EC-containing electrolyte. This unexpected merit of HFiP certainly adds on its potential to be a part of the 5 V electrolytes.

It should be noted here that the above scenarios of employing MPC and PC as neat electrolyte solvents were not meant to demonstrate either one as a practical system; rather, they created such

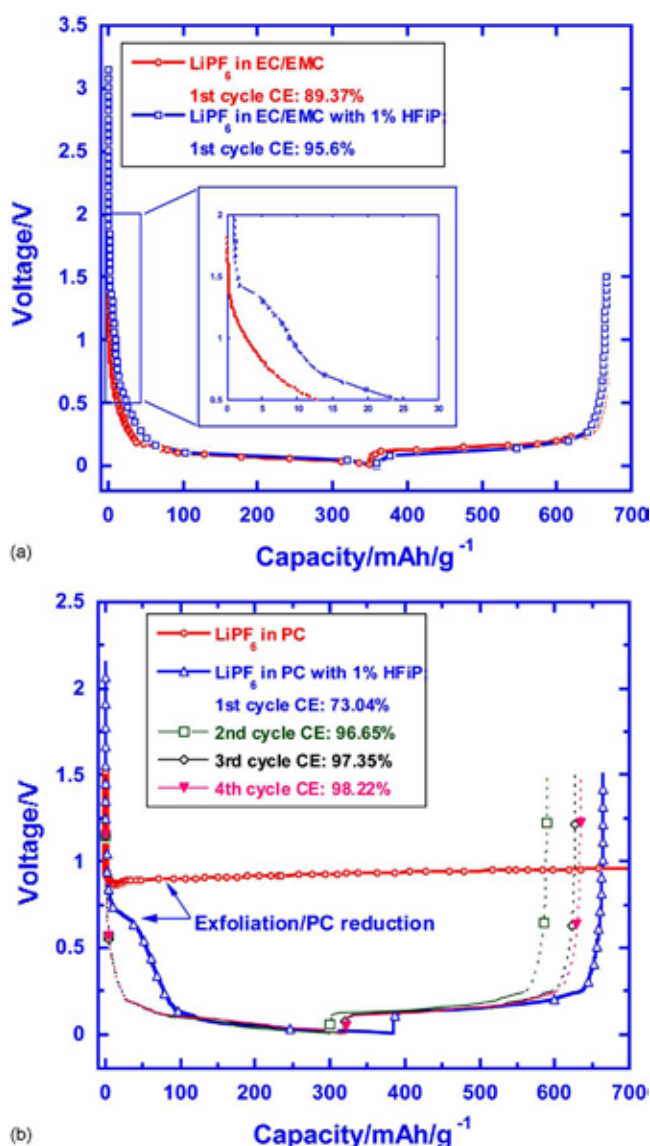


Figure 6. (Color online) (a) Exploring HFIP-effect on interphasial chemistry of graphitic anode: comparison of voltage profiles of graphitic anode in a Li half cell with baseline electrolytes containing none or 1% HFIP. (b) Confirming HFIP effect on interphasial chemistry of graphitic anode under extreme condition: comparison of voltage profiles of graphitic anode in a Li half cell with electrolytes based on PC containing none or 1% HFIP.

conditions under which the effect of our target HFIP could be “exaggerated” to stand out. Apparently, both Figs. 5 and 6b served this purpose perfectly.

Conclusion

Through electrolyte approach to stabilize nonaqueous electrolytes on a 5.0 V class cathode materials, we synthesized and identified an additive that is based on a highly fluorinated phosphate triester and carried electrochemical characterizations in a Li ion

environment. The preliminary yet encouraging results indicate that the new additive not only significantly improved the anodic stability of the electrolyte on a “5.0 V class” spinel $\text{LiNi}_{0.5}\text{Mn}_{1.5}\text{O}_4$ but also provided unexpected protective SEI chemistry on the graphitic anode. Further experiments are underway to understand how this additive participates in interphasial chemistries chemically and mechanistically and to evaluate its practical application in the 5.0 V full Li ion batteries.

Acknowledgment

This project was partially funded by Department of Energy Advanced Battery Research (DOE-ABR) Program. The authors thank Professor Amatucci of Rutgers University for providing cathode materials samples, and Dr. Yufai Lam and Dr. Yue Li for providing NMR services and Mass Spectrum Services, respectively.

U.S. Army Research Laboratory assisted in meeting the publication costs of this article.

References

1. M. Winter and R. J. Brodd, *Chem. Rev.*, **104**, 4245 (2004).
2. M. S. Whittingham, *Chem. Rev.*, **104**, 4271 (2004); J. B. Goodenough and Y. Kim, *Chem. Mater.*, **22**, 587 (2010).
3. Y. Ein-Eli and M. F. Howard, Jr., *J. Electrochem. Soc.*, **144**, L205 (1997); Y. Ein-Eli, W. Howard, S. Lu, S. Mukerjee, J. McBreen, J. Vaughey, and M. Thackeray, *J. Electrochem. Soc.*, **145**, 1238 (1998).
4. Y. Gao, K. Myrtle, M. Zhang, J. N. Reimers, and J. R. Dahn, *Phys. Rev. B*, **54**, 3878 (1996); T. Ohzuku, S. Takeda, and M. Iwanaga, *J. Power Sources*, **81**, 90 (1999); S. Mukerjee, X. Yang, X. Sun, S. Lee, J. McBreen, and Y. Ein-Eli, *Electrochim. Acta*, **49**, 3373 (2004).
5. J. Wolfenstine and J. Allen, *J. Power Sources*, **136**, 150 (2004); J. Wolfenstine, *J. Power Sources*, **142**, 389 (2005).
6. D. Wang, J. Xiao, W. Xu, Z. Nie, C. Wang, G. Graff, and J.-G. Zhang, *J. Power Sources*, In press. [10.1016/j.jpowsour.2010.10.021].
7. L. Yang, B. Ravdel, and B. Lucht, *Electrochem. Solid-State Lett.*, **13**, A95 (2010).
8. K. Xu, *Chem. Rev.*, **104**, 4303 (2004).
9. K. Xu and C. A. Angell, *J. Electrochem. Soc.*, **145**, L70 (1998); K. Xu and C. A. Angell, *J. Electrochem. Soc.*, **149**, A920 (2002).
10. S. Martha, E. Markevich, V. Burgel, G. Salitra, E. Zinigrad, B. Markovsky H. Sclar, Z. Pramovich, O. Heik, and D. Aurbach, *J. Power Sources*, **189**, 288 (2009); V. Borgel, E. Markevich, D. Aurbach, G. Semraub, and M. Schmidt, *J. Power Sources*, **189**, 331 (2009).
11. Y. Watanabe, S.-I. Kinoshita, S. Wada, K. Hoshino, H. Morimoto, and S.-I. Tobishima, *J. Power Sources*, **179**, 770 (2008).
12. A. Abouimrane, I. Belharouak, and K. Amine, *Electrochem. Commun.*, **11**, 1073 (2009).
13. S. Zhang, *J. Power Sources*, **162**, 1379 (2006).
14. J. March, *Advanced Organic Chemistry*, 3rd ed., p. 357, John Wiley & Sons, New York (1985).
15. R. Freeman, *A Handbook of Nuclear Magnetic Resonance*, 2nd ed., Longmans, New York (1997).
16. M. Winter, *Z. Phys. Chem.*, **223**, 1395 (2009).
17. K. Kanamura, S. Toriyama, S. Shiraishi, and Z. Takehara, *J. Electrochem. Soc.*, **142**, 1383 (1995).
18. J. Liu and A. Manthiram, *Chem. Mater.*, **21**, 1695 (2009); J. Liu and A. Manthiram, *J. Phys. Chem. C*, **13**, 15073 (2009).
19. M. J. Franklin, D. C. White, and H. S. Isaacs, *Corros. Sci.*, **33**, 251 (1992); G. Li, L. Niu, J. Lian, and Z. Jiang, *Surf. Coat. Technol.*, **176**, 215 (2004).
20. J. J. Randall, T. H. Nguyen, and C. E. Hutchins, U.S. Pat. 4,470,885 (1984); S. D. Ross, U.S. Pat. 4,541,037 (1985); S. D. Ross and M. Finkelstein, U.S. Pat. 4,580,194 (1986).
21. G. Ramis, P. P. F. Rossi, G. G. Busca, V. V. Lorenzelli, A. A. La Ginestra, and P. Patrono, *Langmuir*, **5**, 917 (1989); M. Francisco, W. Cardozo, and Y. Gushikem, *Langmuir*, **20**, 8707 (2004).
22. M. R. Wagner, J. H. Albering, K. C. Moeller, J. O. Besenhard, and M. Winter, *Electrochem. Commun.*, **7**, 947 (2005); K. Xu, *J. Electrochem. Soc.*, **156**, A751 (2009).
23. K. Xu, S. S. Zhang, B. A. Poese, and T. R. Jow, *Electrochem. Solid-State Lett.*, **5**, A259 (2002); K. Xu, S. S. Zhang, and T. R. Jow, *Electrochem. Solid-State Lett.*, **6**, A117 (2003).

Interfacing Electrolytes with Electrodes in Li Ion Batteries

Kang Xu and Arthur von Cresce

U.S. Army Research Laboratory, Adelphi, MD

ABSTRACT

Since its birth in early 1990s, Li ion battery technology has been powering the rapid digitization of our daily life and finally made its debut in 2010 into the large format application for electrified vehicles such as the Nissan Leaf and GM Chevrolet Volt; however, much of the chemistry and processes underneath this amazing energy storage device still remain to be understood, among which is the interphase between electrolyte and electrodes. Interphases are formed in situ on electrode surfaces from sacrificial decomposition of electrolytes. Their ad hoc chemistry supports the reversible Li^+ -intercalation in both anode and cathode materials at extreme potentials, while preventing parasitic reductions/oxidations on the reactive surfaces of those electrodes; but their existence places restrictions on energy and power densities of the device by impeding Li^+ -transport and setting operating voltage limits, respectively. It has been the dream of battery engineers to maximize the former and minimize the latter. This review summarizes the most recent knowledge about the chemistry and formation mechanism of this elusive battery component on both anode and cathode surfaces. The attempts to tailor a desired interphasial chemistry via diversified means were also discussed.

Journal of Materials Chemistry, Volume 21, Pages 9849-9864 (2011)

Interfacing electrolytes with electrodes in Li ion batteries

Kang Xu* and Arthur von Cresce

Received 9th December 2010, Accepted 7th February 2011

DOI: 10.1039/c0jm04309e

Aqui...

Onde a terra termina

e o mar já não começa

—A poetic definition of a binary liquid/solid interface by Luís de Camões (1572).

Since its birth in early 1990s, Li ion battery technology has been powering the rapid digitization of our daily life and finally made its debut in 2010 into the large format application for electrified vehicles such as the *Nissan Leaf* and *GM Chevrolet Volt*; however, much of the chemistry and processes underneath this amazing energy storage device still remain to be understood, among which is the interphase between electrolyte and electrodes. Interphases are formed *in situ* on electrode surfaces from sacrificial decomposition of electrolytes. Their *ad hoc* chemistry supports the reversible Li^+ -intercalation in both anode and cathode materials at extreme potentials, while preventing parasitic reductions/oxidations on the reactive surfaces of those electrodes; but their existence places restrictions on energy and power densities of the device by impeding Li^+ -transport and setting operating voltage limits, respectively. It has been the dream of battery engineers to maximize the former and minimize the latter. This review summarizes the most recent knowledge about the chemistry and formation mechanism of this elusive battery component on both anode and cathode surfaces. The attempts to tailor a desired interphasial chemistry *via* diversified means were also discussed.

1. Introduction: Interface in electrochemical devices

To material scientists whose major interest lies with the bulk properties, an interface is where one material ends and the other begins; to electrochemists, however, the interface is the essential component that separates electrochemistry from conventional chemical reactions.¹ It was because of these interfaces between electrode and electrolyte materials that the otherwise random and chaotic electron exchanges in a conventional redox reaction are now forced to proceed in an orderly manner, producing orientation movement by electrons (current) in an external circuit, and a simultaneous movement by ions within the cell. Thus, in any electrochemical device, these electrode/electrolyte interfaces are the only “legitimate” locations where cell reactions should happen; otherwise, the reactions are deemed “parasitic” and are usually irreversible and detrimental.

A cell reaction can be either spontaneous, as in a fuel cell, primary battery or rechargeable battery during discharge, or non-spontaneous, as in an electrolytic or electroplating cell, or rechargeable battery during charge.² In the latter case an external electron source is needed to drive the energy-consuming reactions. During the electrochemical cell reactions, the electrode materials are the only chemical reactants consumed or produced,

while electrolyte, at least in theory, must remain chemically inert when providing ionic flow to balance the change in electro-neutrality induced by the oxidation or reduction in the electrodes. In reality, however, the role of an electrolyte is by no means so “inert” in cell reaction. More often than not, its chemical composition is significantly interwoven with the formation chemistry and the subsequent properties of the interfaces, which directly or indirectly dictate how well an electrochemical device functions. In some scenarios the electrolyte formulation even determines whether a desired cell reaction can occur electrochemically or not, and Li-based batteries present the best examples of such scenarios.³

Since electron exchanges can only happen at electrode/electrolyte interfaces, in all the electrochemical scenarios these interfaces always dictate the cell reaction kinetics, which, for a battery, represents the rate at which energy can be released (or captured if a rechargeable system is considered). For a rechargeable battery, an interface also participates in determining whether the cell reactions can be reversed, and if they do, with what Coulombic and energy efficiencies, which represents the reversibility and the cycle life of the rechargeable device. Furthermore, the interface could even indirectly affect the energy density by setting limits of voltage window, within which the devices can operate safely and reversibly. This bottleneck effect of electrolyte becomes especially conspicuous in the efforts of developing a coveted “5 V” class Li ion chemistry.

Electrochemistry Branch, Power and Energy Division, Sensor and Electron Devices Directorate, U. S. Army Research Laboratory, 2800 Powder Mill Road, Adelphi, MD, 20783

In modern electrochemicals, the electrode/electrolyte interface has been treated as a 2-D layer for mathematic convenience, which is an approximation close to reality in most aqueous electrochemical devices. In those devices the low operating voltage ensures that most of the electrolyte components are thermodynamically stable on the surfaces of both cathode and anode materials, therefore the interfaces mainly consist of both electrolyte solvents and solutes adsorbed on the surface of the electrode, also known as the inner-Helmholtz layer. The thickness of interfaces is estimated to be less than 2 nm, so that *trans*-interface electron-tunneling is possible, and kinetics of such electron transfer process can be described by the Butler-Volmer equation.¹

In the most common configuration of electrochemical devices, both electrodes are solid and stationary, while the electrolytes sandwiched between them are either liquid or solid, thus the interface locations are usually stationary and well-defined. However, there are certain electrochemical scenarios where complications in defining electrolyte/electrode interfaces arise due to the use of liquid or mobile electrode materials. One such example is set by the flow battery that employs cell reactants suspended in electrolytes and in constant movement relative to current collectors. In these non-classical cases, the interfaces exist only instantaneously at the surfaces of suspended particles that are colliding with the current collector.⁴ Despite the complication, the essence of an interface remains unchanged nevertheless: it is the demarcation between an electronic conductor (electrode) and an ionic conductor (electrolyte).

2. Interphase in Li ion batteries

The attraction of lithium as the “Holy Grail” anode originates from the fortuitous combination of three factors that can never be duplicated by any elements in the periodic table: (1) its lowest atomic weight as a metal providing the largest theoretical specific capacity of 3860 mAh/g; (2) its smallest density ($5.4 \times 10^2 \text{ Kg m}^{-3}$) as a metal providing the highest possible gravimetric energy density; and (3) its most negative electrochemical potential (-3.10 V vs. SHE) proving the highest possible cell voltage when coupled with given cathode materials. To circumvent the morphological catastrophe arising from lithium dendrite growth, graphite intercalation compounds (GIC) of Li^+ were used instead of lithium metal, resulting in a loss of *ca.* 0.2 V cell voltage and more than 90% original capacity.⁵ Nevertheless, when coupled with a 4.0 V class cathode, which is also an intercalation host for Li^+ , the Li-GIC still produce the rechargeable chemistry of the highest energy density. The state-of-the-art Li ion battery is thus based on the reversible intercalation/de-intercalation chemistries of Li^+ into/from the interstitial spaces in graphite anode and transition metal oxide or phosphate cathodes, generating 100–200 Wh/Kg energy at 3.5–4.0 V.⁶

Because of the reactivity of anode and cathode materials employed in Li-based batteries, there is almost no known electrolyte that can remain thermodynamically stable on their surface at charged states; alternatively, upon the initial activation of a Li ion battery, there is always trace amount of electrolyte sacrificially decompose, whose subsequent products deposit on these active electrode surfaces, and passivate the catalytic sites, preventing sustained decomposition of the bulk electrolyte. Since the subsequent cell reaction, which requires Li^+ -

intercalation/de-intercalation, can still proceed with the presence of this passivating layer, its main characteristic is to insulate any electron-transfer or tunneling between the bulks of electrode and electrolyte but allow Li^+ -migration.^{7,8} In other words, it acts like a thin-layer electrolyte. Obviously this passivating layer, different from both electrode and electrolyte both chemically and morphologically, is no longer a simple 2-D existence as in the classic interface; rather, it is an independent phase. Peled named it “solid electrolyte interphase (SEI)” after its electrolyte nature.⁸ The crucial role of SEI in supporting the reversible Li ion intercalation chemistry is now well recognized.

Perhaps the best example highlighting the importance of interphase is the so-called “EC-PC disparity” and its impact on the history of Li ion technology.⁹ GIC with Li^+ as guest intercalant was first discovered in early 1950’s by reacting graphite with either molten lithium metal or lithium vapor.¹⁰ Almost immediately thereafter, efforts were made to prepare this GIC electrochemically, with obvious hope to explore the possibility of a new anode material. However in the following four decades, despite the discovery of various intercalation hosts as cathode candidates⁶ and the maturing understanding of solid intercalation chemistry,¹¹ there was never a single success in preparing Li-GIC through electrochemical means. The failures are almost exclusively due to the lack of understanding in interphasial chemistry on graphitic surface, and to most part, should be attributed to one non-aqueous polar solvent used popularly at the time, propylene carbonate (PC), whose methyl substituent happens to render the resultant interphasial deposition non-protective.^{9,12} Highly graphitic anodes thus exfoliate in electrolytes based on PC, which reductively decomposes at $\sim 0.70 \text{ V}$ and prevents any Li^+ -intercalation chemistry from occurring. At certain point the frustration even led to the belief that it was beyond any possibility to prepare Li^+ -GIC electrochemically. Not until 1990s did people realize that the above “insurmountable” obstacle can be easily resolved by simply using a close cousin of PC, ethylene carbonate (EC).⁷ Eventually the interphasial chemistry based on EC catalyzed the birth of Li ion battery in today’s configuration. In retrospect, it is without much exaggeration to state that the difference between interphasial chemistries, induced by a single methyl group, delayed the emergence of Li ion technology by nearly four decades!

Like a classic interface, SEI in Li ion devices still significantly affects – and dictates in some cases – the kinetics of cell reaction (or power density of the device); but more importantly, SEI determines the reversibility of the cell chemistry and hence cycle life of the device. In a Li ion battery that employs intercalation hosts as cathode and anode, Li^+ is a limited source, and any loss of Li^+ is at the expense of capacity and energy density of the device. The formation chemistry of SEI leads to such consumption of Li^+ , which are converted into lithium salts insoluble in electrolyte solutions and hence “electrochemically inactive”. Thus, the effectiveness of SEI is often measured by the amount of Li^+ consumed in the initial forming cycles as well as the average loss in following operation cycles. These two parameters, known as “irreversible capacity” and “capacity fading (rate)”, respectively, determines how reversible the cell reactions proceed and how long the service life of the device can last. In the past two decades major efforts on developing new electrolytes and additives have been focused on improving these two parameters.

An excellent kinetic analysis on SEI was conducted by Dahn and coworkers, who developed a high precision coulometry technique to investigate the irreversible loss associated with the reversible lithiation and delithiation chemistries of various electrodes.^{13,14,15} They attributed this lost capacity at each cycle to the continuous growth of SEI, based on the assumption that Li^+ turns electrochemically inactive once becoming part of the interphase. It was found that, at the given temperature, the thickness of SEI increases with time^{1/2}, while its growth rate is inversely proportionate to the thickness. In this sense, decomposition of electrolyte to form the interphase mathematically never ends with cycling, and these reactions are actually dependent on how much time the electrolyte is exposed to the electrode at these lithiation or delithiation potentials, but independent from whether the cells are cycled or not. This study revealed the “leaky” feature of the interphases, which were often misinterpreted as a simple ionic conductor and electronic insulator. In reality, electron-tunneling or transfer can still occur across these interphases under certain conditions, one of which being sufficient polarization potential, as evidenced by the use of redox shuttle chemicals for the purpose of over-charge protection.

On the other hand, although these interphases are known to be pervious to Li^+ transport, Li^+ conductivity across them was never directly measured. A very elegant diagnosis done by Harris *et al.* recently convinced us that Li^+ “trapped” in the SEI are actually rather mobile, although with lower diffusivity compared with their counterparts in bulk electrolyte or electrode interior.¹⁶ They formed SEI on a Cu substrate by using isotopic ^6Li -based electrolyte, which was then soaked in a regular ^7Li -based electrolyte for various time intervals. Subsequent analysis by TOF-SIMS technique found that most of the $^6\text{Li}^+$ “trapped” in the SEI can be displaced by $^7\text{Li}^+$ in the electrolyte solution on a time scale of hours. Thus, the compositions of interphases are “dynamic” in this sense rather than “static”. In an approximation these interphases can be visualized as a cation (Li^+) exchange layer, whose framework is based on organic anions and which allows Li^+ -conduction to proceed in a Grotthuss-like mechanism.

Apparently, SEI functions as a protective layer that prevents the sustained decomposition of electrolyte components and safeguards the reversible Li^+ -intercalation chemistry; at the same time, this new phase also presents a rather resistive component that is serial in the complete circuit with the bulk electrolyte and electrodes.¹⁷ Its bottleneck effect on mass-transfer becomes more pronounced at low temperatures or high drain rates. Therefore, it is of great significance to the Li ion battery industry to reduce the impedances that is associated with the interphases while maintaining its protective function, especially on the graphitic anode side.

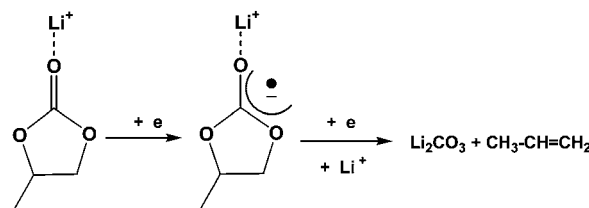
The current state-of-the-art electrolytes used in Li ion batteries are almost exclusively based on organic carbonate esters as solvents, and lithium salts with inorganic fluorinated anions as solutes, the results of compromise when a collection of requirements that an ideal electrolyte should meet are applied.³ SEI formed in such electrolytes can passivate both GIC anode down to the potential lithium metal electrode (~ 0 V vs. Li) and various oxide or phosphate cathodes up to >4.0 V vs. Li. However, these interphases cannot stabilize the carbonate-based electrolytes beyond 4.5 V limit, constituting a severe challenge to the development of new Li ion cathode chemistry that aims at delivering energy at higher voltages in the neighborhood of 5.0 V.¹⁸ Unfortunately, the understanding about formation chemistry of interphase on oxidative surfaces has

been rather limited as compared with the efforts made on interphases of reductive surfaces, especially graphitic carbons. The recent thrust driven by U. S. Department of Energy (DOE) to target new Li ion chemistry of 5 V is expected to divert more resources into this under-investigated area.

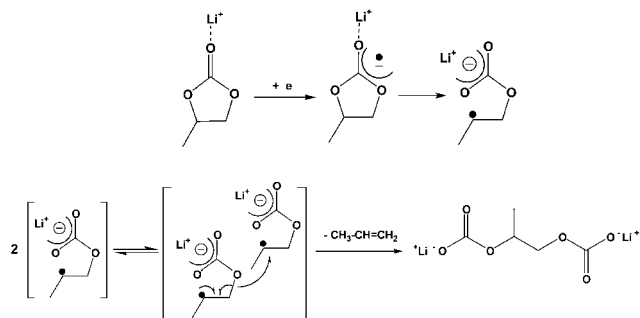
2.1 On graphitic carbon anode

Despite the diversified cathode chemistries used by various manufacturers, the anode material in today’s Li ion batteries stays a constant, which is highly graphitic carbon.⁵ Li^+ intercalates into its inter-layer spaces at voltage *ca.* 0.20 ± 0.05 V with high reversibility, generating a capacity of 372 mAh/g. Compared with cathode materials, in which the lattice is built upon strong Coulombic forces or covalent bonds, the layer structure of graphite is held together only by weak van der Waals interactions between the sp^2 -hybridized graphene slabs, and is therefore rather susceptible to co-intercalation of solvent molecules. It was for this reason that, although Li^+ -GIC was discovered in 1950s, its electrochemical preparation came much later than the cathode counterparts (which was discovered in late 1970s). It was also because of this solvent-sensitivity of graphitic anode that the investigations on SEI in the past two decades were mostly placed on anode side, leaving the cathode surface to oblivion until recently. Thanks to the monumental contributions from Aurbach *et al.*^{19–21} and Besenhard and Winter *et al.*,^{22,23} we now have gained substantial understanding about the chemistry as well as the formation mechanism of these interphases on graphitic anodes.

2.1.1 Chemistry. During the earlier unsuccessful attempts to prepare Li^+ -GIC in PC-based electrolytes, people identified Li_2CO_3 as the major deposit on the exfoliated graphite surface, and a two-electron reduction mechanism was proposed:¹²

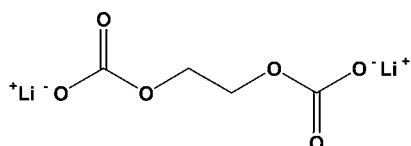


in which the organic moiety is completely lost in the form of gaseous product, leaving behind an inorganic interphase. However, this mechanism was soon challenged by Aurbach *et al.*,¹⁹ who proposed that, considering the poor availability of electrons on the graphite surface, an incomplete reduction should occur instead, consisting of a radical anion as intermediate and subsequent intermolecular electron-transfer between the two radical anions:



Averagely there is only one electron involved per PC molecule, hence this mechanism is called “single-electron” reduction pathway. Obviously, in this single-electron mechanism only half (50%) of the organic moiety is lost in the form of gas, while the rest is maintained in the final anionic product, known as either alkylcarbonate or semi-carbonate, and becomes part of the interphasial layer. Based on the extensive characterization work carried out in Aurbach’s group and others, the spectroscopic signatures of this class of compound were established, which include the asymmetric carbonyl stretching at 1650 cm^{-1} in FTIR^{20,21} and the C 1s electron binding energy at 289 eV in XPS.²⁴ Since lithium salts of these alkylcarbonates are extremely moisture-sensitive, their instantaneous conversion to Li_2CO_3 upon exposure to even trace amount of moisture explained the origin of the two-electron mechanism proposed earlier, which was most likely the consequence of poor moisture-exclusion practice.^{25,26} The moisture-interference issue is of critical importance to all ex-situ experimental tools employed to investigate the interphase in Li ion devices.

Having established the above single-electron reduction mechanism of carbonate solvents on graphitic anode surface, Aurbach went further to suggest that the key ingredient of SEI on anode side was actually such an alkylcarbonate from EC, dilithium ethylene dicarbonate (LEDC), based on its overwhelming presence in spectroscopy:



This in part accounts for the fact that EC is an indispensable electrolyte co-solvent in nearly all Li ion batteries on market despite unique (and proprietary) electrolyte formulations used by each individual manufacturer.

In more systematic effort to establish a baseline knowledge about the interphase formed through reductive pathways, this group at Army Research Lab (ARL) teamed up with scientists at Lawrence Berkeley National Lab (LBNL) and synthesized these alkylcarbonate compounds *in vitro* with high purity, and collected the spectroscopy of these standard references to form a reliable database.^{27,28} These alkylcarbonates consist of an entire series of homologous lithium alkylcarbonates, lithium methylcarbonate (LMC), lithium ethylcarbonate (LEC), dilithium propylene dicarbonate (LPDC) and LEDC, which are supposed to form from the corresponding single-electron reduction pathways of all commonly-used electrolyte solvents in commercial Li ion batteries, as shown in Fig. 1.

The selected NMR and FTIR spectra of these alkylcarbonate compounds are shown in Fig. 2, from which rich structural and morphological information can be extracted. For example, in interpreting the presence of FTIR absorptions, *ab initio* computation on the chemical structure indicated that a better fitting to the experimental data could be achieved if LEDC takes a dimer or even multi-mer conformation,²⁷ which was not observed for LPDC although the latter is also a dilithium salt. It is very likely that LEDC is more prone to form a network instead of remaining a monomer in the SEI as well.

The real importance of the spectroscopic database lies in their service as reliable references of comparison when the cycled electrode surfaces are studied. Often, detailed chemical information can be extracted to either support or deny certain chemical species that were suggested earlier as possible SEI building blocks. For example, based on their dynamic function theory (DFT) computation, Wang *et al.* once proposed that alkylcarbonate of higher order (such as dibutylencarbonate) should be more thermodynamically favored through the single-electron pathway and radical anion recombination.²⁹ However, the NMR spectra unequivocally excluded this possibility, as the unique alkyl substructure should be easily detected. Instead, in all the scenarios, simple alkylcarbonate were the overwhelming

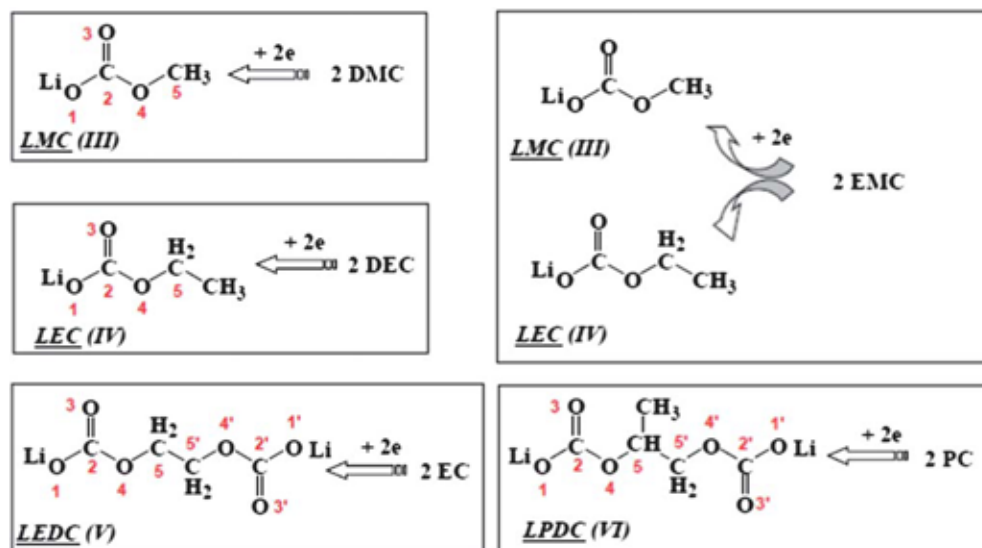


Fig. 1 Model Compounds LMC, LEC, LEDC, and LPDC, as postulated reduction products from DMC, EMC, DEC, EC and PC, respectively, via the single-electron reduction process on the graphitic anode surface (reproduced with permission by the Electrochemical Society from Ref. 26).

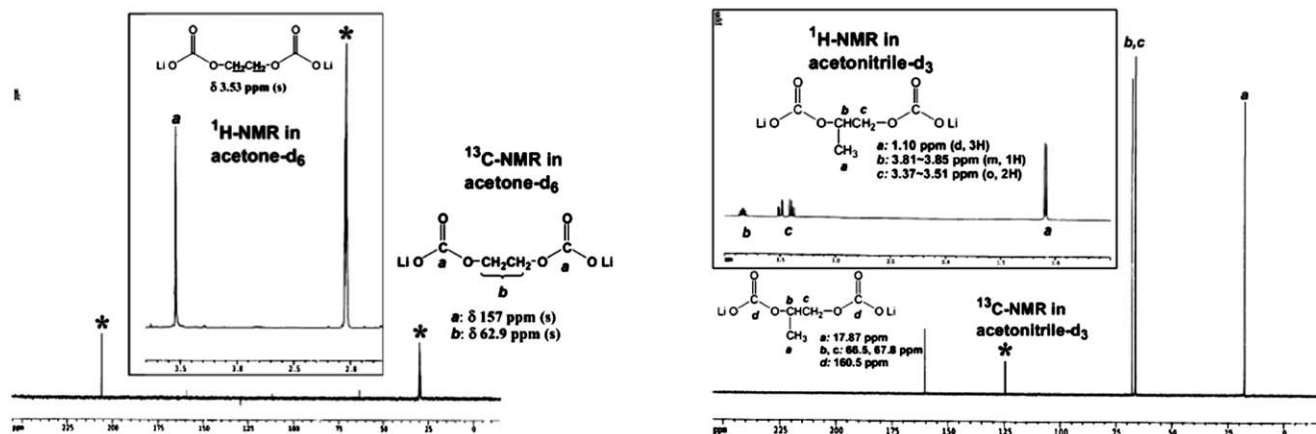


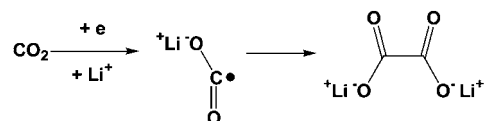
Fig. 2 The ^1H - and ^{13}C -NMR of the synthesized lithium 1,2-ethylene dicarbonate (LEDC, left), the proposed reduction product of EC, and 1,2-propylene dicarbonate (LPDC), the proposed reduction product of PC through single electron mechanisms (Reproduced with permission by the Electrochemical Society from Ref. 26).

products as supported by the reference spectra thus established.^{26–28}

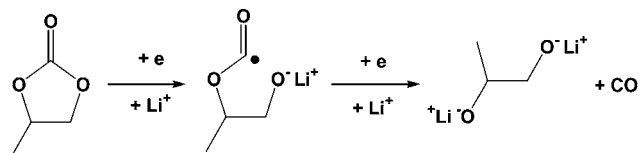
The value of the standard spectra can be best exemplified by the comparison made between synthesized LEDC and the nickel electrode surface polarized to lithiation potential in electrolyte $\text{LiPF}_6/\text{EC}/\text{DMC}$ with 30 : 70.²⁷ The chemical species in the latter is almost an exact replica of the standard LEDC, confirming that at the lithiation potential the single-electron reduction indeed is the major process (Fig. 3). In addition to the below finger-print match between spectra, what surprised us more at the time was that LEDC was the only species detected on the electrode surface, despite the major population of linear carbonate DMC in the electrolyte composition. In closer examination, there is obvious a “shift” between the bulk electrolyte composition and the interphasial chemical species that originated from the various electrolyte solvents. NMR spectra collected from the graphitic anode surface in varying electrolyte compositions verified this disparity. This finding led to the latter investigation of relative

competitiveness of cyclic and linear carbonate for Li^+ -solvation shell and its implication in the eventual interphasial chemistry.

The reduction process on graphitic anode is more complicated than what was detected on nickel surface. In addition to LEDC that remains the major product in SEI, other species including oxalate and alkoxide were also identified.^{30,31} The former (oxalate) obviously resulted from CO_2 , but its source is still unclear. Under the reductive environment at graphitic anode CO_2 is possibly reduced immediately and the resultant radical anion possesses life-time long enough for a bi-molecular recombination reaction:



The latter (alkoxide) is possibly formed in a new two-electron process that involves acyl-oxygen cleavage instead of the alkyl-oxygen cleavage as proposed by Aurbach *et al.*:



In a more recent effort to monitor the gas products generated during the initial forming stage of Li ion batteries, Onuki *et al.* proved the existence of this new process with the detection of CO .³²

It is still unclear why such complications arose on graphitic anode as compared with a simple electrode surface such as nickel. We speculate that the rich functionalities on the graphene edge sites (hydroxyls, alkoxides or quinones, *etc*) might have participated as mediators in the reactions, resulting in diversified reduction pathways. Further investigation on this topic is deemed necessary for a more thorough understanding of the reduction chemistry on graphitic anode materials.

2.1.2 Formation mechanism. Unlike the chemistry of SEI, the formation mechanism has been a subject under debate. The initial models have treated the surface reduction like a simple 2D-

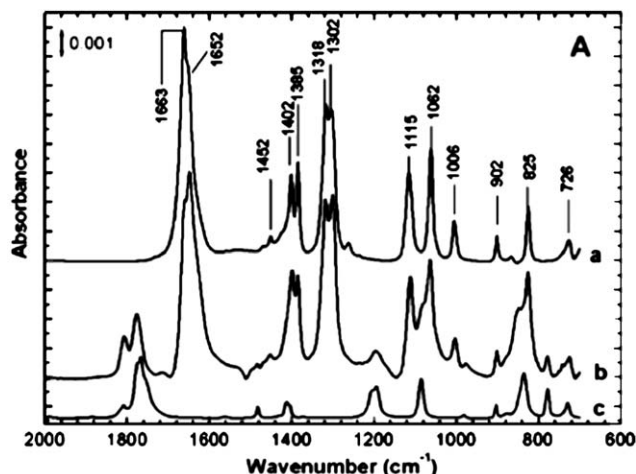


Fig. 3 The FTIR spectra collected from (a) synthesized standard reference LEDC, (b) surface species on a Ni-electrode that has been negatively polarized to lithiation potential, and (c) $\text{Li}(\text{EC})_x$ solvates (Reproduced with permission by the Electrochemical Society from Ref. 27).

surface process, while Besenhard *et al.* proposed a mechanism that involved the unique structure of graphite anodes.²² Based on their earlier studies of intercalation phenomenon of graphite, they know that the electrolyte solvents, especially PC, tend to co-intercalate and form the so-called ternary GIC. Thus it is reasonable to speculate that the formation of SEI must also experience a similar step, *i.e.*, before the potential of graphite anode becomes reductive enough to induce decomposition of electrolyte solvent molecules, these molecules can co-intercalate and exist in the graphene interlayer. In other words, the interphase thus formed, as schematically shown in Fig. 4, should concentrate near the edge sites of the graphite particles and partially penetrate the graphite interior. This formation mechanism is thus known as “3-D model of SEI”.

During the past decade, with more studies focused on the SEI of graphitic anode, the above mechanism gained more experimental evidence, while the most convincing proof came from the *in situ* XRD performed on a graphite anode in PC-based electrolyte at fast scan down to 0.50 V vs. Li.³³ The new series of diffraction peaks appearing at $2\theta = 24^\circ$ and 27.5° obviously indicate the reversible formation of ternary GIC with interlayer distance as wide as 1.59 nm, which can accommodate solvated Li^+ with 3–4 solvent molecules in the primary solvation sheath. Based on these experimental evidences, one can reasonably infer that similar ternary GIC was also formed in commercial Li ion batteries during the formation stage, where the main electrolyte solvents transiently co-intercalate into the graphite interior.

A more recent refinement of the above 3-D model was made by Xu *et al.*,^{34,35} who discovered from the impedance studies that the activation energy barrier (E_{AC}) for Li^+ -transfer measured at electrolyte/graphite interface depends on electrolyte composition, or the ratio between cyclic component EC and Li^+ ,

in a rather particular manner. Using typical electrolyte solvent mixtures of cyclic (EC) and linear carbonates (DMC or EMC), they identified an almost universal dependence for these systems with E_{AC} reaching a near constant when EC/Li ratio is above 4, which happens to be the average solvation number of Li^+ in non-aqueous media.

The above correlation leads to the immediate suspicion that Li^+ -solvation sheath is the underlying cause. Cyclic carbonate molecules such as PC or EC, whose dielectric constants are 65 and 89, respectively, should be the preferred members within the solvation sheath of Li^+ as compared with the linear carbonate molecules such as DMC, DEC and EMC, whose dielectric constants remain below 4. Considering that ternary GIC is the necessary “intermediate state” before an SEI is finally formed, and these inner members of Li^+ solvation sheath are most likely the preferred precursor of interphasial chemistry, Xu *et al.* argued that in the above 3-D model, the first wave of solvent molecules that co-intercalate with Li^+ are predominately cyclic carbonates as long as there are enough in the bulk electrolyte solution to be recruited by Li^+ , and consequently the resultant SEI will preferably consist of reduction products of these cyclic carbonates through the single-electron reductive pathway. Assuming an average solvation number of 4 for Li^+ , the threshold solvent ratio for linear carbonate molecule to be present in Li^+ -solvation sheath (and also subsequently in the interphase) is 30 : 70 by weight. In other words, in majority of the commercial Li ion batteries, SEI would consist of single-electron reduction product of EC because its content was usually above that threshold ratio.

The above arguments concerning the “unsymmetrical” contribution from cyclic and linear carbonate molecules to interphasial chemistry have been receiving increasing support from interphasial analysis efforts. For example, a NMR analysis on

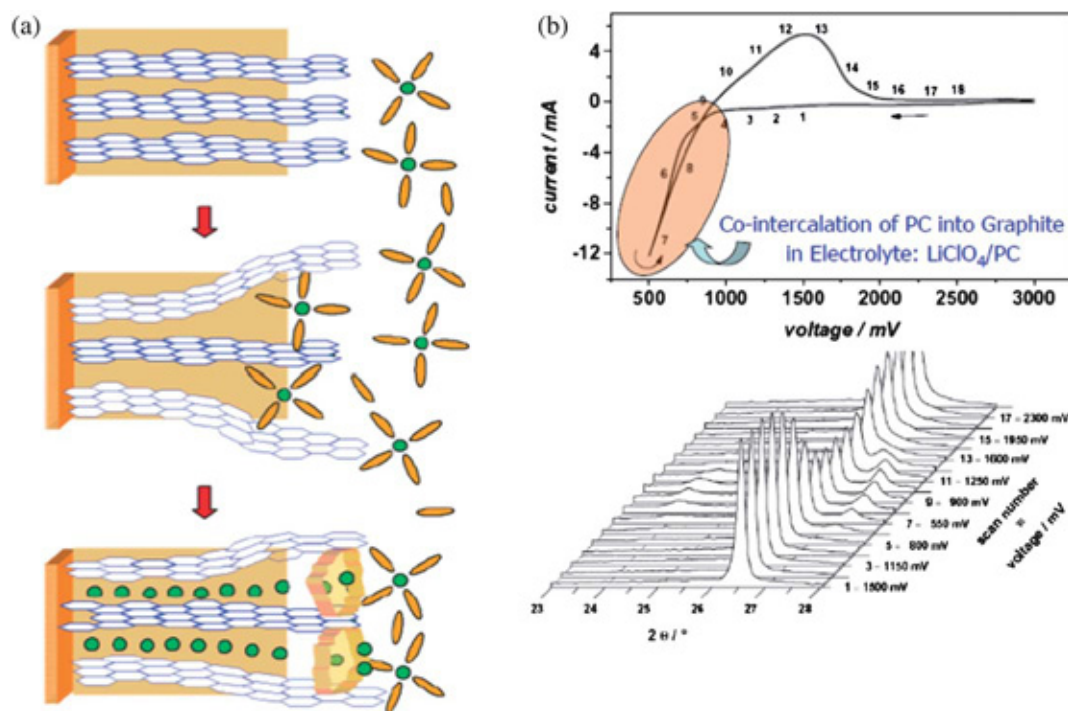


Fig. 4 (a) Schematic drawing of a 3D SEI formed at graphite edge site *via* an intermediate of ternary GIC; (b) *In situ* XRD evidence of the ternary GIC composed of $\text{Li}(\text{PC})_4$ -Graphite (Reproduced with permission by Elsevier from Ref. 33).

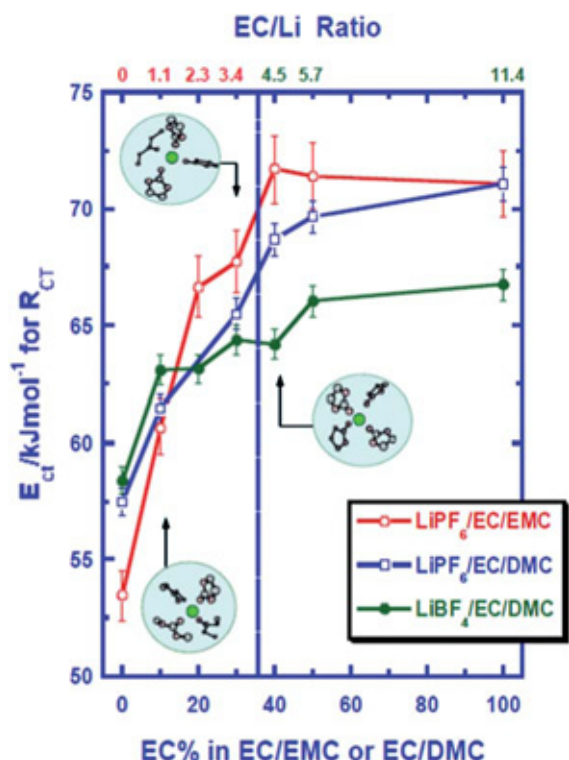
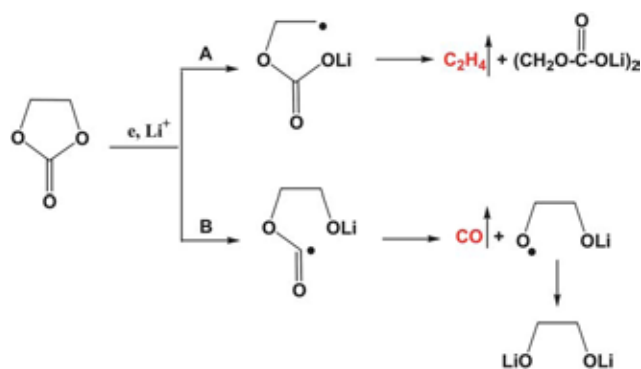


Fig. 5 “Universal” dependence of charge-transfer activation energy at graphite surface on the cyclic/acyclic carbonate ratio in several common electrolyte systems (Reproduced with permission by the Electrochemical Society and the American Chemical Society from Ref. 34 and 35).

interphasial species as collected from cycled graphitic anode corroborates that the alkylcarbonate originating from EMC does not appear until the EC/EMC ratio is lower than 20 : 80;³⁵ whereas in a separate effort, Onuki *et al.* were able to trace the origin of gaseous products during the forming stage of a Li ion battery by labeling the cyclic and linear carbonates with isotopic ^{13}C respectively, and found that the majority of alkene or CO produced were from EC instead of linear carbonates, even though the electrolyte used in the study is still dominated by linear carbonate DEC:³²



All these analyses point to a formation mechanism that is coordinated by the solvation sheath structure of Li^+ in these electrolytes.

Based on the above “solvation sheath” argument, the modified formation mechanism of SEI on graphite surface was

schematically represented in Fig. 7, in which an electrolyte containing more than 30% EC will lead to an EC-dominated Li^+ -solvation sheath, and eventually an interphase that bears heavy — if not exclusive — signature of EC-reduction products.

The Li^+ -solvation factor might also play an important role in the reduction kinetics of solvents molecules. According to computational approach based on DFT,²⁹ the reduction of a neat solvent molecule is thermodynamically forbidden with a high energy barrier for the initial ring-opening process; however, coordination by Li^+ significantly enhances the reduction by stabilizing the high energy intermediates. It is very likely that the bonds of the solvent molecules within the supermolecular structure of a Li^+ -solvation sheath are relaxed due to the effect of a Li^+ in their vicinity.

2.1.3 Efforts to tailor a desired chemistry. The interphase on graphitic anode has been recognized as the main contributor of cell impedance; therefore, in the past two decades, the Li ion battery industry has been favoring a thinner interphase in order to accelerate the Li^+ -transport across this resistive component. The most common approach to this thinner SEI is through incorporating selected additives in electrolytes, whose sacrificial decomposition before any other electrolyte components would form an interphase of different chemistry.³⁶ Since SEI thickness on composite electrodes cannot be directly measured (or even reasonably defined in some cases), the irreversible capacity in the initial cycle was often used to quantify this “thickness” as a measure for the effectiveness of those additives.

The additive approach was made possible by one characteristic of Li ion battery, *i.e.*, the electrode potentials before the initial cell activation are at the discharged state, and open circuit voltage between the lithiated cathode and non-lithiated graphite usually lies below 1.5 V. Only during the initial forming was the potential of graphitic anode gradually lowered to that of Li^+ -intercalation, accompanied by corresponding potential rise and delithiation of cathode. This stepwise change of electrode potential offered an opportunity to reduce only certain “chosen” species before the rest of the electrolyte solution are involved. This selectivity is not possible with a metallic lithium electrode on which reductions occur instantaneously and which is indiscriminate to any species it contacts.³

Due to insufficient understanding of the formation chemistry, selection of these additives has been conducted on a semi-empirical basis. Peled once suggested a kinetic model, assuming that if a species can reductively decompose at faster rate on graphite surface, it will most likely form an SEI of less thickness.³⁷ Using reduction rate constants of chemicals in aqueous media as a relative quantifying tool, he successfully established such correlation for a series of chemicals. Later on an improved model resorted to the thermodynamics instead of kinetics to evaluate the additive candidates, arguing that the electrochemical potential at which the candidate decomposes is more decisive than kinetic rate.^{38,39} Since the reduction/oxidation potentials of a given species are more easily accessible *via* computation than kinetic data, this latter model is now widely adopted by researchers to screen and evaluate potential SEI additives. Nevertheless, those two models share the common belief that a more reactive species might be a better candidate for interphase.

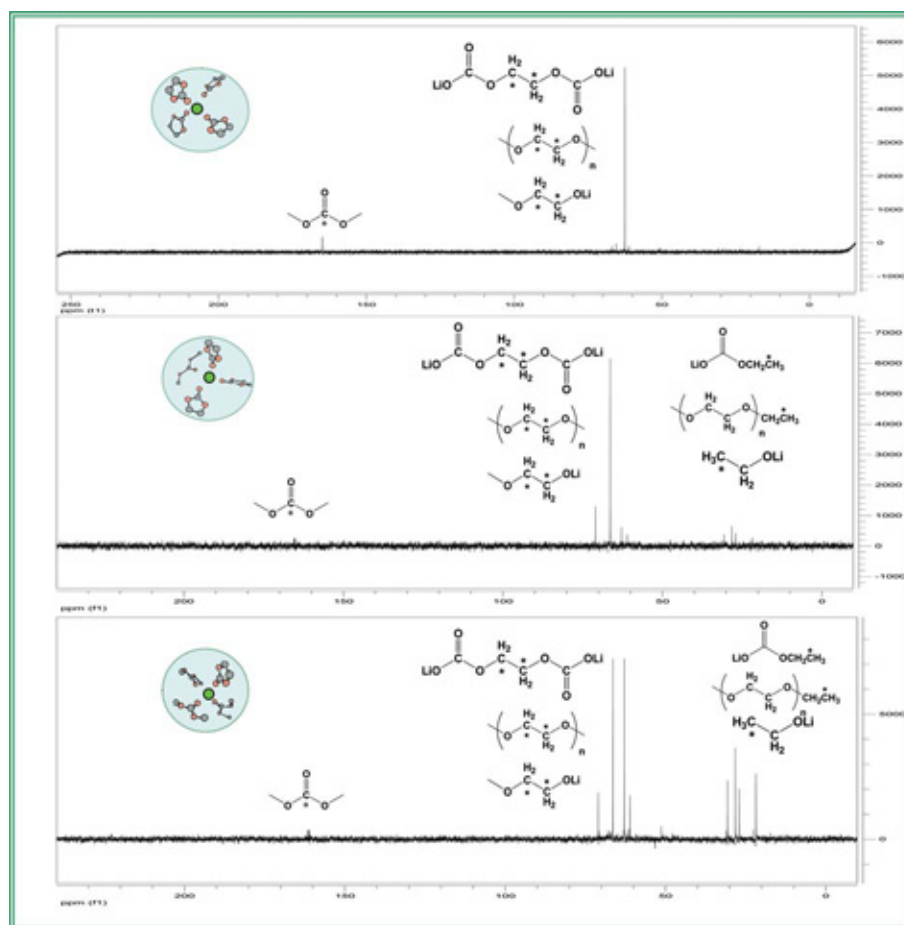


Fig. 6 ^{13}C -NMR spectra of interphasial species collected from the graphitic anodes cycled in electrolytes with varying ratios of cyclic/acyclic carbonates (Reproduced with permission by the American Chemical Society from Ref. 35).

In practice, computation approaches were usually taken to estimate the reduction or oxidation potentials of candidate species, which are related to the energy levels of lowest unoccupied molecular orbital (LUMO) and highest occupied molecular orbital (HOMO), respectively. During the past two decades the main attention were placed on how to improve the SEI on the graphitic anode surfaces,³⁶ therefore the additive species of a lower LUMO are favored because it indicates a higher potential of reduction during the initial lithiation of graphite, hopefully before any component of the electrolyte is reduced. Such examples include vinyl carbonate (VC),⁴⁰ SO_2 ,^{41,42} ethylene sulfite (ES),⁴³ butyl sulfite,⁴⁴ butyl sultone (BS),^{45,46} vinyl ethylene carbonate (VEC),^{47–49} methylpropargyl sulfonate (MPS),^{50,51} *etc.* In particular, VC, whose reduction potential starts at ~ 2.0 V vs. Li, can form a very thin interphase and has been widely used in many commercial electrolyte formulations.⁵²

However, despite its theoretical appearance, this HOMO/LUMO approach is still empirical in nature, because there is no necessary connection between the reduction potential and the effectiveness of the resultant SEI, and the physicochemical properties of the decomposition compounds, which cannot be predicted by mere computation, were not taken into consideration. An ideal SEI additive is required not only to be reduced or oxidized before any electrolyte component does, but also to be able to decompose into such compounds that have minimum

solubility in the bulk electrolyte solvent, maximum Li^+ -conductivity and thermal and chemical stability against all components present, *etc.* Nevertheless, the HOMO/LUMO calculation did provide an easy tool for the preliminary screening of additive candidates, and numerous reports have described its successful application in identifying useful additives.^{36,38,39}

Most of the interphases in Li ion devices are formed *in situ*, *i.e.*, naturally during the slow process of bringing potentials of graphitic anode or cathode down to that of Li^+ intercalation. On the other hand, with increasing understanding about the chemical composition of interphases, there were also efforts to form these interphases artificially with known chemicals that are structurally similar to alkylcarbonates, either during the electrode processing stage or after it as a surface coating *via* various deposition techniques. An obvious advantage of the artificial approach is the minimization or even complete elimination of Li^+ -consumption by irreversible processes during the otherwise *in situ* SEI formation.

Since authentic ingredients of SEI on graphitic anode, lithium alkylcarbonates, are sensitive to moisture and almost insoluble in any non-aqueous solvents, early researchers used stable chemicals as surrogate interphasial building-blocks. Thus various metal oxides or phosphates including Al_2O_3 , ZrO_2 and AlPO_4 , *etc.* have been thus applied directly on graphite particles through sol-gel processes,^{53–58} with improvements in either reduced

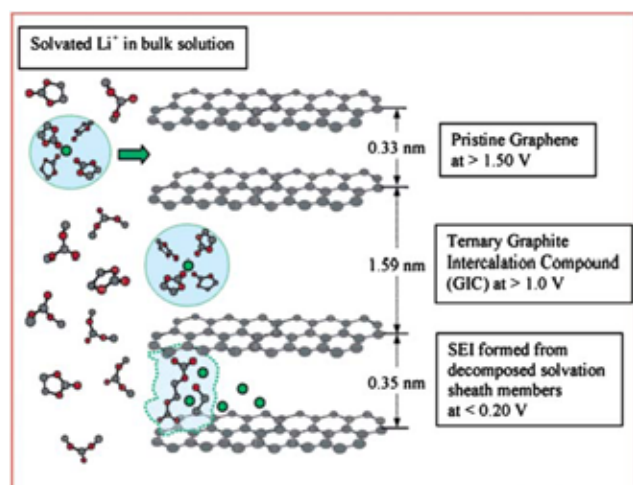


Fig. 7 Refined model of the “3-D” formation mechanism in which Li^+ -solvation sheath plays the central role of forming the intermediate ternary GIC and dictates the initial ingredients of resultant SEI (Reproduced with permission by the American Chemical Society from Ref. 35).

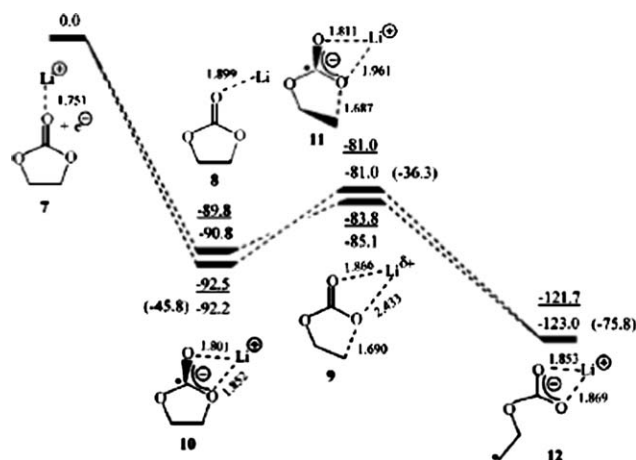


Fig. 8 Role of Li^+ -solvation on kinetics of EC reduction (Reproduced with permission by the American Chemical Society from Ref. 29).

irreversible capacity in the initial cycle, prolonged cycle life, durability against cycling at elevated temperatures, or enhanced safety behavior. Amorphous carbon layer was also applied in a similar manner onto highly graphitic carbon surfaces.⁵⁹

In a similar but much simpler approach, graphite particles were soaked in Li_2CO_3 aqueous solution, which forms a thin coating over the composite electrode upon drying.⁶⁰ When tested in a PC-rich electrolyte that is often a challenge to most highly graphitic structures, it was found that the artificial interphase of Li_2CO_3 not only reduces the irreversible capacity in the initial forming cycle, but also significantly suppresses the self-delithiation rate of a charged graphite anode during long term storage at elevated temperatures. A similar work, inspired by the discovery that lithium bis(oxalato)borate (LiBOB) can form a unique interphasial chemistry capable of withstanding high temperature, employed aqueous solutions of mixed boric and oxalic acids.⁶¹ The interphase in this case is supposed to consist of an oxalato-borate network and also functions efficiently to protect the graphitic anode from a PC-rich electrolyte.

Vacuum deposition techniques were also employed to place desired chemicals onto graphitic anodes. Marrassi and coworkers deposited various metal layers of sub-nano thickness over partially-oxidized graphite *via* vacuum evaporation, and observed improvement of electrochemical performances in all cases but especially in the case of Cu and Sn.^{62,63} This increase in metallic nature of graphite surface helps to reduce the resistance to Li^+ -transport, but more interestingly, their measurement of the activation energy barrier seems to suggest that this improvement in Li^+ -transport may come not only from the mere increase of conductivity at the interphase, but more likely from an accelerated Li^+ -desolvation process.⁶³ To minimize the thickness of the artificial interphase, Jung *et al.* used Atomic Layer Deposition (ALD) technique to coat Al_2O_3 over the particles of both anode and cathode materials, and demonstrated that natural graphite thus treated can be cycled in PC-based electrolyte without exfoliation.⁶⁴ They claimed that ALD does not block the inter-particle electric pathways as sol-gel may do, thus keep the rate capability from being compromised at the expense of protection.

It must be pointed out that, while the interphasial chemistry and physical thickness in these deposition approaches are well-understood and can even be readily manipulated, there are certain disadvantages that prevent their actual applications, the most conspicuous of which is scalability and cost. Electrified vehicle applications, in particular, require large format Li ion batteries with quantities of materials which cannot be supplied with any deposition methods carried out under vacuum. In comparison, electrolyte additives provide a more economical approach.

The pursuit of a merely thinner SEI has also been challenged by the recent revelation of Li^+ -desolvation on Li^+ -transport.⁶⁵ The possible role of Li^+ -solvation in interphasial processes have been ignored until very recently, and the credit for bringing this factor under light should go to Ogumi's group,^{66–70} whose series of pioneering work identified the desolvation process of Li^+ as a highly energy consuming process and initiated a sequence of efforts which led to the discovery that Li^+ -solvation sheath structure plays an important role not only in SEI formation mechanism but also in subsequent Li^+ -transport across the interphase.

Given its small ionic radius, a naked Li^+ is known to exert strong Coulombic forces on its surrounding solvent molecules, and usually the innermost three to five molecules were considered as the members of its primary solvation sheath, which stays with the core Li^+ without being displaced, at least statistically, while Li^+ migrates throughout the bulk electrolyte solution.¹ Such solvation stabilizes Li^+ in electrolyte solution by compensating the increase of Gibbs free energy when lithium salt is dissociated from its original lattice. However, when such a solvated Li^+ migrates to the edge sites of graphitic anode, the formed interphase would only allow naked Li^+ through, therefore the solvation sheath must be stripped off before a naked Li^+ can be intercalated into the graphite interior (Fig. 7). Thus, during the Li^+ -transport across the formed interphase, there exists a high energy transition state, which corresponds to the generation of a naked Li^+ (Li^+ -desolvation) and migration of this naked Li^+ subsequently through the interphase (Fig. 9, above). Since such a desolvation process consumes energy to complete and would

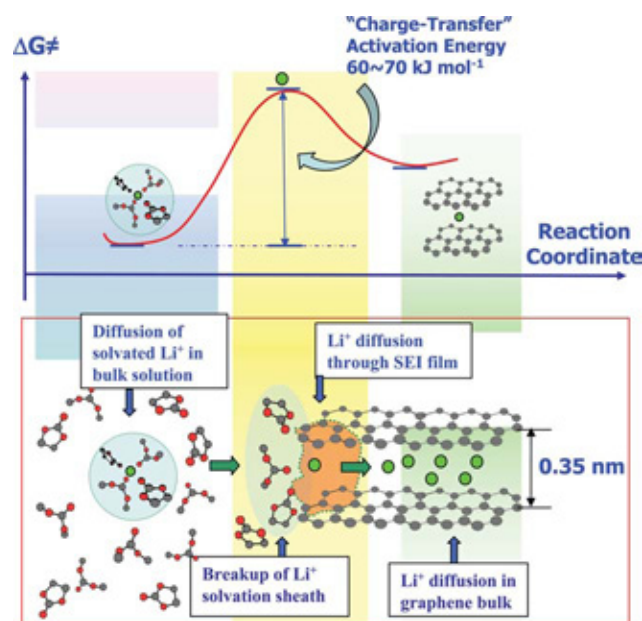


Fig. 9 Differentiating contributions to the interphasial resistance from two sub-processes: (a) generation of naked Li^+ (Li^+ -desolvation) and (b) Migration of naked Li^+ across the interphase (Reproduced with permission by the American Chemical Society from Ref. 65).

naturally induce additional interphasial resistance to the Li^+ -transport.

Unfortunately, the above two sub-processes are closely interwoven, and the so-called “interphasial resistance” in the earlier literature has actually referred to their compounded effects inclusively without differentiation. Not until Ogumi’s work was it realized that the Li^+ -transport consist of two sub-processes: Li^+ -desolvation and the subsequent Li^+ -migration. The differentiation of these sub-processes was eventually made possible by employing an intercalation anode, $\text{Li}_4\text{Ti}_5\text{O}_{12}$,⁶⁵ whose surface is free of any interphase because the reversible intercalation of Li^+ occurs at ~ 1.5 V vs. Li, a potential where no electrolyte component is either reduced or oxidized. It was found that the contribution from Li^+ -desolvation to the activation energy barrier at electrolyte/graphite junction is ~ 50 kJ mol⁻¹. By comparing with the compounded energy barrier of 60~70 kJ mol⁻¹ as derived from a graphitic anode (Fig. 9), it was concluded that Li^+ -desolvation is the rate-determining step at the electrolyte/graphite anode interphase.

In this context, the traditional approach of pursuing thinner SEI certainly encounters its own limitation, because no matter how thin an interphase is, as long as it acts as a layer of electrolyte nature at anode surface, *i.e.*, forbidding any electron-tunneling, the desolvation should always exist and its contribution to the interphasial activation energy barrier would remain a constant. Considering the dominant role of Li^+ -desolvation to the overall cell resistance, we believe that any further improvement in interphasial kinetics than what allowed by current electrolyte additive approach would require a new chemistry that assists in breaking the solvation sheath of Li^+ . This group at ARL has been working on this concept and is making progresses.

2.2 On Si and other alloy surfaces

The above 3D-formation mechanism of interphase is graphite-specific. When the electrode does not possess a structure for intercalation, a simple 2D surface reaction is likely to be responsible for the formation of an interphase. Such examples include metallic lithium or other metals as alloy host for lithium. Although the resultant interphase no longer has the characteristic features as it does on graphite surface, *i.e.*, primary location at graphitic edge *versus* basal sites and partial penetration into the bulk of interstitial spacing, the interphase thus formed is still a 3D and independent entity.

Alloy hosts such as Si and Sn have attracted tremendous interest as the next generation anode materials to replace graphite, due to their much higher capability to accommodate lithium; however, the accompanying huge volume expansion (200%~300%) associated with the lithiation/de-lithiation cycle, as compared with <10% in the case of graphite, has been the major hurdle preventing their practical application. The severe stress during the volume change brings mechanical disintegrity and results in loss of active materials (Fig. 10).^{71,72} Meanwhile, both formation and chemistry of SEI is also perpetually overshadowed by the above volume change. Considering the potentials at which those hosts alloy with lithium (<200 mV vs. Li), electrolyte components, especially carbonate esters, will inevitably be reduced into species that are structurally similar to what identified on graphitic anodes. However, since fresh metal surfaces are created repeatedly in each cycle due to the local disintegrity, additional reduction of electrolyte has to take place to cover those newly exposed surfaces, similar to what happens when a metallic lithium electrode is being cycled in non-aqueous electrolytes. This continuous process builds up interphasial resistance, consumes the limited source Li^+ , and would eventually disable the cell, if it has not been disabled by the sheer loss of active species. Thus, one of the keys to the successful application of Si or other alloy hosts as Li ion battery anode is that the SEI formed thereon must withstand a higher mechanical stress.

To circumvent the problem caused by volume change, Si electrodes with nano-structure or in thin-film configuration (≤ 200 nm) are often employed in place of bulk configuration, as illustrated in Fig. 10.⁷³⁻⁸¹ With the absence of binder and carbon additives that are often present in graphite composite electrodes, the spectroscopy of these electrodes can usually provide compositional information free of interference. It seems that performance and possibly interphasial chemistry of these anodes

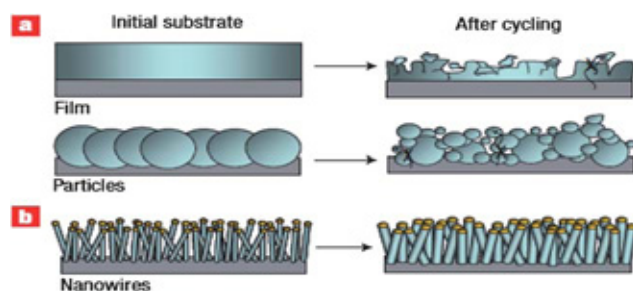


Fig. 10 Schematic illustration of (a) bulk and (b) nano-structured Si during the electrochemical lithiation/delithiation (Reproduced with permission by the Nature Publishing Corp. from Ref. 74).

are sensitive to the synthesis conditions;^{82–84} however, a constant interphasial composition is always detected on Si: the fluorinated derivatives SiF_x , which is obviously arising from the reaction of PF_6^- -based Li salt and whose formation is thermodynamically favored, driven by the high bonding energy of Si–F (565 kJ mol^{−1}).^{85,86} Given the potential as well as the electron-poor characteristic of Si that are similar to graphite, single-electron reduction products from electrolyte solvents were also identified, which include inorganic species such as Li_2CO_3 , LiF, and Li_2O , and organic species such as alkylcarbonates, carboxylates, and polyethylene oxide.^{71–86} What surprised the researchers is that CF_x was also detected by XPS, which was not present on graphitic anode. It has been speculated that HF, produced due to the hydrolysis of PF_6^- -anion by trace moisture, attack on both Si and SiO_2 , and SiF_6^{2-} resulting from HF also catalyzes formation of CF_x species. Interestingly, both SiO_2 on older surfaces and Si on freshly exposed surfaces should compete for HF, but it is difficult to tell from spectroscopy which process or combination results in the SiF_x seen in XPS.⁸⁶ For Si–C alloys and carbon-coated silicon, it is a reasonable assumption that interphases thereon are more similar to those formed on graphite with a lack of SiF_x species,^{85–88} because the surface functionalities mediating the decomposition of the electrolyte are graphite or graphite-like rather than Si lattice.

Significant presence of siloxane was also found in the inner layer of the interphase, which was probably formed by the reaction between solubilized Si with carboxyl radicals in solution and re-deposits on the carbon layer during initial SEI formation.⁸⁶ The presence of siloxane in the SEI has been shown to benefit the reversibility of Si electrodes,⁷⁷ making this a potentially useful improvement to the integrity of the silicon SEI layer. In general, the presence of –Si–C– and –Si–O–C– terminated components bonded with the anode surface would imply some degree of SEI stability, at least at the interface, due to the increased stability of –Si–C– and –Si–O– (318 and 452 kJ mol^{−1}) compared with their carbon counterparts –C–C– and –C–O– (346 and 352 kJ mol^{−1}).

Since the presence of moisture (and hence HF) is inevitable in non-aqueous electrolyte that employs fluorinated Li salt anion, the SEI on a Si anode has the additional responsibility of shielding the surface underneath from HF attack. Both Si and its native oxide film are vulnerable to HF, which convert Si into electrochemically-inactive SiF_6^{2-} and results in capacity loss.⁸⁹ Compared with graphite surface, the interphase on Si-containing alloy hosts have much higher presence of P–F moieties for this reason, which might have originated from PF_6^- anion reduction, HF formation, and resulting incorporation of PF_6^- products into the network. Si might have directly participated in pulling F from PF_6^- anion.

Analysis on a thin-film composite Cu_2Si alloy host revealed evidence of alkyl esters and carbonates with only a weak signal from semi-carbonate compounds like LEDC, very distinct from what is found on graphite and Si anodes. This difference is most likely related to the increased availability of electrons on the Cu-rich anode surface and may result in more two-electron reduction products in the interphase layer. More importantly, this result points to the significance of the surface composition itself in controlling the composition of its interphase layer.^{78–80}

A number of researchers have also attempted to manipulate interphasial chemistry on Si by using electrolyte additives. Lithium bis(oxalateborate) (LiBOB) was used as a minority salt because of its well-studied network forming abilities,^{90,91} and was able to maintain the spectroscopic presence of semi-carbonate species in the SEI through reductive decomposition of the bis(oxalate) borate anion.⁷⁵ Monofluoroethylene carbonate (FEC), on the other hand, presumably provides a more fluorinated SEI layer built on the fluoro-LEDC derivatives.⁷⁶ Both efforts were reasonably successful in maintaining the electrochemical reversibility of a thin (<200 nm) thick Si anode, though only reported for less than 100 cycles, leaving questions about the long-term stability of these SEI layers.⁷⁵ Similar work also claimed that addition of 5 wt% trimethoxymethyl silane extended the cycling life of a thin-film Si anode, though the mechanism is unclear.⁷⁷

For bulk Si and other alloy anodes, as opposed to their nano-structured or thin-film configurations, interphase is still at the mercy of the cyclic volume change, and no SEI is known to inhibit this process. Further studies are needed to understand the failure modes of interphase on these alloy host electrodes, and interphases with unique chemistry and morphology dedicated to these alloy anodes should be tailored to accommodate the new requirements.

2.3 On cathode surfaces

Since the birth of Li ion chemistry in early 1990, most research resources were invested in the pursuit of diversified new cathode chemistries; however, a complete reversal exists in the resource distribution of interphasial studies, and the chemistry on cathode surfaces remains a little-understood regime as of today.

Similar to the scenario with graphitic anode, the potentials of most cathode materials used in Li ion batteries are too high (>3.5 V vs. Li) for almost any electrolyte component to remain thermodynamically stable. Thus the reversible Li^+ -intercalation/de-intercalation must be preceded by the formation of certain interphasial existence, although it is expected that the varying composition, lattice and morphology of cathode materials would render the chemistry and formation mechanism very distinct from (and much more complicated than) the process on their graphitic counterpart.

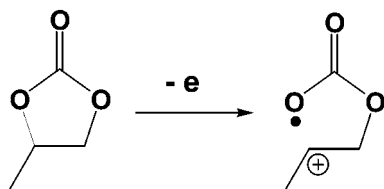
While the interphase on graphitic anode is usually more resistive than that on cathode, the latter tends to increase in magnitude at quicker pace than the former during long term cycling, and would eventually take over the role as the most resistant component at certain point. Cycling or aging at elevated temperatures accelerates this process. The interphase formed on the oxidizing surfaces is under-investigated for historical reasons. While the overwhelming emphasis on graphitic anode can be attributed to graphite sensitivity toward solvent molecule co-intercalation, *i.e.*, driven by “necessity”, several factors are responsible for the scarcity of knowledge on cathode interphase, including the interference of a native surface film of Li_2CO_3 that exists on most of the transition metal oxides, the reaction between this native layer with acidic electrolyte, and the entanglement of cathode species decomposition with the oxidation of organic electrolyte components. Recent studies showed that even olivine phosphate, which

operates at lower potential (3.5 V) and often considered chemically “inert” than oxides, can react with both ambient moisture and electrolytes based on acidic LiPF₆.⁹²

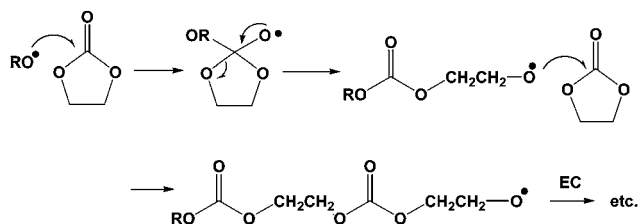
Proving the existence of a SEI on cathode surface is not as straightforward, and surface spectroscopy tools that have been effective for graphite surface yield ambiguous results more often than not. Till today there are still occasional arguments that an SEI in traditional sense does not exist on cathode side. However, more and more attention is drawn toward the cathode side, especially after a DOE-wide effort was started to pursue 5 V-class new Li ion chemistry, which requires in-depth understanding about the oxidation chemistries of electrolyte components.

2.3.1 Oxidative processes on cathode. Unlike the interphase formation process on graphitic anode, Li⁺-solvation structure plays only negligible role on cathode surface during the initial activation of a Li ion cell, primary because this charging process involves the removal of Li⁺ from the cathode lattice, and corresponds to Li⁺-solvation rather than desolvation. Thus, the oxidation no longer has the preference for those solvent molecules in the solvation sheath, but rather offers “equal opportunity” to all electrolyte components that are adsorbed on the cathode surface.

Similar to the reductive decomposition, it is speculated that a cation radical is involved as an intermediate, and the only experimental evidence to the best of our knowledge is the ESR observed on the electrolyte in contact with a charged LiCoO₂.⁹³



The fate of the radical cation was not clear, and there was suggestion that interphase bears chemical similarities to its counterpart on graphite anode,^{94,95} but polycarbonate has been suggested as a possible oxidation product based on surface-enhanced FTIR studies:⁹⁶



Based on an earlier study of polymerization of EC, there is suspicion about the chemical stability of polycarbonate due to the high density of carbonyls in the monomeric units;⁹⁷ and more likely, the polymer would lose part of the carbonyls in the form of CO₂ and result in a copolymer of carbonate and ethylene oxide units. The detection of CO₂ during cathode aging at elevated temperatures seems to support this possibility.^{98,99} Nevertheless, a recent study on the EC oxidation on “5 V” cathode LiNi_{0.5}Mn_{1.5}O₄ using both XPS and FTIR identified polycarbonate species as the main product.¹⁸

Whatever the chemical species were, it is certain that their stabilization of the electrolyte/cathode junction is valid only below 4.5 V, above which sustained electrolyte oxidation would occur.¹⁸ This upper limit set by the interphasial chemistry originating from organic carbonate solvents has been a major road-block to the efforts to pursue Li ion chemistries of higher voltage quality (~5.0 V).

The thickness of SEI on cathode has also been a subject of controversy. In general the interphases were considered as much thinner when compared with its counterpart on graphitic anode. Reports have placed a wide range from a few to 10² nm.^{100–102} However, with continuous cycling and especially high temperature aging, the interphase increases in thickness, while its resistance takes over as the kinetic bottleneck. Dupre *et al.* carried out a rather interesting study on the interphase formed over LiNi_{0.5}Mn_{0.5}O₂ by using ⁷Li-magic angle spinning NMR technique.¹⁰² By soaking the cathode materials with electrolyte, they monitored the evolution of ⁷Li-signals and discovered that the reaction between active species and electrolyte solvents happens in the timescale of 30 s, accompanied by the global disappearance of the native Li₂CO₃ film. The eventual species identified include decomposition products from PF₆[−] anion, polymeric or organic species, and also alkylcarbonate salt that is a popular species often found on graphitic anode surface. Combined SEM/TEM analysis estimated an average of 2–20 nm thickness for the film after the reaction, but since the cathode surface is not covered by a homogenous layer, they thus argued that this reaction is not a “real passivation”.¹⁰²

2.3.2 Solvents and additives for cathode passivation. While the anions of lithium salts have been recognized to participate in the passivation chemistry on surfaces of cathode materials and their substrates,³ the hope of improving anodic stability of electrolytes has always been with the solvents. This is mainly due to the higher difficulty associated with developing a new lithium salt, whose qualification must be subject to many more criteria beyond oxidation chemistry. Instead, modern chemical reservoirs offer a rich source of solvents and especially additives with diversified structures and redox properties for considerations of tailoring an interphase with tolerance of higher potential.

With the appearance of 4 V class cathode chemistry based on transition metal oxides, the selection of solvents has been increasingly focused on organic esters, especially dialkyl esters of carbonic acid. A few attempts to seek after alternative structures have yielded varying results.

Sulfones were perhaps the first family of solvents shown to have better anodic stability over the carbonates. By rendering the molecules unsymmetrical so that their melting points are depressed to the vicinity of room temperature, Xu *et al.* described a series of sulfone compounds whose solution of lithium salts can withstand potentials beyond 5.5 V vs. Li on the surface of Li_xMn₂O₄, as shown in Fig. 11a.¹⁰³ More interestingly, when the sulfones were mixed in different ratios with acyclic carbonates DMC and EMC in order to reduce the viscosity of the results electrolyte, it was found that the presence of linear carbonates has negligible effect on the anodic stability (Fig. 11b),¹⁰⁴ which is counter intuitive with the common knowledge that these carbonate are not stable beyond 4.0 V and would compromise the overall oxidation stability limit. This indicates that, even in

the presence of linear carbonates at high ratios, the interphasial chemistry on cathode surface is still dominated by the sulfone, which is the more polar co-solvent in the system. In other words, the more polar component seems to have more significant contribution to the formation of interphase, in striking similarity to what observed on graphite surface where the more polar EC is favored. Considering the oppositely charged surfaces as reaction locations in those cases, one would infer that the unsymmetrical contribution to interphasial chemistry must be related to the stronger interaction of the more polar solvent molecules with either cation (Li^+) or anion (PF_6^-). This phenomenon certainly merits further investigations to understand the interphase formation mechanism.

The composite electrode based on $\text{Li}_x\text{Mn}_2\text{O}_4$ used in the above work serves as a more convincing working electrode in demonstrating anodic stability limit than does non-porous surfaces such as glassy carbon or platinum; however, it is not a real high (5 V) voltage cathode, and practicality of sulfones needs further confirmation. In more recent efforts, these sulfone solvents were revisited with either carboxylate or carbonic esters act as co-solvents, and cycling results on a 5 V class cathode based on $\text{LiNi}_{0.5}\text{Mn}_{1.5}\text{O}_4$ led to the conclusion that anodic stability superior to neat carbonates was obtained.^{105,106} Especially, Abouimrane *et al.* demonstrated impressive stability in the prolonged cycling of a “5 V” class cathode cell using a sulfone-linear carbonate mixture (Fig. 12), confirming that the presence of acyclic carbonate EMC co-solvent does not compromise the oxidation stability at those high potentials.¹⁰⁶

Organic nitriles represent another family of solvents that were investigated as alternative to carbonates.^{107–111} Nitrile functionality is one of the few organic compounds that are polar enough to dissolve various alkali salts (including most lithium salts whose lattice energy ranks top) but still remain aprotic, and there have been numerous reports on their use in electrochemical capacitors, the most popular representative being acetonitrile. There have been conflicting data regarding its electrochemical stability, and the source of ambiguity seems to be the manner in which such stability is determined.¹⁰⁷ However, several high order derivatives of nitrile have been tested on different cathode surfaces and seem to remain stable at potentials near 4.0 V, such

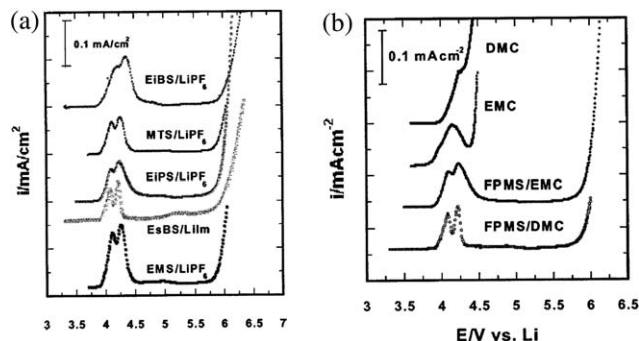


Fig. 11 (a) Anodic stability of various sulfone-based electrolytes on spinel LiMn_2O_4 cathode surface obtained by linear sweep (Reproduced with permission by the American Chemical Society from Ref. 104). (b) Effect of linear carbonates on anodic stability of sulfone-based electrolytes on spinel LiMn_2O_4 cathode surface (Reproduced with permission by the American Chemical Society from Ref. 104).

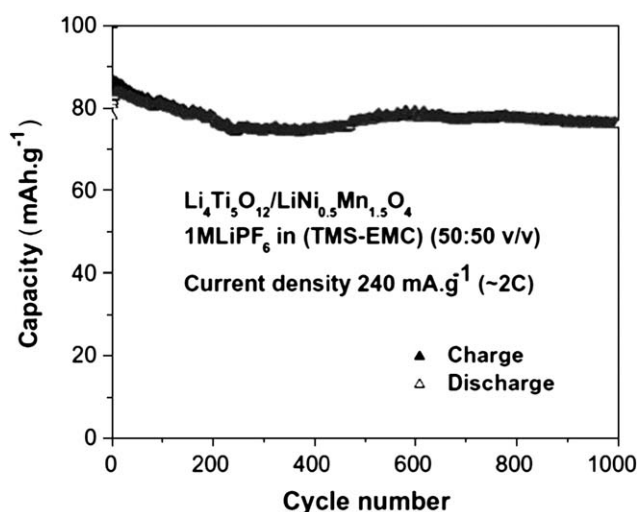


Fig. 12 Cycling of a “5 V” cathode $\text{LiNi}_{0.5}\text{Mn}_{1.5}\text{O}_4$ in an electrolyte based on the mixture of tetramethylene sulfone (TMS) and EMC (Reproduced with permission by the Elsevier from Ref. 106).

examples including acrylic acid nitrile on $\text{Li}_x\text{Mn}_2\text{O}_4$,¹⁰⁸ and 3-ethoxypropionitrile, 3-(2,2,2-trifluoro)ethoxypropionitrile,¹⁰⁹ and adiponitrile¹¹⁰ on LiCoO_2 . The only dinitrile molecule that was tested on a true “5 V” class cathode is sebaconitrile, which was reported to be able to support Li^+ deintercalation above 5.0 V in $\text{Li}_2\text{NiPO}_4\text{F}$, although no cycle life data was presented.¹¹¹ Despite the electrochemical stability window of 6.0 V as measured on non-porous electrodes and positive effect on cycling behavior with these cathodes, whether they can truly withstand oxidation on surfaces of 5 V cathode species still remain to be investigated.

Compared with the efforts of developing alternative bulk solvents to replace the carbonate solvents, the additive approach proves more convenient and economical and therefore more likely to be acceptable to the industry, because their presence in the electrolyte system is often too small to cause any undesirable impact on the already-established systems in terms of both properties and costs. Additives to improve the interphases on graphitic anode surfaces have been widely used in Li ion battery industry, while the additives designed to tailor cathode surface has been very rare. The few such additives found in the reports are the natural extension from the work on anode side. For example, vinylene carbonate (VEC), which has been known as additive to form polymeric species on graphite surface, was also tested as an additive on cathode surface, and reported to stabilize the electrochemical performance of $\text{LiNi}_{0.8}\text{Co}_{0.2}\text{O}_2$,^{112,113} while furan- and lactone-derivatives were also described as being able to inhibit electrolyte oxidation on $\text{Li}_{1.17}\text{Mn}_{0.58}\text{Ni}_{0.25}\text{O}_2$ surface at potentials up to 4.9 V.¹¹⁴

Recently, spinel $\text{LiNi}_{0.5}\text{Mn}_{1.5}\text{O}_4$ was more and more targeted as a reliable “5 V” class cathode candidate, and efforts aiming at stabilizing conventional carbonate-based electrolytes on this cathode began to take momentum. Cresce *et al.* identified an additive, tris(hexafluoro-iso-propyl)phosphate (or HFIP), which is based on phosphate ester structure with highly fluorinated alkyl arms, whose presence in a carbonate-based electrolyte at merely 1% can effectively stabilize both interphasial impedance and capacity retention of spinel $\text{LiNi}_{0.5}\text{Mn}_{1.5}\text{O}_4$ cathode

(Fig. 13a and b);¹¹⁵ meanwhile, Abouimrane *et al.* reported a thiophene-based additive, which can form polymeric film on the same cathode surface and yielded similar improvement.¹¹⁶ While the electrolyte additive remains a more economical approach for the industry to accept, the interphasial chemistry involved remains unclear and merits further investigation.

Different routes were also explored in order to directly coat the cathode with an artificial interphase. Similar to what was done on graphitic anode, Al_2O_3 and AlPO_4 was used for LiCoO_2 through either sol-gel or atomic layer deposition approach, and better cycling stability was claimed when more than half of the stoichiometric Li^+ can be removed from lattice of LiCoO_2 , which was otherwise inaccessible due to both electrolyte decomposition and lattice instability at potentials above 4.2 V.^{43,117–120} The concern on cost and scalability remains.

Among these coating approaches, perhaps the most promising and feasible was the electrostatic self-assembly technique that Liu *et al.* developed.^{121–124} By adjusting pH value of the solution so that the surface of the cathode particles remain negatively charged, they successfully covered it with a series of oxide or phosphate adsorbents, which bear positive charges in the suspension and, after high temperature processing, turns into a nm-thickness protective layer as shown in Fig. 14a. They applied this technique onto several high voltage cathode materials and obtained rather reversible operations in the region near 5.0 V (Fig. 14b).

It must be noted here that these nano-coatings, as well as any such coatings that were directly applied to the electrode material particles in the bulk before they are attached to a current collector, are not interphases themselves in the traditional sense, otherwise the active mass would be electronically insulated from the circuit; rather, during the cell operation, the electrons must be allowed to tunnel through them in order for the electrochemistry to occur. In other words, an additional SEI should be formed from the electrolyte components on top of these nano-coatings once the Li ion cell is charged for the first time. The role of those nano-coatings might be more than just a physical barrier that regulates the flow of Li^+ ; instead their specific chemistry and morphology could be interfering or even directing the decomposition chemistry of the electrolyte components. The eventual “interphase” in this case could be a composite film consisting of the inorganic inner and an organic outer layer.

3. Concluding remarks

As the past two decades witnessed the glory and frustration of Li ion batteries, it is well recognized that the interphases between electrolyte and electrodes in Li ion batteries played important roles in determining the performance of the device. Thanks to advancements from fundamental research, we have learned much about the chemistry and formation mechanism of this elusive component, although it remains the least understood

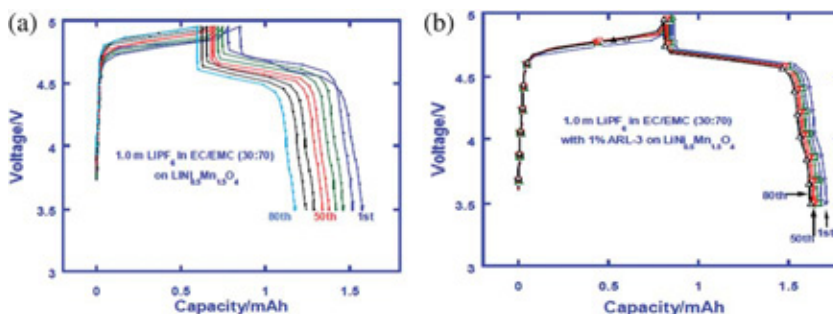


Fig. 13 (a) Voltage profiles of “5 V” class cathode $\text{LiNi}_{0.5}\text{Mn}_{1.5}\text{O}_4$ in standard electrolyte $\text{LiPF}_6/\text{EC}/\text{EMC}$ (30 : 70) without additive (a) and with 1% HFiP as additive (b) (Reproduced with permission by the Electrochemical Society from Ref. 115).

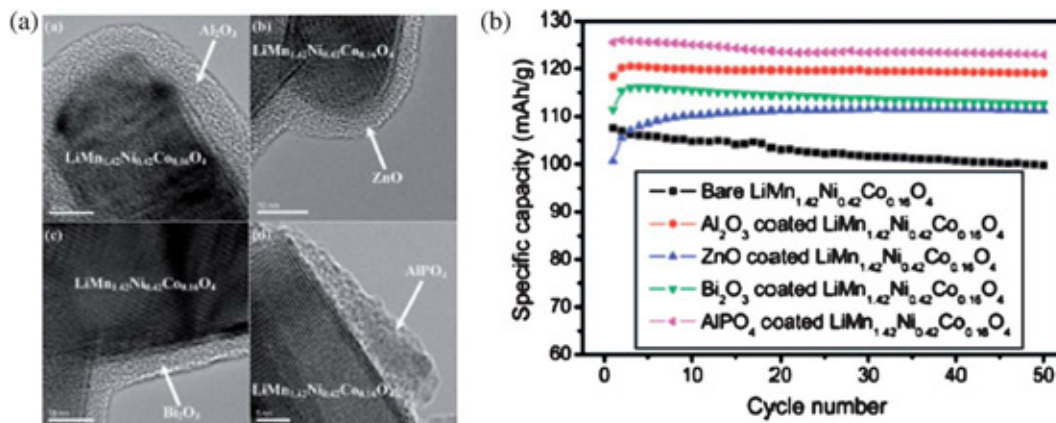


Fig. 14 TEM picture of artificial interphases consisting of Al_2O_3 , ZnO , Bi_2O_3 and AlPO_4 on $\text{LiMn}_{0.42}\text{Mn}_{1.42}\text{Co}_{0.16}\text{O}_4$ through electrostatic self-assembly (a) and the cycling performance (b) (Reproduced with permission by the American Chemical Society from Ref. 124).

within the device and merits our further and intensified investigation. It is predicted that the interphases on cathode surfaces, especially on those of the high voltage ("5 V") materials, will attract most of the attention in the next 5–10 years.

Acknowledgements

The work was partially funded by U. S. Department of Energy Advanced Battery Research (DOE-ABR) Program. The authors want to thank Dr Peter Faguy of DOE and Prof. Jeff Dahn of Dalhousie University for useful discussions.

References

- 1 J. O'M. Bockris, and A. K. N. Reddy, *Modern Electrochemistry*, 2nd Edition, Vol. 2, Plenum Press, New York, 2000.
- 2 M. S. Whittingham, R. F. Savinell and T. Zawodzinski, *Chem. Rev.*, 2004, **104**, 4243.
- 3 K. Xu, *Chem. Rev.*, 2004, **104**, 4303.
- 4 Y. Chiang, C. Carter, B. Ho, and M. Duduta, U. S. Patent Pub. No. WO 2009/151639A1.
- 5 J. R. Dahn, *Phys. Rev. B: Condens. Matter*, 1991, **44**, 9170.
- 6 M. S. Whittingham, *Chem. Rev.*, 2004, **104**, 4271.
- 7 R. Fong, U. von Sacken and J. R. Dahn, *J. Electrochem. Soc.*, 1990, **137**, 2009.
- 8 E. Peled, *J. Electrochem. Soc.*, 1979, **126**, 2047.
- 9 K. Xu, *J. Electrochem. Soc.*, 2009, **156**, A751.
- 10 A. Hérol, *Bull. Soc. Chim. France*, 1955, **187**, 999.
- 11 J. B. Goodenough and Y. Kim, *Chem. Mater.*, 2010, **22**, 587.
- 12 A. N. Dey and B. P. Sullivan, *J. Electrochem. Soc.*, 1970, **117**, 222.
- 13 A. J. Smith, J. C. Burns and J. R. Dahn, *Electrochem. Solid-State Lett.*, 2010, **13**, A177.
- 14 A. J. Smith, J. C. Burns, S. Trussler and J. R. Dahn, *J. Electrochem. Soc.*, 2010, **157**, A196.
- 15 J. C. Burns, J. Gauray, A. J. Smith, K. W. Eberman, E. Scott, J. P. Gardner and J. R. Dahn, *J. Electrochem. Soc.*, 2011, **158**, A255.
- 16 S. Harris, and P. Lu, *MRS Fall Meeting*, 2010, Nov. 28–Dec. 3, Boston, MA, Abstract No. KK 11.2.
- 17 S. S. Zhang, K. Xu and T. R. Jow, *J. Power Sources*, 2003, **115**, 137.
- 18 L. Yang, B. Ravdel and B. Lucht, *Electrochem. Solid-State Lett.*, 2010, **13**, A95.
- 19 D. Aurbach, M. L. Daroux, P. W. Faguy and E. Yeager, *J. Electrochem. Soc.*, 1987, **134**, 1611.
- 20 D. Aurbach, I. Weissman, A. Schechter and H. Cohen, *Langmuir*, 1996, **12**, 3991.
- 21 A. Schechter, D. Aurbach and H. Cohen, *Langmuir*, 1999, **15**, 3334.
- 22 J. O. Besenhard, M. Winter, J. Yang and W. Biberacher, *J. Power Sources*, 1993, **54**, 228.
- 23 M. Winter, *Z. Phys. Chem.*, 2009, **223**, 1395.
- 24 D. Bar-Tow, E. Peled and L. Burstein, *J. Electrochem. Soc.*, 1999, **146**, 824.
- 25 A. Naji, J. Ghanbaja, B. Humbert, P. Willmann and D. Billaud, *J. Power Sources*, 1996, **63**, 33.
- 26 K. Xu, U. Lee, S. Zhang and T. R. Jow, *J. Phys. Chem. B*, 2006, **110** (15), 7708.
- 27 G. V. Zhuang, H. Yang, P. N. Ross, K. Xu and T. R. Jow, Jr, *Electrochem. Solid-State Lett.*, 2006, **9**, A64–A68.
- 28 G. V. Zhuang, K. Xu, H. Yang, T. R. Jow and P. N. Ross, Jr, *J. Phys. Chem. B*, 2005, **109**, 17567.
- 29 Y. Wang, S. Nakamura, M. Ue and P. Balbuena, *J. Am. Chem. Soc.*, 2001, **123**, 11708.
- 30 G. V. Zhuang and P. N. Ross, *Electrochem. Solid-State Lett.*, 2003, **6**, A136.
- 31 A. Augustsson, M. Herstedt, J.-H. Guo, K. Edstrom, G. V. Zhuang, P. N. Ross, Jr, J.-E. Rubensson and J. Nordgren, *Phys. Chem. Chem. Phys.*, 2004, **6**, 4185.
- 32 M. Onuki, S. Kinoshita, Y. Sakata, M. Yanagidate, Y. Otake, M. Ue and M. Deguchi, *J. Electrochem. Soc.*, 2008, **155**, A794.
- 33 M. R. Wagner, J. H. Albering, K. C. Moeller, J. O. Besenhard and M. Winter, *Electrochem. Commun.*, 2005, **7**, 947.
- 34 K. Xu, *J. Electrochem. Soc.*, 2007, **154**, A162.
- 35 K. Xu, Y. Lam, S. Zhang, T. R. Jow and T. Curtis, *J. Phys. Chem. C*, 2007, **111**, 7411.
- 36 S. S. Zhang, *J. Power Sources*, 2006, **162**, 1379.
- 37 E. Peled, D. Golodnitsky, C. Menachem and D. Bar-Tow, *J. Electrochem. Soc.*, 1998, **145**, 3482.
- 38 M. Yoshio, H. Nakamura and N. Dimov, in *Lithium Ion Rechargeable Batteries: Materials, Technology, and New Applications*, Ed. K. Ozawa, Wiley-VCH Verlag GmbH & Co. KGaA, Weinheim, Germany.
- 39 M. D. Halls and K. Tasaki, *J. Power Sources*, 2010, **195**, 1472.
- 40 B. Simon, J. P. Boeue, U. S. Patent 5,626,981, 1997.
- 41 D. Aurbach, K. Gamolsky, B. Markovsky, Y. Gofer, M. Schmidt and U. Heider, *Electrochim. Acta*, 2002, **47**, 1423.
- 42 Y. Ein-Eli, S. R. Thomas and V. R. Koch, *J. Electrochem. Soc.*, 1997, **144**, 1159.
- 43 G. H. Wrodnigg, J. O. Besenhard and M. Winter, *J. Electrochem. Soc.*, 1999, **146**, 470.
- 44 R. Chen, F. Wu, L. Li, Y. Guan, X. Qiu, S. Chen, Y. Li and S. Wu, *J. Power Sources*, 2007, **172**, 395.
- 45 M. Q. Xu, X. X. Zuo, W. S. Li, H. J. Zhou, J. S. Liu and Z. Z. Yuan, *Acta Phys.-Chim. Sin.*, 2006, **22**, 335.
- 46 M. Q. Xu, W. S. Li, X. X. Zuo, J. S. Liu and X. Xu, *J. Power Sources*, 2007, **174**, 705.
- 47 J. M. Vollmer, L. A. Curtis, D. R. Vissers and K. Amine, *J. Electrochem. Soc.*, 2004, **151**, A178.
- 48 J. Liu, Z. Chen, S. Busking, I. Belharouak and K. Amine, *J. Power Sources*, 2007, **174**, 852.
- 49 Y. Hu, W. Kong, Z. Wang, H. Li, X. Huang and L. Chen, *Electrochem. Solid-State Lett.*, 2004, **7**, A442.
- 50 K. Abe, H. Yoshitake, T. Kitakura, T. Hattori, H. Wang and M. Yoshio, *Electrochim. Acta*, 2004, **49**, 4613.
- 51 K. Abe, Y. Ushigoe, H. Yoshitake and M. Yoshio, *J. Power Sources*, 2006, **153**, 328.
- 52 O. Matsuoka, A. Hiwara, T. Omi, M. Toriida, T. Hayashi, C. Tanaka, Y. Saito, T. Ishida, H. Tan, S. S. Ono and S. Yamamoto, *J. Power Sources*, 2002, **108**, 128.
- 53 J. Cho, Y. J. Kim, T. J. Kim and B. W. Park, *Angew. Chem., Int. Ed.*, 2001, **40**, 3367.
- 54 J. Cho, Y. W. Kim, B. Kim, J. G. Lee and B. W. Park, *Angew. Chem., Int. Ed.*, 2003, **42**, 1618.
- 55 S. S. Kim, Y. Kadoma, H. Ikuta, Y. Uchimoto and M. Wakihara, *Electrochem. Solid-State Lett.*, 2001, **4**, A109.
- 56 I. R. M. Kottegoda, Y. Kadoma, H. Ikuta, Y. Uchimoto and M. Wakihara, *J. Electrochem. Soc.*, 2005, **152**, A1595.
- 57 I. R. M. Kottegoda, Y. Kadoma, H. Ikuta, Y. Uchimoto and M. Wakihara, *Electrochem. Solid-State Lett.*, 2002, **5**, A275.
- 58 S. E. Lee, E. Kim and J. Cho, *Electrochem. Solid-State Lett.*, 2007, **10**, A1.
- 59 M. Yoshio, H. Wang and K. Fukuda, *Angew. Chem., Int. Ed.*, 2003, **42**, 4203.
- 60 S. S. Zhang, K. Xu and T. R. Jow, *Electrochem. Commun.*, 2003, **5**, 979.
- 61 S. S. Zhang, K. Xu and T. R. Jow, *J. Power Sources*, 2004, **129**, 275.
- 62 F. Nobili, S. Dsoke, M. Mancini, R. Tossici and R. Marassi, *J. Power Sources*, 2008, **180**, 845.
- 63 M. Mancini, F. Nobili, S. Dsoke, F. D'Amico, R. Tossici, F. Croce and R. Marassi, *J. Power Sources*, 2009, **190**, 141.
- 64 Y. S. Jung, A. S. Cavanagh, L. A. Riley, S. H. Kang, A. C. Dillon, M. D. Groner, S. M. George and S. H. Lee, *Adv. Mater.*, 2010, **22**, 2172.
- 65 K. Xu, A. v. Cresce and U. Lee, *Langmuir*, 2010, **26**, 11538.
- 66 T. Abe, H. Fukuda, Y. Iriyama and Z. Ogumi, *J. Electrochem. Soc.*, 2004, **151**, A1120.
- 67 T. Abe, M. Ohtsuka, F. Sagane, Y. Iriyama and Z. Ogumi, *J. Electrochem. Soc.*, 2004, **151**, A1950.
- 68 T. Abe, F. Sagane, M. Ohtsuka, Y. Iriyama and Z. Ogumi, *J. Electrochem. Soc.*, 2005, **152**, A2151.
- 69 Y. Yamada, F. Sagane, Y. Iriyama, T. Abe and Z. Ogumi, *J. Phys. Chem. C*, 2009, **113**, 14528.
- 70 Y. Yamada, Y. Iriyama, T. Abe and Z. Ogumi, *Langmuir*, 2009, **25**, 12766.
- 71 U. Kasavajjula, C. Wang and J. Appleby, *J. Power Sources*, 2007, **163**, 1003.
- 72 W. Zhang, *J. Power Sources*, 2011, **196**, 13.
- 73 X. W. Zhang, P. K. Patil, C. Wang, A. J. Appleby, F. E. Little and D. L. Cocke, *J. Power Sources*, 2004, **125**, 206.

- 74 C. K. Chan, H. Peng, G. Liu, K. McIlwrath, X. F. Zhang, R. A. Huggins and Y. Cui, *Nat. Nanotechnol.*, 2008, **3**, 31.
- 75 N. Choi, K. Yew, K. Lee, M. Sung, H. Kim and S. Kim, *J. Power Sources*, 2006, **161**, 1254.
- 76 N. Choi, K. Yew, H. Kim, S. Kim and W. Choi, *J. Power Sources*, 2007, **172**, 404.
- 77 S. Song and S. Baek, *Electrochem. Solid-State Lett.*, 2009, **12**, A2.
- 78 S. Baek, S. Hong, D. Kim and S. Song, *J. Power Sources*, 2009, **189**, 660.
- 79 S. Song, R. Reade, E. Cairns, J. Vaughey, M. Thackeray and K. Striabel, *J. Electrochem. Soc.*, 2004, **151**, A1012.
- 80 S. Song and S. Baek, *Electrochim. Acta*, 2009, **54**, 1312.
- 81 L. Y. Beaulieu, K. C. Hewitt, R. L. Turner, A. Bonakdarpour, A. A. Abdo, L. Christensen, K. W. Eberman, L. J. Krause and J. Dahn, *J. Electrochem. Soc.*, 2003, **150**, A149.
- 82 J. Kim, H. Lee, K. Lee, S. Lim and S. Lee, *Electrochem. Commun.*, 2003, **5**, 544.
- 83 T. Moon, C. Kim and B. Park, *J. Power Sources*, 2006, **155**, 391.
- 84 T. Takamura, M. Uehara, J. Suzuki, K. Sekine and K. Tamura, *J. Power Sources*, 2006, **158**, 1401.
- 85 D. Mazouzi, B. Lestriez, L. Roue and D. Guyomard, *Electrochem. Solid-State Lett.*, 2009, **12**, A215.
- 86 Y. Yen, S. Chao, H. Wu and N. Wu, *J. Electrochem. Soc.*, 2009, **156**, A95.
- 87 J. Guo, X. Chen and C. Wang, *J. Mater. Chem.*, 2010, **20**, 5035–5040.
- 88 J. Guo and C. Wang, *Chem. Commun.*, 2010, **46**, 1428.
- 89 J. Flake, M. Rieger, G. Schmid and P. Kohl, *J. Electrochem. Soc.*, 1999, **146**, 1960.
- 90 K. Xu, U. Lee, S. Zhang, M. Wood and T. R. Jow, *Electrochem. Solid-State Lett.*, 2003, **6**, A144.
- 91 K. Xu, S. S. Zhang, B. A. Poesse and T. R. Jow, *Electrochem. Solid-State Lett.*, 2002, **5**, A259.
- 92 M. Koltypin, D. Aurbach, L. Nazar and B. Ellis, *J. Power Sources*, 2007, **174**, 1241.
- 93 S. Matsuta, Y. Kato, T. Ota, H. Kurokawa, S. Yoshimura and S. Fujitani, *J. Electrochem. Soc.*, 2001, **148**, A7.
- 94 D. Aurbach, M. D. Levi, E. Levi, H. Teller, B. Markovsky, G. Salitra, U. Heider and L. Heider, *J. Electrochem. Soc.*, 1998, **145**, 3024.
- 95 D. Aurbach, *J. Power Sources*, 2000, **89**, 206.
- 96 D. Aurbach, K. Gamolsky, B. Markovsky, G. Salitra, Y. Gofer, U. Heider, R. Oesten and M. Schmidt, *J. Electrochem. Soc.*, 2000, **147**, 1322.
- 97 L. Vogdanis and W. Heitz, *Makromol. Chem. Rapid Commun.*, 1986, **7**, 543.
- 98 M. Broussely, Ph. Biensan, F. Bonhomme, Ph. Blanchard, S. Herreyre, K. Nechev and R. J. Staniewicz, *J. Power Sources*, 2005, **146**, 90.
- 99 J. Vetter, P. Novak, M. R. Wagner, C. Veit, K. C. Moller, J. O. Besenhard, M. Winter, M. Wohlfahrt-Mehrens, C. Vogler and A. Hammouche, *J. Power Sources*, 2005, **147**, 269.
- 100 N. Liu, H. Li, Z. Wang, X. Huang and L. Chen, *Electrochem. Solid-State Lett.*, 2006, **9**, A328.
- 101 M. Jo, Y.-S. Hong, J. Choo and J. Cho, *J. Electrochem. Soc.*, 2009, **156**, A430.
- 102 N. Dupre, J.-F. Martin, J. Oliveri, P. Soudan, D. Guyomard, A. Yamada and R. Kanno, *J. Electrochem. Soc.*, 2009, **156**, C180.
- 103 K. Xu and C. A. Angell, *J. Electrochem. Soc.*, 1998, **145**, L70.
- 104 K. Xu and C. A. Angell, *J. Electrochem. Soc.*, 2002, **149**, A920.
- 105 Y. Watanabe, S. Kinoshita, S. Wada, K. Hoshino, H. Morimoto and S. Tobishima, *J. Power Sources*, 2008, **179**, 770.
- 106 A. Abouimrane, I. Belharouak and K. Amine, *Electrochem. Commun.*, 2009, **11**, 1073.
- 107 K. Xu, S. Ding and T. R. Jow, *J. Electrochem. Soc.*, 1999, **146**, 4172.
- 108 H. J. Santner, K. C. Moller, J. Ivanko, M. G. Ramsey, F. P. Netzer, S. Yamaguchi, J. O. Besenhard and M. Winter, *J. Power Sources*, 2003, **119–121**, 368.
- 109 Q. Wang, P. Pechy, S. M. Zakeeruddin, I. Exnar and M. Gratzel, *J. Power Sources*, 2005, **146**, 813.
- 110 Y. Abu-Lebdeh and I. Davidson, *J. Electrochem. Soc.*, 2009, **156**, A60.
- 111 M. Nagahara, N. Hasegawa and S. Okada, *J. Electrochem. Soc.*, 2010, **157**, A748.
- 112 J. Li, W. Yao, Y. S. Meng and Y. Yang, *J. Phys. Chem. C*, 2008, **112**, 12550.
- 113 Y. Fu, C. Chen, C. Qiu and X. Ma, *J. Appl. Electrochem.*, 2009, **39**, 2597.
- 114 L. Yang and B. Lucht, *Electrochem. Solid-State Lett.*, 2009, **12**, A229.
- 115 A. v. Cresce and K. Xu, *J. Electrochem. Soc.*, 2011, **158**, A337.
- 116 A. Abouimrane, S. A. Odom, H. Wu, W. Weng, Z. Zhang, J. S. Moore, and K. Amine, *MRS Fall Meeting*, 2010, Nov. 28–Dec. 3, Boston, MA, Abstract No. KK 4.9.
- 117 A. S. Arico, P. Bruce, B. Scrosati, J.-M. Tarascon and W. V. Schalkwijk, *Nat. Mater.*, 2005, **4**, 366.
- 118 C. Li, H. P. Zhang, L. J. Fu, H. Liu, Y. P. Wu, E. Rahm, R. Holze and H. Q. Wu, *Electrochim. Acta*, 2006, **51**, 3872.
- 119 Y. K. Sun, Y. S. Lee, M. Yoshio and K. Amine, *Electrochem. Solid-State Lett.*, 2002, **5**, A99.
- 120 Y. S. Jung, A. S. Cavanagh, A. C. Dillon, M. D. Groner, S. M. George and S. H. Lee, *J. Electrochem. Soc.*, 2010, **157**, A75.
- 121 J. Liu and A. Manthiram, *J. Electrochem. Soc.*, 2009, **156**, A66.
- 122 J. Liu and A. Manthiram, *J. Electrochem. Soc.*, 2009, **156**, A833.
- 123 J. Liu and A. Manthiram, *J. Phys. Chem. C*, 2009, **113**, 15073.
- 124 J. Liu and A. Manthiram, *Chem. Mater.*, 2009, **21**, 1695.

Distinguishing Li^+ Charge Transfer Kinetics at NCA/Electrolyte and Graphite/Electrolyte Interfaces, and NCA/Electrolyte and LFP/Electrolyte Interfaces in Li-Ion Cells

T. Richard Jow, Michelle B. Marx, and Jan L. Allen

U.S. Army Research Laboratory, Adelphi, MD

ABSTRACT

In examining the Li^+ charge transfer kinetics at the graphite anode and the lithium nickel cobalt aluminum oxide, $\text{LiNi}_{0.80}\text{Co}_{0.15}\text{Al}_{0.05}\text{O}_2$ (NCA), cathode in a full cell, we found that the activation energy, E_a , for the charge transfer at the graphite/electrolyte interface is about 68 kJ/mol, which is consistent with recently reported values. However, the E_a for the charge transfer at the NCA/electrolyte interface is about 50 kJ/mol, which is lower than at the graphite anode. With desolvation as the predominate step for limiting the kinetics and both electrodes subjected to the same electrolyte, the difference in E_a suggests that it is greatly influenced with respect to the nature of the electrode materials and their associated SEIs. This is further confirmed by the examination of Li^+ charge transfer at the LiFePO_4 (LFP)/electrolyte and the graphite/electrolyte interfaces using a LFP/graphite full cell.

Journal of The Electrochemical Society, Volume 159, Number 5,
Pages A604-A612 (2012)



Distinguishing Li⁺ Charge Transfer Kinetics at NCA/Electrolyte and Graphite/Electrolyte Interfaces, and NCA/Electrolyte and LFP/Electrolyte Interfaces in Li-Ion Cells

T. Richard Jow,^{*,z} Michelle B. Marx,^{*} and Jan L. Allen^{*}

U.S. Army Research Laboratory, Adelphi, Maryland 20783, USA

In examining the Li⁺ charge transfer kinetics at the graphite anode and the lithium nickel cobalt aluminum oxide, LiNi_{0.80}Co_{0.15}Al_{0.05}O₂ (NCA), cathode in a full cell, we found that the activation energy, E_a, for the charge transfer at the graphite/electrolyte interface is about 68 kJ/mol, which is consistent with recently reported values. However, the E_a for the charge transfer at the NCA/electrolyte interface is about 50 kJ/mol, which is lower than at the graphite anode. With desolvation as the predominate step for limiting the kinetics and both electrodes subjected to the same electrolyte, the difference in E_a suggests that it is greatly influenced with respect to the nature of the electrode materials and their associated SEIs. This is further confirmed by the examination of Li⁺ charge transfer at the LiFePO₄ (LFP)/electrolyte and the graphite/electrolyte interfaces using a LFP/graphite full cell.

© 2012 The Electrochemical Society. [DOI: 10.1149/2.079205jes] All rights reserved.

Manuscript submitted November 22, 2011; revised manuscript received February 9, 2012. Published March 2, 2012. This was Paper 488 presented at the Las Vegas, Nevada, Meeting of the Society, October 10–15, 2010.

In developing high power Li-ion batteries, reducing resistance that limits the charge and discharge rates is important to improve the power capability of Li-ion cells. Various resistances existing in cells such as contact resistance between the current collector of the electrodes and the cell container and electrolyte resistance can be reduced through engineering and the use of a more conductive electrolyte, respectively. For the same electrode material, the use of thinner electrodes will result in lower resistance cells as the length of the electrodes is increased when packaging them in the same size of cells such as 18650. This is simply due to the fact that the resistance is proportional to the thickness of the electrodes and inversely proportional to the area of the electrodes. The reduction of the particle size of the active materials can increase the number of electrochemical reaction sites for Li⁺ and reduce the time to utilize the active materials. However, the Li⁺ charge transfer resistance, R_{ct}, the resistance that Li⁺ encounters when moving from a solvated ionic state in the electrolyte solution crossing the electrode-electrolyte interface and inserting into the electrodes is one critical source of resistance that requires further understanding and reduction.

During the charge process, for a state-of-the-art Li-ion battery, an electron leaves the lithium metal oxide cathode via an external circuit and moves to the graphite anode. To retain the charge neutrality of the cathode, Li⁺ is released from the cathode moving across the cathode SEI and entering the electrolyte. The Li⁺, which is solvated by the solvent molecules in electrolyte, needs to be desolvated before moving across the graphite anode SEI, inserts into the graphite providing charge neutrality by compensating or accepting the electron coming from the cathode through the external circuit. This process is reversed during discharge. The Li⁺ charge transfer process, described in this paper, involves the desolvation of the solvated Li⁺ in the liquid electrolyte, crossing of Li⁺ through the SEI layer formed at the electrolyte/electrode interface and the acceptance of an electron from the external circuit while inserting into the intercalation type of electrode materials. The resistance resulting from this process is R_{ct}. If the charge transfer across the interface is a thermally activated process, R_{ct} follows the relationship,¹

$$\frac{1}{R_{ct}} = A_0 e^{-E_a/RT}, \quad [1]$$

where A₀, E_a, R and T are a constant, the activation energy, the gas constant and the temperature in Kelvin, respectively. The E_a of the Li⁺ charge transfer process or kinetics represents the barrier that the

Li⁺ needs to overcome to cross the interface between the electrolyte and the electrode. The value of E_a can be obtained from the slope of a log(1/R_{ct}) versus the inverse of temperature (1/T) plot.

In a practical cell, however, the cell resistance is consisted of other resistances in addition to R_{ct} as shown below.

$$R_{cell} = R_e + R_{electrolyte} + R_{SEI} + R_{ct}, \quad [2]$$

where R_e is the contact resistance, R_{electrolyte} is the resistance of the electrolyte and R_{SEI} is the resistance of the SEI layers on the electrodes.

The R_{ct} value is usually determined using an AC impedance technique that potentially can separate the various resistances by measuring the impedance in wide frequency ranges. At higher frequencies, R_s is often used to represent the combined R_e and R_{electrolyte} resistances. R_{SEI} is usually determined using the impedance spectrum at the medium frequencies and R_{ct} at lower frequencies. A DC pulse impedance technique can also be used to estimate the value of R_{ct} when R_{ct} is the dominating resistance in the cell, which is often the case at low temperatures. Using this technique, the DC resistance is estimated from the voltage change by applying a pulse current to the cell. This downside of this technique is that it is unable to separate the various resistances in a cell.

Li⁺ charge transfer kinetics across various electrode/electrolyte interfaces was extensively studied by the group led by Ogumi and Abe^{2–8} using an AC impedance technique. The study of HOPG (highly oriented pyrolytic graphite)/liquid electrolyte [1 m LiClO₄ in EC (ethylene carbonate):DMC (dimethyl carbonate) (1:1)] interface as reported by Abe et al.² and Yamada et al.³ found the value of E_a for Li⁺ charge transfer across this interface to be 58 kJ/mol in a temperature range of 25°C to around 50°C. Abe et al.⁴ also reported the Li⁺ charge transfer kinetics at the interface between the solid-state Li⁺ conductor, Li_{0.35}La_{0.55}TiO₃ (LLT), and the Li⁺ liquid electrolyte. At this interface, the Li⁺ moves between a solvated state in the liquid to a de-solvated state in the solid. The Li⁺ charge transfer, in this case, involves only the Li⁺ de-solvation and solvation step without the electron transfer step associated with the electrode (anode or cathode)/electrolyte interface, in which the electron is involved. It is also found by the same authors that the E_a value varies with solvent selected. Yamada et al.⁵ reported an E_a of 51 kJ/mol for the interface of LLT/1 m LiClO₄ in EC:DMC (1:1) electrolyte. Considering this value is similar or slightly lower than that at the HOPG/electrolyte interface, this seems to affirm that de-solvation is the predominant step for the Li⁺ charge transfer across the graphite/electrolyte interface.

Li⁺ charge transfer kinetics at the interface between thin film lithium transition metal oxide electrodes such as Li₄Ti₅O₁₂,⁶ LiMn₂O₄⁷ and LiCoO₂⁸ and the electrolyte of 1 m LiClO₄ in EC:DEC (diethyl carbonate) or in PC (propylene carbonate) solvent have

* Electrochemical Society Active Member.

^z E-mail: t.r.jow.civ@mail.mil

recently been reported by Doi et al.⁶ and Yamada et al.^{7,8} The $\text{Li}_4\text{Ti}_5\text{O}_{12}$ thin film electrode was prepared using sol-gel process while LiMn_2O_4 and LiCoO_2 were prepared using pulse laser deposition technique. The values of E_a obtained for Li^+ charge transfer across the $\text{Li}_4\text{Ti}_5\text{O}_{12}$ /electrolyte, LiMn_2O_4 /electrolyte and LiCoO_2 /electrolyte interfaces are about 44–48 kJ/mol, 50 kJ/mol and 46 kJ/mol,^{6–8} respectively, in a temperature range of 10°C to 40–45°C. These values are lower than that for Li^+ charge transfer across the HOPG/electrolyte interface with varying amounts. However, the E_a values are still quite large for Li^+ to move across the lithium transition metal oxide and electrolyte interface. It seems reasonable to attribute the large E_a values to the de-solvation step as identified by Ogumi and Abe et al.^{2–8}

Li^+ charge transfer resistance at the interface between lithium iron phosphate (LiFePO_4 or LFP) electrode and electrolyte of LiPF_6 in EC with linear carbonate mixtures was recently reported by X. Liao et al.⁹ and L. Liao et al.¹⁰ In these studies, the electrodes were made of a mixture of LFP active material with carbon diluents and binder. As with previous studies,^{2–8} the cells with Li as a counter electrode and a reference electrode were used in these studies. L. Liao et al.¹⁰ also reported activation energy values of 33.8 kJ/mol for LFP electrode at the fully charged state (or fully de-lithiated state). Li et al.¹¹ recently also reported activation energy of electrode reaction of 58 kJ/mol and 66 kJ/mol at LFP and graphite electrodes using LFP/Li and graphite/Li half cells in LiPF_6 in EC:PC:EMC mixtures, respectively, in a configuration of two electrodes button cells. Liaw et al.¹² studied the power and capacity fades of NCA/graphite 18650 cells containing LiPF_6 in EC:EMC electrolyte correlating with the cell impedance through the evaluation of activation energies of these parameters. Activation energy values of 50–55 kJ/mol for the initial stage of degradation of various degrees of aged cells were reported. The activation energy of the static heat generation rate of un-aged cells about 55 kJ/mol was also reported. The reported cell impedance of the cells aged in different conditions in medium frequencies seems to correlate with the power and capacity degradation and static heat generation.

As the Li ions are brought from the electrolyte to Li in the electrode by crossing the electrode/electrolyte interfaces for completing a charge or discharge process, it is reasonable to suggest that the solvated Li^+ in the electrolyte goes through the same solvation and desolvation steps during charge/discharge at either the graphite/electrolyte or the cathode/electrolyte interface. As suggested by previous reports, the desolvation of solvent molecules from Li^+ is the rate limiting step. This suggests that the E_a for Li^+ charge transfer at either electrode would be similar. However, at different interfaces, the different SEIs, or different interphases formed on electrode surfaces and different nature of the electrodes could have played a role in affecting the Li^+ charge transfer kinetics and their activation energy. Such distinction has not been well studied before.

The R_{ct} was recently examined at the NCA/electrolyte interface and at the graphite/electrolyte interface at the same time in a 3-electrode pouch cell using a DC pulse current measuring resistance changes at both electrodes at the same time at temperatures from 25°C to –40°C.¹³ It was found that the E_a value at the graphite/electrolyte interface is 61 kJ/mol, which is consistent with the values reported by Jow et al.¹⁴ and Xu.¹⁵ However, the E_a value for the NCA/electrolyte is 41 kJ/mol, which is substantially lower than at the graphite/electrolyte interface. This result suggests that the nature of the electrode and the associated SEI or interphases formed at the interface could have played significant roles in influencing the Li^+ charge transfer kinetics.

The R_{ct} values measured using a DC pulse current technique includes other resistance such as electrolyte resistance and contact resistance, which could compromise the accuracy of the R_{ct} values although insignificant at temperatures at or below –20°C. While believing the conclusion is qualitatively correct, it was decided to further confirm these results by measuring R_{ct} using an AC impedance method on NCA/Graphite. LFP/graphite systems were also added, in which the LFP electrode is of different nature from other lithium transition metal oxides, for closer examination of the Li^+ charge transfer kinetics at both the graphite/electrolyte and LFP/electrolyte interfaces. The importance of the nature of the electrode and how the electrode kinetics

could be affected are what were set out to be understood through such examinations.

Experimental

Electrode materials, electrodes and cell configurations.— Two different Li-ion cell chemistries were examined in this study, NCA/graphite and LFP/graphite. The 3-electrode NCA/graphite pouch cells include the same cathode and anode as those used in the Saft VL6A cells plus a third electrode made of pure Li as a reference electrode. Both the NCA and the graphite electrodes are porous electrodes. The dimension of the NCA cathode was 6.35 cm × 3.81 cm, the dimension of the graphite anode was 7.62 cm × 5.08 cm, and the reference electrode was roughly 2 cm × 1 cm. The electrolyte is made of 1M LiPF_6 in EC:DMC:MB (methyl butyrate) + VC (vinylene carbonate) mixtures with MB content greater than 50 volume percent and VC content smaller than 3 but larger than 0.5 weight percent. In each cell, 1.5 mL of electrolyte was used. This electrolyte could stay as liquid and perform at temperatures as low as –40°C.¹⁶ The nominal capacity at C rate at 4.1 V/2.5 V at 25°C is 16 mAh. The 3-electrode LFP/graphite pouch cells were similarly constructed with the dimensions of the cathode, anode, and reference electrode being the same as for the NCA cell. The electrolyte and the amount of electrolyte used was also the same. The nominal capacity of LFP/graphite cells at C rate at 3.6 V/2.5 V at 25°C is approximately 15 mAh. For NCA/electrolyte cells, the AC impedance measurements were carried out at 3.91 V and 0.22 V vs. Li/Li^+ for the NCA cathode and the graphite anode, respectively. For LFP/graphite cells, the impedance measurements were carried out at 3.43 V (at a 50% SOC) and 0.14 V vs. Li/Li^+ for the LFP cathode and the graphite anode, respectively. The potentials of graphite anode vs. Li/Li^+ in NCA/graphite and LFP/graphite cells are both in the highly lithiated state. At this state, the graphite electrode is conductive and of similar resistance. The potential of the graphite electrode changed only little from the initial chosen potential under our experimental conditions.

DC pulse current resistance and AC impedance measurements.

The DC pulse current resistance of the cell, cathode, and anode were determined by the following steps. A pulse current, I_{pulse} , was applied to the cell, which was equilibrated for one hour at a voltage, V_o , before applying a current, and measuring the cell voltage, V_t , as a function of time for fifteen seconds. The DC pulse resistance of the cell during charge, R_c , or during discharge, R_d , was obtained by dividing the voltage change, $\Delta V = V_t - V_o$, by I_{pulse} depending on the directions of the current. The experiment was carried out at 25, 0, –20, –30, and –40°C. For LFP/graphite cells, the cell was charged and then discharged for one hour at a rate of C/2 to assure the cell was at the 50% of the state-of-charge for each measurement. The pulse current values, for the NCA/graphite cell, from 25°C to –40°C, were 80 mA (5C), 16 mA (C), 8 mA (C/2), 2.67 mA (C/6), and 1 mA (C/16) respectively. The pulse current values for the LFP/graphite cell, from 25°C to –40°C, were 30 mA (2C), 15 mA (C), 7.5 mA (C/2), 1.875 mA (C/8), and 0.75 mA (C/20) respectively. The reason different I_{pulse} values were used for the cells was based on the resistance values at 25°C and adjusted so that the change in voltage would be noticeable but not too extensive. A Solartron ModuLab Potentiostat with a Frequency Response (FRA) module was used to measure the DC pulse resistance.

The AC impedance of the cell, cathode, and anode were determined using a galvanostatic AC impedance method. An AC current was applied across the graphite anode and the cathode terminals of the cell, in which both the graphite anode and the cathode were subjected to the same current perturbation. The AC voltage responses of the cell and each electrode monitored using the reference Li electrode were then recorded and the AC impedances calculated. The AC impedance of the cell and electrodes were measured from 100 kHz to 10 mHz. The experiments were carried out at the same temperatures as those used for the DC pulse methods. The amplitudes for the NCA/graphite

cell, from 25°C to −40°C, were 5 mA (C/3.2), 2 mA (C/8), 1.5 mA (C/10.67), and 0.5 mA (C/32) respectively. The amplitudes for the LFP/graphite cell, from 25°C to −40°C, were 7.5 mA (C/2), 3.75 mA (C/4), 2.5 mA (C/6), 1.5 mA (C/10), and 1.07 mA (C/14). The reason different amplitudes were used for the cells was based on the impedance values at 25°C and adjusted so that the change in voltage would be noticeable but not too extensive. A Solarton ModuLab Potentiostat with a Frequency Response Analyzer (FRA) module was used to measure the AC impedance.

Results and Discussion

The Li^+ charge transfer kinetics at graphite/electrolyte, NCA/electrolyte and LFP/electrolyte interfaces were examined using two full NCA/graphite and LFP/graphite pouch cells with Li as a reference electrode with both cell chemistries in the same electrolyte. A DC pulse resistance method and an AC impedance method were employed to measure the resistance associated with the Li^+ charge transfer kinetics. The resistance, R , was measured at temperatures from 25°C down to −40°C using each method. The R value as shown in Eq. 1 is determined by the pre-factor A_0 and the activation energy, E_a , for the thermally activated process. A_0 could be varied with the accessibility of intercalation sites or the availability of lithium ions on the electrode surfaces. A_0 could be different for different electrode materials and electrode morphologies in the same electrolyte. For this study, A_0 is assumed to be a constant and independent of temperature.

DC pulse resistance of NCA/graphite and LFP/graphite cells.—The DC pulse resistance of the NCA/graphite cell, NCA cathode and graphite anode at various temperatures were measured and reported by Jow et al.¹³ At 25°C, the cell resistance is largely due to the NCA cathode with less than 10% contribution coming from the anode resistance at 15 s charge or discharge. With decreasing temperature, the contribution of the graphite anode resistance increases. As a result, the activation energy, E_a , for Li^+ charge transfer at the graphite/electrolyte interface is 61 kJ/mol, which is higher than the 41 kJ/mol that was found at the NCA/electrolyte interface. A similar trend was found in the DC pulse resistance of LFP/graphite cells as shown in Fig. 1.

The slopes of the plot of $\log(1/R)$ vs. $1/T$ for both the graphite anode and LFP cathode, as shown in Fig. 2, were used to calculate the E_a s of both electrodes. The E_a values for the Li^+ charge transfer across the LFP/electrolyte and the graphite/electrolyte interfaces were 31 kJ/mol and 58 kJ/mol, respectively. The E_a value for the graphite anode in the LFP/graphite cell is consistent with that for the graphite anode in the NCA/graphite cell. However, a lower E_a value was found at the LFP/electrolyte interface than at the NCA/electrolyte interface.

AC impedance of NCA/graphite cells.—A galvanostatic AC impedance method was used to measure the impedance of 3-electrode pouch cells. The 3-electrode cell configuration allowed for impedance measurements of the full cell and the individual electrodes simultaneously. The AC impedance of the graphite anode, the NCA cathode and the full cell plotted as Nyquist plots at temperatures 25°C, 0°C, −20°C, −30°C and −40°C are shown in Fig. 3. The potentials of the NCA cathode at 3.91 V and the graphite cathode at 0.22 V were selected for impedance measurement. The results show that there are two depressed and overlapped semicircles with a straight line at low frequencies indicating resistance associated with diffusion at the NCA cathode. At −30°C or below, the diffusional behavior has disappeared. At the graphite anode, only one semicircle was observed for the most part. The distinct differences in impedance spectra between the two electrodes reflect a clear distinction in Li^+ charge transfer kinetics between the graphite anode and the NCA cathode. The graphite anode behaviors at 25 and 0°C are hard to explain. The semicircle turned into another semicircle below the x-axis and then went up as almost a straight line at lower resistance values. This behavior could be due to the substantially low resistance at the graphite anode such that the inductive component of the measuring system became dominant at these two temperatures. The diameter of the semicircle above the x-

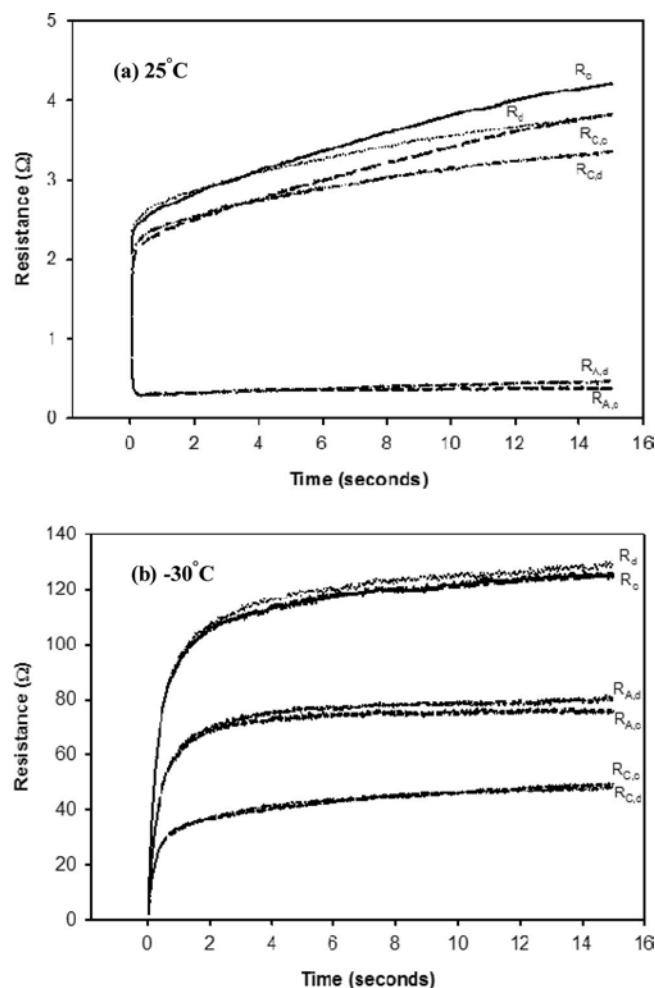


Figure 1. The cell impedance, R_c and R_d , the graphite anode impedance, $R_{A,c}$ and $R_{A,d}$, and the LFP cathode impedance, $R_{C,c}$ and $R_{C,d}$, during charge and discharge, respectively, at 25°C and −30°C measured at LFP: 3.43 V and graphite: 0.15 V.

axis was assigned as the real resistance of the anode. The measured impedance was so small that the impact of the inductive loop on the determination of E_a is insignificant.

Interpretation of impedance data of NCA/graphite cell.—The electrodes used in this study are industrial Li-ion electrodes, which are

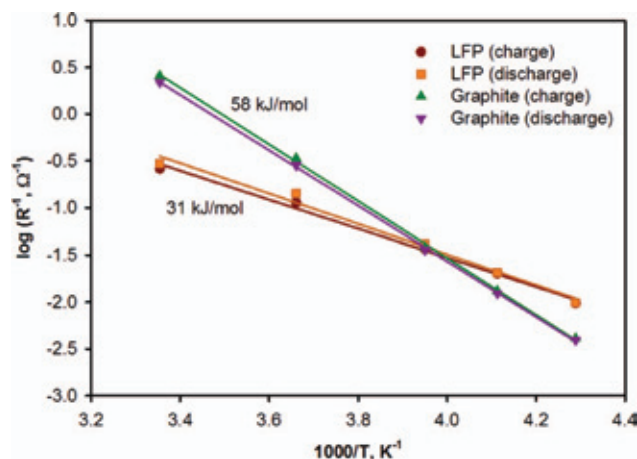


Figure 2. The $\log(1/R)$ versus $1/T$ plots for the LFP cathode and the graphite anode during charge and discharge of the 3-electrode pouch cell at 15 s.

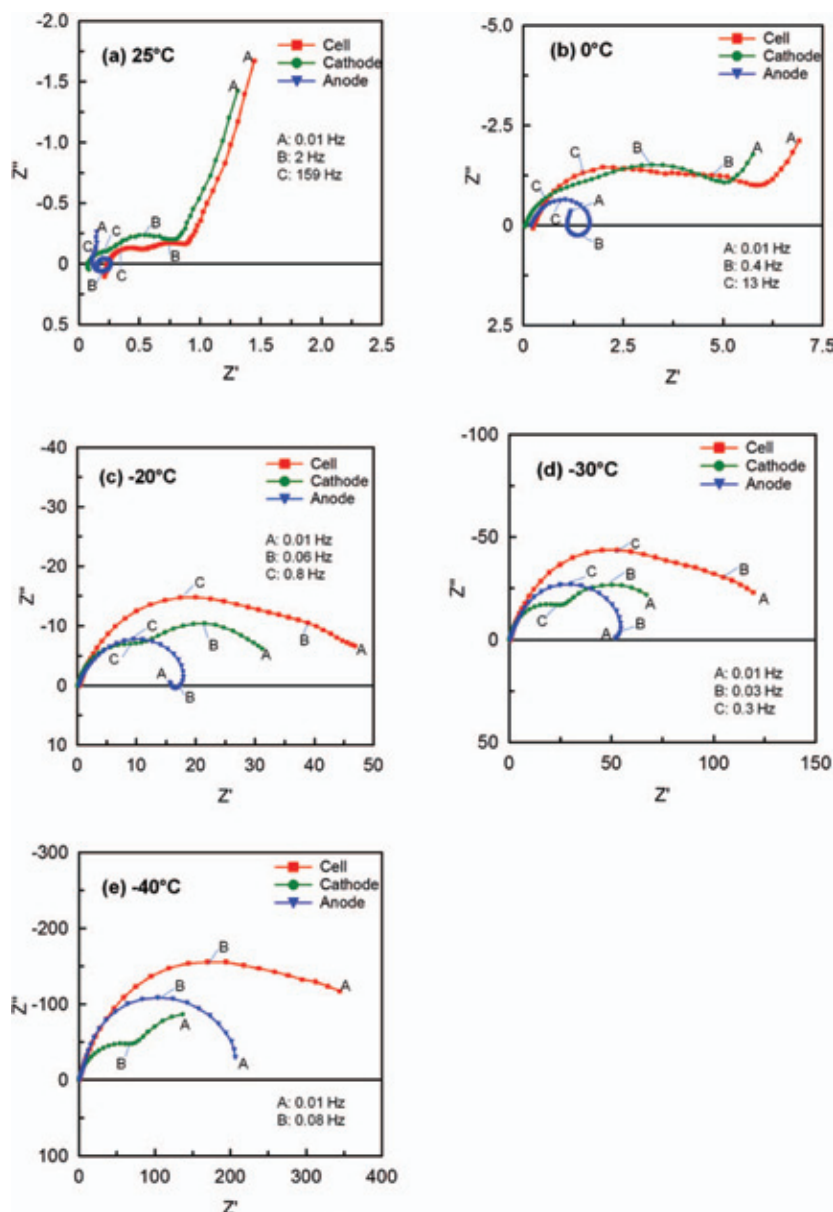
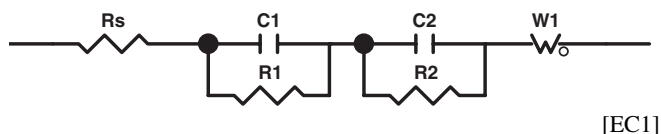


Figure 3. Nyquist plots of galvanostatic AC impedance of a NCA/graphite cell at (a) 25°C, (b) 0°C, (c) -20°C, (d) -30°C and (e) -40°C, where the graphite anode is shown in blue, the NCA cathode is green and the full cell is red.

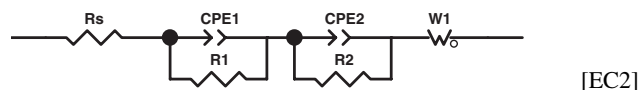
porous and may contain active materials of different particle sizes. The Nyquist plots shown in Fig. 3 could not be fitted using the equivalent circuit (EC) made of simple RCs and Warburg impedance as shown below.



One simple way to look at the data is to use apparent resistance (or the total length of resistance on the x-axis) as the total resistance of the Li^+ charge transfer process. The apparent resistance is defined as resistance from the intersection of the semicircle on the x-axis at the high frequency end to the intersection of the semicircle at the lower frequency, which for some plots needed to be extended in order to intersect the axis. The R_{ct} values obtained by this method were used to estimate the activation energy for Li^+ charge transfer kinetics at both electrodes as discussed in the following sub-section.

Since the Li^+ charge transfer resistance that was measured reflects the nature of heterogeneity of the SEI and possibly distributed time-constant for charge transfer reactions, a constant phase element

(CPE)¹⁷ approach was adopted. The equivalent circuit made of R_s , two circuits in series, each is made of R and CPE in parallel, and a Warburg impedance as shown in EC2 was used to fit the impedance of the NCA electrode at 25°C, 0°C, -20°C and -30°C.



At -40°C, the equivalent circuit made of R_s , two circuits, each is made of R and CPE in parallel without a Warburg impedance as shown in EC3 was used to fit the impedance of NCA electrode.



The impedance of the graphite anode in the NCA/graphite cell was fitted using the equivalent circuit made of one single R -CPE in parallel

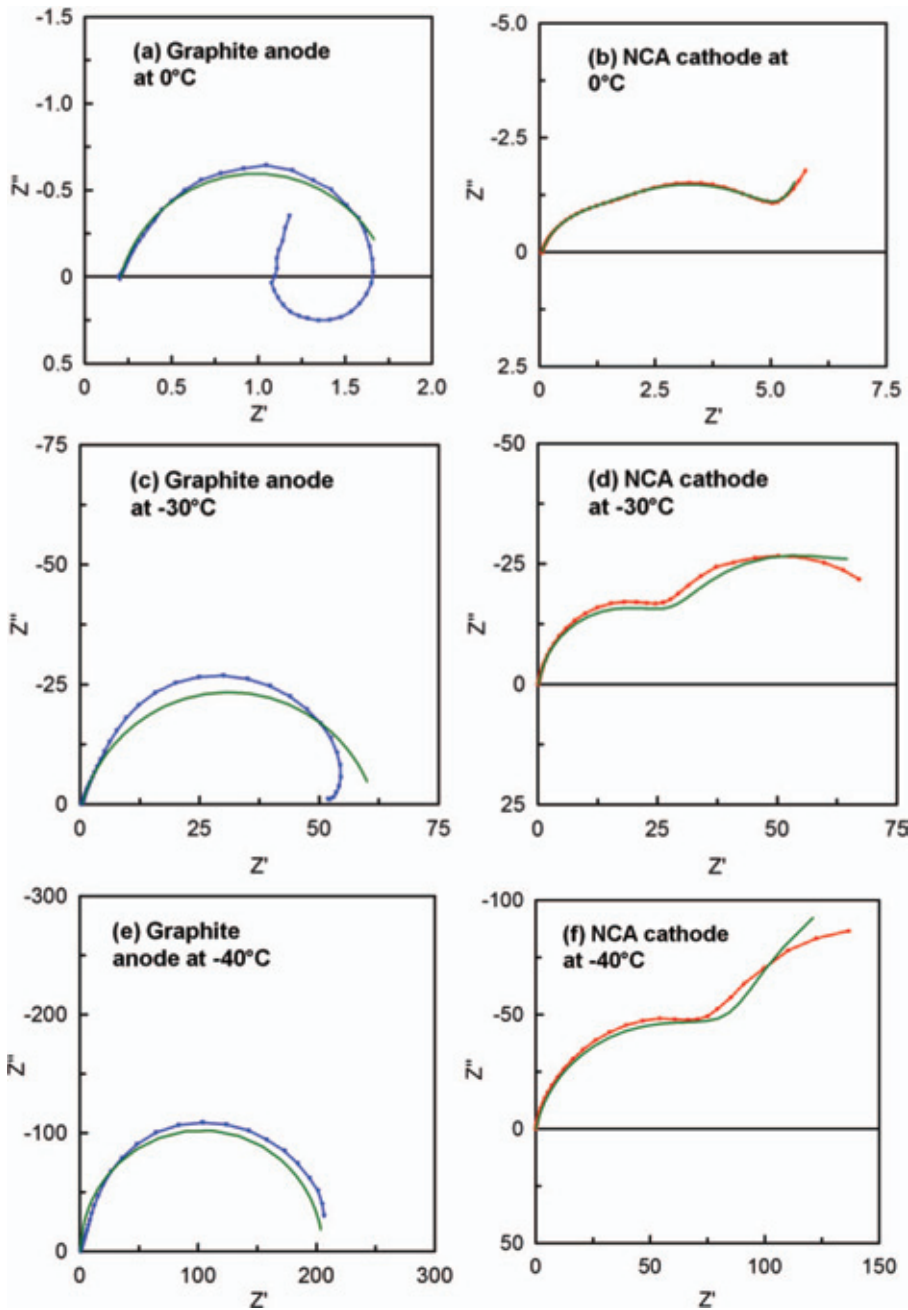


Figure 4. The curves that fit the Nyquist plots shown in Fig. 3 using the equivalent circuits EC2, EC3 or EC4 are plotted. Only fitting curves at 0°C, -30°C and -40°C are shown. R1 is the charge transfer resistance due to the faster process (at higher frequencies) and R2 is the charge transfer resistance due to the slower process (at lower frequencies). (a) Graphite electrode at 0°C (fitted with EC4), (b) NCA electrode at 0°C (fitted with EC 2), (c) Graphite electrode at -30°C (fitted with EC4), (d) NCA electrode at -30°C (fitted with EC2), (e) Graphite electrode at -40°C (fitted with EC4), (f) NCA electrode at -40°C (fitted with EC3).

as shown in EC4 at all temperatures.



[EC4]

Using these equivalent circuits, a reasonably well fit was obtained. Data fitting using the equivalent circuits, EC2 to EC4 at 0°C, -30°C and -40°C for the graphite anode and NCA cathode are shown in Fig. 4. Through the above impedance data fitting, R values obtained from R1 and R2 processes were used to estimate Eas of these processes as discussed in the following sub-sections.

Activation energy for Li^+ charge transfer at NCA and at graphite electrodes.—The R values obtained in the previous section were used to estimate the E_a values of the Li^+ charge transfer kinetics at both the graphite and NCA electrode. These values are calculated from the slopes of the $\log(1/R)$ vs. $1/T$ plots. Fig. 5 shows the $\log(1/R)$ vs. $1/T$ for the total apparent resistance estimated from Fig. 3. The E_a

values for the NCA cathode and the graphite anode are 49 kJ/mol and 68 kJ/mol, respectively, as calculated from the slopes and are also shown in the figure.

R values could also be obtained by fitting the data in Nyquist plots using the equivalent circuits containing CPE such as EC2 to EC4 as shown in Fig. 4. The activation energy of the NCA cathode and graphite anode could also be calculated from the slopes of the $\log(1/R)$ vs. $1/T$ plots. For the NCA cathode, the impedance spectra suggest two processes represented by R1 and R2. R1 could be due to surface films or the interphases formed on the NCA cathode and R2 could be the charge transfer resistance. For the graphite anode, the impedance spectra suggest only one major process R2 representing charge transfer. The R1 representing SEI layer at the graphite anode was too small relatively to R2 to be observed. Fig. 6 shows the $\log(1/R)$ vs. $1/T$ for R1 and R2 for the NCA cathode and R2 for the graphite anode. The E_a values for the NCA cathode are 55 kJ/mol (R1) and 51 kJ/mol (R2) and the graphite anode 68 kJ/mol as calculated from the slopes and are also shown in Fig. 6. The E_a value for the graphite anode

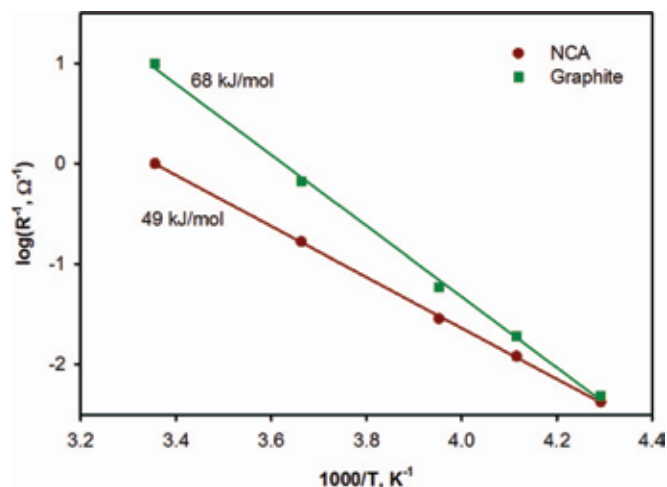


Figure 5. Log(1/R) vs. 1/T plot for R values obtained using the total apparent charge transfer resistance for the NCA/graphite cell as seen from the x-axis of the Nyquist plots shown in Fig. 3.

in the NCA/graphite cell is consistent with that reported by Jow et al.¹⁴ and Xu.¹⁵ The activation energy for the two processes at the NCA cathode is similar. Liaw et al.¹² reported 50–55 kJ/mole activation energy values for the initial stage of degradation of NCA/graphite cell and the static heat generation of un-aged 18650 NCA/graphite full cells in a temperature range of 25 to 65°C. These numbers are close to the average of the activation energies for NCA/electrolyte and graphite/electrolyte obtained here. This also suggests that there is a link between the charge transfer resistance, cell heat generation and cell degradation.

AC impedance of LFP/graphite cells.— The AC impedance of the graphite anode and the LFP cathode plotted as Nyquist plots are shown in Figs. 7 and 8, respectively. The plots at a smaller scale are shown as an insert in the figures in order to see the results obtained at 25°C and 0°C. The potentials of the LFP cathode at 3.45 V and the graphite anode at 0.15 V were selected for impedance measurement.

The impedance spectra of the LFP electrode also exhibited more depressed semicircles than the graphite electrode in the LFP/graphite cell similar to that of the NCA electrode in NCA/graphite cell. Similar to the NCA/graphite system, the Nyquist plots shown in Figs. 7 and

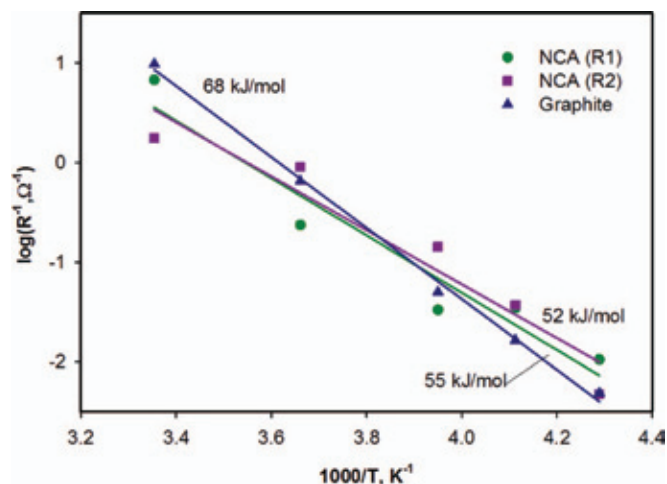


Figure 6. Log(1/R) vs. 1/T plot for R values obtained using the equivalent circuit containing CPE for the NCA/graphite cell shown in the Nyquist plots in Fig. 4.

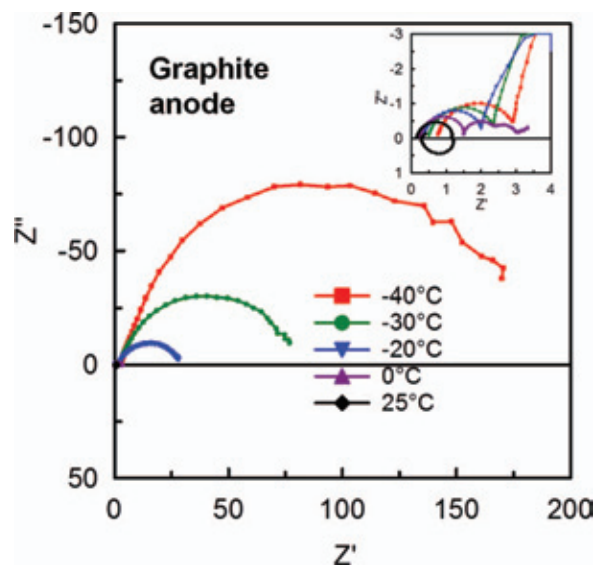


Figure 7. Nyquist plots of galvanostatic AC impedance of the graphite anode at 25, 0, -20, -30 and -40°C in a LFP/graphite cell. The insert shows the impedance curves at a smaller scale.

8 could not be fitted using the equivalent circuit made of simple RCs and Warburg impedance. With the use of the constant phase element (CPE),¹⁷ the Nyquist impedance plots could be fitted nicely. One example is shown in Fig. 9 for the LFP and the graphite impedance fitting in a LFP/graphite cell at -20°C. The values of R1 and R2 for the LFP and graphite anode at various temperatures are shown in Fig. 10a. R1 represents the resistance resulting from SEI or surface films on either graphite anode or LFP cathode. R2 represents the charge transfer resistance, R_{ct} , at either interface. The figure clearly indicates that R values from the R2 process for the graphite anode increases faster than those for the LFP electrode. The E_a values for the LFP cathode are 2.3 kJ/mol (R1) and 33 kJ/mol (R2) and the graphite anode are 7 kJ/mol (R1) and 67 kJ/mol (R2) as calculated from the slopes of the log(1/R) versus 1/T plots as shown in Fig. 10b.

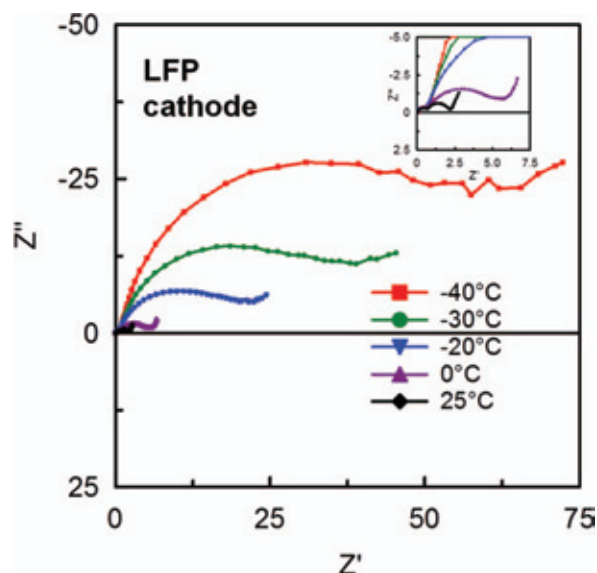


Figure 8. Nyquist plots of galvanostatic AC impedance of the LFP cathode at 25°C, 0°C, -20°C, -30°C and -40°C in a LFP/graphite cell. The insert shows the impedance curves at a smaller scale so that the results from 25°C and 0°C can be observed.

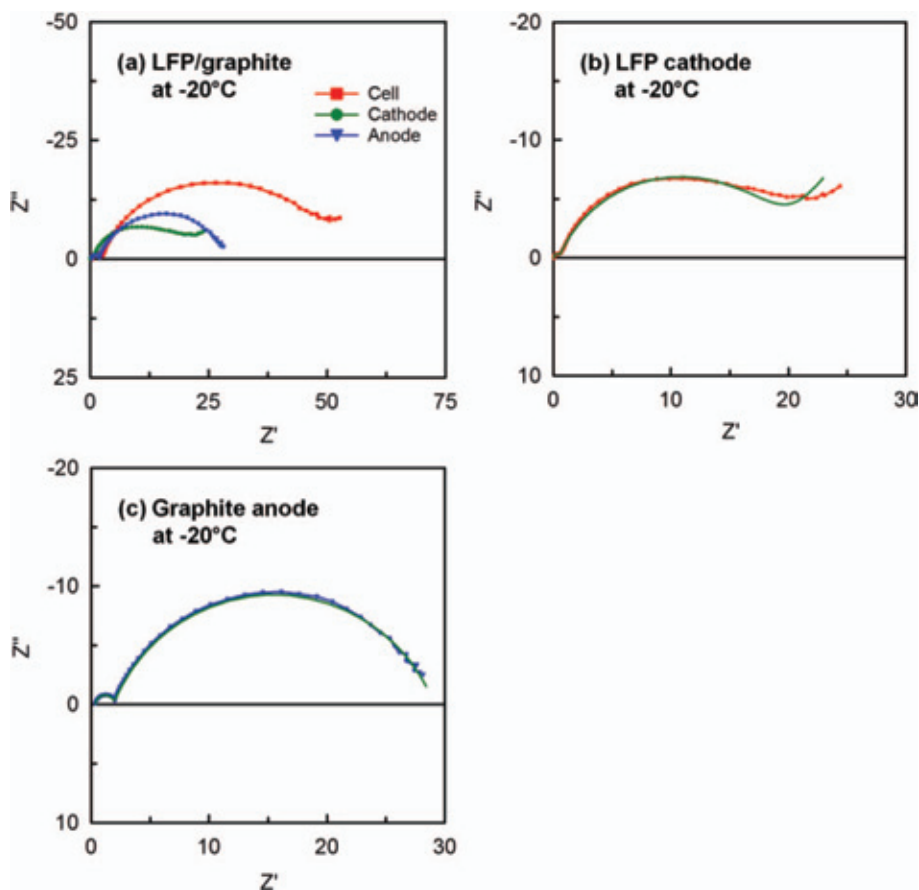


Figure 9. (a) The Nyquist plots of the impedance of the LFP/graphite cell, LFP cathode and graphite anode. (b) The fitting curve of the LFP cathode using EC2. (c) The fitting curve of the graphite anode using EC3.

The E_a value for the graphite anode in the LFP/graphite cell is also consistent with that reported by Jow et al.¹⁴ and Xu.¹⁵ The obtained E_a for charge transfer process is very close to that obtained by L. Liao et al.¹⁰ at the fully charged state and 32 kJ/mol E_a values calculated based on Eq. 1 using R_{ct} values reported by X. Liao et al.⁹ However, these values are lower than that obtained by Li et al.¹¹ using LFP film electrode and two electrodes button cells.

Distinguishing Li^+ charge transfer kinetics at different electrode/electrolyte interfaces.— The impedance spectra for graphite anode, NCA cathode and LFP cathode obtained from the AC impedance measurements using NCA/graphite and LFP/graphite full cells as shown in Figs. 3, 7, and 8 provide an insightful look at how electrode materials affect the impedance behavior and therefore the kinetics at each electrode. For the graphite anode, the semicircle as shown in the impedance spectra indicates that the charge transfer process dominates with little or no observable R_{SEI} contribution. For the NCA cathode, two depressed semi-circles represent two processes, one at medium frequencies represents process due to surface film or interphases layer formed at the NCA/electrolyte interface and one at lower frequencies represents charge transfer process. Both processes contribute almost equally to the impedance of the NCA electrode. For the LFP cathode, two depressed semicircles were also observed while only one at the lower frequencies dominates. The faster one, R1, is small relative to the charge transfer process.

By analyzing the impedance spectra using the equivalent circuits as shown in EC2 to EC4, we determined the charge transfer resistance, R_{ct} , or R2 process for each interface. The activation energy, E_a , values for Li^+ charge transfer at the different interfaces obtained using the AC method along with the DC method are summarized in Table I. The E_a values obtained using the DC method are lower than that using the AC method as R values obtained using DC methods include more than just the charge transfer resistance, R_{ct} , which is

less dominant at temperatures above -20°C . Qualitatively, the results are in good agreement that the E_a values at the graphite/electrolyte interface are significantly larger than at either the NCA/electrolyte or the LFP/electrolyte interface. The E_a values of 68 kJ/mole or 67 kJ/mol obtained from AC impedance method using equivalent circuit fitting for graphite/electrolyte interface in either NCA/graphite or LFP/graphite cells were consistent with earlier reports.^{13–15} E_a values at the NCA/electrolyte interface appear to be consistent with those at other lithium transition metal oxide/electrolyte interfaces.^{6–8}

The E_a values of 52 kJ/mol and 33 kJ/mol for the NCA/electrolyte interface in the NCA/graphite cell and LFP/electrolyte interface in LFP/graphite cell, respectively, strongly suggest that the electrode materials have a significant impact on the activation energy for the Li^+ charge transfer kinetics across the electrode/electrolyte interface.

How the nature of the electrode material is impacting the activation energy of the Li^+ charge transfer across the electrode/electrolyte interfaces is not clear. However, the fact that the nature of the SEI formed on the electrode surface is impacted by the electrode material is clear. El Ouatani et al.^{18,19} reported that the polymerization of VC, which was used as an additive in the electrolyte, was detected only on the surfaces of certain electrode materials even the electrochemical potential of these electrodes relative to Li/Li^+ were similar. For example, the VC polymerization is observed at the surface of the graphite electrode and LiCoO_2 electrode in LiCoO_2 /graphite cells.¹⁸ However, the VC polymerization is not observed at the surface of the LFP electrode when VC is present in the LFP/graphite cells.¹⁹ The difference in surface films, which could be SEI or other interphases, on the cathode is consistent with the fact that Co^{4+} , which is present in the charged $\text{Li}_{1-x}\text{CoO}_2$ electrode, will be more oxidizing than the Fe^{3+} found in FePO_4 , the charged composition of the iron phosphate cathode. These results appear to support the observation that the activation energy for the Li^+ charge transfer kinetics at the LFP/electrolyte interface is smaller than that at the NCA/electrolyte interface.

Table I. Activation energy, E_a , values for Li^+ charge transfer at the NCA and the graphite electrodes in the NCA/graphite cell and at the LFP and the graphite electrodes in the LFP/graphite cell obtained using both DC and AC methods, where R1 and R2 are obtained by fitting the data using the equivalent circuits.

Measuring Method	E_a , kJ/mole							
	At Cathode/electrolyte Interface				At Graphite/electrolyte interface			
	DC Pulse	AC Impedance			DC Pulse	AC Impedance		
Resistance	R	R, Total Apparent	R ₁	R ₂	R	R, Total Apparent	R ₁	R ₂
NCA/Graphite cell	41	49	55	52	61	68	—	68
LFP/Graphite cell	31	—	2.3	33	58	—	7	67

At the graphite/electrolyte interface, a rather well defined SEI, solid electrolyte interface (or interphase), is formed.²⁰ Desolvation is identified as the limiting factor for the Li^+ charge transfer at the graphite/electrolyte interface.²⁻⁵ This is supported by the measurements that the activation energy for solvated Li^+ to de-solvate and get into the solid electrolyte is similar to that for solvated Li^+ to desolvate and get into SEI and into graphite.²⁻⁵ At the NCA/electrolyte or LFP/electrolyte interface, no well defined SEI layers like that on graphite/electrolyte have been reported. It is believed that the surface films formed on the cathode resulting from oxidative reactions could be thin and varied with the nature of the electrode materials as in-

dicated by El Ouatani et al.^{18,19} This may also attributed to the low activation energy for Li^+ charge transfer at the cathode/electrolyte interface compared to that at the graphite/electrolyte interface.

From a practical point of view, at temperatures above 0°C, the larger R_{ct} values at the cathodes, NCA or LFP, rather than at the graphite anode dictates the cell rate performance. At temperatures below -20°C, the cell kinetics is increasingly dominated by the higher R_{ct} at the graphite/electrolyte interface because of higher activation energy at the graphite/electrolyte interface.

Conclusions

The Li^+ charge transfer kinetics at the graphite/electrolyte interface, the NCA/electrolyte interface, and the LFP/electrolyte interface were studied in the NCA/graphite and the LFP/electrolyte full cells with a Li reference electrode using DC pulse resistance and AC impedance methods. With such cells, the impedance behavior and the Li^+ charge transfer kinetics at the graphite anode and NCA cathode or LFP cathode could be studied at the same time in the same electrolyte. Impedance behaviors at different interfaces were distinctively different. A much less depressed semicircle observed on graphite electrode than those observed on NCA or LFP cathode suggests a better defined SEI existed at the graphite anode. The charge transfer resistance, R_{ct} , values derived from the DC resistance and AC impedance measurements were used to calculate the activation energies at various interfaces. The activation energy values were consistent between these two methods. The activation energies at the graphite/electrolyte interface, the NCA/electrolyte interface and the LFP/electrolyte interface obtained from the AC impedance method are 67 kJ/mol, 52 kJ/mol and 33 kJ/mol, respectively. The differences in activation energies at different interfaces link to the different nature of the electrode materials and their surface films, which could be SEI or other interphase materials, formed on the electrodes. The higher activation energy at the graphite/electrolyte interface was reasonably attributed to well-defined SEI on graphite with desolvation as the limiting factor. The lower activation energy at the NCA/electrolyte or the LFP/electrolyte interface could be attributed to less well defined thin surface films of different nature. In brief, the difference in E_a suggests that Li^+ charge transfer kinetics is greatly influenced with respect to the nature of the electrode materials and their associated SEIs.

Acknowledgments

The authors thank K. Nechev, B. Deveney and S. Rickman at Saft America, Inc. for providing electrodes and helpful discussion and the DOE Office of Renewable Energy and Vehicle Technologies, Applied Battery Research for Transportation Program for partial financial support.

References

1. Z. Ogumi, *Electrochemistry*, **78**(5), 319 (2010).
2. T. Abe, H. Fukuda, Y. Iriyama, and Z. Ogumi, *J. Electrochem. Soc.*, **151**(16), A1120 (2004).

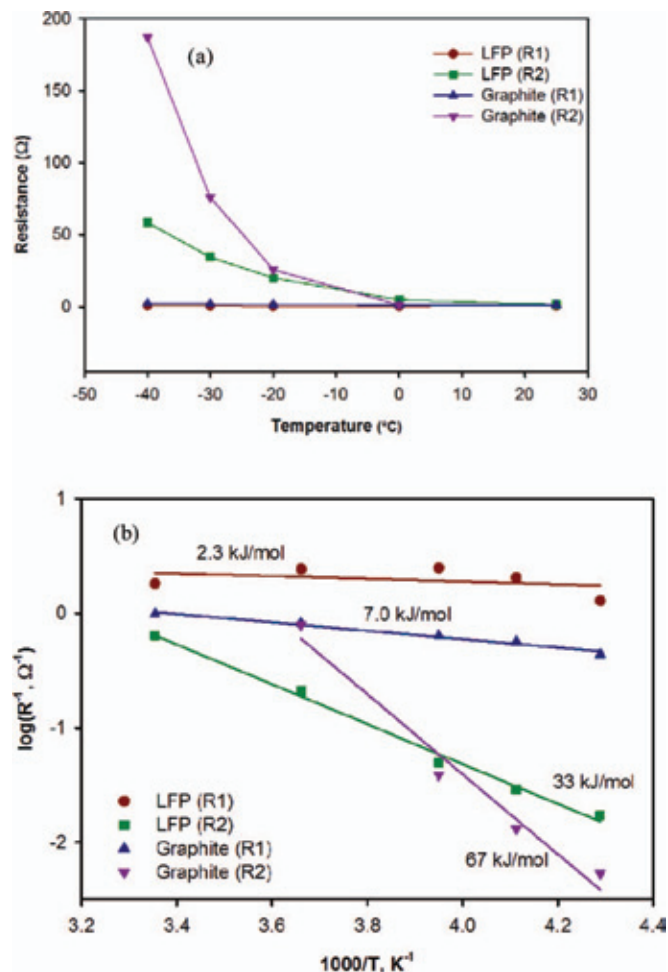


Figure 10. (a) The R1 and R2 impedance values of the LFP cathode and the graphite anode from the LFP/graphite cell. (b) The log ($1/R$) vs. $1/T$ plots for the LFP cathode and the graphite anode. The E_a values calculated from the slopes of each linear fitting are also shown.

3. Y. Yamada, Y. Iriyama, T. Abe, and Z. Ogumi, *Langmuir*, **25**, 12766 (2009).
4. T. Abe, F. Sagane, M. Ohtsuka, Y. Iriyama, and Z. Ogumi, *J. Electrochem. Soc.*, **152**(11), A2151 (2005).
5. Y. Yamada, F. Sagane, Y. Iriyama, T. Abe, and Z. Ogumi, *J. Phys. Chem.*, **113**, 14528 (2009).
6. T. Doi, Y. Iriyama, T. Abe, and Z. Ogumi, *Anal. Chem.*, **77**, 1696 (2005).
7. I. Yamada, T. Abe, Y. Iriyama, and Z. Ogumi, *Electrochem. Commu.*, **5**, 502 (2003).
8. I. Yamada, Y. Iriyama, T. Abe, and Z. Ogumi, *J. Power Sources*, **172**, 933 (2007).
9. X.-Z. Liao, Z. F. Ma, Q. Gong, Y. S. He, L. Pei, and L. J. Zeng, *Electrochem. Comm.*, **10**, 691 (2008).
10. L. Liao, P. Zuo, Y. Ma, X. Chen, Y. An, Y. Ga, and G. Yin, *Electrochim. Acta*, **60**, 269 (2012).
11. J. Li, C. F. Yuan, Z. H. Guo, Z. A. Zhang, Y. Q. Lai, and J. Liu, *Electrochim. Acta*, **59**, 69 (2012).
12. B. Y. Liaw, E. P. Roth, R. G. Jungst, G. Nagasubramanian, H. L. Case, and D. H. Doughty, *J. Power Sources*, **119–121**, 874 (2003).
13. T. R. Jow, J. L. Allen, M. Marx, K. Nechev, B. Deveney, and S. Rickman, *ECS Transactions*, **25**(36), 3 (2010).
14. T. R. Jow, S. Zhang, K. Xu, and J. L. Allen, *ECS Trans.*, **3**(27), 51 (2007).
15. K. Xu, *J. Electrochem. Soc.*, **154**(3), A162 (2007).
16. S. Herreyre, O. Huchet, S. Barusseau, F. Pertion, J. M. Bodet, and Ph. Biensan, *J. Power Sources*, **97–98**, 576 (2001).
17. M. E. Orazem and B. Tribollet, *Electrochemical Impedance Spectroscopy*, p. 233, John Wiley & Sons, Inc., Hoboken, New Jersey (2008).
18. L. El Ouatani, R. Dedryvère, C. Siret, P. Biensan, S. Reynaud, P. Iratçabal, and D. Gonbeau, *J. Electrochem. Soc.*, **156**(2), A103 (2009).
19. L. El Ouatani, R. Dedryvère, C. Siret, P. Biensan, and D. Gonbeau, *J. Electrochem. Soc.*, **156**(6), A468 (2009).
20. R. Fong, U. von Sacken, and J. R. Dahn, *J. Electrochem. Soc.*, **137**, 2009 (1990).

A New Direction for the Performance Improvement of Rechargeable Lithium/Sulfur Batteries

Sheng S. Zhang and Jeffrey A. Read

U.S. Army Research Laboratory, Adelphi, MD

ABSTRACT

In this work we introduce a new direction for the performance improvement of rechargeable lithium/sulfur batteries by employing an electrolyte that promotes Li anode passivation in lithium polysulfide solutions. To examine our concept, we assemble and characterize Li/Li₂S₉ liquid cells by using a porous carbon electrode as the current collector and a 0.25 m Li₂S₉ solution as the catholyte. Results show that Li/Li₂S₉ liquid cells are superior to conventional Li/S cells in specific capacity and capacity retention. We also find that use of LiNO₃ as a co-salt in the Li₂S₉ catholyte significantly increases the cell's Coulombic efficiency. More importantly, the cells with LiNO₃ have a ~2.5 V voltage plateau before the end of charging and demonstrate a steep voltage rise at the end of charging. The former is indicative of the formation of elemental sulfur from soluble lithium polysulfides on the carbon electrode, and the latter provides a distinct signal for full charging. Electrochemical analyses on Li plating and stripping in Li₂S₉ catholyte solutions indicate that LiNO₃ participates in the formation of a highly protective passivation film on the Li metal surface, which effectively prevents the Li anode from chemical reaction with polysulfide anions in the electrolyte and meanwhile prevents polysulfide anions from electrochemical reduction on the Li surface.

Journal of Power Sources, Volume 200, Pages 77-82 (2012)



A new direction for the performance improvement of rechargeable lithium/sulfur batteries

Sheng S. Zhang*, Jeffrey A. Read

U.S. Army Research Laboratory, RDRL-SED-C, Adelphi, MD 20783-1197, USA

ARTICLE INFO

Article history:

Received 26 September 2011

Received in revised form 17 October 2011

Accepted 19 October 2011

Available online 25 October 2011

Keywords:

Lithium/sulfur battery

Sulfur

Polysulfide

Catholyte

Lithium plating

ABSTRACT

In this work we introduce a new direction for the performance improvement of rechargeable lithium/sulfur batteries by employing an electrolyte that promotes Li anode passivation in lithium polysulfide solutions. To examine our concept, we assemble and characterize Li/Li₂S₉ liquid cells by using a porous carbon electrode as the current collector and a 0.25 m Li₂S₉ solution as the catholyte. Results show that Li/Li₂S₉ liquid cells are superior to conventional Li/S cells in specific capacity and capacity retention. We also find that use of LiNO₃ as a co-salt in the Li₂S₉ catholyte significantly increases the cell's Coulombic efficiency. More importantly, the cells with LiNO₃ have a ~2.5 V voltage plateau before the end of charging and demonstrate a steep voltage rise at the end of charging. The former is indicative of the formation of elemental sulfur from soluble lithium polysulfides on the carbon electrode, and the latter provides a distinct signal for full charging. Electrochemical analyses on Li plating and stripping in Li₂S₉ catholyte solutions indicate that LiNO₃ participates in the formation of a highly protective passivation film on the Li metal surface, which effectively prevents the Li anode from chemical reaction with polysulfide anions in the electrolyte and meanwhile prevents polysulfide anions from electrochemical reduction on the Li surface.

Published by Elsevier B.V.

1. Introduction

Lithium/sulfur (Li/S) batteries have attracted increasing interest in developing high density energy storage devices due to their high theoretical capacity. Based on the complete reduction of elemental sulfur to lithium sulfide (Li₂S), Li/S batteries can deliver a specific capacity as high as 1675 mAh g⁻¹ sulfur. However, the specific capacity of a practical cell is lower than the theoretical value and the cell suffers low charging efficiency, high self-discharge and short cycle life [1,2]. All these problems are known to be related to the high solubility of lithium polysulfides, the series of sulfur reduction intermediates, in organic electrolyte solutions. Dissolution of lithium polysulfides not only results in the loss of sulfur active materials from the cathode, but also causes serious “redox shuttle” reactions between polysulfide anions in the electrolyte and the Li metal anode. Recently, a number of publications have reported a reduction in the dissolution of lithium polysulfides by making sulfur-carbon composite materials [3–14]. Based on physical adsorption, these composites in different contexts reduce the dissolution of lithium polysulfides from the cathode. However, these approaches are fundamentally ineffective since polysulfide anions carry negative charges, in discharging the electric field between two

electrodes will drive polysulfide anions migrating toward Li anode. Furthermore, the incorporation of electrochemically inert carbons reduces the gravimetric energy density of Li/S batteries. In addition, we have noticed that most of decent capacities reported previously were obtained through two lows, that is, low sulfur content in composition and low sulfur loading in cathode. In many cases, the total sulfur content in the cathode is not more than 65% by weight and the sulfur loading is not higher than 2 mg sulfur per cm² of cathode [4–7,14–18].

Since dissolution of lithium polysulfides (Li₂S_x, $x > 2$) in organic electrolytes is inevitable, in this work we propose a different approach for the performance improvement of rechargeable Li/S batteries by employing a liquid electrolyte that is able to promote the formation of a highly protective passivation film on lithium surface in lithium polysulfide solutions. We expect that the resulting passivation film not only protects lithium metal from chemical reaction with the polysulfide anions but also prevents polysulfide anions from electrochemical reduction on the Li anode. Our effort will be focused on increasing Li cycling efficiency in highly concentrated lithium polysulfide solutions. To examine our idea, we selected Li/Li₂S₉ liquid cell [19,20], instead of the conventional Li/S cell, as the testing vehicle by employing a porous carbon electrode as the cathode current collector and a Li₂S₉ solution as the catholyte. Due to the known ability of LiNO₃ in facilitating the formation of a better passivation film on Li metal surface [21,22], in this work we study the effect of LiNO₃ on cycling performance

* Corresponding author. Tel.: +1 301 394 0981; fax: +1 301 394 0273.

E-mail address: shengshui.zhang@us.army.mil (S.S. Zhang).

of Li/Li₂S₉ liquid cells and on cycling efficiency of Li metal in Li₂S₉ catholyte solutions by adding LiNO₃ as a co-salt of the Li₂S₉ catholyte.

2. Experimental

Elemental sulfur (S₈, 99.5%), lithium sulfide (Li₂S, 99%), and lithium nitrate (LiNO₃, 99.99%) were purchased from Aldrich and used as received. Lithium bis(trifluoromethane sulfone)imide (LiN(SO₂CF₃)₂, LiTFSI, 3M Company) was dried at 110 °C under vacuum for 10 h and triethylene glycol dimethyl ether (TG3, 99%, Aldrich) was dried over 4 Å molecular sieves for a week. For conventional Li/S cells, a liquid electrolyte was prepared by dissolving 0.2 m (molality) LiTFSI in TG3 in Ar-filled glove-box and a sulfur cathode with a composition of 77% S, 20% Super-P carbon and 3% binder by weight was coated onto a carbon-coated aluminum foil by using poly(acrylonitrile-methyl methacrylate) (ANMMA, AN/MMA = 94:6, MW = 100 000, Polysciences Inc.) as binder and N-methyl pyrrolidinone (NMP) as solvent. Resulting cathode, dried at 80 °C under vacuum for 2 h, had an average loading of 2.4 mg sulfur per cm². For Li/Li₂S₉ liquid cells, a carbon electrode having a composition of 90% Super-P carbon and 10% binder by weight was prepared using the same materials and procedure as was used in preparation of the sulfur cathode and dried at 110 °C under vacuum for 10 h. The carbon electrode was measured to have an average loading of 0.78 mg carbon per cm².

Following Rauh et al's procedure [19,23], lithium polysulfide (Li₂S_x, x = 9) solution was prepared by adding stoichiometric amounts of elemental sulfur (S₈) and Li₂S into the electrolyte solution, followed by heating at 80 °C with magnetic stirring for 6 h. In this work, we prepared two catholyte solutions with composition below:

Catholyte-A: 0.25 m Li₂S₉–0.2 m LiTFSI in TG3

Catholyte-B: 0.25 m Li₂S₉–0.1 m LiTFSI–0.2 m LiNO₃ in TG3

Both solutions were red-dark color and had moderate viscosity. Li/S coin cells with an electrode area of 1.27 cm² were assembled using sulfur cathode and filled with 10 μL electrolyte. Li/Li₂S₉ liquid cells were assembled by using a 1.27 cm² carbon electrode as the cathode current collector (also serving as catalyst for the reduction of elemental sulfur and lithium polysulfides) and 10 μL catholyte solution as the electrolyte and cathode. It should be noted that the assembly of Li/Li₂S₉ liquid cells should be conducted in an oxygen-free environment so as to avoid the oxidization of polysulfide anions by oxygen. For easy comparison with conventional Li/S cells, the specific capacity of Li/Li₂S₉ liquid cells was normalized as "mAh g⁻¹ sulfur". Thus, the theoretical capacity of Li₂S₉ was calculated to be 1489 mAh g⁻¹ sulfur (i.e., 1675 × 8/9 = 1489), and each Li/Li₂S₉ liquid cell contained ~1.65 mg sulfur as calculated based on the amount of Li₂S₉ in the catholyte.

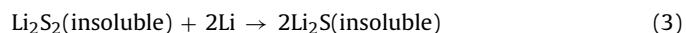
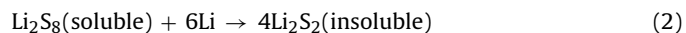
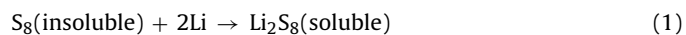
Both Li/S and Li/Li₂S₉ cells were cycled at 0.2 mA cm⁻² on a Macor Series 4000 cyler with a 1.5 V discharge cutoff voltage. The charging process was terminated either by a 3.0 V cutoff voltage or by a capacity equaling to 150% of the last discharge capacity, whichever came first. To measure Li plating and stripping efficiency, a Li/Ni cell with a 1.27 cm² electrode area was assembled and cycled by discharging (Li plating) at 0.2 mA cm⁻² for 1 h and then charging (Li stripping) until the cell's voltage reached 1.0 V. Coulombic efficiency of Li cycling was defined as the percentage of charging time over discharging time. In addition, three-electrode coin cells were assembled for electrochemical measurements by using a 0.97 cm⁻² Ni foil as working electrode, two Li foils as the counter electrode and reference electrode, respectively. Detailed descriptions about cell structure and assembly procedure are

referred to our previous works [24,25]. The impedance and cyclic voltammetry measurements were run on a Solartron SI 1287 Electrochemical Interface and a SI 1260 Impedance/Gain-Phase Analyzer. Impedance was measured at open-circuit potential (OCP) in the frequency range from 0.01 to 100 kHz with an ac oscillation of 10 mV amplitude. Before each test, the cell rested for 1 h after Li plating or Li stripping to get the same conditions.

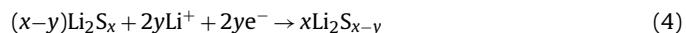
3. Results and discussion

3.1. Li/S cell vs. Li/Li₂S₉ liquid cell

Fig. 1 shows voltage profiles of the first and fifth cycles of a conventional Li/S cell and a Li/Li₂S₉ liquid cell, respectively. For the conventional Li/S cell (Fig. 1a), the initial discharging consists of three voltage regions: (1) a short plateau at 2.3 V as indicated by the arrow, (2) a linear sloping decline, and (3) a long plateau at ~2.0 V until the end of discharge. Combining the conclusions of previous publications [16,26–29], we ascribe these three discharging voltage regions to the following three reactions:



In the following charge step, the cell voltage responds to the reversible processes of Eqs. (2) and (3) until 2.5 V, at which the voltage stays constantly, indicating that Eq. (1) is irreversible. In the fifth cycle, the voltage plateau observed at 2.3 V in the first cycle no longer appears, and the charge voltage does not exceed 2.5 V. For the Li/Li₂S₉ liquid cell (Fig. 1b), the first discharge does not show voltage plateau near 2.3 V since no elemental sulfur exists in the system. However, in the following charge, the cell voltage reaches 3.0 V, achieving a cycling efficiency of 91%. Discharging and charging voltage profiles of the fifth cycle are very similar as those observed in the conventional Li/S cell. We tested many other Li/Li₂S₉ cells and the similar results were repeatedly observed. It should be mentioned that except for the initial few cycles, both the Li/S and Li/Li₂S₉ cells cannot be charged to higher than 2.5 V, i.e., the reversal process of Eq. (1) does not occur. The reason is because soluble lithium polysulfides (Li₂S_x, x > 2), especially those having long S–S chain, dissolve and diffuse to the surface of the Li anode, where polysulfide anions not only are electrochemically reduced as described by Eq. (4) but also are chemically reacted with Li metal as described by Eq. (5).



Thus, the soluble polysulfide anions act as a redox shuttle between the cathode and Li anode, resulting in low charging efficiency.

Fig. 2 compares capacity retention of the conventional Li/S cell and Li/Li₂S₉ liquid cell. It is shown that these two cells have the similar initial capacities (about 610 mAh g⁻¹ S) in spite of the fact that Li₂S₉ has a relatively lower theoretical capacity than elemental sulfur. However, the Li/Li₂S₉ cell exhibits more stable capacity retention. By the end of testing (50 cycles), the Li/Li₂S₉ cell remains 452 mAh g⁻¹ capacity (equaling to 72% of the initial capacity), while the Li/S cell retains only 196 mAh g⁻¹ S (32% of its initial capacity). These results reveal that Li/Li₂S₉ liquid cells are superior to the conventional Li/S cells in capacity retention.

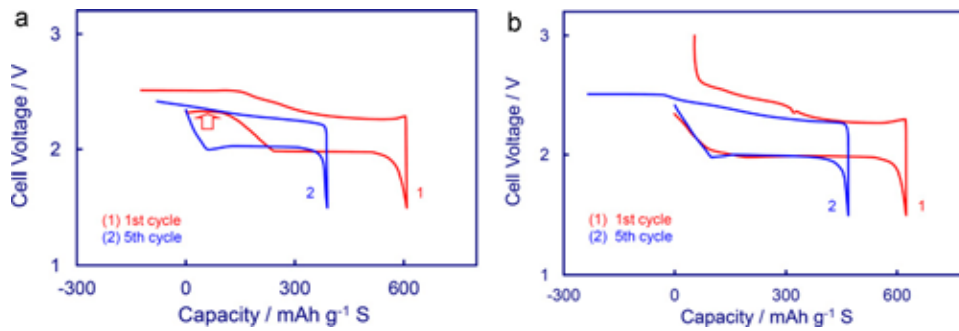


Fig. 1. Discharging voltage profiles of the first and fifth cycles of (a) a conventional Li/S cell and (b) a Li/Li₂S₉ liquid cell.

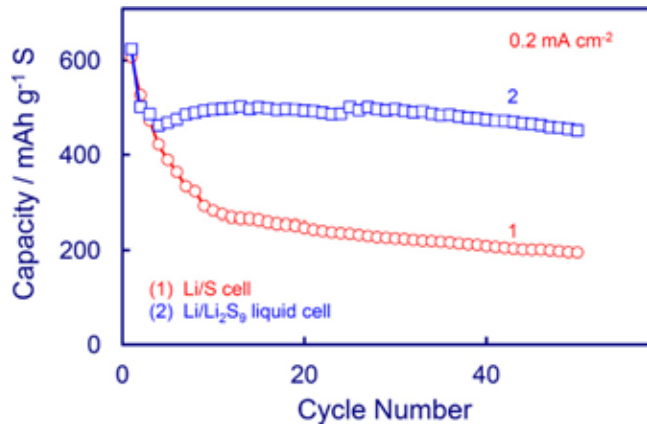


Fig. 2. Comparison of the capacity retention of a conventional Li/S cell and a Li/Li₂S₉ liquid cell.

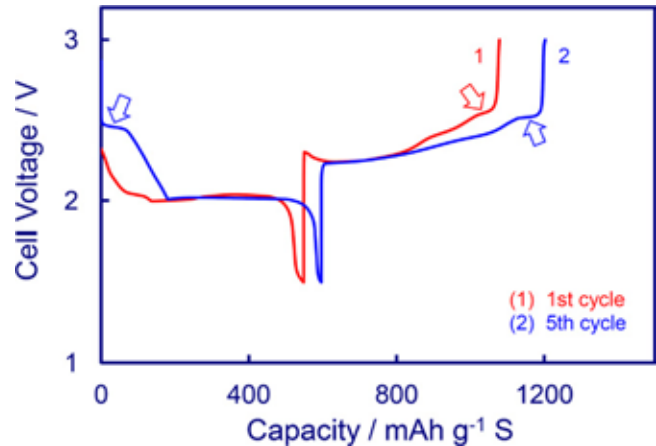


Fig. 4. Voltage profiles of the first and fifth cycles of a Li/Li₂S₉ liquid cell with Catholyte-B.

3.2. Effect of LiNO₃ on cycling performance

Reactions (4) and (5) are believed to be the main cause for the low charging efficiency and high self-discharge rate of Li/S batteries. Furthermore, their reaction products will permanently deposit on the surface of the Li anode if insoluble Li₂S_x ($x \leq 2$) is formed. When this happens, the performance of Li/S cells will be dramatically affected. For this reason, in this work we focused our effort on suppressing Reactions (4) and (5) by adding LiNO₃ as a co-salt in the Li₂S₉ catholyte. Fig. 3 compares discharging and charging voltage profiles of two Li/Li₂S₉ cells with and without LiNO₃ as co-salt. As indicated in Fig. 3a, the most significant difference between these two cells is that Cell-2 with LiNO₃-containing Catholyte-B can repeatedly be charged to 3 V while Cell-1 with Catholyte-A free of LiNO₃ can be charged above 2.5 V only in the first cycle. Another difference is that Cell-2 exhibits a pair of additional voltage plateaus

at ~2.3 V in discharge and charge processes, as indicated by two arrows in Fig. 3b. This pair of voltage plateaus can be attributed to the reversible reaction of Eq. (1).

To further verify this, we plot discharge and charge curves for the first and fifth cycles of Cell-2 in Fig. 4. It can be seen that the first discharge does not show voltage plateau near 2.3 V although Li₂S₉ has a longer S-S chain than elemental sulfur (S₉ vs. S₈), instead, the fifth discharge shows a distinct plateau at 2.3 V. In charging, both the first and fifth cycles distinctly show a 2.3 V plateau, followed by a steep voltage rise to the cutoff voltage (3.0 V). These results indicate that the 2.3 V plateau is not related to the length of polysulfide anions (i.e., the x value in Li₂S_x), instead to the two-phase Reaction-1 occurring between Li₂S_x in solution and elemental sulfur in cathode.

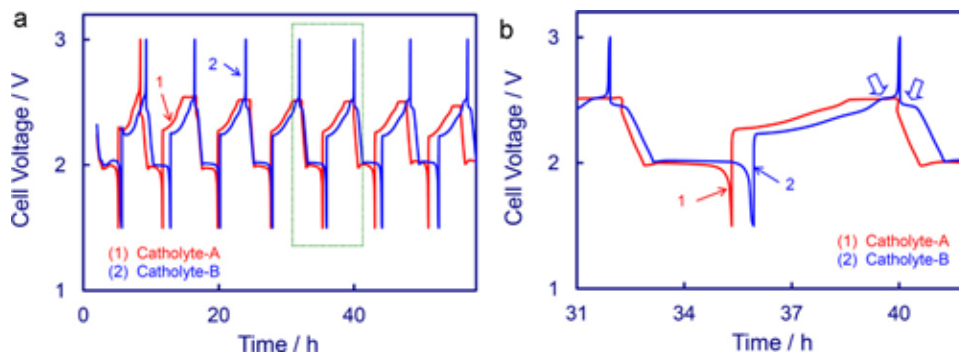


Fig. 3. Voltage profiles of the discharging and charging cycles of two Li/Li₂S₉ liquid cells with Catholyte-A and Catholyte-B, respectively: (a) overall view of the voltage profiles and (b) cell voltages of a typical cycle.

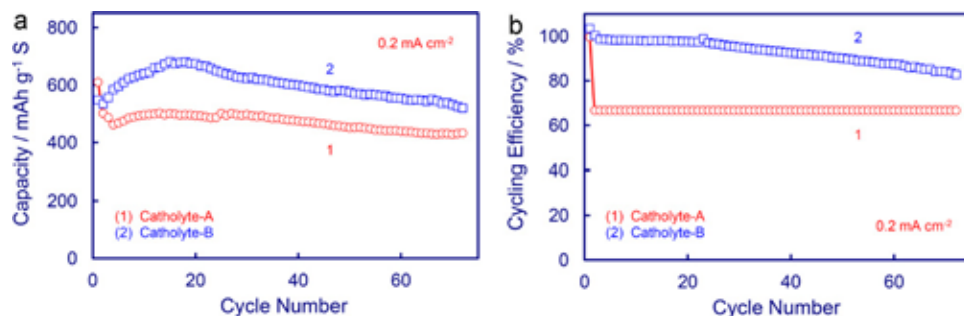


Fig. 5. Effect of LiNO₃ co-salt on cycling performance of Li/Li₂S₉ liquid cells: (a) capacity retention and (b) Coulombic efficiency of cycling.

The effect of LiNO₃ on cycling efficiency and capacity retention is presented in Fig. 5a and b, respectively, where Cell-1 uses Catholyte-A free of LiNO₃ and Cell-2 employs Catholyte-B containing 0.2 m LiNO₃. As compared with Cell-1, Cell-2 not only has higher capacity (Fig. 5a), but also has significantly higher Coulombic efficiencies (Fig. 5b). The latter would be the most important benefit added by the use of LiNO₃ co-salt. For Cell-1, except for the first cycle the charging voltages can never reach the cutoff voltage (3.0 V, see Fig. 3), all charging processes are ended by the pre-set charging time. Since we setup 150% of the last discharge capacity as one of the charge limits, Coulombic efficiencies for all cycles are 66.7% (i.e., the reciprocal of 150%). For Cell-2, charge voltages repeatedly reach the pre-set cutoff voltage and the charge processes are terminated by the cutoff voltage, resulting in higher Coulombic efficiencies.

3.3. Understanding the role of LiNO₃ in Li/S cell

Assuming that Reactions (4) and (5) are the main reason for low Coulombic efficiency of Li/S cells and that both reactions occur on the Li anode surface, we believe that the important role of LiNO₃ in Li/S cells can be understood from the viewpoint of the Li anode. Therefore, we place our attention on the plating and stripping behavior of Li metal in highly concentrated Li₂S_x ($x > 2$) solutions. Fig. 6 exhibits the potential curves of the first plating and stripping of Li metal on a fresh Ni surface in Catholyte-A and Catholyte-B, respectively. In Catholyte-A, the potential of Ni working electrode shows multiple plateaus between OCP and 1.3 V, followed by a slow and smooth decline. Even at the end of the plating test, the potential of Ni still remains at +0.15 V vs. Li/Li⁺. This is because the Li metal plated on the Ni surface is not dense, measured is a mixed poten-

tial of the Li metal and polysulfide solution. Subsequent Li stripping test gives a 26% Li cycling efficiency. In Catholyte-B, the potential remains a plateau for 82 min, and then steeply drops to a constant negative value (−50 mV vs. Li/Li⁺), at which Li plates progressively, giving a 50% cycling efficiency as shown by the subsequent Li stripping test. It is clearly shown that in both catholyte solutions, Li metal cannot be plated until a protective passivation film is formed on the Ni surface, and that such a film must be formed by the irreversible electrochemical reduction of polysulfides, as expressed by Eq. (4).

Coulombic efficiencies of Li plating and stripping in Catholyte-A and Catholyte-B are compared in Fig. 7. Obviously, the efficiencies in Catholyte-B are significantly higher than those obtained in Catholyte-A, verifying that LiNO₃ promotes the formation of a more protective (normally denser) passivation film. It is interesting to note that in both Cathode-A and Cathode-B, Li cycling efficiencies are increased slowly with cycle number, probably because the passivation film becomes denser and denser, resulting in better protection of Li metal from Reactions (4) and (5).

On the other hand, the essential role of LiNO₃ in the formation of a passivation film on the Li surface can be examined by impedance analyses. Fig. 8 shows the impedance spectrums of the Ni surface after Li plating and after subsequent Li stripping. For the Li-plated Ni surfaces indicated by Curves 1 and 2 in Fig. 8, the impedance spectrum is composed of two flattened semicircles. In general, the semicircle in higher frequency range corresponds to a passivation film and the one in lower frequency range corresponds to the charge-transfer process occurring on the electrolyte–electrode interface [30,31]. For Li metal electrode, the charge-transfer usually reflects the following reversible electrochemical process:

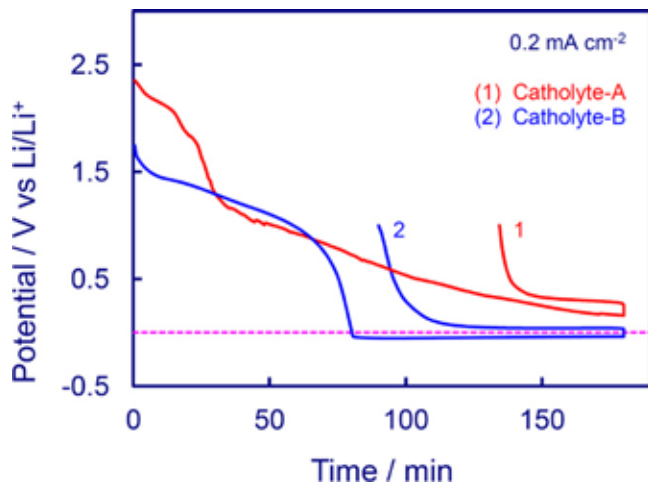


Fig. 6. Potential profiles of the first Li plating and stripping on a fresh Ni surface, which were recorded at 0.2 mA cm⁻² for 3 h on a 3-electrode cell: (1) Catholyte-A and (2) Catholyte-B.

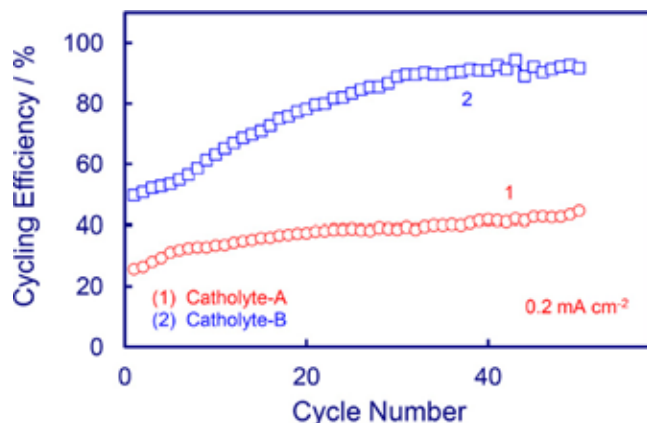


Fig. 7. Coulombic efficiency of Li plating and stripping on Ni surface in Catholyte-A and Catholyte-B, respectively.

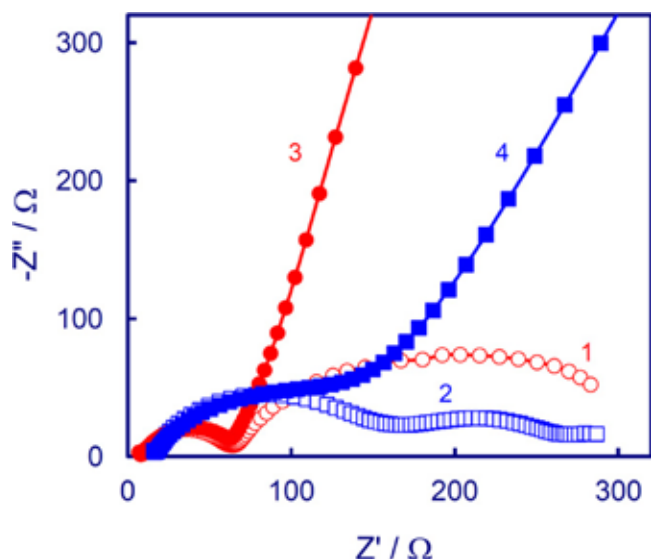


Fig. 8. Impedance spectroscopies of a Ni electrode in Catholyte-A and Catholyte-B, respectively, which were recorded at open-circuit potential on a 3-electrode cell: (1) after Li plating at 0.2 mA cm^{-2} for 3 h in Catholyte-A, (2) after Li plating at 0.2 mA cm^{-2} for 3 h in Catholyte-B, (3) after Li stripping at 0.2 mA cm^{-2} to 1.0 V following (1), and (4) after Li stripping at 0.2 mA cm^{-2} to 1.0 V following (2).

Comparison of Curves 1 and 2 shows that the Li metal plated in Catholyte-B (Curve-2) has a higher passivation resistance and a much lower charge-transfer resistance. The higher passivation resistance is a good indication that the passivation film formed in the presence of LiNO_3 co-salt is denser and hence more protective. After subsequent Li stripping, the charge-transfer process as expressed by Eq. (6) no longer takes place due to the absence of Li metal, and therefore the semicircle in the lower frequency range disappears as indicated by Curves 3 and 4, respectively. By comparing Curve-1 with Curve-3 and Curve-2 with Curve-4, one sees that the passivation film still remains even after Li stripping, indicating that the passivation film is permanently present on the electrode surface once it has formed.

The benefit of LiNO_3 also can be observed from cyclic voltammetric results as shown in Fig. 9. First, the cyclic voltammogram (CV) in Catholyte-B has much higher peak currents. This result coincides with the impedance results (i.e., much lower charge-transfer resistance in Catholyte-B). Second, the CV in Catholyte-B gives much higher Li cycling efficiency (i.e., 65% vs. 29% in Catholyte-A, calculated from the cyclic voltammograms). This result agrees with those obtained from galvanostatic plating and stripping tests

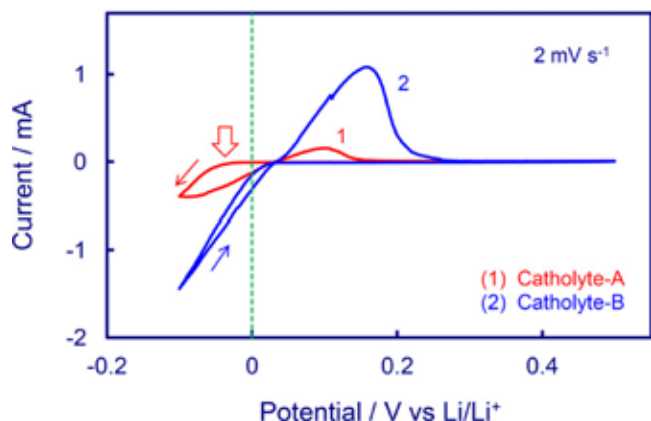


Fig. 9. Cyclic voltammograms of Ni electrode in Catholyte-A and Catholyte-B, which were recorded by scanning potential at 2 mV s^{-1} between 0.1 V and 0.5 V vs. Li/Li^+ .

as shown in Fig. 7. Third, Li plating in Catholyte-B has no polarization while that in Catholyte-A shows polarization, as indicated by the arrow in Fig. 9.

Based on the discussion above, the charging voltage profiles of Cell-2 in Figs. 3a, b and 4 can be explained as follows: as Eq. (5) shows, Li metal and Li_2S_x chemically react with each other. While protecting Li metal, the passivation film meanwhile protects Li_2S_x from attack by the highly reductive Li metal. Moreover, the passivation film serves as a solid electrolyte interphase (SEI) to prevent soluble Li_2S_x ($x > 2$), especially those species having long S-S chain near the full charge state, from being electrochemically reduced, as expressed by Eq. (4). Instead, the soluble Li_2S_x species are electrochemically oxidized to elemental sulfur on the cathode, resulting in an additional voltage plateau at 2.3 V, higher charging efficiency, and accordingly a steep voltage rise upon the full charge.

4. Conclusions

This work demonstrates an alternative approach for the performance improvement of rechargeable Li/S batteries. While dissolution of lithium polysulfides (Li_2S_x , $x > 2$) in organic electrolytes is inevitable, research efforts focusing on the protection of the lithium anode to increase Li cycling efficiency in highly concentrated polysulfide solutions may be more feasible. LiNO_3 is excellent in promoting the formation of a denser and more protective passivation film on the Li surface. The film formed not only increases Li cycling efficiency, but also protects soluble polysulfide anions from chemical and electrochemical reductions on the Li anode. Use of LiNO_3 as a co-salt makes the two-phase reaction of " S_8 (insoluble) + $2\text{Li} \rightarrow \text{Li}_2\text{S}_8$ (soluble)" reversible, resulting in a 2.3 V plateau, higher specific capacity and higher charging efficiency. Moreover, Li/S cells with LiNO_3 co-salt can be repeatedly charged to cutoff voltage ($> 2.5 \text{ V}$) and indicate a steep voltage rise as the signal of full charge. On the contrary, the conventional Li/S cells can only be charged to 2.5 V at which the voltage stays constant until the charging process is manually terminated, resulting in low specific capacity and low charging efficiency, due to the chemical and electrochemical reductions of polysulfide anions on the Li anode.

References

- [1] Y.V. Mikhaylik, J.R. Akridge, *J. Electrochem. Soc.* 151 (2004) A1969.
- [2] V.S. Kolosnitsyn, E.V. Karaseva, *Russ. J. Electrochem.* 44 (2008) 506.
- [3] J.L. Wang, J. Yang, J.Y. Xie, N.X. Xu, Y. Li, *Electrochem. Commun.* 4 (2002) 499.
- [4] Y.J. Choi, Y.D. Chung, C.Y. Baek, K.W. Kim, H.J. Ahn, J.H. Ahn, *J. Power Sources* 184 (2008) 548.
- [5] C. Lai, X.P. Gao, B. Zhang, T.Y. Yan, Z. Zhou, *J. Phys. Chem. C* 113 (2009) 4712.
- [6] X. Ji, K.T. Lee, L.F. Nazar, *Nat. Mater.* 8 (2009) 500.
- [7] C. Liang, N.J. Dudney, J.Y. Howe, *Chem. Mater.* 21 (2009) 4724.
- [8] B. Zhang, C. Lai, Z. Zhou, X.P. Gao, *Electrochim. Acta* 54 (2009) 3708.
- [9] L. Yuan, H. Yuan, X. Qiu, L. Chen, W. Zhu, *J. Power Sources* 189 (2009) 1141.
- [10] C. Wang, J.J. Chen, Y.N. Shi, M.S. Zheng, Q.F. Dong, *Electrochim. Acta* 55 (2010) 7010.
- [11] B. Zhang, X. Qin, G.R. Li, X.P. Gao, *Energy Environ. Sci.* 2 (2010) 1531.
- [12] J.Z. Wang, L. Lu, M. Choucair, J.A. Stride, X. Xu, H.K. Liu, *J. Power Sources* 196 (2011) 7030.
- [13] H. Wang, Y. Yang, Y. Liang, J.T. Robinson, Y. Li, A. Jackson, Y. Cui, H. Dai, *Nano Lett.* 11 (2011) 2644.
- [14] S.R. Chen, Y.P. Zhai, G.L. Xu, Y.X. Jiang, D.Y. Zhao, J.T. Li, L. Huang, S.G. Sun, *Electrochim. Acta* (2011), doi:10.1016/j.electacta.2011.03.005.
- [15] S.E. Cheon, K.S. Ko, J.H. Cho, S.W. Kim, E.Y. Chin, H.T. Kim, *J. Electrochem. Soc.* 150 (2003) A800.
- [16] H.S. Ryu, H.J. Ahn, K.W. Kim, J.H. Ahn, J.Y. Lee, *J. Power Sources* 153 (2006) 360.
- [17] Y.J. Choi, K.W. Kim, H.J. Ahn, J.H. Ahn, *J. Alloys Compd.* 449 (2008) 313.
- [18] J.J. Chen, X. Jia, Q.J. She, C. Wang, Q. Zhang, M.S. Zheng, Q.F. Dong, *Electrochim. Acta* 55 (2010) 8062.
- [19] R.D. Rauh, K.M. Abraham, G.F. Pearson, J.K. Surprenant, S.B. Brummer, *J. Electrochem. Soc.* 126 (1979) 523.
- [20] H. Yamin, A. Gorenshtein, J. Penciner, Y. Sternberg, E. Peled, *J. Electrochem. Soc.* 135 (1988) 1045.

- [21] Y.V. Mikhaylik, U.S. Patent (2008) 7,352,680.
- [22] D. Aurbach, E. Pollak, R. Elazari, G. Salitra, C.S. Kelley, J. Affinito, J. Electrochem. Soc. 156 (2009) A694.
- [23] R.D. Rauh, F.S. Shuker, J.M. Marston, S.B. Brummer, J. Inorg. Nuclear Chem. 39 (1977) 1761.
- [24] S.S. Zhang, J. Power Sources 163 (2006) 567.
- [25] S.S. Zhang, J. Power Sources 163 (2007) 713.
- [26] S.E. Cheon, K.S. Ko, J.H. Cho, S.W. Kim, E.Y. Chin, H.T. Kim, J. Electrochem. Soc. 150 (2003) A796.
- [27] J.R. Akridge, Y.V. Mikhaylik, N. White, Solid State Ionics 175 (2004) 243.
- [28] S.S. Jeong, Y.T. Lim, Y.J. Choi, G.B. Cho, K.W. Kim, H.J. Ahn, K.K. Cho, J. Power Sources 174 (2007) 745.
- [29] H.S. Ryu, Z. Guo, H.J. Ahn, G.B. Cho, H. Liu, J. Power Sources 189 (2009) 1179.
- [30] S.S. Zhang, M.H. Ervin, D.L. Foster, K. Xu, T.R. Jow, J. Solid State Electrochem. 9 (2005) 77.
- [31] S.S. Zhang, J. Power Sources 180 (2008) 586.

Oxygen Reduction Reaction Catalyst on Lithium/Air Battery Discharge Performance

Xiaoming Ren, Sheng S. Zhang, Dat T. Tran, and Jeffrey A. Read

U.S. Army Research Laboratory, Adelphi, MD

ABSTRACT

Lithium/air batteries have the potential to substantially outperform the best battery system nowadays on the market. Oxygen reduction reaction (ORR) at the cathode in an aprotic organic lithium electrolyte is well-known to limit the discharge rate and capacity of the lithium/air batteries. In this study, the discharge characteristics of Li/air cells with cathodes made of different carbon materials were examined. The results showed that the ORR kinetics in the lithium/air batteries can be drastically improved by using an effective catalyst, achieving higher discharge voltage and rate. The discharge capacity of the lithium/air battery was found to be correlated to the cathode pore volume, to which the mesopore volume of the carbon material has a large contribution. An ORR mechanistic model involving a reaction product deactivating the catalytic sites on the carbon surface is proposed to explain the experimental results.

Journal of Materials Chemistry, Volume 21, Pages 10118-10125 (2011)

Oxygen reduction reaction catalyst on lithium/air battery discharge performance

Xiaoming Ren,* Sheng S. Zhang, Dat T. Tran and Jeffrey Read

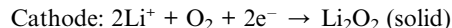
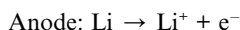
Received 30th November 2010, Accepted 25th January 2011

DOI: 10.1039/c0jm04170j

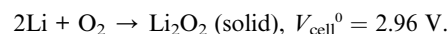
Lithium/air batteries have the potential to substantially outperform the best battery system nowadays on the market. Oxygen reduction reaction (ORR) at the cathode in an aprotic organic lithium electrolyte is well-known to limit the discharge rate and capacity of the lithium/air batteries. In this study, the discharge characteristics of Li/air cells with cathodes made of different carbon materials were examined. The results showed that the ORR kinetics in the lithium/air batteries can be drastically improved by using an effective catalyst, achieving higher discharge voltage and rate. The discharge capacity of the lithium/air battery was found to be correlated to the cathode pore volume, to which the mesopore volume of the carbon material has a large contribution. An ORR mechanistic model involving a reaction product deactivating the catalytic sites on the carbon surface is proposed to explain the experimental results.

1. Introduction

Lithium/air batteries have the potential of achieving a higher energy density and are safer than the leading commercial lithium batteries, primary or secondary, by utilizing ambient air as the oxidant, thus removing the need to store any oxidant within enclosed cells. A Li/air battery is expected to have a theoretical charge capacity 5–10 times higher than that of a lithium battery,¹ which is limited by the amount of lithium that can be reversibly inserted in the intercalation cathode material such as Li_xCoO_2 , $0.5 < x < 1$. Since the first introduction of a rechargeable Li/air battery by Abraham and Jiang in 1996,² there has been much progress being made in enhancing and understanding its performance. For practical applications, electrolyte solutions made with non-hydrolytic lithium salts and aprotic organic solvents with low volatility and high electrochemical stability were used.³ Other electrolyte systems were also reported, such as Deng *et al.*⁴ for the use of a hydrophobic ionic liquid–silica–PVdF–HFP polymer composite electrolyte membrane to minimize moisture exposure to the lithium anode and Wang and Zhou⁵ for an aqueous electrolyte at the air cathode and aprotic organic electrolyte at the lithium anode with the two electrolyte solutions separated by a super-ionic glass conductor. In aprotic organic electrolyte, the cell electrode reactions involved in the discharge process are:



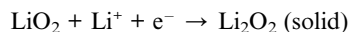
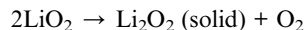
and the complete cell reaction:



The lithium anode has shown very little polarization at the discharge current density of interest, at less than a few mA cm^{-2} ,⁶ and the loss in cell voltage from the reversible value (V_{cell}^0) occurs largely at the cathode. Many studies have been devoted to address this cathode voltage loss by exploring oxygen reduction reaction (ORR) catalysts for the cathode and by studying the ORR mechanism in aprotic organic electrolyte solutions. Cathode catalysts, such as carbon supported MnO_x ,⁷ $\alpha\text{-MnO}_2$ nanowires,⁸ carbon supported nanosized $\gamma\text{-MnOOH}$ (manganite),⁹ carbon supported Fe_2O_3 , Fe_3O_4 , CuO , CoFe_2O_4 and Co_3O_4 ,¹⁰ carbon supported Pt and Au,¹¹ and carbon supported pyrolyzed Co macrocycles,² have not shown much improvement to the Li/O₂ (air) battery discharge voltage over what has been obtained with using carbon only as the ORR catalyst in the cathode. From such observations, it has been assumed that the ORR in a Li–air cathode is not a catalytically sensitive process or that the carbon itself can provide better catalytic activity than those catalysts of interest which themselves are supported on carbon.¹¹ Furthermore, study on the ORR mechanism in aprotic organic lithium electrolyte solution on glassy carbon electrode by Laoire *et al.*¹² using cyclic voltammetry and rotating disc electrode technique showed the initial formation of lithium superoxide (LiO_2), which can further be converted to lithium peroxide

U.S. Army Research Laboratory, RDRL-SED-C, Adelphi, MD, 20783-1197, USA. E-mail: xiaoming.ren@us.army.mil; Fax: +1 (301) 394-0273; Tel: +1 (301) 394-0379

either by disproportionation reaction (eqn (4)) or by further reduction reaction:



Computational studies^{13,14} indicate that LiO_2 is likely very unstable at room temperature at less than 1 atm. O_2 pressure, favoring the disproportionation to Li_2O_2 , which has been identified as the major reaction product by *ex situ* examination of the cathode products from discharged Li/O_2 cells using Raman spectroscopy² and by oxygen consumption stoichiometry in the discharge process.³ At a low discharge current density, Zhang *et al.*⁶ found part of the initially deposited Li_2O_2 at the cathode can be further converted to Li_2O at a highly polarized voltage below 2 V.

The precipitation of Li_2O_2 as a solid product on the carbon surface in the cathode further complicates the ORR process in discharging a Li/air cell by either blocking the oxygen diffusion pathways in the pores or by occupying and deactivating the catalytic sites. Zhang *et al.*⁶ found the impedance of the air electrode is progressively increased with polarization cycles, indicating the carbon surfaces are gradually covered by the insoluble products, which prevents oxygen from diffusing to the reaction sites on carbon. Mirzaei and Hall¹⁵ found the discharge capacity and discharge voltage of Li/air cell depend on the morphology of carbon, which exerts a combined effect of pore volume, pore size and surface area of carbon on the storage capacity, with carbon with a larger pore volume and a wider pore size preferred. Williford and Zhang¹⁶ analyzed several approaches in designing the air electrode by considering the electrode porosity and catalyst reactivity distributions to minimize diffusion limitations and maximize air electrode material utilization. Tran *et al.*¹⁷ proposed a model mechanism based on gas diffusion electrode passivation by the reaction products in blocking small pores and thus preventing them from further utilization, again emphasizing the use of carbon materials possessing high surface area and large pore diameter in the cathode. On the contrary, Read *et al.*¹⁸ found the BET surface area of the carbon in the air electrode is not a significant factor in determining the discharge capacity, which is correlated to oxygen transport in organic electrolyte. Dramatic decrease in the discharge capacity at a high current density was linked to the rapid decrease in cell voltage and uneven distribution of Li_2O_2 deposition concentrating at the air interface.⁶ The uneven Li_2O_2 deposition may have been one of the factors in explaining the vast difference in the specific discharge capacities reported in literature, up to a high value of 5800 mA h per g carbon,¹⁹ when normalized to a low carbon mass in the cathode. Xu *et al.*²⁰ explored using tris(pentafluorophenyl)borane as a functional additive and co-solvent in electrolytes to dissolve part of Li_2O and Li_2O_2 in order to achieve higher Li/air battery discharge capacity, although other factors introduced by the same additive adversely affect the discharge capacity.

It is evident that the poor ORR cathode performance severely limits the discharge rate and capacity of a Li/air cell. However, no clear and systematic results have been obtained in finding an

effective catalyst to improve the ORR kinetics. In addition, it is still not clear on the air cathode performance loss mechanism as whether it is from Li_2O_2 deposits blocking the narrow pores of the carbon material or Li_2O_2 covering and deactivating the ORR catalytic sites on the carbon surface. To address these issues, we examined in this study the discharge characteristics of Li/air cells with cathodes made of three carbon materials: Super P carbon (SP-carbon), Ketjen carbon (K-carbon) and pyrolyzed CuFe macrocycle compounds on Ketjen carbon (CuFe catalyzed K-carbon). These three carbon materials differ in the type and number of the catalytic sites for the ORR, and in the carbon pore volume and pore distribution. Comparison of the Li/air cell discharge behaviors under identical test conditions for the cells made with these cathode materials could provide the opportunity to identify the key contributing factors to the cell performance in terms of cell discharge voltage, rate and capacity, and thus shed light on the complex Li/air discharge process. Based on experimental results, an ORR mechanistic model involving a reaction product deactivating the catalytic sites on the carbon surface is proposed.

2. Experimental

Super P carbon (SP-carbon) was obtained from TIMCAL Graphite Carbon, and Ketjenblack EC-600 JD carbon black (K-carbon) from Akzo Nobel. The CuFe-catalyzed Ketjenblack EC-600 JD (CuFe-catalyzed K-carbon) was a non-precious metal-oxygen reduction catalyst produced on a commercial scale and provided by Acta SpA, Italy. This carbon supported catalyst was made first by absorbing a mixture of iron and copper complexes with phthalocyanine-based ligands onto the carbon support, and then heat-treated at between 800 and 900 °C in Ar atmosphere. The CuFe-catalyzed K-carbon has a Cu content at 1.7 wt% and a Fe content at 1.5 wt%, corresponding to an atomic ratio of Cu to Fe at 1 to 1.

X-Ray powder diffraction (XRPD) patterns of the carbon materials were collected on a Rigaku Ultima III diffractometer using a Bragg-Brentano geometry and Cu $K\alpha$ radiation ($\lambda = 1.5418 \text{ \AA}$) over a 2θ scan range of 10–90° with a resolution of 0.02° at a scan rate of 0.2° per min. The surface areas of the carbon materials were measured with a Micromeritics ASAP 2010 system using N_2 gas as adsorptive. The pore size distributions of the carbon materials were obtained from Barrett-Joyner-Halenda (BJH) desorption pore distribution using ASAP 2010 V1.00 software.

Lithium triflate (LiSO_3CF_3 , 96%, Aldrich) was dried at 100 °C under vacuum for 8 h. Electrolyte grade propylene carbonate (PC, Ferro) was used as received. Tris(2,2,2-trifluoroethyl) phosphate (TFP) was synthesized by reacting sodium trifluoroethoxide with phosphorus oxychloride and purified by repeated fractionation under reduced pressure. Detailed descriptions on the synthesis and characterization of TFP are referred to in ref. 21 and 22.

Electrolyte solution with a fixed solvent composition of PC : TFP at a 7 : 3 weight ratio containing 0.2 M lithium triflate was prepared in a glove-box. Physical properties of this electrolyte solution, such as kinematic viscosity, ionic conductivity, oxygen solubility, and boiling point, are referred to in ref. 23.

Cathodes with a composition of 90 wt% carbon materials and 10 wt% polytetrafluoroethylene (PTFE) were prepared by mixing calculated amounts of carbon materials and PTFE emulsion (Teflon®, solid content = 61.5%, DuPont Co.), and then rolling the resulting paste mixture into a freestanding cathode sheet, which was punched into disks with an area of 0.97 cm² and dried at 100 °C under vacuum for over 8 h. Li/air cells with an air access window of 0.97 cm² were assembled in a dry-room having a dew point below −90 °C by stacking sequentially a Li foil, a Celgard® 3500 membrane, a cathode, a Ni mesh (as cathode current collector), and an air-window frame into a coin cell cap. To activate the cell, a volume of 200 µL liquid electrolyte solution was added through the air-window, followed by applying vacuum for 20 s to ensure complete filling of the electrolyte into the cell internal space. Excessive electrolyte solution over the cathode outer surface was removed by gently swiping with a filter paper over the Ni mesh. The electrolyte-activated cell was rested for 2 h before commencing discharging tests, which were carried out at room temperature (22 °C) in the dry-room on an Arbin BT-2000 tester galvanostatically from OCV until reaching the cutoff voltage at 1.5 V. Specific capacity of the cell was normalized by the mass of the carbon materials in the air cathode, which was in the range of 6–7 mg cm^{−2}.

3. Results and discussions

3.1. Characterization of carbon materials and cathodes

The XRD patterns of the carbon materials shown in Fig. 1 reveal the relative degree of graphitization of the three carbon materials. SP-carbon has the highest degree of graphitization of the three carbon materials as shown by the sharp graphitic basal plane (002) peak at a *d*-spacing of 3.573 Å. Relative to K-carbon, the heat-treatment at around 800–900 °C in producing CuFe catalyzed K-carbon increased carbon graphitization degree, and shrank basal plane *d*-spacing (from 3.722 to 3.620 Å) towards that of an ideal graphite (3.354 Å). The sizes of the crystallites parallel to the graphite basal plane for the carbon materials listed in Table 1 are calculated by using the equation $L = 1.84\lambda/(B\cos\theta)$, where λ is the wavelength of the X-ray beam, B is the angular width of the basal plane diffraction (002) peak at the half-maximum intensity, and θ is the Bragg angle. The Brunauer–Emmett–Teller (BET) surface areas obtained using N₂ gas adsorption at 77 K for these three carbon materials are listed in Table 1, and the carbon pore distribution and accumulated pore volume as a function of pore diameter obtained using BJH method is plotted in Fig. 2. SP-carbon possesses little internal pore volume and a rather low surface area, as compared to those of K-carbon and CuFe catalyzed K-carbon. The loss of carbon pore volume by the heat treatment used in making CuFe catalyzed K-carbon is consistent with the increase in graphitization degree of the carbon material as revealed by the XRD pattern. Also, the pore volume distribution of CuFe catalyzed K-carbon remains the same as that of the original K-carbon, which suggests a uniform structural collapse occurred during the heat treatment. This evidence does not support the suggestion of CuFe filling up or blocking some pores of K-carbon, especially at a metal loading at less than 3% of the carbon support.

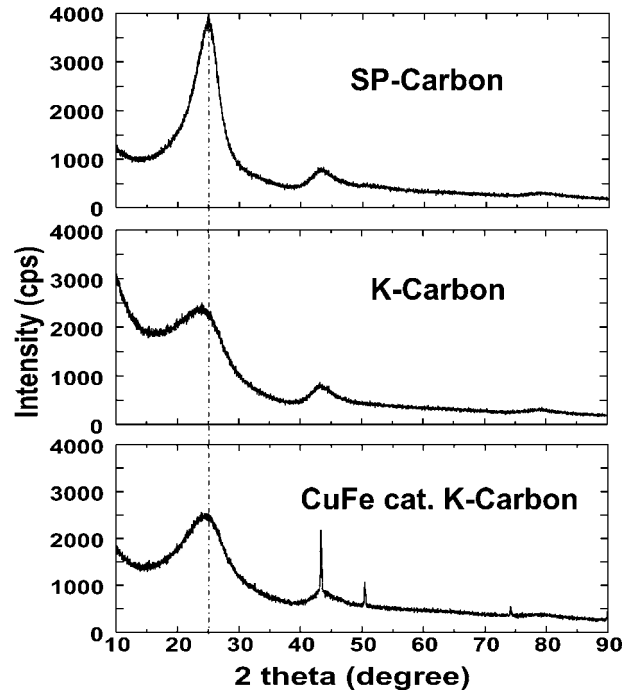


Fig. 1 XRD patterns for SP-carbon, K-carbon and CuFe catalyzed K-carbon.

The porosities of the cathodes made of the three carbon materials were measured using two separate methods: solvent filling and wet thickness. With the solvent filling method, the cathodes were vacuum filled with PC solvent, followed by removing excessive solvent on the electrode surfaces by gently dabbling on both sides with filter papers until reaching a stable mass. The carbon electrode porosity obtained using the solvent method is calculated according to the following equation:

$$\rho = \frac{(W_{\text{wet}} - W_{\text{dry}})d_c}{(W_{\text{wet}} - W_{\text{dry}})d_c + W_{\text{dry}}d_{\text{sol}}} 100\%$$

where W_{dry} is the dry mass of the electrode, W_{wet} is the electrode mass wetted with solvent, d_c is the density of carbon (2.0 g cm^{−3}), and d_{sol} is the density of solvent (1.206 g cm^{−3} for PC). With the thickness method, the porosities were calculated from the dry mass and the wet thickness when filled with PC solvent. The porosity obtained using the thickness method is calculated according to the following equation:

$$\rho = \left(1 - \frac{W_{\text{dry}}}{\delta A d_c}\right) 100\%$$

where A is the electrode area and δ is the thickness of electrode wetted with solvent. Both these methods yielded consistent results for the electrode porosity measurements listed in Table 1. A trend observed is that a cathode made of a carbon material possessing a higher internal volume of mesopores (and consequently a higher surface area) has a higher electrode pore volume.

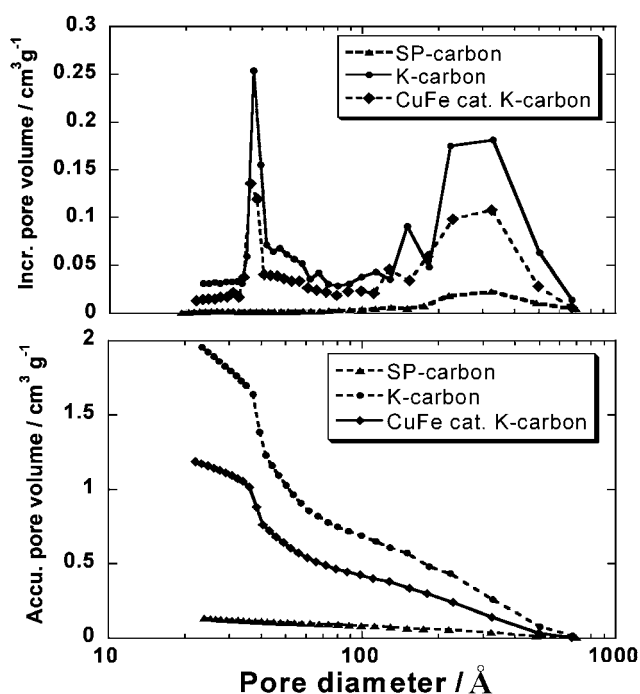
3.2. Li/air cell discharge curves

In Fig. 3, cell voltage curves during discharge at a constant current density of 0.2 mA cm^{−2} for the Li/air cells with cathodes

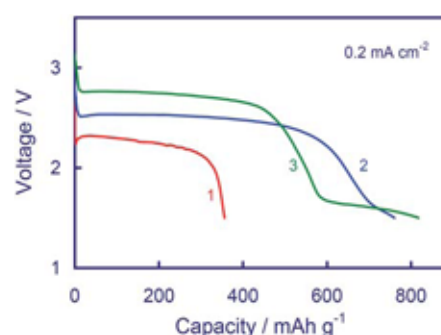
Table 1 Physical properties of carbon materials, cathode porosity and specific discharge capacity of Li/air cells with cathodes made of the carbon materials

	SP-carbon	K-carbon	CuFe catalyzed K-carbon
Graphitic basal plane d -spacing/ \AA	3.573	3.722	3.620
Crystallite size parallel to basal plane/ \AA	39.6	20.8	30.2
BET surface/ $\text{m}^2 \text{g}^{-1}$	69.3	1413	751
Total pore vol. @ $>20 \text{\AA}$ dia./ $\text{cm}^3 \text{g}^{-1}$	0.14	2.06	1.23
Electrode porosity by solvent method ^a	$77.3 \pm 1.8\%$	$90.8 \pm 0.5\%$	$86.8 \pm 0.7\%$
Electrode pore vol., ^b / $\text{cm}^3 \text{g}^{-1}$ carbon	1.89	5.46	3.64
Electrode porosity by thickness method ^a	$75.3 \pm 2.2\%$	$90.9 \pm 1.1\%$	$87.9 \pm 1.5\%$
Li/air cell discharge capacity, mA h g^{-1} carbon			
@ $0.05/\text{mA cm}^{-2}$	531	1286	1339
@ $0.20/\text{mA cm}^{-2}$	356	761	817
@ $0.50/\text{mA cm}^{-2}$	205	430	597
@ $1.00/\text{mA cm}^{-2}$	—	165	390

^a Average and standard deviation from measurements on 6 samples. ^b Calculated from electrode porosity by solvent method.

**Fig. 2** Incremental pore volume and accumulated pore volumes as a function of pore diameters obtained using BJH method for SP-carbon, K-carbon and CuFe catalyzed K-carbon.

made of three carbon materials are compared. Without catalyst, a cell with a K-carbon cathode out-performed a cell with a SP-carbon cathode in terms of cell discharge voltage and capacity. A cell with a CuFe catalyzed K-carbon cathode exhibited two distinguishable voltage plateaus in its discharge voltage curve, with the first discharge plateau at a cell voltage above 2.5 V demonstrating a substantial improvement in cell discharge voltage of over 200 mV higher than that of a cell with a K-carbon cathode, and over 500 mV higher than that of a cell with a SP-carbon cathode; while the second discharge plateau at a voltage window between 1.7 to 1.5 V has a substantially higher discharge capacity than that of a cell with a K-carbon cathode. The discharge curve of the cell with a SP-carbon cathode did not have the second discharge plateau in the voltage window studied.

**Fig. 3** Li/air cell discharge voltage curves at 0.2 mA cm^{-2} for cells with cathodes made of (1) SP-carbon, (2) K-carbon and (3) CuFe catalyzed K-carbon.

Results of further efforts carried out to identify the origin of the second discharge plateau observed for the Li/air cells with K-carbon and CuFe catalyzed K-carbon cathodes, especially from the charge contribution by the possible cathode process of Li_2O_2 to Li_2O conversion, are presented in Fig. 4. As will be shown by the experimental results, there is negligible charge contribution by the Li_2O_2 to Li_2O conversion for the Li/air cells. Shown in Fig. 4 (top), the Li/air cells were first discharged at a constant current density of 0.2 mA cm^{-2} from point A to point B to reach a state of discharge at a capacity of 300 mA h g^{-1} . After that, the two cells were reassembled in sealed coil cells to close off the air access to the cells, and then discharged as Li/C cells at a current density of 0.05 mA cm^{-2} from point B until reaching the cutoff voltage at 1.5 V. For the cell with a K-carbon cathode, the Li/C cell discharge step reached a discharge capacity close to 80 mA h g^{-1} ; while for the cell with a CuFe catalyzed K-carbon cathode, a discharge capacity over 480 mA h g^{-1} , which is by far higher than what would be expected if the charge were originated from further reduction of Li_2O_2 produced at a charge capacity of 300 mA h g^{-1} during the initial Li/air cell discharge step (from point A to point B in Fig. 4a). To further verify if there is any charge contribution by the possible cathode process of Li_2O_2 to Li_2O conversion, hermetic Li/C cells with fresh cathodes were built and discharged in the absence of oxygen access. As shown in Fig. 4b, the charges obtained with the fresh cathodes almost

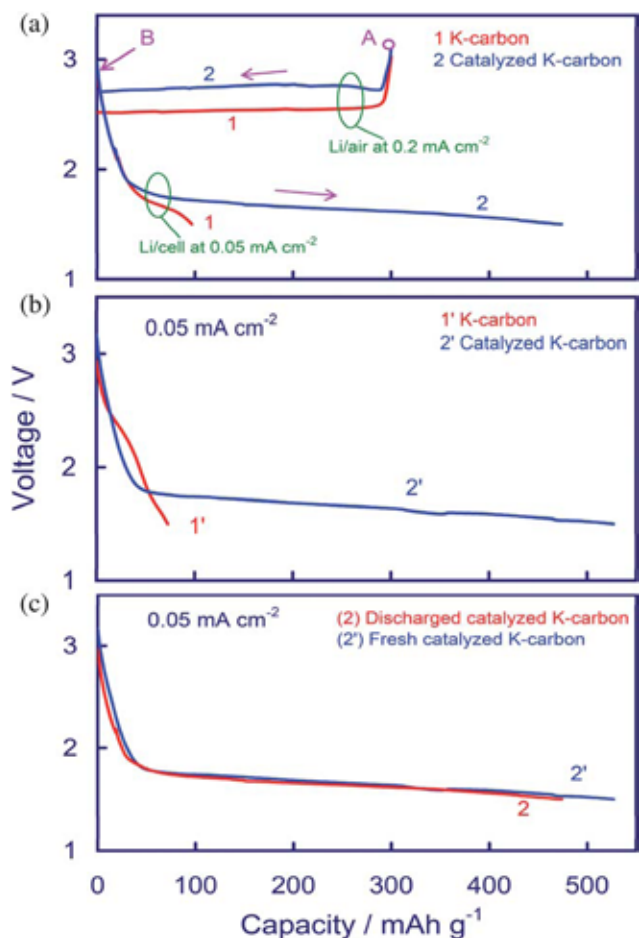


Fig. 4 a) Li/air cells with cathode made of (1) K-carbon and (2) CuFe catalyzed K-carbon discharged from point A to point B at 0.2 mA cm^{-2} for 300 mA h g^{-1} , then the cells containing Li_2O_2 produced were re-assembled in enclosed coin cells to block off the air access, and then discharged as Li/C cells without oxygen access from point B at 0.05 mA cm^{-2} to 1.5 V . (b) Li/C cells discharge voltage curves obtained at 0.05 mA cm^{-2} for cells with cathodes made of (1') K-carbon and (2') CuFe catalyzed K-carbon. Initial capacity at voltage greater than 2 V is due to the oxygen absorbed in electrolyte solution. (c) Discharge voltage curves for cells with CuFe catalyzed K-carbon, where curve (2) is obtained in (a) from point B discharge process and curve (2') in (b).

account for all of the charges obtained from the corresponding two cells shown in Fig. 4a in the discharge step starting from point B. The two discharge curves shown in Fig. 4b and that in Fig. 4a starting from point B for cells with CuFe catalyzed K-carbon cathodes are re-plotted in Fig. 4c, where the two curves overlap each other completely, verifying the negligible charge contribution by the Li_2O_2 to Li_2O conversion for the Li/air cells tested. This conclusion could be rationalized by the non-electronic conductivity and low solubility of Li_2O_2 in the chosen electrolyte solution.

The second discharge plateau observed for the cell with a K-carbon cathode (shown in Fig. 3, 4a from point B, and 4b) could be attributed to the surface adsorbed oxygen on the carbon material, and for the cell with a CuFe catalyzed K-carbon cathode to both of the surface adsorbed oxygen on the carbon material and solvent reduction. The lack of surface adsorbed

oxygen on SP-carbon could be attributed to its much lower surface area and a more ordered surface structure. Solvent reduction often occurs on the carbonaceous anode in the formation cycling of Li-ion for Li rechargeable batteries, albeit at a lower voltage plateau around 0.9 V without using catalyzed carbon materials at the electrode. To understand the reaction mechanism of the CuFe catalyzed carbon in catalyzing the solvent reduction further investigation is needed. With purposeful selection and optimization of the solvent and catalyst pairs, the solvent redox process catalyzed by the cathode material could be utilized as new cell chemistry in designing rechargeable Li batteries.

3.3. Li/air cell discharge rate and capacity

The discharge voltages obtained for cells with K-carbon and CuFe catalyzed K-carbon cathodes at various discharge current densities are shown in Fig. 5, and these results are summarized in Table 1 and in Fig. 6 in a plot of cell energy density as a function of discharge current density. The discharge voltage of the cell with a CuFe catalyzed K-carbon cathode is over 200 mV higher than that of the cell with a K-carbon cathode at a low discharge current density, and over 1 V higher at a high discharge current density. The Li/air cell with a CuFe catalyzed K-carbon cathode discharged at a relatively high current density of 1 mA cm^{-2} demonstrated an energy density over 0.8 Wh g^{-1} , which is more than twice of that of the cell with a K-carbon cathode.

The discharge capacities of the Li/air cells, shown in Fig. 3 and 5a, are plotted as a function of the cathode pore volume in Fig. 7. There is a good correlation between the cell discharge capacity and electrode pore volume for these three carbon materials, especially at a low discharge current density of 0.05 mA cm^{-2} , where it is estimated 10% of the cathode pore volume is filled by the electrode reaction product of Li_2O_2 at the end of the discharge process. At a higher discharge current density, there is a rapid decrease in the discharge capacity. At the fast discharge rate of 1 mA cm^{-2} , no visible depositions of the reaction products

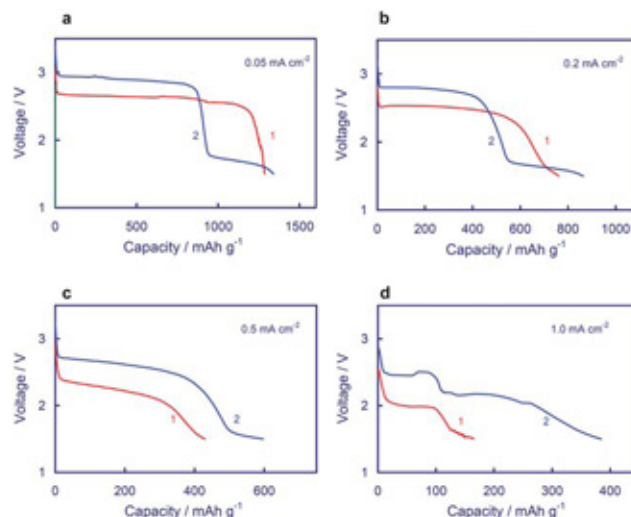


Fig. 5 Li/air cell discharge voltage curves obtained at various discharge current densities for cells with cathodes made of (1) K-carbon and (2) CuFe catalyzed K-carbon.

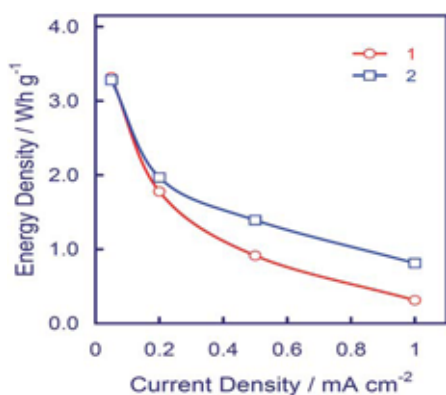


Fig. 6 Plot of energy density as a function of discharge current density from data shown in Fig. 5 for Li/air cells with cathodes made of (1) K-carbon and (2) CuFe catalyzed K-carbon.

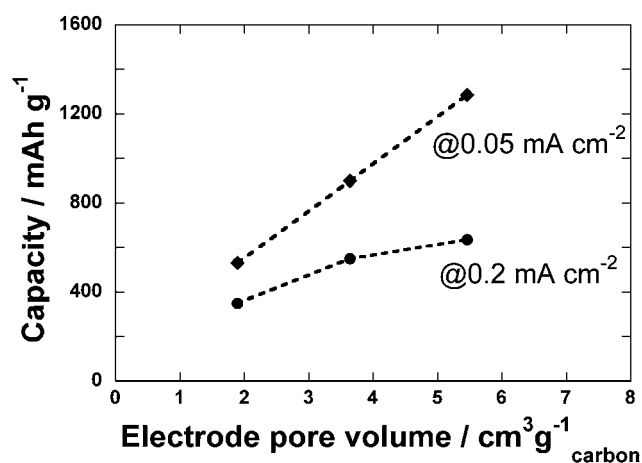


Fig. 7 Plots of Li/air cell specific discharge capacities as a function of cathode pore volume.

at the cathode out-surface were observed, likely due to the low capacity obtained. For the three types of carbon cathodes, the difference in the obtained discharge capacity is significant: the capacity of SP-carbon is at near zero, and that of CuFe catalyzed K-carbon is about twice that of the original K-carbon. These results would argue against the clogging pore at the cathode surface being the limiting factor for the discharging capacitance at the fast discharging rate. Furthermore, if it were clogging pores at the carbon surface in limiting the discharge capacity, the original K-carbon would have a higher capacitance than the CuFe-catalyzed K-carbon due to its higher carbon pore volume. The rapid build-up of lithium peroxide covering the active sites for ORR on the carbon surface at a higher discharging current density may have caused the fast passivation of the cathode, as shown by the slant discharge voltage plateau, attributing to the early termination of the cell discharge process.

3.4. Micrographs of cathodes after discharge

Because of the low solubility of the Li_2O_2 produced in discharging a Li/air battery, several factors are expected to affect its production and precipitation during the discharging process, and

subsequently, its final location within the cathode, which can be examined with a microscope after the discharge step is completed. It has been observed that as the discharge current density increases, the Li_2O_2 particles tend to be found within the cathode at a location close to the air interface rather than the electrolyte interface. Even at the same discharge current density, more Li_2O_2 deposits were observed on the surface of the cathode facing air for a cell with CuFe catalyzed K-carbon than those with K-carbon, as shown in Fig. 8, where large crystals of Li_2O_2 were found on the cathode surface and in the cracks close to the air surface with CuFe catalyzed K-carbon. The formation of large Li_2O_2 crystals on the surface and within the cracks of the electrode implies a meaningful solubility and mobility of Li_2O_2 in the electrolyte solution needed for the crystal growth from the Li_2O_2 initially produced on the ORR catalytic sites during the discharging process. The fact that Li_2O_2 was found at a location close to the air surface of the cathode also indicates the rather slow diffusion of dissolved oxygen in the non-aqueous electrolyte solution. At a high discharging current density or with a cathode material possessing a higher density of active sites as offered by the CuFe catalyzed K-carbon cathode material, the ORR reaction zone moves to the air surface of the cathode. The severe

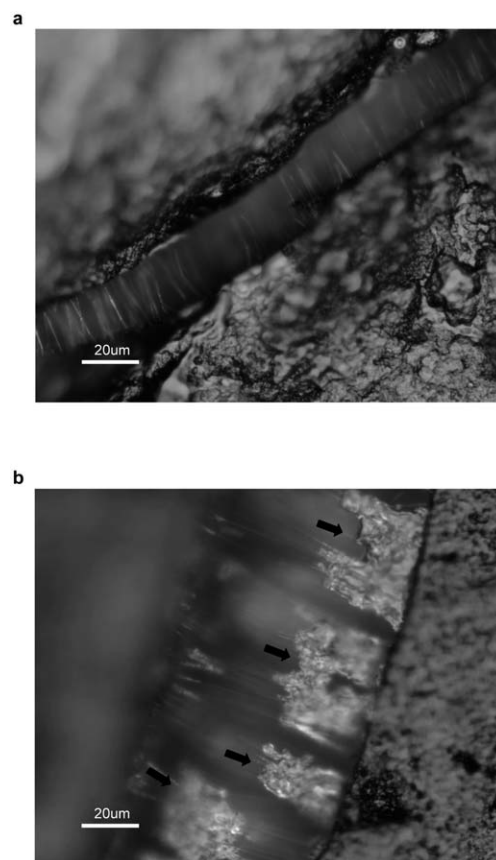


Fig. 8 Optical microscope pictures of cathodes facing air for cathodes made of (1) K-carbon and (2) CuFe catalyzed K-carbon in Li/air cells discharged at 1.0 mA cm^{-2} to 1.5 V , rested for 5 h, and then discharged at 0.05 mA cm^{-2} to a total capacity of 850 mA h g^{-1} . Deposits from cathode reaction of discharging Li/air cells were seen as the white spots on the black carbon surface and as colorless crystals formed (shown by arrows) within the cracks of the cathode.

decrease in cell discharge capacity at high current density is attributed to both increased cathode passivation and uneven distribution of Li_2O_2 deposits within the pore volume of the cathode.

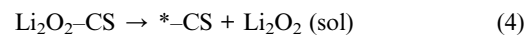
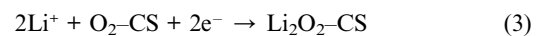
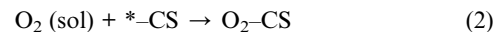
3.5. Li/air cell polarization

The dynamic Li/air cell discharging polarization curves, shown in Fig. 9 dashed lines, were obtained at a current density scan rate of $0.02 \text{ mA cm}^{-2} \text{ s}^{-1}$ for cells with K-carbon cathode and CuFe catalyzed K-carbon cathode after both cells were discharged to a charge capacity of 300 mA h g^{-1} and then followed by a rest period of two hours. Previous study has shown that the lithium anode has negligible polarization, and the cell voltage polarization is largely attributed to the cell cathode polarization and cell IR drop. Under the dynamic scan conditions, the polarization curves for both cells are similar, with the cell with a CuFe catalyzed K-carbon cathode showing a slightly better ORR kinetics at the low current density range, and the cell with a K-carbon cathode a slightly better mass transport at the high current density range. However, when the cell polarization curves representing the steady state discharge as obtained from data shown in Fig. 5a–d are compared, there are large differences between the dynamic and steady-state conditions for the two cells. For the cell with a CuFe catalyzed carbon cathode, the polarization curve at steady-state shifts downward by about 80 mV from that at dynamic scan; while for the cell with a K-carbon cathode, the corresponding downward shift in polarization curve is over 300 mV, and increasing with the current density to over 500 mV at 1 mA cm^{-2} . It was expected that the ORR polarization from the increased mass transportation limitation from the dynamic state to steady-state is similar for the two cells. The much larger voltage downward shift, especially at a higher current density, for a cell with a K-carbon cathode than that for a cell with a CuFe catalyzed K-carbon cathode indicates that there is added sluggishness in the ORR kinetics under the steady-state conditions. Under the steady-state conditions, there is a continuous formation of Li_2O_2 on the ORR catalytic sites, and its subsequent removal by dissolution and crystal growth keeps the number of

active sites constant, and the number of available free active sites decreases with the increase in discharge current density. The higher ORR catalytic activity provided by a higher level of free site density found in CuFe catalyzed K-carbon material, which contains catalytic sites consisting of CuFe and those on K-carbon, decreases the ORR polarization under the steady-state conditions.

3.6. ORR electrode process

It becomes evident from above test results and observations that the performance of a Li/air cell is limited by the ORR electrode process, which could involve the following key steps:



In this cathode reaction mechanism, the oxygen gas molecule ($\text{O}_2(\text{g})$) from air first dissolves in the electrolyte solution forming dissolved oxygen molecules ($\text{O}_2(\text{sol})$), which then adsorbs onto a free ORR catalytic site ($*-\text{CS}$) on the carbon surface. The subsequent ORR reaction produces one Li_2O_2 molecule attached to the catalytic site ($\text{Li}_2\text{O}_2-\text{CS}$) resulting in deactivating the catalytic site for further ORR. The deactivated catalytic site by attached Li_2O_2 is only freed by removal of the Li_2O_2 molecule into the surrounding electrolyte solution. The driving forces for such a removal process come from the Li_2O_2 diffusion into the electrolyte solution within the electrode pore volume, and from the aging-growth process of some Li_2O_2 crystals at nearby locations. The sustainable Li/air cell discharge rate would thus depend on the initial number of free catalytic sites on the carbon surface and the balancing act of Li_2O_2 production and its removal in maintaining a sufficient number of free catalytic sites to sustain the ORR. At an excessively high discharge current density, the free catalytic sites diminish rapidly because of the relatively slow rate of Li_2O_2 removal from the deactivated catalytic sites, resulting in fast increase in ORR polarization. As shown in Fig. 5d, the Li/air cell with a CuFe catalyzed K-carbon cathode has two distinguishable cell voltage plateaus at above 2 V when discharged at a relatively high current density of 1 mA cm^{-2} . The two voltage plateaus reflect the ORR process carried out at two different types of catalytic sites in the cathode material. The first discharge plateau arises from ORR catalyzed by the more active CuFe catalytic sites. After these CuFe sites are deactivated at the end of the first discharge plateau, the ORR proceeds at the less active catalytic sites on the supporting carbon surface, forming a second voltage plateau, which is at a similar voltage to what was observed for a Li/air cell with a K-carbon cathode where only the active sites provided by the K-carbon exist. At the fast discharge rate, all active sites are deactivated and cause rapid termination of the discharge process. For the CuFe-catalyzed K-carbon, the highly active CuFe catalytic sites are deactivated first at a high cathode voltage, followed by the

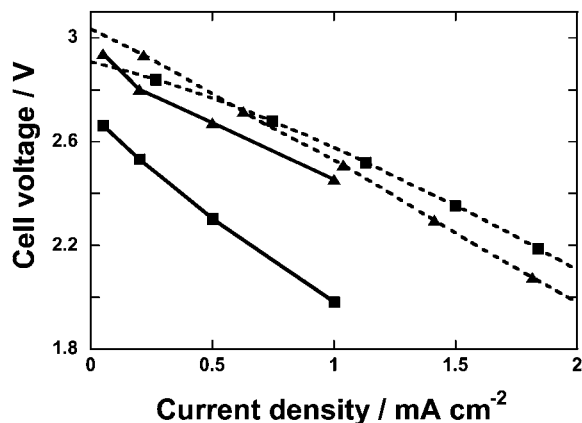


Fig. 9 Li/air cell polarizations at steady-state (solid line) and at dynamic scan at $0.02 \text{ mA cm}^{-2} \text{ s}^{-1}$ (dashed line), measured after discharged to 300 mA h g^{-1} for cells with cathodes made of K-carbon (■) and CuFe catalyzed K-carbon (▲).

deactivation of the less active sites of the carbon surface at a lower cathode voltage. The charge contribution from absorbed oxygen only occurs at the start of the discharging process, and since oxygen supply is not the limiting factor in an operating Li/air cell, the overall impact of absorbed oxygen on the discharge capacity of a Li/air cell at a cell voltage >2.0 V is small at less than 35 mA h g^{-1} . The charge contribution from solvent reduction occurs at a cell voltage below 1.8 V.

As for the Li/air battery discharge capacity obtained at a low discharging current density, available electrode pore volume is a determining factor. Carbon material possessing a high mesopore volume at a pore diameter greater than 20 \AA provides additional electrode pore volume accessible for the ORR and for accommodating the Li_2O_2 deposit. The Li/air cell discharge capacity is also impacted by the cell discharging current density, which affects the rate of cathode catalytic sites deactivation and the distribution of Li_2O_2 within the cathode. The ability to redistribute the Li_2O_2 reaction product more evenly throughout the cathode pore volume in the thickness direction could provide substantial improvement in the Li/air cell discharge capacity, from currently 10% of the potential capacity estimated based on the full occupancy of the electrode pore volume by the Li_2O_2 deposit. There are several possible approaches to address this issue, and these measures include: (1) increasing the solubility of Li_2O_2 in the electrolyte solution with a better selection of solvents and electrolytes, (2) a further decrease in the lithium electrolyte concentration to move the reaction zone from the air interface towards the electrolyte interface of the cathode and (3) modifying electrode structures to provide less tortuous diffusion paths for the oxygen and Li_2O_2 .

4. Conclusions

Based on the observations and test results of the Li/air batteries with cathodes made of different carbon materials, a mechanism for the ORR electrode process is proposed where the newly formed Li_2O_2 molecules deactivate the catalytic sites, and the density and activity of free catalytic sites on the surface of carbon and the removal rate of attached Li_2O_2 from the deactivated catalytic sites determine the ORR polarization, and thus the discharge cell voltage.

It has been demonstrated that by increasing the catalytic site density and activity on the carbon surface for the ORR, as shown from the graphite-like SP-carbon, to the defect-rich amorphous K-carbon, and to the CuFe catalyzed K-carbon, the ORR polarization experienced during the Li/air discharging process

can be significantly decreased, thus considerably increase the discharge cell voltage and rate for the Li/air batteries. Cells with a CuFe catalyzed K-carbon cathode demonstrated a higher cell discharging voltage of over 200 mV than that with K-carbon, and of over 500 mV than that with SP-carbon.

It was observed that there is a negligible amount of Li_2O_2 being converted to Li_2O during the Li/air cell discharge process. A cell with a CuFe catalyzed K-carbon cathode has a distinguishable second discharge plateau in the voltage window from 1.7 to 1.5 V attributed to the solvent reduction catalyzed by the CuFe catalyst.

References

- 1 T. Ogasawara, A. Debart, M. Holzapfel, P. Novak and P. G. Bruce, *J. Am. Chem. Soc.*, 2006, **128**, 1390–1393.
- 2 K. M. Abraham and Z. Jiang, *J. Electrochem. Soc.*, 1996, **143**, 1–5.
- 3 J. Read, *J. Electrochem. Soc.*, 2002, **149**, A1190–A1195.
- 4 Z. Deng, L. Ruoshi, H. Tao and Y. Aishui, *J. Power Sources*, 2010, **195**, 1202–1206.
- 5 Y. G. Wang and H. S. Zhou, *J. Power Sources*, 2010, **195**, 358–361.
- 6 S. S. Zhang, D. Foster and J. Read, *J. Power Sources*, 2010, **195**, 1235–1240.
- 7 H. Cheng and K. Scott, *J. Power Sources*, 2010, **195**, 1370–1374.
- 8 A. Debart, A. J. Paterson, J. Bao and P. G. Bruce, *Angew. Chem., Int. Ed.*, 2008, **47**, 4521–4524.
- 9 V. M. B. Crisostomo, J. K. Ngala, S. Alia, A. Doble, C. Morein, C. H. Chen, X. Shen and S. L. Suib, *Chem. Mater.*, 2007, **19**, 1832–1839.
- 10 A. Debart, J. Bao, G. Armstrong and P. G. Bruce, *J. Power Sources*, 2007, **174**, 1177–1182.
- 11 Y. C. Lu, H. A. Gasteiger, M. C. Parent, V. Chiloyan and Y. Shao-Horn, *Electrochem. Solid-State Lett.*, 2010, **13**, A69–A72.
- 12 C. O. Laoire, S. Mukerjee, K. M. Abraham, E. J. Plichta and M. A. Hendrickson, *J. Phys. Chem. C*, 2009, **113**, 20127–20134.
- 13 N. Seriani, *Nanotechnology*, 2009, **20**, 1–7.
- 14 V. S. Bryantsev, M. Blanco and F. Faglioni, *J. Phys. Chem. A*, 2010, **114**, 8165–8169.
- 15 M. Mirzaei and P. J. Hall, *Electrochim. Acta*, 2009, **54**, 7444–7451.
- 16 R. E. Williford and J. G. Zhang, *J. Power Sources*, 2009, **194**, 1164–1170.
- 17 C. Tran, X. Yang and D. Qu, *J. Power Sources*, 2010, **195**, 2057–2063.
- 18 J. Read, K. Mutolo, M. Ervin, W. Behl, J. Wolfenstine, A. Driedger and D. Foster, *J. Electrochem. Soc.*, 2003, **150**, A1351–A1356.
- 19 S. D. Beattie, D. M. Manolescu and S. L. Blair, *J. Electrochem. Soc.*, 2009, **156**, A44–A47.
- 20 W. Xu, J. Xiao, D. Y. Wang, J. Zhang and J. G. Zhang, *J. Electrochem. Soc.*, 2010, **157**, A219–A224.
- 21 K. Xu, M. S. Ding, S. S. Zhang, J. L. Allen and T. R. Jow, *J. Electrochem. Soc.*, 2003, **150**, A161–A169.
- 22 K. Xu, S. S. Zhang, J. L. Allen and T. R. Jow, *J. Electrochem. Soc.*, 2003, **150**, A170–A175.
- 23 S. S. Zhang, K. Xu and J. Read, *J. Power Sources*, 2011, **196**, 3906–3910.

Effect of Substitution (Ta, Al, Ga) on the Conductivity of $\text{Li}_{6.75}\text{La}_3\text{Zr}_{1.75}\text{O}_{12}$

Jan L. Allen¹, Jeffrey Wolfenstine¹, Ezhiylmurugan Rangasamy², and Jeff Sakamoto²

¹ U.S. Army Research Laboratory, Adelphi, MD

² Department of Chemical Engineering and Materials Science, Michigan State University, East Lansing, MI

ABSTRACT

Cubic garnets of composition $\text{Li}_{6.75}\text{La}_3\text{Zr}_{1.75}\text{Ta}_{0.25}\text{O}_{12}$, $\text{Li}_{6.15}\text{La}_3\text{Zr}_{1.75}\text{Ta}_{0.25}\text{Al}_{0.2}\text{O}_{12}$, and $\text{Li}_{6.15}\text{La}_3\text{Zr}_{1.75}\text{Ta}_{0.25}\text{Ga}_{0.2}\text{O}_{12}$ were prepared from a co-precipitated precursor and consolidated by hotpressing to a relative density of ~96–98%. The total Li-ion conductivities at 298 K and activation energies (in parentheses) of $\text{Li}_{6.75}\text{La}_3\text{Zr}_{1.75}\text{Ta}_{0.25}\text{O}_{12}$, $\text{Li}_{6.15}\text{La}_3\text{Zr}_{1.75}\text{Ta}_{0.25}\text{Al}_{0.2}\text{O}_{12}$ and $\text{Li}_{6.15}\text{La}_3\text{Zr}_{1.75}\text{Ta}_{0.25}\text{Ga}_{0.2}\text{O}_{12}$ were 0.87 mS cm^{-1} (0.22 eV), 0.37 mS cm^{-1} (0.30 eV) and 0.41 mS cm^{-1} (0.27 eV), respectively. The above results suggest that cubic stabilizing substitutions outside of the Li-ion sub-lattice are preferable to obtain faster Li-ion conductivity.

Journal of Power Sources, Volume 206, Pages 315-319 (2012)



Short communication

Effect of substitution (Ta, Al, Ga) on the conductivity of $\text{Li}_7\text{La}_3\text{Zr}_2\text{O}_{12}$ J.L. Allen^{a,*}, J. Wolfenstine^a, E. Rangasamy^b, J. Sakamoto^b^a US Army Research Laboratory, RDRL-SED-C, 2800 Powder Mill Road, Adelphi, MD 20783, United States^b Department of Chemical Engineering and Materials Science, Michigan State University, East Lansing, MI 48824, United States

ARTICLE INFO

Article history:

Received 27 December 2011

Received in revised form 18 January 2012

Accepted 21 January 2012

Available online 30 January 2012

Keywords:

Garnet

Li

Ta

Cubic

Ionic conductivity

Hot-pressing

ABSTRACT

Cubic garnets of composition $\text{Li}_{6.75}\text{La}_3\text{Zr}_{1.75}\text{Ta}_{0.25}\text{O}_{12}$, $\text{Li}_{6.15}\text{La}_3\text{Zr}_{1.75}\text{Ta}_{0.25}\text{Al}_{0.2}\text{O}_{12}$, and $\text{Li}_{6.15}\text{La}_3\text{Zr}_{1.75}\text{Ta}_{0.25}\text{Ga}_{0.2}\text{O}_{12}$ were prepared from a co-precipitated precursor and consolidated by hot-pressing to a relative density of ~96–98%. The total Li-ion conductivities at 298 K and activation energies (in parentheses) of $\text{Li}_{6.75}\text{La}_3\text{Zr}_{1.75}\text{Ta}_{0.25}\text{O}_{12}$, $\text{Li}_{6.15}\text{La}_3\text{Zr}_{1.75}\text{Ta}_{0.25}\text{Al}_{0.2}\text{O}_{12}$ and $\text{Li}_{6.15}\text{La}_3\text{Zr}_{1.75}\text{Ta}_{0.25}\text{Ga}_{0.2}\text{O}_{12}$ were 0.87 mS cm^{-1} (0.22 eV), 0.37 mS cm^{-1} (0.30 eV) and 0.41 mS cm^{-1} (0.27 eV), respectively. The above results suggest that cubic stabilizing substitutions outside of the Li-ion sub-lattice are preferable to obtain faster Li-ion conductivity.

Published by Elsevier B.V.

1. Introduction

Li-ion solid electrolytes have been long sought after in order to obtain a safe, reliable, long-lived battery system without use of flammable, volatile and relatively unstable organic liquid-based electrolytes. The advantages are numerous including long shelf life, ability to operate at high voltage or high temperature and ease of manufacturing. However, solid electrolytes have not been able to provide sufficient conductivity and/or have been unstable to Li, air or moisture. The Li-stuffed Al-substituted cubic garnet $\text{Li}_7\text{La}_3\text{Zr}_2\text{O}_{12}$ (LLZO) is a promising fast Li-ion conducting ceramic electrolyte owing to its fast ionic conductivity ($\sigma_{\text{total}} \sim 0.2 \text{ mS cm}^{-1}$ at 298 K) and Li and moisture stability [1,2]. High voltage Li-ion cathodes [3] that increase the demands on flammable, liquid organic electrolytes for high voltage stability [4] and safety considerations make a solid state electrolyte an attractive option. Furthermore, Li-air or Li-S batteries [5] can be enabled by the discovery and development of faster Li-ion conducting solids.

The challenge has been to stabilize the cubic form since LLZO can also exist with a tetragonal garnet structure [6,7] of lower Li-ion conductivity. The tetragonal structure results from ordering of the Li-ion sub-lattice. The first approach to stabilization of the cubic form was the serendipitous discovery that the inclusion of Al as an impurity from contamination during processing [2,7] stabilized the higher conducting cubic phase. Later Al was intentionally added

[8–11] and a dense (relative density > 90%) material with a cubic structure was obtained. Geiger et al. [7] have suggested that Al substitutes for Li and thereby stabilizes the cubic phase relative to the tetragonal phase. An Al substitution for Li will lead to a reduction in Li content in order to maintain electro-neutrality ($1\text{Al}^{3+} = 3\text{Li}^{+}$). Others have speculated that Al addition yields a denser material by acting as a sintering aid [9,10]. A similar stabilization of cubic phase is observed with Ga substitution [12]. Thus it is desirable to look at other substitutions which like the Geiger et al. approach may stabilize the cubic garnet structure through a reduction in Li content and/or increased Li vacancy concentration. Ta substitution for Zr follows this approach and it is desirable for a couple reasons. First, Ta is stable relative to Li [13]. Second, Ta substitution on the Zr site will not hinder Li-ion motion whereas Al substitution on Li sites will (as discussed later). Li et al. [13] recently reported $\text{Li}_6\text{La}_3\text{ZrTaO}_{12}$ cubic garnet with relatively high total Li-ion conductivity (0.18 mS cm^{-1} at 298 K). The sample was prepared in an alumina crucible and contained 1.3 wt% Al. Also, Logéat et al. [14] recently reported that Al-free, Ta substitution for Zr could stabilize the cubic garnet ($\text{Li}_{7-x}\text{La}_3\text{Zr}_{2-x}\text{Ta}_x\text{O}_{12}$). Conductivity data was not included in their report. Similarly to Ta, Nb substitution for Zr should also lower the Li content of the LLZO and a high Li ion conductivity (0.8 mS cm^{-1} at 298 K) cubic garnet sample has been reported with Nb substitution for Zr by Ohta et al. [15]. However, Ta is preferable to Nb since Nb is not chemically stable with Li [16–18] and would change LLZO from an ionic conductor to a mixed conductor. In this paper, we have chosen a level of Ta substitution equal to the level of Nb substitution reported by Ohta et al. [15] to have the highest conductivity and lowest activation energy. It is the purpose

* Corresponding author. Tel.: +1 301 394 0291; fax: +1 301 394 0273.

E-mail addresses: jan.l.allen8.civ@mail.mil, jallen@arl.army.mil (J.L. Allen).

of this paper to report on the effects of Ta, Ta + Ga and Ta + Al substitutions in order to further the understanding of Li-ion conductivity in LLZO.

2. Experimental

$\text{Li}_{6.75}\text{La}_3\text{Zr}_{1.75}\text{Ta}_{0.25}\text{O}_{12}$, $\text{Li}_{6.15}\text{La}_3\text{Zr}_{1.75}\text{Ta}_{0.25}\text{Al}_{0.2}\text{O}_{12}$ and $\text{Li}_{6.15}\text{La}_3\text{Zr}_{1.75}\text{Ta}_{0.25}\text{Ga}_{0.2}\text{O}_{12}$ were prepared for study from a co-precipitated precursor. Li_2CO_3 , $\text{La}(\text{OH})_3$, “[ZrO_2] $_2\cdot\text{CO}_2\cdot x\text{H}_2\text{O}$ ” (zirconium carbonate, basic hydrate; equivalent ZrO_2 content determined from thermogravimetric analysis) $\text{Al}(\text{OH})_3$ and Ga_2O_3 weighed in the desired stoichiometry were dissolved in $\sim 1.4\text{ M}$ HNO_3 (aq). A 3 wt% excess of Li was used to compensate for Li volatilization during synthesis. The desired amount of TaCl_5 was first dissolved in anhydrous ethanol and then added to the acid solution. The resulting clear solution was evaporated to dryness in a microwave oven contained inside a fume hood. Evolution of NO_x was observed during this step. The dried co-precipitate was lightly ground with a mortar and pestle and pressed into a pellet using a Carver laboratory die and press. The pellet was placed on a ZrO_2 plate and heated in air at 923 K for 15 h and subsequently at 1273 K for 3–4 h. The furnace was turned off and the sample was removed.

$\text{Li}_{6.75}\text{La}_3\text{Zr}_{1.75}\text{Ta}_{0.25}\text{O}_{12}$, $\text{Li}_{6.15}\text{La}_3\text{Zr}_{1.75}\text{Ta}_{0.25}\text{Al}_{0.2}\text{O}_{12}$ and $\text{Li}_{6.15}\text{La}_3\text{Zr}_{1.75}\text{Ta}_{0.25}\text{Ga}_{0.2}\text{O}_{12}$ dense discs were prepared by hot-pressing. The powders were hot-pressed at 1323 K at 40 MPa pressure for 1 h under air. From the hot-pressed discs rectangular parallelepipeds were cut using a low-speed diamond saw for density, microstructural and electrical property measurements.

X-ray diffraction (Cu $\text{K}\alpha$ radiation) was used to characterize the phase purity of the powders and the material after hot-pressing. Lattice constants were calculated from the peak positions of the X-ray diffraction pattern using Rietveld refinement of data collected in parallel beam geometry. The bulk density of the hot-pressed samples was determined from the weight and physical dimensions. The relative density values were determined by dividing the bulk density by the theoretical density. The microstructure of the hot-pressed samples was examined on fracture surfaces using scanning electron microscopy (SEM).

AC measurements were undertaken to determine ionic conductivity as a function of temperature in the range of 298–373 K. Au was sputter coated on to the top and bottom surface of the specimens. AC impedance was measured using a Solatron 1260 Impedance Analyzer in the frequency range of $1\text{--}10^6$ Hz.

3. Results and discussion

Conventional garnets are described by the formula $\text{A}_3\text{B}_3\text{O}_{12}$ where A, B, and C have 8, 4, and 6 oxygen coordination, respectively. In a cubic stuffed garnet, La occupies A sites, Zr occupies C sites and Li occupies the B sites and additional distorted octahedral sites that are unoccupied in the conventional garnet [19]. Awaka et al. [20] label the tetrahedral B site Li1 and the distorted octahedral site Li2 and they describe the basic unit of the Li sub-lattice to be loop of Li1 and Li2 sites. The Li1 site is the only connection between loops and these junctions of the basic loop unit form the complete 3-D Li ion sub-lattice and enable fast Li-ion conduction. A very high conductivity [2] was reported for cubic “ $\text{Li}_7\text{La}_3\text{Zr}_2\text{O}_{12}$ ” that was later shown to be a result of Al substitution for Li [7]. We believe that Al substitution lowers the Li content and stabilizes a cubic structure as hypothesized by Geiger et al. [7]. Ga can stabilize cubic garnet in a fashion similar to Al [12]. However based on the Awaka et al. structural model of Li-stuffed cubic garnet [20], the presence of Al or Ga on the Li site will be detrimental to Li-ion conduction and we therefore focused on substitutions that are

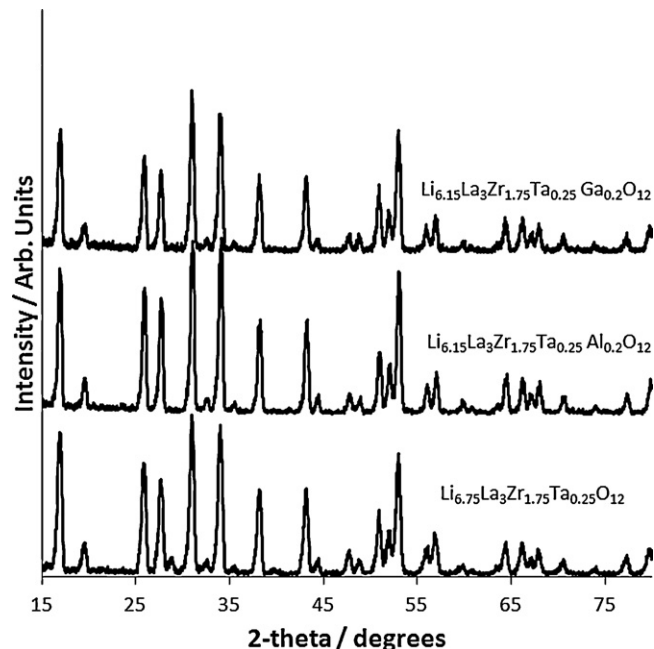


Fig. 1. The X-ray diffraction patterns of $\text{Li}_{6.75}\text{La}_3\text{Zr}_{1.75}\text{Ta}_{0.25}\text{O}_{12}$, $\text{Li}_{6.15}\text{La}_3\text{Zr}_{1.75}\text{Ta}_{0.25}\text{Al}_{0.2}\text{O}_{12}$ and $\text{Li}_{6.15}\text{La}_3\text{Zr}_{1.75}\text{Ta}_{0.25}\text{Ga}_{0.2}\text{O}_{12}$.

not part of the Li-ion conduction pathway. Nuclear magnetic resonance (NMR) data has shown Al occupying both the Li1 and the Li2 sites with preference for the Li1 site [7]. We speculated that Al on these sites, and in particular Al on the Li1 site, might hinder ionic conductivity since this site forms the junction between loops.

Thus, we wanted to control the Li content in order to stabilize the cubic stuffed garnet structure without placing ions such as Al or Ga on the Li sub-lattice. With this in mind, we prepared $\text{Li}_{6.75}\text{La}_3\text{Zr}_{1.75}\text{Ta}_{0.25}\text{O}_{12}$ where La occupies A sites, Zr and Ta occupy C sites and Li occupies B (Li1) sites as well as distorted octahedral sites (Li2) that are unoccupied in conventional garnet. We also prepared $\text{Li}_{6.15}\text{La}_3\text{Zr}_{1.75}\text{Ta}_{0.25}\text{Al}_{0.2}\text{O}_{12}$ and $\text{Li}_{6.15}\text{La}_3\text{Zr}_{1.75}\text{Ta}_{0.25}\text{Ga}_{0.2}\text{O}_{12}$ in order to determine how substitutions of Li by Ga or Al would affect the Li-ion conductivity and to shed light on the role of Ga or Al as either a substituting atom on the Li sub-lattice which reduces the Li content or as a sintering aid. Based on crystal chemistry, we expect Al to have a site preference for the tetrahedral site (B, Li1) and Ga to prefer the distorted octahedral site (Li2) [21]. We therefore expected that there may be some benefit to using Ga over Al since it may not preferentially occupy the critical Li1 junction.

The X-ray diffraction patterns for $\text{Li}_{6.75}\text{La}_3\text{Zr}_{1.75}\text{Ta}_{0.25}\text{O}_{12}$, $\text{Li}_{6.15}\text{La}_3\text{Zr}_{1.75}\text{Ta}_{0.25}\text{Al}_{0.2}\text{O}_{12}$ and $\text{Li}_{6.15}\text{La}_3\text{Zr}_{1.75}\text{Ta}_{0.25}\text{Ga}_{0.2}\text{O}_{12}$ after hot-pressing are shown in Fig. 1, confirming a predominantly single phase of cubic symmetry with space group $la\bar{3}d$. From Fig. 1, it is observed that Ta does indeed stabilize the cubic LLZO phase at room temperature. The lattice parameters are shown in Table 1. By comparison, Logéat et al. [14] reports a lattice parameter of 12.96 Å for $\text{Li}_{6.75}\text{La}_3\text{Zr}_{1.75}\text{Ta}_{0.25}\text{O}_{12}$ which is in exact agreement with our result. Li et al. [13] reported a lattice parameter of 12.89 Å for the composition $\text{Li}_6\text{La}_3\text{ZrTaO}_{12}$. The lattice parameter change with increasing Ta content is consistent with the relative ionic radii of Ta^{5+} (64 pm) and Zr^{4+} (72 pm) [22]. Turning back to our samples, Ga or Al substitution on the Li sub-lattice has little effect on the lattice constant.

A representative micrograph of the fracture surface of the hot-pressed $\text{Li}_{6.75}\text{La}_3\text{Zr}_{1.75}\text{Ta}_{0.25}\text{O}_{12}$ sample is shown in Fig. 2. From SEM analysis, a couple of important points are noted. First, the material is very dense in agreement with the relative density $\sim 96\%$, determined from the physical dimensions, weight and

Table 1

Density, conductivity and lattice constants of samples prepared for this study.

Composition	Lattice constant (Å)	Relative density (%)	Total Li-ion σ at 298 K (mS cm^{-1})	Activation energy (eV)
$\text{Li}_{6.75}\text{La}_3\text{Zr}_{1.75}\text{Ta}_{0.25}\text{O}_{12}$	12.96	96	0.87	0.22
$\text{Li}_{6.15}\text{La}_3\text{Zr}_{1.75}\text{Ta}_{0.25}\text{Al}_{0.2}\text{O}_{12}$	12.95	98	0.37	0.30
$\text{Li}_{6.15}\text{La}_3\text{Zr}_{1.75}\text{Ta}_{0.25}\text{Ga}_{0.2}\text{O}_{12}$	12.95	98	0.41	0.27

the theoretical density. Almost no porosity is observable. A high relative density is extremely important for device applications. Second, no second phases were observed at grain boundaries. Third, the fracture surface is very flat indicating transgranular fracture, revealing high grain boundary strength which should lead to low inter-granular ionic resistance. The $\text{Li}_{6.15}\text{La}_3\text{Zr}_{1.75}\text{Ta}_{0.25}\text{Al}_{0.2}\text{O}_{12}$ and $\text{Li}_{6.15}\text{La}_3\text{Zr}_{1.75}\text{Ta}_{0.25}\text{Ga}_{0.2}\text{O}_{12}$ samples also have near theoretical density (see Table 1) and exhibit microstructures similar to that shown in Fig. 2 in that very little porosity is observed and the fracture surface is very flat. In contrast the microstructure of the only other Ta-substituted LLZO material, $\text{Li}_6\text{La}_3\text{ZrTaO}_{12}$ [13], consolidated by conventional sintering revealed a higher percentage of intergranular fracture, which reveals that the grain boundaries are not as strong as for the present study. This should lead to a higher inter-granular resistance compared to the hot-pressed samples used in the present study. In addition, the microstructure of cubic LLZO without Ta consolidated by conventional sintering [9,10,23,24] tends to reveal a higher percentage of intergranular fracture when compared to the present hot-pressed materials which should also result in a higher inter-granular resistance.

In a device, the total Li-ion conductivity rather than bulk Li-ion conductivity is the important measure for practical application and so we will focus on total Li-ion conductivity. Furthermore, our samples because of their desirable, high density and negligible grain-boundary impedance have a total ionic conductivity nearly equal to their lattice conductivity. This point is illustrated by the room temperature Nyquist plots of all 3 samples (Fig. 3) which revealed only a nearly straight line at a slope of $\sim 45^\circ$ without any clear semi-circles. Since we used Au Li-ion blocking electrodes, the shape of the curve represents a material which is a pure Li-ion conductor. The lack of clear semi-circles at the highest frequencies is

characteristic of a material with low grain boundary impedance. This is in agreement with the results of Kotobuki et al. [9] who suggested that the lack of clear semicircles at the highest frequencies in their impedance plots implied that grain boundary impedance is negligible compared to lattice impedance and Kumazaki et al. [8] who suggested that the lack of a clear semicircle in the highest conductivity sample reveals almost complete removal of the sample grain boundary resistance.

Fig. 4 shows the Arrhenius plot of the total Li-ion conductivity of $\text{Li}_{6.75}\text{La}_3\text{Zr}_{1.75}\text{Ta}_{0.25}\text{O}_{12}$, $\text{Li}_{6.15}\text{La}_3\text{Zr}_{1.75}\text{Ta}_{0.25}\text{Al}_{0.2}\text{O}_{12}$ and $\text{Li}_{6.15}\text{La}_3\text{Zr}_{1.75}\text{Ta}_{0.25}\text{Ga}_{0.2}\text{O}_{12}$ as a function of temperature. The activation energy was estimated from the slope of the line in the temperature range of 298–373 K. From Fig. 4, several important points can be made. First, the total Li-ion conductivity of $\text{Li}_{6.75}\text{La}_3\text{Zr}_{1.75}\text{Ta}_{0.25}\text{O}_{12}$ is highest at all temperatures. Second, the activation energy (0.22 eV) for the total Li-ion conductivity of $\text{Li}_{6.75}\text{La}_3\text{Zr}_{1.75}\text{Ta}_{0.25}\text{O}_{12}$ is considerably lower than the other two samples (0.30 eV for $\text{Li}_{6.15}\text{La}_3\text{Zr}_{1.75}\text{Ta}_{0.25}\text{Al}_{0.2}\text{O}_{12}$ and 0.27 eV for $\text{Li}_{6.15}\text{La}_3\text{Zr}_{1.75}\text{Ta}_{0.25}\text{Ga}_{0.2}\text{O}_{12}$). It is also lower than the other reported Ta-substituted LLZO garnet fast lithium-ion conductors $\text{Li}_6\text{La}_3\text{ZrTaO}_{12}$ (0.42 eV) [13] and lower than that reported for (Al-substituted) $\text{Li}_{7-x}\text{La}_3\text{Zr}_2\text{O}_{12}$ (0.30 eV) [2] and $\text{Li}_{6.75}\text{La}_3\text{Zr}_{1.75}\text{Nb}_{0.25}\text{O}_{12}$ (0.31 eV) [15]. Third, the conductivity of the Ga, Ta substituted sample is roughly the same as the Al, Ta substituted sample. Fourth, the activation energy of the Ga, Ta substituted sample is slightly lower than that of the Al, Ta substituted sample. Understanding the slight difference in activation energy between Ga, Ta-substituted LLZO and Al, Ta substituted LLZO is difficult owing to the small difference in activation energy. First, the two materials have very similar or equal densities, lattice constants, grain size, charge of the substituting atoms (Ta^{5+} and Al^{3+} or Ga^{3+})

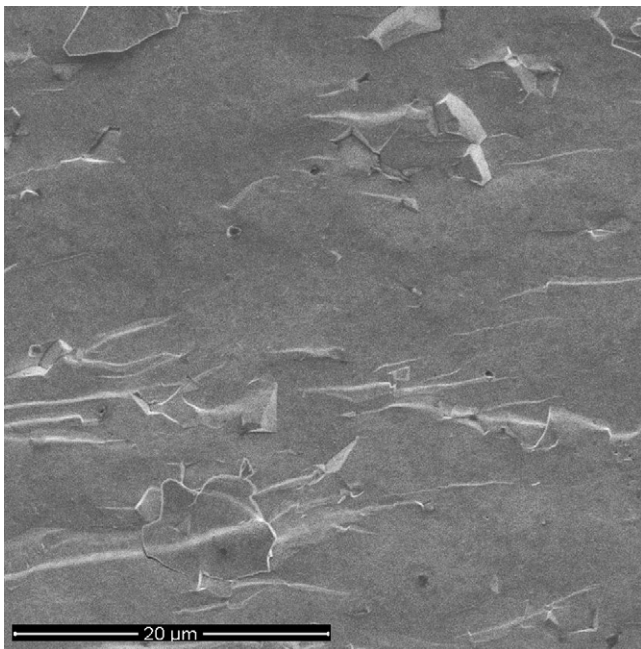


Fig. 2. Representative SEM image of a fracture surface of hot-pressed $\text{Li}_{6.75}\text{La}_3\text{Zr}_{1.75}\text{Ta}_{0.25}\text{O}_{12}$.

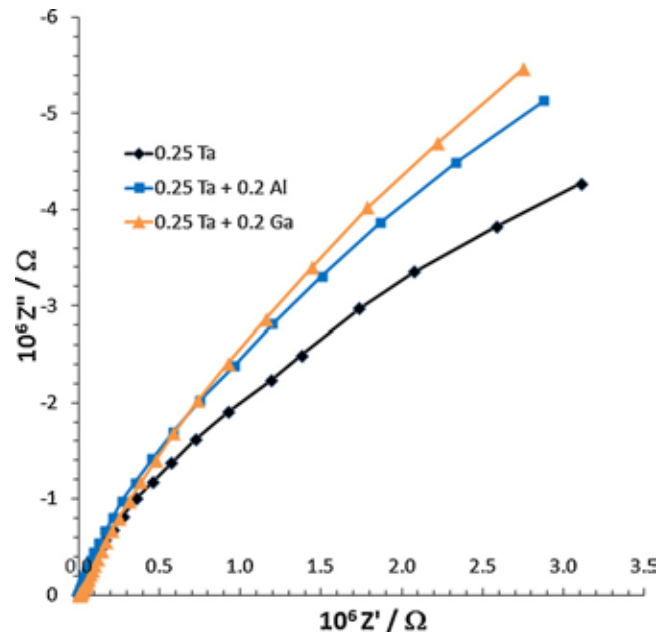


Fig. 3. Nyquist plots of the ac impedance spectra for hot-pressed samples of $\text{Li}_{6.75}\text{La}_3\text{Zr}_{1.75}\text{Ta}_{0.25}\text{O}_{12}$, $\text{Li}_{6.15}\text{La}_3\text{Zr}_{1.75}\text{Ta}_{0.25}\text{Al}_{0.2}\text{O}_{12}$ and $\text{Li}_{6.15}\text{La}_3\text{Zr}_{1.75}\text{Ta}_{0.25}\text{Ga}_{0.2}\text{O}_{12}$ with Li-blocking Au electrodes at 298 K in air.

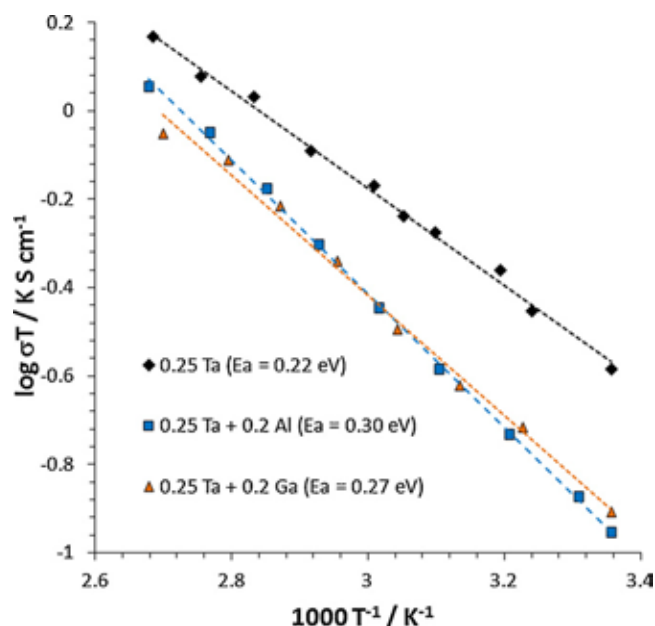


Fig. 4. Conductivity of $\text{Li}_{6.75}\text{La}_3\text{Zr}_{1.75}\text{Ta}_{0.25}\text{O}_{12}$, $\text{Li}_{6.15}\text{La}_3\text{Zr}_{1.75}\text{Ta}_{0.25}\text{Al}_{0.2}\text{O}_{12}$ and $\text{Li}_{6.15}\text{La}_3\text{Zr}_{1.75}\text{Ta}_{0.25}\text{Ga}_{0.2}\text{O}_{12}$ as a function of temperature.

and Li content. The only difference is the size of Al^{3+} relative to Ga^{3+} which in turn leads to different site preferences in garnets [21]. The trend is in agreement with the supposition that Ga would prefer to occupy the distorted octahedral Li2 site and Al the tetrahedral Li1 site, as discussed earlier. However, the small differences in conductivities and activation energies imply that most likely Al and Ga occupy both sites, though perhaps with a higher concentration of Ga on Li2 relative to Ga on Li1 and a higher concentration of Al on Li1 relative to Al on Li2.

Table 1 summarizes the data for all samples. Since our samples are of similar, high density (~96–98%) a good relative comparison of the effect of substitutions is possible. A couple important points can be made. First, as discussed for Fig. 4, the Ta substitution for Zr without Al or Ga leads to the highest conductivity (0.87 mS cm^{-1} at 298 K) and a very low activation energy (0.22 eV). Second, the results in Table 1 provide confirmation of the hypothesis that substitution within the Li sub-lattice by Al or Ga would be detrimental owing to its hindrance of the Li-ion conduction path. As discussed by Ohta et al. [15], the Li-ion conductivity is a function of the Li-ion concentration and the Li-ion mobility. The calculation of the Li-ion concentration difference between $\text{Li}_{6.75}\text{La}_3\text{Zr}_{1.75}\text{Al}_{0.2}\text{O}_{12}$ and $\text{Li}_{6.15}\text{La}_3\text{Zr}_{1.75}\text{Ta}_{0.25}\text{Al}_{0.2}\text{O}_{12}$ and $\text{Li}_{6.15}\text{La}_3\text{Zr}_{1.75}\text{Ta}_{0.25}\text{Ga}_{0.2}\text{O}_{12}$ analyzed via the method of Ohta et al. [15] shows that the Li concentrations of $\text{Li}_{6.15}\text{La}_3\text{Zr}_{1.75}\text{Ta}_{0.25}\text{Al}_{0.2}\text{O}_{12}$ and $\text{Li}_{6.15}\text{La}_3\text{Zr}_{1.75}\text{Ta}_{0.25}\text{Ga}_{0.2}\text{O}_{12}$ are 90% of $\text{Li}_{6.75}\text{La}_3\text{Zr}_{1.75}\text{Al}_{0.2}\text{O}_{12}$. This 10% difference in Li-ion concentration cannot explain the >2-fold increase in conductivity. Therefore, the Li-ion mobility difference is the predominant factor which controls the conductivity difference. This is further supported by the lower activation energy of $\text{Li}_{6.75}\text{La}_3\text{Zr}_{1.75}\text{Al}_{0.2}\text{O}_{12}$ (0.22 eV) relative to $\text{Li}_{6.15}\text{La}_3\text{Zr}_{1.75}\text{Ta}_{0.25}\text{Al}_{0.2}\text{O}_{12}$ (0.30 eV) and $\text{Li}_{6.15}\text{La}_3\text{Zr}_{1.75}\text{Ta}_{0.25}\text{Ga}_{0.2}\text{O}_{12}$ (0.27 eV). Al or Ga on the Li sub-lattice hinders the Li-ion mobility. Third, at least for hot pressing, Al or Ga substitution is not needed in order to obtain a sample with high density and fast Li-ion conductivity.

By way of comparison, Li et al. [13] reported a total Li-ion conductivity at 298 K of 0.18 mS cm^{-1} for the Ta-substituted LLZO garnet of composition $\text{Li}_6\text{La}_3\text{ZrTaO}_{12}$. Al was also found in the sample at a weight percent of 1.3 which is about 0.4 M or about twice as much as our Al-containing sample. This is the only other reported

conductivity for Ta-substituted LLZO however the comparison is not ideal since we do not know the density of the Li et al. sample and the Ta content and Al content is different. In contrast, our Ta, Al substituted sample ($\text{Li}_{6.15}\text{La}_3\text{Zr}_{1.75}\text{Ta}_{0.25}\text{Al}_{0.2}\text{O}_{12}$) had a conductivity of $\sim 0.37 \text{ mS cm}^{-1}$. Qualitatively, we can say that first, the lower conductivity of the Li et al. [13] sample may result from lower sample density and the higher Al (reduced Li-ion mobility) and Ta content (reduced Li-ion concentration). Second, the activation energy of the Li et al. sample is considerably higher (0.42 eV) which is probably a result of higher grain boundary resistance as well as some blockage of the Li sub-lattice by the higher content of Al.

Also, as comparison, the total Li-ion conductivity and activation energy of our sample of composition $\text{Li}_{6.75}\text{La}_3\text{Zr}_{1.75}\text{Ta}_{0.25}\text{O}_{12}$ (0.87 mS cm^{-1} and 0.22 eV) can be compared to the Nb-substituted LLZO of composition, $\text{Li}_{6.75}\text{La}_3\text{Zr}_{1.75}\text{Nb}_{0.25}\text{O}_{12}$ (0.8 mS cm^{-1} and 0.31 eV) [15]. The conductivity values are in excellent agreement. The activation energy of our sample is lower as a result of the higher relative density (96%) obtained via hot-pressing relative to sintering (89–92%). These values approach the calculated (via molecular dynamics simulation) bulk lattice conductivity of 1 mS cm^{-1} reported by Adams et al. [25].

Turning once again to our samples, these results support the supposition that high ionic conductivity can be achieved by Ta substitution for Zr cubic garnet stabilizing substitutions that do not place the substituting atom (Al or Ga) in the conductive pathway of Li. Both Nb [15] and Ta (this work) substituted LLZO exhibited higher conductivity than Al-substituted LLZO [2]. Ta is preferred owing to its higher stability against Li reduction.

4. Conclusion

Cubic LLZO can be stabilized at room temperature by the addition of Ta. Hot-pressed $\text{Li}_{6.75}\text{La}_3\text{Zr}_{1.75}\text{Ta}_{0.25}\text{O}_{12}$, $\text{Li}_{6.15}\text{La}_3\text{Zr}_{1.75}\text{Ta}_{0.25}\text{Al}_{0.2}\text{O}_{12}$ and $\text{Li}_{6.15}\text{La}_3\text{Zr}_{1.75}\text{Ta}_{0.25}\text{Ga}_{0.2}\text{O}_{12}$ have a relative density of ~96–98%. The room temperature AC conductivity results for the hot-pressed $\text{Li}_{6.75}\text{La}_3\text{Zr}_{1.75}\text{Ta}_{0.25}\text{O}_{12}$ sample yields a total ionic conductivity value $\sim 0.87 \text{ mS cm}^{-1}$ and activation energy of 0.22 eV. Addition of Al or Ga to Ta-substituted LLZO reduces the conductivity and increased the activation energy suggesting that Al or Ga substitutions in the Li-ion sub-lattice tend to lower the Li-ion conductivity.

Acknowledgments

J.L.A. and J.W. would like to acknowledge support of the US Army Research Laboratory (ARL). E.R. and J.S. authors would like to acknowledge the support of the US Army Research Office (ARO).

References

- [1] Y. Shimonishi, A. Toda, T. Zhang, A. Hirano, N. Imanishi, O. Yamamoto, Y. Takeda, *Solid State Ionics* 183 (2011) 48.
- [2] R. Murugan, V. Thangadurai, W. Weppner, *Angew. Chem. Int. Ed.* 46 (2007) 7778.
- [3] J.L. Allen, T.R. Jow, J. Wolfenstine, *J. Power Sources* 196 (2011) 8656.
- [4] A. von Cresce, K. Xu, *Electrochem. Solid State Lett.* 158 (2011) A337.
- [5] P.G. Bruce, L.J. Hardwick, K.M. Abraham, *MRS Bull.* 36 (2011) 506.
- [6] J. Awaka, N. Kijami, H. Hayakawa, J. Akimoto, *J. Solid State Chem.* 182 (2009) 2046.
- [7] C.A. Geiger, E. Alekseev, B. Lazic, M. Fisch, T. Armbruster, R. Langner, M. Fechtelkord, N. Kim, T. Pettke, W. Weppner, *Inorgan. Chem.* 50 (2011) 1089.
- [8] S. Kumazaki, Y. Iriyama, K.-H. Kim, R. Murugan, K. Tanabe, K. Yamamoto, T. Hirayama, R. Murugan, Z. Ogumi, *Electrochem. Commun.* 13 (2011) 509.
- [9] M. Kotobuki, H. Munakata, K. Kanamura, Y. Sato, T. Yoshida, *J. Power Sources* 196 (2011) 7750.
- [10] Y. Jin, P.J. McGinn, *J. Power Sources* 196 (2011) 8683.
- [11] E. Rangasamy, J. Wolfenstine, J. Sakamoto, *Solid State Ionics* 206 (2012) 28.
- [12] J. Wolfenstine, J. Ratchford, E. Rangasamy, J. Sakamoto, J.L. Allen, *Mater. Chem. Phys.*, under review.
- [13] Y. Li, C.-A. Wang, H. Xie, J. Cheng, J.B. Goodenough, *Electrochem. Commun.* 13 (2011) 1289.

- [14] A. Logéat, T. Kohler, U. Eisele, B. Stiaszny, A. Harzer, M. Tovar, A. Senyshyn, H. Ehrenberg, B. Kozinsky, *Solid State Ionics* 206 (2012) 33.
- [15] S. Ohta, T. Kobayashi, T. Asaoka, *J. Power Sources* 196 (2011) 3342.
- [16] N. Kumagai, N. Ikenoya, I. Ishiyama, K. Tanno, *Solid State Ionics* 28 (1998) 862.
- [17] Y. Li, C. Sun, J.B. Goodenough, *Chem. Mater.* 23 (2011) 2292.
- [18] J.M. Amarilla, B. Casal, E. Ruiz-Hitzky, *J. Mater. Chem.* 6 (1996) 1005.
- [19] E.J. Cussen, T.W.S. Yip, G. O'Neill, M.P. O'Callaghan, *J. Solid State Chem.* 184 (2011) 470.
- [20] J. Awaka, A. Takashima, K. Kataoka, N. Kijima, Y. Idemoto, J. Akimoto, *Chem. Lett.* 40 (2011) 60.
- [21] S. Geller, *Z. Kristallogr.* 125 (1967) 1.
- [22] R.D. Shannon, *Acta Crystallogr. A* 32 (1976) 751.
- [23] J. Tian, A. Tiwari, *Electrochem. Solid State Lett.* 15 (2012) A37.
- [24] M. Huang, T. Liu, Y. Deng, H. Geng, Y. Shen, Y. Lin, C.-W. Nan, *Solid State Ionics* 204–205 (2011) 41.
- [25] S. Adams, P.R. Rayavarapu, *J. Mater. Chem.* 22 (2012) 1426.

Shock-Induced Behavior of Cubic Gauche Polymeric Nitrogen

William D. Mattson and Radhakrishnan Balu

U.S. Army Research Laboratory, Aberdeen Proving Ground, MD

ABSTRACT

Quantum-mechanical calculations based on density functional theory are used to study the shock response of the polymeric cubic gauche phase of nitrogen (cg-N), proposed as an alternative energetic ingredient to those used in conventional explosive formulations. The shocked polymeric nitrogen undergoes multiple complex phase transformations and spontaneously forms defects. The occurrence of these dynamic phenomena absorbs the shock energy which subsequently slows the compression wave. Additionally, no reaction occurs immediately behind the shock front; rather reactions result from the unraveling of the material at the free edge of the filament opposite to shock propagation. As the material unravels, numerous polyatomic transients are formed, including five-membered rings and polymeric chains, which subsequently undergo secondary reactions to form the final diatomic products. The speed at which these reactions propagate through the material is much slower than the sound speed, and combined with the slowing compression wave, indicates that the material may not detonate under these conditions.

Physical Review B, Volume 83, Page 174105 (2011)

Shock-induced behavior of cubic gauche polymeric nitrogen

William D. Mattson and Radhakrishnan Balu

U.S. Army Research Laboratory, RDRL-WML-B (Bldg. 4600), Aberdeen Proving Ground, Maryland 21005-5069, USA

(Received 26 January 2011; revised manuscript received 8 April 2011; published 11 May 2011)

Quantum-mechanical calculations based on density functional theory are used to study the shock response of the polymeric cubic gauche phase of nitrogen (cg-N), proposed as an alternative energetic ingredient to those used in conventional explosive formulations. The shocked polymeric nitrogen undergoes multiple complex phase transformations and spontaneously forms defects. The occurrence of these dynamic phenomena absorbs the shock energy which subsequently slows the compression wave. Additionally, no reaction occurs immediately behind the shock front; rather reactions result from the unraveling of the material at the free edge of the filament opposite to shock propagation. As the material unravels, numerous polyatomic transients are formed, including five-membered rings and polymeric chains, which subsequently undergo secondary reactions to form the final diatomic products. The speed at which these reactions propagate through the material is much slower than the sound speed, and combined with the slowing compression wave, indicates that the material may not detonate under these conditions.

DOI: [10.1103/PhysRevB.83.174105](https://doi.org/10.1103/PhysRevB.83.174105)

PACS number(s): 62.50.Ef, 82.40.Fp, 61.50.Ah, 61.72.Cc

I. INTRODUCTION

Pressure-induced transitions of molecular solids to polymeric forms have been the subject of intense activity for several decades. One of the more widely studied systems both theoretically^{1–24} and experimentally^{25–40} is nitrogen, which in its ambient state is a homonuclear diatomic molecule with one of the strongest bonds in nature, making it an ideal candidate for energy storage if a stable high-density polymeric form can be realized. Theoretical predictions have indicated a variety of possible molecular and polymeric phases over a range of pressures and temperatures; however, until recently, only the diatomic molecular high-pressure phases were observed experimentally within the predicted pressure and temperature regimes. Phase transitions to the more exotic polymeric^{31,33,34} and nondiatomic molecular phases³⁶ have been observed well above the predicted transition pressure range for the diatomic to cubic gauche (cg-N) transition.⁵ This cg-N form of nitrogen is a bulk three-dimensional covalent network, similar to diamond, in which every atom has three neighbors. This structure was observed in diamond-anvil-cell experiments³⁹ in which nitrogen is compressed to 180 GPa and heated to 2200 K. The sample was only partially cg-N and included amorphous polymeric nitrogen. The material was not recoverable at ambient conditions, although phonon calculations indicate that the cg-N structure should be stable at ambient pressures.⁴¹ However, all theoretical calculations have assumed an ideal crystal structure, which is not attainable under the extreme experimental conditions used in its synthesis, and thus the presence of these other phases most likely introduces instabilities preventing the recovery of the cg-N at ambient conditions. Continued theoretical and experimental explorations to understand the principle physical and chemical laws which govern bonding, phase behavior, and thermodynamic stability of high-pressure polymeric phases are necessary for developing the technologies required to recover polymeric forms of nitrogen at the ambient state.

These new types of materials are not only of academic interest, as the large energy densities of some of the various polymeric forms make them promising high-performing alter-

natives to currently fielded conventional energetic materials (EM). The calculated energy of complete conversion of cg-N to the ground state diatomic nitrogen ranges from 0.75 to 1.55 eV per atom,¹² several times that of conventional explosives.⁴² However, before cg-N can be considered for use in a practical EM application, its stability and dynamic response under a variety of conditions must be well understood. This study is the first in a series in which such factors are explored, where we present quantum molecular-dynamics (QMD) results of shocked cg-N initially at low temperature and ambient pressure.

Finally, one of the primary goals of this paper is to determine whether shock impact will initiate a self-sustained reaction wave within the defect-free cg-N material. In addition to presenting results demonstrating the dynamic response of shocked cg-N, this paper will briefly describe the theoretical methods, the computational details, software explored to enable adequate treatment of the calculations, and results of the calculations to date.

II. DETAILS OF THE CALCULATION

The first-principles calculations reported herein use the Kohn-Sham density functional theory (DFT) with the generalized gradient approximation (GGA) exchange-correlation functional of Perdew, Burke, and Ernzerhof (PBE).⁴³ QMD simulations were performed using the Gaussian and plane-wave-method code QUICKSTEP as implemented in CP2K (Ref. 44) and the double-zeta with valence polarization basis. Total energies and forces were converged to 2.6×10^{-5} and 1.6×10^{-4} a.u., respectively, for all calculations. The equations of motion are from the Born-Oppenheimer approximation with a time step of 1 fs for all simulations.

The direct shock-wave simulations here are implemented with a long thin filament⁴⁵ composed of blocks of eight-atom simple cubic cells. Each block is constructed using two instances of the primitive cell of cg-N (space group $I2_135$) with one centered at the origin (0,0,0) and the other at the body-centered site (1/2,1/2,1/2). The blocks are used to create

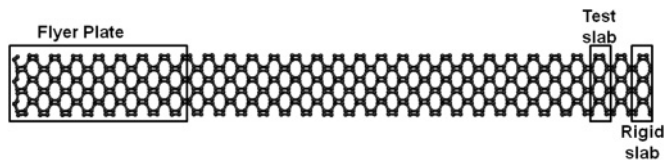


FIG. 1. A schematic of the filament used in the QMD simulations of shock-impacted cg-N. The filament can be described as a series of blocks composed of $(1 \times 3 \times 3)$ unit cells of cg-N. The block at the far right edge of the filament (outlined in black) denotes the material that is fixed during the simulation; to its left is the “test” block, used to determine shock-wave approach (see text). The eight blocks at the far left edge of filament contain the flyer plate atoms.

a “slab” which is defined to be a $(1 \times 3 \times 3)$ supercell of blocks with dimensions of $(3.8, 11.3, 11.3)$ Å. The filament is then composed of 32 slabs of cg-N. The simulation cell, shown in Fig. 1, contains 2304 atoms. In order to generate an initial configuration for use in the shock simulation, the 0 K configuration was first obtained through geometry optimization of the filament. Next, the optimized simulation cell was first subjected to an isothermal isochoric (NVT) MD simulation at either $T = 200$ or 300 K for 5 ps. The final configuration of the NVT-MD simulation was then used in an isothermal-isobaric (NPT) MD simulation at either $T = 200$ or 300 K, $P = 1$ bar for 5 ps to produce the filaments that would be used in the shock simulations. In all of the aforementioned simulations, periodic boundary conditions were imposed in all directions.

For the shock-wave simulations, computational schemes for reducing the costs of MD simulations of shocked crystals were employed; specifically, that outlined by Rice.⁴⁶ In this scheme, a shock wave is initiated in the filament composed of quiescent material [denoted as cg-N(V) and shown in Fig. 1] through flyer plate impact. Periodic boundary conditions are imposed in the two directions perpendicular to the direction of the shock impact and propagation (in this case, the x direction). For these simulations, the shock will be introduced at the far-left side of the filament by a “flyer plate” composed of cg-N. These correspond to the eight leftmost slabs shown in Fig. 1. The edge of the simulation cell opposite to shock impact is bounded by a slab of constrained atoms (located at the right edge of Fig. 1). Within this scheme, as the shock wave approaches the rigid layer, additional undisturbed material is inserted before the rigid layer to allow continuance of the shock wave. The shock wave can be initiated through instantaneously increasing the x component of the velocity of each atom within the flyer plate by an additional 10 km/s. Following Rice *et al.*, a $(1 \times 3 \times 3)$ test slab was monitored for shock-wave approach and is located one slab length to the left of the rigid slab of atoms in the filament (see Fig. 1). The center-of-mass displacement within the “test slab” is evaluated at each integration step and when this value exceeded that of thermally equilibrated bulk cg-N by 0.1 Å, material composed of thermally equilibrated bulk cg-N is inserted between the rightmost slab of moving atoms and the rigid layer. The filament has a “free edge” at the leftmost region (the flyer plate) with vacuum to the left. We confirmed that the material with the free edge was stable at both $T = 200$ or 300 K using NVT-MD simulations integrated for 15 ps. In these simulations, the initial configuration of the free-edge

filament was that of the final configuration of the heretofore described NPT-MD simulation in which periodic boundary conditions were imposed in all three dimensions. During these NVT-MD simulations the atoms at the free edge exhibited larger oscillations about their lattice sites than those in the interior of the filament; however, no reaction was observed. Also, relaxation of the atoms near the free surface occurred, resulting in a slight decrease in lattice spacing relative to that within the interior of the filament.

A potential source of error is the small cross-sectional area (11.3×11.3 Å) normal to the direction of the shock front. However, previous quantum molecular-dynamics shock simulations have successfully used cells with similarly sized cross-sectional areas.^{47,48} These calculations were performed in conjunction with the multiscale shock technique (MSST) for systems of either 64 water molecules or 360 carbon atoms. In both studies, exploration of the effect of system size showed that the simulation cells were sufficiently large to reach converged results. Also, QMD calculations of the shock Hugoniot of nitrogen over a large range of temperatures and densities using systems composed of 32, 54, and 64 atoms showed that of the measured properties, only the Gruneisen parameter showed a dependence on size, and only for the region of the shock Hugoniot where the smaller system predicted a negative value.⁴⁹ Since our simulations have substantially larger cross-sectional areas than in Ref. 49, we do not expect the results to be affected by our choice of system size.

Another potential source of error is that these simulations were performed using Born-Oppenheimer QMD and therefore the electrons in the system are treated adiabatically. Shock simulations on deuterium⁵⁰ and water⁴⁷ has shown that treating the electrons nonadiabatically within Car-Parrinello QMD (CPMD) had little effect on simulations with shock velocities less than 15 and 12 km/s, respectively. Since the electron-ion coupling constant for nitrogen is smaller than that for deuterium and hydrogen, it is expected that shock simulations of nitrogen will be insensitive to the nonadiabatic deviations of CPMD at the shock velocity investigated in this study (10 km/s). While the nonadiabatic excitation reflected by CPMD might not adequately represent that in a shock event, the insensitivity of the simulations to CPMD excitations for shock velocities of 10 km/s implies that the Born-Oppenheimer approximation is reasonable for the simulations presented here. The shock velocity for the simulation was chosen to impart sufficient energy that might lead to reaction, but was not likely to induce nonadiabatic effects.

To illustrate the evolution of the material under shock, temporal profiles of various properties within the filament will be described; this is accomplished by taking a weighted moving average of the properties in local regions of the material along the direction of the shock. For each plane normal to the x axis on intervals of 0.5 Å, the weighted moving average is calculated by summing the weighted value of the property of each atom within 4 Å of the plane under consideration. The weight assigned for each atom is proportional to its distance from the plane. For example, at 4 Å the weight is 0, and at 0 Å from the plane the weight is 0.25. This scheme produces temporally averaged values that make the relevant aspects of the simulation clear, and maintains correspondence

of the property depicted in the temporal profiles to that of the material property. Finally, in this work, chemical bonds are depicted between atom pairs with interatomic separations that are less than 1.6 Å. This value was selected after observing the temporal behavior of such bonds in the shocked lattice and in various vibrationally hot product species.

III. RESULTS

The shock-wave simulations for filaments at 200 and 300 K were performed within the microcanonical ensemble (NVE-MD) using the final configurations and atomic velocities from the NVT-MD simulations of the free-edge filament (with flyer plate atoms given the appropriate impact velocity as described heretofore). As the shock wave propagated through the material, its effects reached the test slab after 480 fs, at which time the simulations were stopped. The features of the shocked material were similar for both 200 and 300 K filaments up to this time, including phase transitions and spontaneous formation of defects, as will be discussed hereafter. Thus, further investigation is limited to the 300 K filament. For the 300 K filament simulation, an additional 25 slabs (containing 1800 atoms) were inserted immediately to the left of the rightmost rigid slab to allow the continuation of the shock simulation, increasing the total number of atoms in the filament to 4104. As shown in earlier classical molecular-dynamics studies of shocked filaments, such a scheme allows for simulation of only the area of immediate interest (i.e., the shocked region), with the idea that simulating infinitely large material well ahead of the shock discontinuity provides no extra information on the shock phenomena.⁴⁶ All results discussed hereafter refer to the simulation using the 300 K filament.

A. Complex phase transitions and defects

A series of snapshots of atomic positions at various times during the simulation (Fig. 2) illustrates the very complex

behavior of shocked cg-N, with the formation of numerous phases as well as interesting reaction intermediates displayed. Figure 2(a) shows that the original honeycomb structure of the cg-N collapses to a herringbonelike lattice as the flyer plate drives the material forward. This phase [denoted HB(l)] continues to grow as the simulation progresses to a maximum width of ~ 50 Å and propagates through the material in the direction of the initial shock at a gradually diminishing velocity as will be discussed in greater detail in Sec. III C. In this phase transition, no bonds are broken or formed. At 400 fs [Fig. 2(c)] additional complexity in the form of a region of compressed cg-N behind the leading phonon but ahead of the HB(l) phase emerges. This region will be denoted hereafter as the leading compression zone (LCZ). The LCZ continues to develop behind the shock front for the remainder of the trajectory. Also in Fig. 2(c), the appearance of a spontaneously formed stacking fault is apparent between the HB(l) phase (denoted as D_1 and enclosed by a box) and the LCZ. In Fig. 2(d), the material immediately to the right of D_1 deforms to a HB lattice configuration that corresponds to a shifting of the HB(l) crystal along the vertical axis by half of the original lattice vector [denoted hereafter as HB(r)]. The formation of this stacking fault was unexpected and has significant consequences, as will be discussed below. Finally, as the HB(l) phase relaxes and expands on the left, the material reforms to the cg-N structure. Note that the reformed cg-N phase has a different crystalline orientation than the initial structure. The undisturbed crystal ahead of the leading phonon has the long axis of the large honeycomblike rings oriented vertically, but the reformed region in Fig. 2(f) has the long axis of the rings oriented horizontally. Therefore, the material in the reformed cg-N phase will be denoted as cg-N(H) hereafter, whereas the material ahead of the shock front will be denoted as cg-N(V). The nearest neighbors of the nitrogen atoms in the cg-N(H) region are the same as that of cg-N(V), as is the handedness of the crystal.

More complex structures evolve in this shocked material as the trajectory continues. Specifically, at 690 fs, a new “defect”

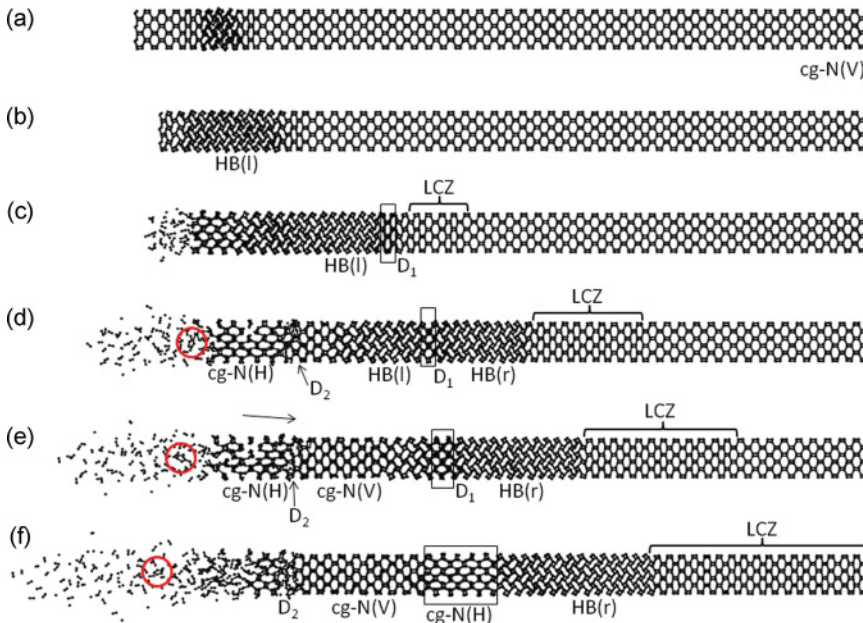


FIG. 2. (Color online) Snapshots of the cg-N system at (a) $t = 90$ fs, (b) 160 fs, (c) 400 fs, (d) 690 fs, (e) 830 fs, and (f) 1040 fs. For clarity, the block of stationary atoms at the far-right edge of the simulation cell are not shown; also, quiescent crystal is added to the snapshots in (a)–(c) to have the same x dimension as those in (d)–(f). See text for explanation of the larger simulation cells used in (d)–(f).

appears (denoted D_2), which is bounded by the cg-N(H) structure on the left and a reformed cg-N(V) on the right. To the right of these are the HB phases (which also have in their midst D_1 , discussed above) and the LCZ. In D_2 , bonds are broken and formed, unlike the material associated with D_1 . At 830 fs [Fig. 2(e)], D_1 has widened and by 1040 fs has transitioned into the cg-N(H) phase [see the region enclosed by the box in Fig. 2(f)]. The width of the HB(l) phase decreases during the transition of D_1 to the cg-N(H) phase, a result both from back transition to cg-N(V) at its left boundary and from back transition of D_1 to cg-N(H) at its right boundary. The HB(r) phase to the right of D_1 is maintained as the LCZ transitions to HB(r); the LCZ material to its right continues to widen.

B. Chemical reaction

Reactions in the shocked material are equally complex and interesting. Initially, as seen in the snapshot at 400 fs [Fig. 2(c)], most of the products ejected from the free cg-N surface at the left are diatomic nitrogen, with a few short-lived N_3 molecules. As soon as two N_3 molecules approach each other, they rapidly react to form three N_2 molecules. By 690 fs [Fig. 2(d)], chains with one end connected to the leftmost free surface start to form, break free at the surface, and subsequently decompose. As chains continue to form, their lengths increase and disintegration occurs within the chains rather than detachment at the surface. The lengthening of these chains indicates that surface disintegration of the cg-N lattice occurs more quickly than formation of the more stable N_2 product. By 1040 fs [Fig. 2(f)], large fragments of crystal have disintegrated into chains. This process creates a reaction zone with little to no N_2 forming at the cg-N surface, but rather N_2 resulting from reactions of the detached chains. Additionally, other more complicated structures are formed including N_5 rings [see, for example, the ring in Figs. 2(d)–2(f) bounded by the red circle]. Some of the N_5 rings also have chains attached to one of the atoms in the ring. Figure 3 shows a time history of the formation and progression of the N_5 ring highlighted in the snapshots in Fig. 2. This five-membered ring within the red circle has a lifetime of in excess of 450 fs as evidenced by the temporal history of the bonds labeled on the moiety shown in Fig. 4. Up to 770 fs, the pentazole ring has a six-membered nitrogen chain attached to it at which point the nitrogen chain subsequently decomposes into three nitrogen molecules. The chain decomposes first by simultaneously forming two nitrogen molecules from the four terminal nitrogen atoms of the chain, followed by the dissociation of the remaining two nitrogen atoms from the pentazole ring to form the final nitrogen molecule. By 820 fs, the three nitrogen molecules oscillate about the equilibrium gas phase value (1.1 Å), while the bonds corresponding to the pentazole ring oscillate about larger values (~1.3–1.4 Å) for the remainder of the trajectory integration. Pentazole structures have been shown to be stable⁵¹ and similar structures have recently been observed in simulations calculating the high-temperature phase diagram of nitrogen.^{52,53} Interestingly, both Boates *et al.*⁵² and Donadio *et al.*⁵³ have observed a liquid-liquid phase transition where the liquid molecular nitrogen transforms into nitrogen chains and five-membered rings, similar to the reaction intermediates shown in the simulations herein.

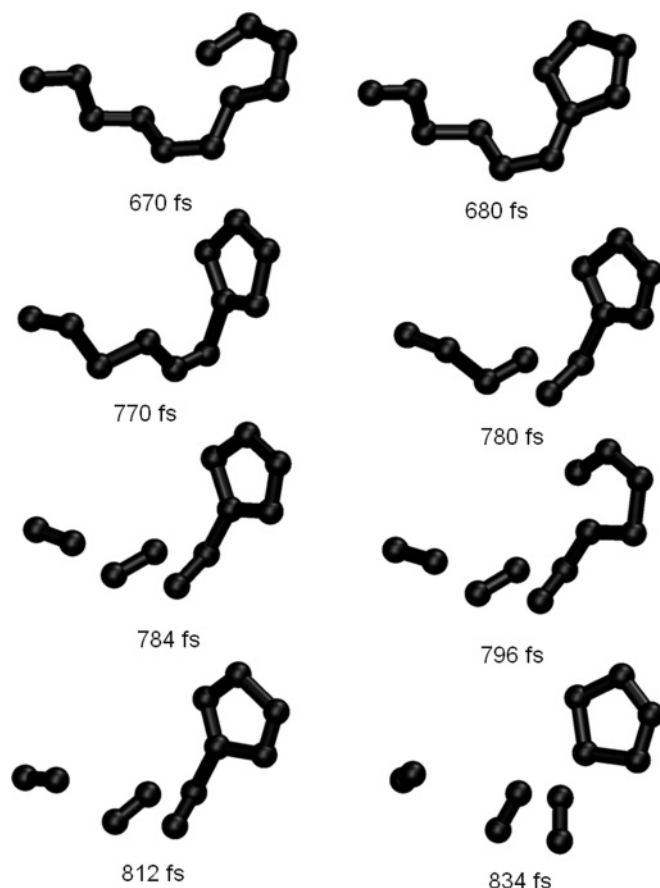


FIG. 3. Snapshots of one of the longer-lived polyatomic transients formed in the reaction zone of the material. Times during the simulation are denoted in the figure.

C. Spatial-temporal profiles of material properties

Spatial-temporal profiles of the velocity of particles of the material in the supercell along the direction of shock propagation are given in Fig. 5. In the figure the length of the supercell in the direction of shock propagation corresponds to the x axis and the simulation time corresponds to the y axis. The red triangular region in the lower left-hand area of the figure corresponds to the initial flyer plate. Partitions corresponding to a portion of the vacuum region to the left of the initial flyer plate position and corresponding to the fixed slab (far right of the simulation cell) are not shown. The phonons emanating in front of the shock discontinuity are clearly apparent in Fig. 5, with an initial phonon generated by the shock impact (~150 fs) and progressing ahead of a series of evolving shock fronts. We define a shock front as a nearly discontinuous change in material state during the simulation. Additionally, density profiles along the filament at later times indicate a series of subsequent phonons emanating ahead of the leading shock front. By the end of the simulation, five very distinct phonons have appeared and are traveling at a constant speed of 16.5 ± 0.5 km/s. The compressed region behind the phonons, however, is clearly slowing down. At the initial stages of its formation, the velocity of the leading edge of the HB(l) phase aligns with the initial phonon. Interestingly, at 40 Å, ~150 fs, a second phonon emanates, with an almost discontinuous decrease in velocity of the shock front. A similar

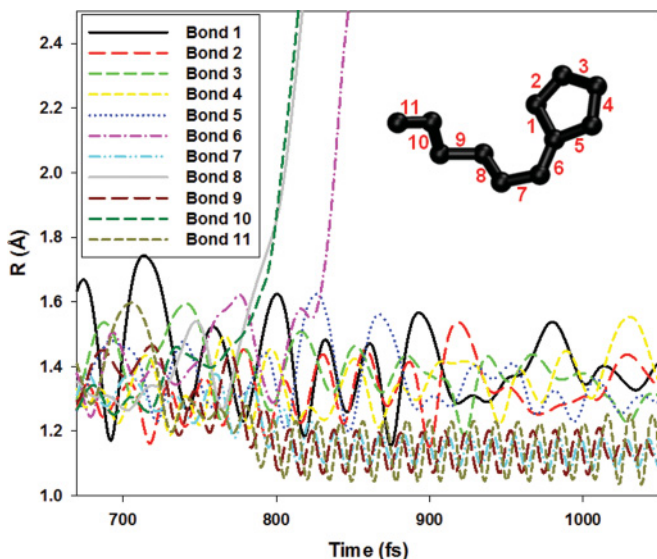


FIG. 4. (Color online) Time trace of the bond lengths of the bonds shown in Fig. 3. The bonds are numbered in the inset moiety which is a copy of the 680 fs snapshot in Fig. 3.

manifestation of this behavior is apparent at 90 Å, 550 fs, in which a third phonon appears with a corresponding decrease in velocity of the shock front. Beyond that, two additional phonons appear and the shock front continues to slow.

Figure 6 shows the instantaneous temperature profile of the material in the supercell along the direction of shock propagation. The local temperatures within the material were calculated by first subtracting the weighted center-of-mass velocity of all atoms in the local region around each plane from the individual atomic velocities in the local region, and then used to calculate an instantaneous local temperature. There is significant heterogeneity within the material phases as shown in Fig. 6. Of most importance is the region where the initial spontaneously formed stacking fault (D_1) resides. It is notable that the temperature of the area around the fault remains lower than the material on either side of it. The stacking fault, which first appears at ~ 400 fs, corresponds to the point in Fig. 6 at

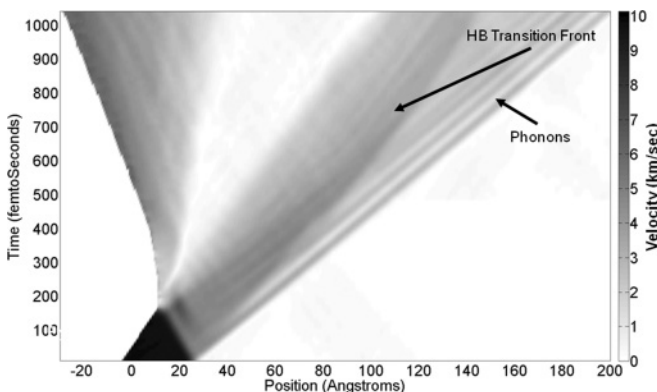


FIG. 5. Temporal velocity profiles. Phonons emanate from the shock front and propagate at a velocity of 16.5 km/s away from the shock front. The shock front (HB transition front) itself slows down. Legends for the color range are given in the figure for the range of 0 to 10.1 km/s.

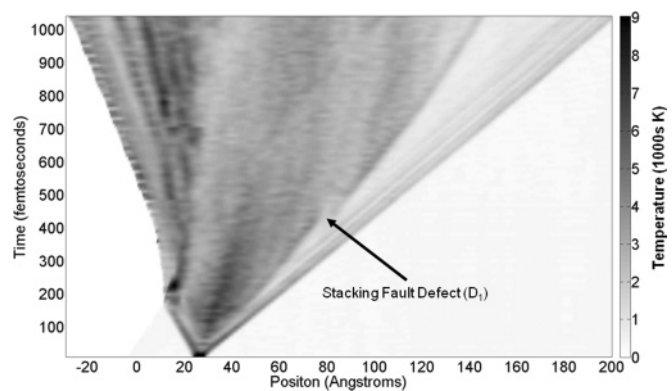


FIG. 6. Temporal instantaneous temperature profiles. The temperature of the defect is lower than the surrounding compressed region. Legends for the color range are given in the figure for the range of 0 to 9000 K.

which the velocities of the second phonon, and the following compressed region, separate. The region corresponding to D_1 remains lower in temperature than the material ahead or behind it all throughout the simulation, indicating that the stacking fault acts as an energy sink.

IV. DISCUSSION

It was expected that cg-N, like all other forms of polymeric nitrogen, would be an advanced, new type of energetic material due to its stored structural energy. The transition to gaseous nitrogen would release 1.55 eV/atom,¹² a substantially higher energy release than that of conventional energetic materials. Unfortunately, the results of these simulations indicate that the mechanical properties of cg-N in its purest, defect-free, form enable it to disperse shock energy through extremely complex phase transitions such that initiation to a self-sustained exothermic shock-driven reaction is improbable. Most likely, the reaction within the rarefaction region could continue until the material is consumed but at a rate that would preclude cg-N from consideration as an advanced high explosive.

It is worth noting at this point that Chen *et al.*¹⁹ performed first-principles calculations of mechanical properties and failure modes for cg-N, and concluded that this material has “exceptional mechanical properties.” They evaluated the failure modes for cg-N using the method of Roundy *et al.*⁵⁴ in which the lattice vectors are incrementally deformed in the direction of the applied stress and the atomic coordinates are fully relaxed between increments. In this study they found that the dominant mode of lattice failure is shear, a condition not imposed in the shock simulations contained in this effort. The size of the simulation cell used in this study is too small to allow the formation of shock-induced shear bands and therefore, the role of shear on dynamic response cannot be evaluated using these results.

An equally important consideration is the role of defects on the shock response of cg-N. Synthesized cg-N will include defects, which could influence the shock behavior, as evidenced by the role spontaneously formed defects play in the dynamic response of the pure material discussed above. Although it is well beyond the scope of the current study, a thorough QMD investigation of a shocked defected material could identify

fundamental mechanisms that contribute to the physical response of the material, including plasticity, fragmentation, defect-nucleated reactions, and melting. In light of the possible roles of shear and/or defects in the shocked material on reactivity and energy release, it would be premature to conclude that cg-N would not be useful as an energetic material.

V. SUMMARY

Quantum MD simulations have been used to provide an atomic-level description of the material response of the defect-free cg-N polymeric form of solid nitrogen to shock. The cg-N solid showed extremely complex shock-wave structure involving several structural phase changes and spontaneous formation of material defects behind the shock front that absorbed and dispersed the shock energy. Reaction did not occur directly behind the shock front, but rather at the free edge of the filament opposite to the direction of shock propagation, unraveling into a variety of polyatomic and polymeric transients, including chains and five-member rings. These transients subsequently decomposed or underwent collision with other transients to form the final diatomic product gas. The

heat released in the reactions was localized in this dense-gas region behind the disintegrating filament and not transferred to the remaining intact filament. Although the simulations suggest that the pure form of cg-N might not be a good candidate for use as an explosive, its unique energy dispersion properties due to the complex phase transitions initiated by shock could be exploited for other applications in which such a response would be advantageous.

ACKNOWLEDGMENTS

Calculations were performed using the DOD Supercomputing Resource Centers (DSRCs) located at the U.S. Army Research Laboratory and the Air Force Research Laboratory under the Computing Challenge Project C2L awarded by the DOD High Performance Computing Modernization Program. R.B. acknowledges support from the Research Participation Program for the U.S. Army Research Laboratory administered by the Oak Ridge Institute for Science and Education. The authors wish to thank Betsy Rice for helpful comments and discussions.

- ¹R. LeSar, *J. Chem. Phys.* **81**, 5104 (1984).
- ²A. K. McMahan and R. LeSar, *Phys. Rev. Lett.* **54**, 1929 (1985).
- ³R. M. Martin and R. J. Needs, *Phys. Rev. B* **34**, 5082 (1986).
- ⁴S. P. Lewis and M. L. Cohen, *Phys. Rev. B* **46**, 11117 (1992).
- ⁵C. Mailhot, L. H. Yang, and A. K. McMahan, *Phys. Rev. B* **46**, 14419 (1992).
- ⁶L. Mitás and R. M. Martin, *Phys. Rev. Lett.* **72**, 2438 (1994).
- ⁷M. M. G. Alemany and J. L. Martins, *Phys. Rev. B* **68**, 024110 (2003).
- ⁸L. N. Yakub, *Low. Temp. Phys.* **29**, 780 (2003).
- ⁹W. D. Mattson, D. Sanchez-Portal, S. Chiesa, and R. M. Martin, *Phys. Rev. Lett.* **93**, 125501 (2004).
- ¹⁰F. Zahariev, A. Hu, J. Hooper, F. Zhang, and T. Woo, *Phys. Rev. B* **72**, 214108 (2005).
- ¹¹H. L. Yu, G. W. Yang, X. H. Yan, Y. Xiao, Y. L. Mao, Y. R. Yang, and M. X. Cheng, *Phys. Rev. B* **73**, 012101 (2006).
- ¹²J. Uddin, V. Barone, and G. E. Scuseria, *Mol. Phys.* **104**, 745 (2006).
- ¹³T. Zhang, S. Zhang, Q. Chen, and L.-M. Peng, *Phys. Rev. B* **73**, 094105 (2006).
- ¹⁴F. Zahariev, S. V. Dudiy, J. Hooper, F. Zhang, and T. K. Woo, *Phys. Rev. Lett.* **97**, 155503 (2006).
- ¹⁵A. R. Oganov and C. W. Glass, *J. Chem. Phys.* **124**, 244704 (2006).
- ¹⁶F. Zahariev, J. Hooper, S. Alavi, F. Zhang, and T. K. Woo, *Phys. Rev. B* **75**, 140101 (2007).
- ¹⁷R. Caracas and R. J. Hemley, *Chem. Phys. Lett.* **442**, 65 (2007).
- ¹⁸X. L. Wang, X. He, Y. M. Ma, T. Cui, Z. M. Liu, B. B. Liu, J. F. Li, and G. T. Zou, *J. Phys.: Condens. Matter* **19**, 425226 (2007).
- ¹⁹X. Q. Chen, C. L. Fu, and R. Podlucky, *Phys. Rev. B* **77**, 064103 (2008).
- ²⁰Y. Yao, J. S. Tse, and K. Tanaka, *Phys. Rev. B* **77**, 052103 (2008).
- ²¹H. Katzke and P. Toledano, *Phys. Rev. B* **78**, 064103 (2008).
- ²²J. Kotakoski and K. Albe, *Phys. Rev. B* **77**, 144109 (2008).
- ²³Y. Ma, A. R. Oganov, Z. Li, Y. Xie, and J. Kotakoski, *Phys. Rev. Lett.* **102**, 065501 (2009).
- ²⁴X. Wang, F. Tian, L. Wang, T. Cui, B. Liu, and G. Zou, *J. Chem. Phys.* **132**, 024502 (2010).
- ²⁵A. F. Schuch and R. L. Mills, *J. Chem. Phys.* **52**, 6000 (1970).
- ²⁶R. Reichlin, D. Schiferl, S. Martin, C. Vanderborgh, and R. L. Mills, *Phys. Rev. Lett.* **55**, 1464 (1985).
- ²⁷R. L. Mills, B. Olinger, and D. T. Cromer, *J. Chem. Phys.* **84**, 2837 (1986).
- ²⁸P. M. Bell, H. K. Mao, and R. J. Hemley, *Physica B & C* **139-140**, 16 (1986).
- ²⁹R. Bini, M. Jordan, L. Ulivi, and H. J. Jodl, *J. Chem. Phys.* **108**, 6849 (1998).
- ³⁰H. Olijnyk and A. P. Jephcoat, *Phys. Rev. Lett.* **83**, 332 (1999).
- ³¹A. F. Goncharov, E. A. Gregoryanz, H. K. Mao, Z. Liu, and R. J. Hemley, *Phys. Rev. Lett.* **85**, 1262 (2000).
- ³²R. Bini, L. Ulivi, J. Kreutz, and H. J. Jodl, *J. Chem. Phys.* **112**, 8522 (2000).
- ³³M. I. Eremets, R. J. Hemley, H. K. Mao, and E. Gregoryanz, *Nature (London)* **411**, 170 (2001).
- ³⁴E. Gregoryanz, A. F. Goncharov, R. J. Hemley, and H. K. Mao, *Phys. Rev. B* **64**, 52103 (2001).
- ³⁵A. F. Goncharov, E. Gregoryanz, H.-K. Mao, and R. J. Hemley, *Low Temp. Phys.* **27**, 866 (2001).
- ³⁶E. Gregoryanz, A. F. Goncharov, R. J. Hemley, and H. K. Mao, *Phys. Rev. B* **66**, 224108 (2002).
- ³⁷M. I. Eremets, A. G. Gavriliuk, I. A. Trojan, D. A. Dzivenko, and R. Boehler, *Nat. Mater.* **3**, 558 (2004).
- ³⁸M. I. Eremets, A. G. Gavriliuk, N. R. Serebryanaya, I. A. Trojan, D. A. Dzivenko, R. Boehler, H. K. Mao, and R. J. Hemley, *J. Chem. Phys.* **121**, 11296 (2004).
- ³⁹E. Gregoryanz, A. F. Goncharov, C. Sonloup, M. Somayazulu, H. Mao, and R. J. Hemley, *J. Chem. Phys.* **126**, 184505 (2007).
- ⁴⁰M. I. Eremets, A. G. Gavriliuk, and I. A. Trojan, *Appl. Phys. Lett.* **90**, 171904 (2007).
- ⁴¹T. W. Barbee III, *Phys. Rev. B* **48**, 9327 (1993).

- ⁴²C. J. Wu and L. E. Fried, *J. Phys. Chem. A* **101**, 8675 (1997).
- ⁴³J. P. Perdew, K. Burke, and M. Ernzerhof, *Phys. Rev. Lett.* **77**, 3865 (1996).
- ⁴⁴J. VandeVondele, M. Krack, F. Mohamed, M. Parrinello, T. Chassaing, and J. Hutter, *Comput. Phys. Commun.* **167**, 103 (2005).
- ⁴⁵B. M. Rice, W. Mattson, and S. F. Trevino, *Phys. Rev. E* **57**, 5106, (1998); B. M. Rice, W. Mattson, J. Grosh, and S. F. Trevino, **53**, 611 (1996); **53**, 623, (1996).
- ⁴⁶B. M. Rice, *Molecular Simulation of Detonation, in Modern Methods for Multidimensional Dynamics Computations in Chemistry*, edited by D. L. Thompson (World Scientific Press, New Jersey, 1998).
- ⁴⁷N. Goldman, E. J. Reed, I.-F. W. Kuo, L. E. Fried, C. J. Mundy, and A. Curioni, *J. Chem. Phys.* **130**, 124517 (2009).
- ⁴⁸C. J. Mundy, A. Curioni, N. Goldman, I.-F. W. Kuo, E. J. Reed, L. E. Fried, and M. Ianuzzi, *J. Chem. Phys.* **128**, 184701 (2008).
- ⁴⁹J. D. Kress, S. Mazevet, L. A. Collins, and W. W. Wood, *Phys. Rev. B* **63**, 024203 (2000); S. Mazevet, J. D. Johnson, J. D. Kress, L. A. Collins, and P. Blottiau, **65**, 014204 (2001).
- ⁵⁰F. Gygi and G. Galli, *Phys. Rev. B* **65**, 220102 (2002).
- ⁵¹M. Noyman, S. Zilberg, and Y. Haas, *J. Phys. Chem. A* **113**, 7376 (2009).
- ⁵²B. Boates and S. A. Bonev, *Phys. Rev. Lett.* **102**, 015701 (2009).
- ⁵³D. Donadio, L. Spanu, I. Duchemin, F. Gygi, and G. Galli, *Phys. Rev. B* **82**, 020102 (2010).
- ⁵⁴D. Roundy, C. R. Krenn, M. L. Cohen, and J. W. Morris Jr., *Phys. Rev. Lett.* **82**, 2713 (1999).

Optical Cell for In Situ Vibrational Spectroscopic Measurements at High Pressures and Shear

Jennifer A. Ciezak¹ and Timothy A. Jenkins²

¹ U.S. Army Research Laboratory, Aberdeen Proving Ground, MD

² National Institute for Standards and Technology, Gaithersburg, MD

ABSTRACT

An optical cell is described for performing simultaneous static high-pressure and shear experiments. This cell design is a modification of the previously designed megabar diamond anvil cell used by Mao and Bell that allows for controlled, remote shear. With this diamond anvil cell, it is possible to use a wide range of existing experimental techniques and pressure media. The cell was validated on a sample of calcite at 5 kbar. Raman measurements show the onset of the phase transformation from calcite to aragonite at 10° of rotation.

Review of Scientific Instruments 82, 073905 (2011)

Optical cell for *in situ* vibrational spectroscopic measurements at high pressures and shear

Jennifer A. Ciezak^{1,a)} and Timothy A. Jenkins²

¹US Army Research Laboratory, RDRL-WML-B (Building 390), Aberdeen Proving Grounds, Maryland 21005, USA

²NIST Center for Neutron Research, 100 Bureau Drive, MS 6100, Gaithersburg, Maryland 20899, USA

(Received 19 May 2011; accepted 2 June 2011; published online 19 July 2011)

An optical cell is described for performing simultaneous static high-pressure and shear experiments. This cell design is a modification of the previously designed megabar diamond anvil cell used by Mao and Bell that allows for controlled, remote shear. With this diamond anvil cell, it is possible to use a wide range of existing experimental techniques and pressure media. The cell was validated on a sample of calcite at 5 kbar. Raman measurements show the onset of the phase transformation from calcite to aragonite at 10° of rotation. [doi:10.1063/1.3606640]

I. INTRODUCTION

The diamond anvil cell, developed over 50 years ago^{1,2} is a ubiquitous, versatile tool for the study of materials subjected to thermomechanical extremes of pressure, temperature, and stress. In recent years, a broad range of diamond anvil cells have been designed and adapted for numerous experimental techniques, such as laser heating, NMR, magnetic measurements, and synchrotron-based experiments, the results of which have revealed new fundamental knowledge within physics, chemistry, and materials science.³

While the phase behavior of materials subjected to quasi-hydrostatic pressure and temperature has been extensively examined since the inception of the diamond anvil cell, it is primarily only in the last 15 years that the effect of nonhydrostatic pressure and its resulting deviatoric stress on material behavior have been examined. X-ray diffraction along the radial direction of the diamond anvil cell has been previously used to examine the elastic and rheological properties of materials^{4,5} as a function of pressure, but such techniques do not allow for *in situ* control of the stresses within the cell. Such capability is only possible with a rotational (or shear) diamond anvil cell, which permits rotation of one diamond anvil perpendicular to the axis of compression, while the second anvil remains fixed. Originally designed by Bridgman in the 1930s with tungsten carbide anvils,⁶ the rotation of one anvil relative to the fixed anvil generates additional shear stress and strain on the sample, resulting in severe plastic deformation. The modification of the early Bridgman design to substitute diamond anvils made exploration of the material response to pressure and shear possible using the numerous experimental probes available for diamond anvil cells. Several measurements of utilizing this type of diamond anvil cell have been reported during the past two decades;^{7–21} these reports have studied phase behavior in semiconductors,^{7,8} C₆₀ fullerene,⁹ sodium azide²¹ as well as elements¹⁰ and energetic materials.¹⁹

Despite the critical scientific insight provided by such experiments, rotational diamond anvil cells are not widely avail-

able. Here we report on a rotational adaptation of the widely used Mao–Bell megabar cell,²² which provides a robust experimental apparatus capable of generating simultaneous high pressure and shear. The shear capabilities of the cell can be used to pressures exceeding 50 GPa and, although not detailed in this paper, to temperatures beyond 2500 K. Additionally, unlike previous designs,^{7–21} the rotational capability can be precisely controlled via an encoded motor. To illustrate the room temperature capabilities of the cell, *in situ* Raman spectroscopic measurements of calcite at elevated pressures and shear are presented.

II. CELL DESIGN AND USE

A cross section of the major components of the assembled rotational diamond anvil cell (RDAC) is shown in Fig. 1. The main body of the RDAC, made of *Vascomax T-250 steel*,²³ is an adaptation of the Mao–Bell megabar cell²² with additional gearing for use in rotational shear experiments. The additional gearing enables the rotation of the piston anvil relative to the fixed cylinder anvil. Using a set screw, the position and orientation of the cylinder can be fixed to prevent concurrent rotation with the piston. A minimum clearance of 7 μm between the piston and cylinder was necessary to maintain anvil alignment while allowing unhindered rotation of the piston. Careful machining of the piston and cylinder is required to allow for unhindered rotation. Polished tungsten carbide disks with highly parallel flat faces were used as diamond anvil mounts and fixed positionally with set screws to prevent rotation. The diamonds are then attached to the tungsten carbide mounts with epoxy resin and aligned similar to a conventional diamond anvil cell. The preparation of the RDAC for experimental measurements is similar to that of traditional diamond anvil cells and the cell can be with any experimental technique adapted for use with the Mao–Bell megabar cell.²²

The lever arm and body assembly are constructed of *Vascomax T-250 steel* (Ref. 23) and have dimensions comparable to previous designs. The lever arm is designed to smoothly compress the piston and cylinder under a uniform

^{a)}Electronic mail: Jennifer.ciezak@us.army.mil.

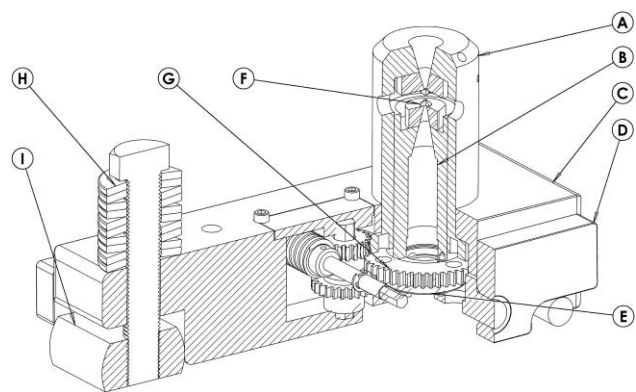


FIG. 1. Cutaway view of rotational DAC. A indicates the diamond anvil cylinder, B is the diamond anvil piston, C is the cell body, D is the lever arm, E is the thrust bearing, F is the diamonds and tungsten carbide mounts, G is the gear assembly for the rotational cell, H is the Bellville washer and bolt assembly, and I is threaded load block for loading the lever arms.

load. Rotation of the cylinder occurs via the additional gearing, as detailed in Fig. 2; a worm gear, with a worm gear to cylinder ratio of 180:1, was chosen both for space constraints and its anti-backlash capabilities. The worm gear shaft can be easily interfaced with an encoded motor drive system to allow for both precision control of the rotation and remote usage. Similar to the conventional Mao–Bell megabar cell,²² the RDAC is pressurized by tightening a half inch hex bolt with Belleville spring washers stacked in an alternating direction with the lever arms yielding a force multiplier of 5.25. To facilitate the rotation of the piston, a thrust bearing is used in conjunction with the thrust block. The thrust bearing is seated in a centering mount on the thrust block and allows for removal of washers and screws that may be employed during gas loading applications.^{24,25}

In the RDAC design, the maximum pressure is limited by the thrust bearing, which, with a rotational speed of 50 rpm, allows for upward of 50 GPa of pressure on 100 μm diameter diamond culets. As rotational speed increases, the available pressure decreases. Without the use of the thrust bearing the cell operates similar to a conventional Mao–Bell megabar cell,²² with the maximum pressure dictated by the culet size of the diamond anvils.

III. *IN SITU* RAMAN SPECTROSCOPIC MEASUREMENTS

To demonstrate the capabilities of the rotational diamond anvil cell, Raman spectra were collected for polycrystalline calcium carbonate ($\geq 99\%$) (Calcite-I) using Type I diamond anvils with 800 μm culets. A 600 μm sample well was drilled via electron discharge machining into a rhenium gasket, which was preindented to a thickness of 100 μm and then mounted on the diamond culet. The *in situ* pressure was monitored during the experimental measurements using the ruby fluorescence method, which correlates the Raman spectroscopic shifts of the R_1 and R_2 lines of ruby to a well-defined equation of state.²⁶ High-pressure Raman spectroscopic experiments were performed in backscattering geometry utilizing the 473 nm line of a cw diode pumped solid state laser as the excitation source, with an output power of ~ 50 mW. A 500 mm focal length $f/6.5$ imaging spectrograph equipped with an 1800 grooves/mm grating and a resolution of ± 0.5 cm^{-1} was used. The intensities of all Raman spectra were normalized and truncated at 1200 cm^{-1} as the first order scattering of diamond precluded definitive identification of the fundamental Raman active mode near 1430 cm^{-1} .

The Raman spectrum of calcite at ambient conditions is well known and characterized.^{27–29} At ambient pressure, calcite has five fundamental Raman active modes attributed to two sets of doubly degenerate E_g modes near 155, 280, 710, and 1430 cm^{-1} and an intense A_{1g} mode near 1085 cm^{-1} .²⁹ Representative Raman spectra of calcite collected upon only isothermal compression at room temperature within the rotational diamond anvil cell to near 20 kbar are presented in Fig. 3. At ambient pressure, four of the five fundamental Raman-active modes of calcite-I are observed A_{1g} (~ 1085 cm^{-1}) + 3 E_g (712 cm^{-1} , 282 cm^{-1} , and 151 cm^{-1}) with vibrational frequencies nearly identical to those previously reported.^{27–29} Upon compression, the bands shift nearly linearly to pressures approaching 17 kbar (Fig. 4). At 17 kbar, several modifications in the spectral pattern were discerned which are associated with the well documented calcite \rightarrow aragonite transition. The fundamental E_g Raman mode of the CO_3 bending mode splits into two resolvable maxima near 703 and 710 cm^{-1} (inset Fig. 3). At pressures above the transition, one new phonon band appears in the spectrum of aragonite near 190 cm^{-1} and the spectral intensity of the band

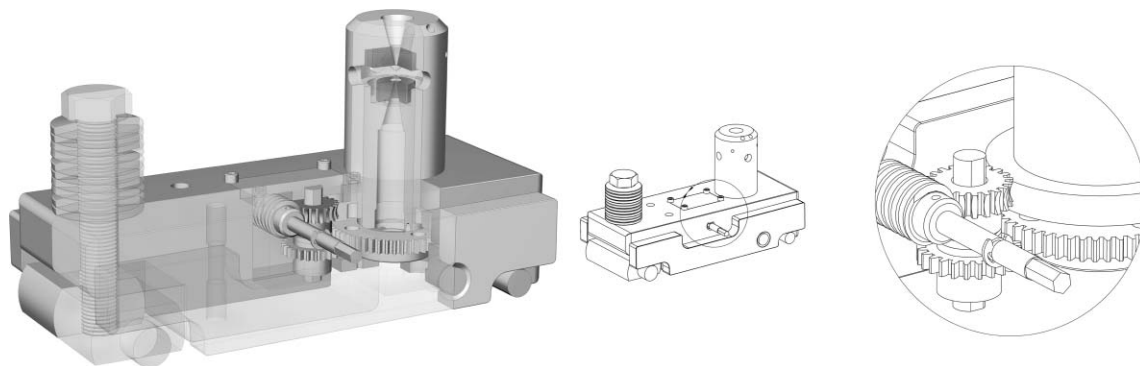


FIG. 2. Cutaway view of rotational diamond anvil design, showing the gearing in relation to the typical megabar cell.

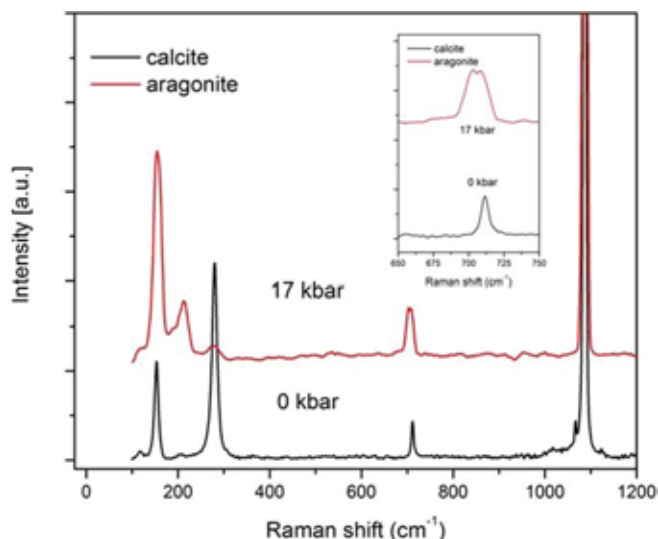


FIG. 3. (Color online) *In situ* Raman spectra of calcium carbonate obtained upon compression in the RDAC. During these experiments, the rotational capability of the RDAC was not used. The inset shows the splitting of the E_g bending mode that occurs upon the calcite – aragonite transition. Spectra are normalized with respect to spectral intensity but offset for clarity.

$\sim 215 \text{ cm}^{-1}$ significantly increases. The band which appears in the calcite spectrum near 215 cm^{-1} has not been previously observed,^{27–29} so it is likely the sample used for the experiments detailed herein contained a small aragonite impurity. Additionally, the appearance of two bands between 190 and 225 cm^{-1} suggests there may also be a concentration of vaterite (calcite-III). Upon decompression, no barrier to hysteresis was observed and the polymorphic phase transformation was reversible.

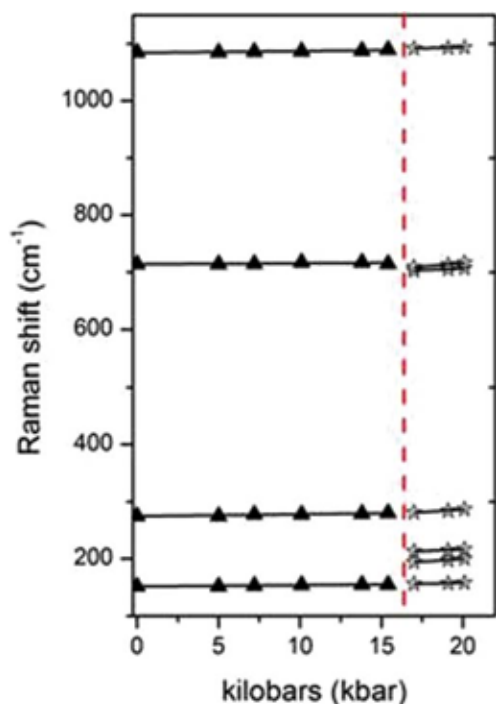


FIG. 4. (Color online) Pressure dependence of the fundamental Raman active modes of calcite. Dashed lines indicate apparent phase boundaries. Linear fits are shown for the frequency shifts.

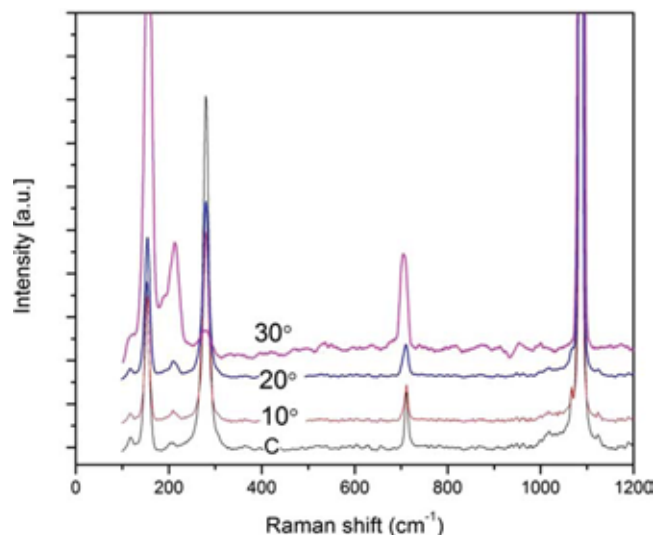


FIG. 5. (Color online) *In situ* Raman spectra of calcium carbonate held at 5 kbar and subjected to rotation (shear) in the RDAC. The degree of rotation corresponds to the rotation of the piston anvil. Spectra are normalized with respect to spectral intensity but offset for clarity.

Representative Raman spectra of calcite held at 5 kbar and then subjected to incremental degrees of rotation, and thus shear, within the rotational diamond anvil cell are presented in Fig. 5. At the low pressures studied by these experiments, rotation of the anvil did not change the *in situ* pressure appreciably, concurrent with previous observations.²⁰ A comparison of the integrated spectral intensity of the vibrational feature near 215 cm^{-1} observed during rotation and that present at ambient conditions indicates the onset of the calcite \rightarrow aragonite transition is near 10° at 5 kbar. When the anvil was rotated 30° relative to its normal, the resulting Raman spectrum was nominally identical to the spectrum of aragonite obtained at 17 kbar and shown in Fig. 3. Upon decompression, only the pressure was manually released and interestingly the transition was found to be irreversible, suggesting frictional hysteresis may be associated with the shear transition.

IV. CONCLUSION

A diamond anvil cell capable of generating simultaneous high pressure and shear for optical spectroscopies has been developed. The cell can be pressurized to 50 GPa with full 360° of rotation of the piston anvil relative to the fixed cylinder anvil, which is locked into position with a set screw. An encoded motor can be attached to the worm gear shaft which controls the degree of rotation for precision measurements. Raman spectroscopic measurements of the shear induced phase transitions of calcite were used to demonstrate the capabilities of the RDAC under combined pressure and shear.

¹C. E. Weir, E. R. Lippincott, A. V. Valkenburg, and E. N. Bunting, *J. Res. Natl. Bur. Stand.* **63A**, 55 (1959).

²J. C. Jamieson, A. W. Lawson, and N. D. Nachtrieb, *Rev. Sci. Instrum.* **30**, 1016 (1959).

³W. A. Basset, *High Press. Res.* **29**, 163 (2009).

- ⁴H. K. Mao, J. F. Shu, G. Shen, R. J. Hemley, B. Li, and A. K. Singh, *Nature (London)* **396**, 741 (1998).
- ⁵T. S. Duffy, G. Shen, D. L. Hein, J. Shu, Y. Ma, H.-K. Mao, and R. J. Hemley, *Phys. Rev. B* **60**, 15063 (1999).
- ⁶P. W. Bridgman, *Phys. Rev.* **48**, 825 (1935).
- ⁷M. M. Alexandrova, V. D. Blank, A. E. Golobokov, Y. S. Konyaev, and E. I. Estrin, *Solid State Phys.* **29**, 2573 (1987).
- ⁸N. R. Serebryanaya, V. D. Blank, and V. A. Ivdenko, *Phys. Lett. A* **197**, 63 (1995).
- ⁹V. D. Blank, M. Popov, S. G. Buga, V. Davydov, V. N. Denisov, A. N. Ivlev, B. N. Mavrin, V. Agafonov, R. Ceolin, H. Szwarc, and A. Passat, *Phys. Lett. A* **188**, 281 (1994).
- ¹⁰M. M. Alexandrova, V. D. Blank, and S. G. Buga, *Solid State Phys.* **35**, 1308 (1993).
- ¹¹N. V. Novikov, S. B. Polotnyak, L. K. Shvedov, and V. I. Levitas, *J. Superhard Mater.* **21**, 36 (1999).
- ¹²V. D. Blank, Y. Y. Boguslavski, M. I. Eretnetz, E. S. Izkevich, Y. S. Konyaev, A. M. Shirokov, and E. I. Estrin, *JETP* **87**, 922 (1984).
- ¹³V. I. Levitas, J. Hashemi, and Y. Z. Ma, *Europhys. Lett.* **68**, 550 (2004).
- ¹⁴V. I. Levitas, Y. Z. Ma, and J. Hashemi, *Appl. Phys. Lett.* **86**, 071912 (2005).
- ¹⁵V. I. Levitas and L. K. Shvedov, *Phys. Rev. B* **65**, 104109 (2002).
- ¹⁶V. I. Levitas, *J. Mech. Phys. Solids* **45**, 923 (1997).
- ¹⁷V. I. Levitas, *Phys. Rev. B* **70**, 184118 (2004).
- ¹⁸Y. Ma, V. I. Levitas, and J. Hashemi, *J. Phys. Chem. Solids* **67**, 2083 (2006).
- ¹⁹P. Hébert, A. Isambert, J.-P. Petitot, and A. Zerr, *High Press. Res.* **30**, 24 (2010).
- ²⁰V. I. Levitas, Y. Ma, J. Hashemi, M. Holtz, and N. Guven, *J. Chem. Phys.* **125**, 044507 (2006).
- ²¹M. Popov, *Phys. Lett. A* **334**, 317 (2005).
- ²²H. K. Mao and P. M. Bell, *Design and Varieties of the Megabar Cell* (Year Book, Carnegie Institute, Washington, D.C., 1978), Vol. 77, p. 904.
- ²³Certain commercial equipment, instruments, or materials are identified in this paper to foster understanding. Such identification does not imply recommendation or endorsement by the National Institute of Standards and Technology nor does it imply that the materials or equipment identified are necessarily the best available for the purpose.
- ²⁴R. L. Mills, D. H. Liebenberg, J. C. Bronson, and L. C. Schmidt, *Rev. Sci. Instrum.* **51**, 891 (1980).
- ²⁵A. Jayaraman, *Rev. Mod. Phys.* **55**, 65 (1983).
- ²⁶C. S. Zha, H. K. Mao, and R. J. Hemley, *Proc. Natl. Acad. Sci. U.S.A.* **97**, 13494 (2000).
- ²⁷M. Y. Fong and M. Nicol, *J. Chem. Phys.* **54**, 579 (1971).
- ²⁸P. Gillet, J.-M. Malezieux, and M.-C. Dhamelincourt, *Bull. Mineral.* **111**, 1 (1988).
- ²⁹L.-G. Liu and T. P. Mernagh, *Am. Mineral.* **75**, 801 (1990).

The First Launch of an Autonomous Thrust-Driven Microrobot Using Nanoporous Energetic Silicon

Wayne A. Churaman¹, Luke J. Currano¹, Christopher J. Morris¹,
Jessica E. Rajkowski², and Sarah Bergbreiter³

¹ U.S. Army Research Laboratory, Adelphi, MD

² Currently with The Mitre Corporation, McLean, VA

³ Department of Mechanical Engineering, University of Maryland,
College Park, MD

ABSTRACT

As the capability and complexity of robotic platforms continue to evolve from the macro to the micron scale, the challenge of achieving autonomy requires the development of robust, lightweight architectures. These architectures must provide a platform upon which actuators, control, sensing, power, and communication modules are integrated for optimal performance. In this paper, the first autonomous jumping microrobotic platform is demonstrated using a hybrid integration approach to assemble on-board control, sensing, power, and actuation directly onto a polymer chassis. For the purposes of this paper, jumping is defined as brief parabolic motion achieved via an actuation pulse at takeoff. In this paper, the actuation pulse comes from the rapid release of chemical energy to create propulsion. The actuation pulse lasts several microseconds and is achieved using a novel high-force/low-power thrust actuator, nanoporous energetic silicon, resulting in 250 μJ of kinetic energy delivered to the robot and a vertical height of approximately 8 cm.

Journal of Microelectromechanical Systems, Volume 21, Number 1,
pages 198-205 (2012)

The First Launch of an Autonomous Thrust-Driven Microrobot Using Nanoporous Energetic Silicon

Wayne A. Churaman, Luke J. Currano, *Member, IEEE*, Christopher J. Morris, *Member, IEEE*,
Jessica E. Rajkowski, and Sarah Bergbreiter, *Member, IEEE*

Abstract—As the capability and complexity of robotic platforms continue to evolve from the macro to the micron scale, the challenge of achieving autonomy requires the development of robust, lightweight architectures. These architectures must provide a platform upon which actuators, control, sensing, power, and communication modules are integrated for optimal performance. In this paper, the first autonomous jumping microrobotic platform is demonstrated using a hybrid integration approach to assemble on-board control, sensing, power, and actuation directly onto a polymer chassis. For the purposes of this paper, jumping is defined as brief parabolic motion achieved via an actuation pulse at takeoff. In this paper, the actuation pulse comes from the rapid release of chemical energy to create propulsion. The actuation pulse lasts several microseconds and is achieved using a novel high-force/low-power thrust actuator, nanoporous energetic silicon, resulting in 250 μJ of kinetic energy delivered to the robot and a vertical height of approximately 8 cm. [2011-0030]

Index Terms—Autonomy, microrobot, porous silicon.

I. INTRODUCTION

SMALL autonomous robotic platforms hold the potential to help target the efforts of first responders, provide stealthy surveillance, or add mobility to sensor networks. However, existing microrobot platforms have limited autonomy [1]–[11]. Autonomous microrobot platforms require essential components including sensors, actuators, electronic circuits, and a power supply. These components must further be integrated to provide certain essential functions including conversion of sensor data to actionable information, intelligence to make decisions based on the information, and mobility to take action on the decisions. Integration of sensing, control, power, and actuation on a single chassis increases the utility of robots, allowing them to be placed in environments where they can sense, think, and act with limited or no human intervention [1]–[5]. These enabling features of autonomy lead to robots that

will eventually traverse environments unreachable by humans, while providing critical data, and the ability to adapt to ever changing surroundings.

As robot length scales decrease below the centimeter scale, it becomes an increasing challenge to integrate systems to deliver complex functionality on a single platform. Larger robots like RoACH [6] or Alice [7] are assembled using commercial off-the-shelf (COTS) components including motors, sensors, and electronics with little difficulty. Application-specific integrated circuits (ASICs) provide a unique approach to developing control architectures for millimeter scale platforms by reducing the chip area [5]. This paper will take a new hybrid integration approach that includes both custom fabrication (similar to the bottom-up design of ASICs) and COTS components (similar to simple assembly available to larger robots).

Recent work in microrobotics has made progress toward achieving autonomous functionality, which the authors define as the integration of sensing, actuation, power, and control on a single chassis. These characteristics are available to the robot independent of the operating environment. A number of the published microrobots can be characterized as “actuator only” platforms because they rely on a controlled operating environment to function, cannot make decisions based on the environment, and cannot carry their power supply. The microrobot in [8] maneuvers using an integrated scratch drive actuator and a cantilever steering arm, allowing it to achieve speeds greater than 200 $\mu\text{m}/\text{sec}$. The operation of the microrobot depends on an underlying electrical grid, which provides power and control. The “walking chip” in [9], designed to carry a maximum external load of 2.5 g on its back, relies on external power in the form of tethered wires that measure up to 10 cm in length and lacks sensing and on-board control. The bio-inspired fly in [10] demonstrates insect-like wing trajectories with integrated actuation and mechanics, but does not yet possess integrated on-board sensing, power, or control.

The complexity of the design and integration increases as more functionality is incorporated directly onto the chassis. The microrobot in [11] appears to come close to our definition of autonomy using solar cells for power, electrostatic motors for actuation, and a CMOS finite state machine for control. These components are fabricated individually and integrated using a hybrid approach involving wirebonding to electrically connect each component. However, the robot does not have integrated sensors to allow it to observe and react to changes in the environment. The only robots that appear to include all components necessary for individual autonomy are several centimeters in size or larger [6], [12].

Manuscript received January 28, 2011; revised September 23, 2011; accepted September 28, 2011. Date of publication December 5, 2011; date of current version February 3, 2012. This work was supported by the U.S. Army Research Laboratory. This work was also supported in part by the National Science Foundation under Award CNS0931878. Subject Editor C. Mastrangelo.

W. A. Churaman, L. J. Currano, and C. J. Morris are with the U.S. Army Research Laboratory, Adelphi, MD 20783 USA (e-mail: wayne.a.churaman.civ@mail.mil; luke.j.currano.civ@mail.mil; christopher.j.morris58.civ@mail.mil).

J. E. Rajkowski is with the University of Maryland, College Park, MD 20783 USA. She is now with The Mitre Corporation, McLean, VA 22102 USA (e-mail: jrajkowski@mitre.org).

S. Bergbreiter is with the Mechanical Engineering Department, University of Maryland, College Park, MD 20783 USA (e-mail: sarahb@umd.edu).

Color versions of one or more of the figures in this paper are available online at <http://ieeexplore.ieee.org>.

Digital Object Identifier 10.1109/JMEMS.2011.2174414

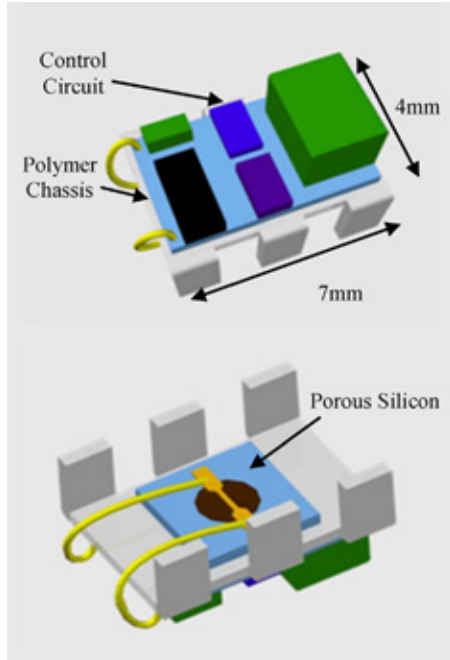


Fig. 1. Computer model of jumping microrobot showing the polymer chassis and control circuit. The energetic thrust actuator is underneath, on the “belly” of the robot.

While these microrobots have demonstrated ingenious functionality, the goal remains to develop a platform that is truly autonomous, where all required functionality is provided on-board the microrobotic platform. To overcome the challenges associated with implementation and integration on a sub-centimeter scale, the authors have developed a novel hybrid integration approach to fabricate a microrobotic platform, conceptually shown in Fig. 1. The microrobotic platform is designed with a polymer chassis, upon which micron-scale electrical traces are lithographically defined and patterned to integrate power (capacitors), sensing (a phototransistor), and the most rudimentary form of decision making (a single transistor). Nanoporous energetic silicon, a solid energetic formulation that produces gas when ignited [13], [14], functions as a thruster to provide mobility. The nanoporous energetic silicon is mounted underneath the polymer chassis. The microrobotic platform can detect a change in the ambient light and respond to the change by triggering ignition of the energetic material. This produces an upward thrust.

This work offers two key contributions toward greater autonomy in microrobotics along with a demonstration of this autonomy. First, a novel energetic silicon-based actuator is proposed to enhance mobility (Section II). Mobility is demonstrated in the form of vertical thrust as stored chemical energy is rapidly converted to mechanical energy. While only a single propulsion event is demonstrated, the nanoporous energetic silicon can be arrayed on-chip to provide multiple propulsion events in different directions. The second contribution develops a hybrid integration approach used to mechanically and electrically integrate this actuator with sensing and control elements (Section III). The integration of on-chip, chemical-based actuation with electronic controls results in sufficient autonomy for applications ranging from mobile sensor networks to dynam-

TABLE I
PHYSICAL DIMENSIONS OF SYSTEM COMPONENTS
USED TO DESIGN THE HEXAPOD

Component	Mass (mg)	Footprint Dimensions
10uF cap	9	0.8 x 1.6 mm ²
100uF cap	133	2.6 x 3.4 mm ²
FET	8	2.9 x 1.3 mm ²
Phototransistor	3	1.2 x 2.0 mm ²
10k resistor	5	1.5 x 0.8 mm ²
Chassis w/ alloy	62-69	4.0 x 7.0 mm ²
Silicon chip	22-28	4.0 x 4.0 mm ²
Metal pads	14-18	n/a
Wires	11-15	n/a
Extra polymer	13-36	n/a

ically controlled microthrusters. These two contributions are combined to demonstrate the first robot at this size scale with the ability to sense, think, and act (Section IV).

II. SYSTEM ARCHITECTURE

The goal for the microrobot system architecture was to develop a robotic platform that could sense a change in light intensity and respond by jumping. To simplify matters, the microrobot would jump vertically with a takeoff angle of 90° rather than follow a particular direction. To accomplish this goal, the system architecture required a sensor, control circuit, actuator, and power, each of which needed to be integrated on a polymer chassis. The electronics were designed and fabricated with COTS parts to provide both on-board power and logic to sense a change in light intensity and to provide an electrical stimulus to trigger the energetic material. Table I summarizes the size and weight of each of the components of the system, and the following subsections describe in detail the function of each part. The total mass of the assembled system was approximately 300 mg. In our experiments, three hexapods were assembled and tested. The overall mass of the hexapod varied from 280 mg to 318 mg across the platforms that were assembled. The largest contributor to this variation in mass was an additional layer of polymer that was applied to the hexapod once it was assembled to encapsulate the IC components and increase the robustness of the robot.

A. Actuation

Instead of using a mechanical spring to store energy as seen in [15], nanoporous energetic silicon was chosen to store and release energy chemically. The primary benefit to this approach is reduced complexity and lower part count due to eliminating the need for a separate electrically controlled actuator to compress a spring. Nanoporous energetic silicon is formed in an electrochemical etch process as outlined in [13]. It is initially inert, and only becomes energetic when infused with an oxidizer such as sodium perchlorate. The exothermic reaction can be triggered with heat, friction, or focused light. Multiple actuators can be integrated onto the chassis of a microrobot, allowing it to achieve multiple jumps in different directions. For this work, actuation was demonstrated using a single, 2 mm diameter region of nanoporous energetic silicon.

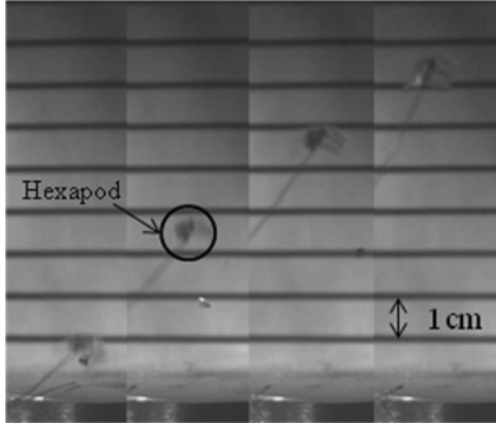


Fig. 2. Tethered jump of 100-mg hexapod platform, tethered by 12-mil wire. The images are spaced 10 frames (10 ms) apart. In frames 1–3, a portion of the silicon chip detached from the hexapod.

Propulsion of a hexapod platform was demonstrated using the nanoporous energetic silicon. Fig. 2 shows an initial (tethered) experiment with a 2 mm diameter, 40 μm thick volume of nanoporous energetic silicon incorporated on the polymer hexapod chassis [16]. The nanoporous silicon was attached to the underside of the hexapod, and connected via wires to an external DC power supply. The components of the control circuit were not attached to the hexapod in this experiment, resulting in a significantly lower system mass. Including the wire leads and the energetic silicon chip, the hexapod weighed 100 mg in this configuration. The hexapod travelled up out of the ~ 11 cm field of view. The takeoff velocity was measured at 2.8 m/s from high-speed video frames captured at 1000 frames/s. Based on this, the projected jump height was 40 cm. This experiment showed that nanoporous energetic silicon is a viable actuator for a jumping robot, so the authors proceeded to integrate sensing, control, and power functions onto the chassis.

B. Sensing and Control

The microrobotic platform is designed to jump in response to “seeing” a change in light level, as an insect which may jump in response to sensing the shadow of a predator. Sensing is achieved using a light-sensitive phototransistor (SFH3710) shown in Fig. 3. The space available to integrate electronic control, sensing, and actuation is limited to the top and bottom of the chassis, approximately 56 mm² total area. The top of the chassis is used to integrate a circuit composed of five discrete surface-mount components (shown in Fig. 3), while the underside of the chassis houses the energetic material used for actuation. The control circuit itself consists of a 2N7002, single n-channel enhancement MOSFET, and a 10 k Ω resistor used to bias the gate of the MOSFET.

The spectral sensitivity of the NPN phototransistor chosen is 350 nm to 950 nm with a maximum sensitivity at 570 nm. When the lighting condition is varied from an illuminance of ~ 0.3 lux, which is comparable to a full moon on a clear night [17], to approximately 26 lux, somewhat less than the illuminance of a family room [18], the voltage at the gate of the MOSFET rises to 5 V. This closes the MOSFET transistor.

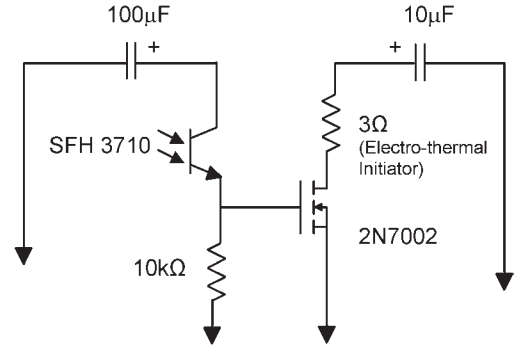


Fig. 3. Circuit designed to provide sensing and actuation. The 3 Ω resistor represents the hotwire used to ignite the energetic material.

A series connection of a 10 μF capacitor and 3 Ω resistor with the MOSFET is shown in Fig. 3. The 3 Ω resistor is used to model the electrical characteristics of an electrothermal initiator used to ignite the energetic material. Details about the electrical initiator design and performance are discussed in [13]. The 10 μF capacitor is precharged to 6 V for the experiments discussed here. As the MOSFET closes, it provides a path for current to flow through the electrical initiator, producing heat to ignite the energetic material. The electrothermal initiator requires at least 150 mA to ignite the energetic material. However, it should be noted that this current is only required for at most 100 μs . In this system, the capacitor discharges directly through the electrothermal initiator wire, without voltage or current regulation. This arrangement simplifies the circuit, reduces the part count, and is sufficient to ignite the energetic silicon.

C. Power

The two capacitors shown in Fig. 3 provide power to the phototransistor and the initiator on the nanoporous energetic silicon. The 100 μF capacitor provides power to bias the phototransistor. The 10 μF capacitor is used to provide power to ignite the nanoporous energetic silicon once the phototransistor detects the increase in light intensity. Both the 100 μF and 10 μF capacitors in Fig. 3 are precharged to 6 V. Both power sources are isolated until an event is detected, triggering the actuation response. A larger capacitor is chosen to power the phototransistor to increase the time constant and supply a larger amount of energy to accommodate leakage. While the longevity of the capacitors as power sources is not investigated in detail, the 100 μF capacitor is able to retain sufficient charge to power the phototransistor for up to 8 min in a dimly lit room (~ 0.3 lux). While the expected discharge time, based on the off-state resistance, for the phototransistor and the FET is approximately 40 min, a significant amount of leakage current across the phototransistor results from exposure to the low-level ambient light. It should be noted that the 100 μF capacitor used to bias the phototransistor is the heaviest single part of the robot (Table I), with the much smaller capacitor only acting to initiate the energetic material. In the future, the requirement for this larger capacitor may be removed through better sensors or through the use of a low-volume, high-capacity thin film battery. The energy associated with the capacitors and the nanoporous energetic silicon is summarized in Table II.

TABLE II
SUMMARY OF ENERGY SUPPLIED BY THE CAPACITORS AND
ENERGY SUPPLIED TO AND GENERATED BY THE
NANOPOROUS ENERGETIC SILICON

Component	Type of Energy	Energy
10 μF Capacitor	Electrical	0.18 mJ
100 μF Capacitor	Electrical	1.8 mJ
Energetic Porous Si	Electrical (ignition)	0.18 mJ
Energetic Porous Si	Chemical	1.9 J

III. HYBRID INTEGRATION

To electrically and mechanically integrate the sensing, power, and control components with the actuator and robot chassis with minimal added mass, a new hybrid integration process was designed. This approach used a polymer chassis for structural support to carry a payload as well as a substrate for electrical traces for the integration of the control circuit.

A. Polymer Chassis

The hexapod style chassis was chosen to enable walking in future iterations of the platform, and the polymer was chosen for robustness, durability, light weight, and ease of fabrication. The chassis provided the robot's functional skeleton as well as a point of assembly on which to integrate all other components in this hybrid integration approach (Fig. 1). It is 4 mm by 7 mm by 0.5 mm in dimensions and was fabricated using a rapid prototyping process [19]. A photodefinable polymer (Loctite3525 modified acrylic) was first spread evenly on a transparent plastic sheet, and another transparent sheet was placed on top of the polymer film. Glass slides were placed between the two sheets to define the thickness. A photolithographic mask, with the hexapod features defined as clear windows in an opaque field, was then placed on top, and UV light was used to expose the hexapod features through the mask. The exposed polymer was hardened, and the unexposed polymer could then be removed with a methanol rinse. The metal traces for assembly of the control circuit were deposited and patterned (described in the following section), then the legs were bent out of plane, and an additional layer of polymer, [shown in Fig. 4(c)], was applied to the inside corner between the legs and the body and cured. This resulted in the 3-D hexapod structure similar to that in Fig. 4(d), which allows for future integration of leg actuators for bimodal (walking/jumping) mobility or to orient the robot for a jump in a particular direction.

B. Metallization

A copper film was deposited on top of the polymer chassis using metal evaporation at room temperature. Once deposited, the electrical traces were lithographically patterned on the copper film. With photoresist protecting the underlying copper metal traces, the exposed copper was etched using a 2:1 mixture of water to nitric acid. To facilitate attaching the circuit elements to a flexible substrate, the copper traces were then coated with a low melting temperature solder (Indalloy 117 from Indium Corporation) using a dipping process discussed

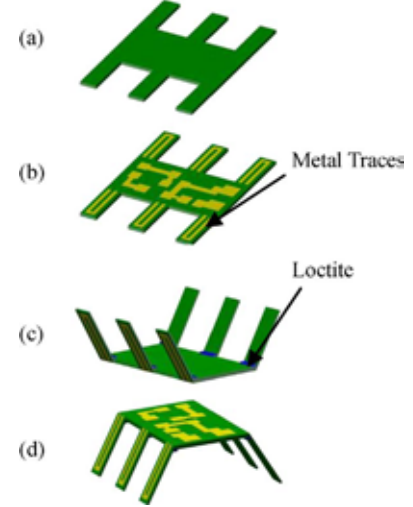


Fig. 4. Process flow to fabricate 3-D hexapod structure. This process flow shows metal patterned on the legs. For the purpose of our experiment, metal was only patterned on the body.

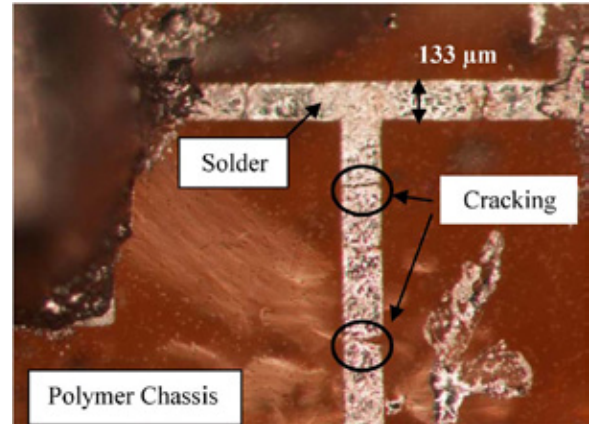


Fig. 5. Metalized layer begins to crack when submerged in low-temperature solder. Copper traces were subsequently widened to 472 μm to allow enough solder to heal the cracks.

in [20]. Indalloy 117 melts at 47 $^{\circ}\text{C}$, and was chosen because the Loctite polymer softens above 100 $^{\circ}\text{C}$ and using a solder iron to heat the solder would result in damage to the polymer substrate. The circuit components can be attached by reflowing the low-temperature solder without damaging the substrate. For this process, the solder was kept at 65 $^{\circ}\text{C}$ to ensure the robustness of the polymer chassis. A mixture of ethylene glycol and hydrochloric acid was added to the solder dipping crucible to remove any surface oxides on the copper traces and on the solder. The polymer chassis was slowly submerged into the molten alloy, and retracted after 10 s. About 50% of the time, a visual inspection revealed incomplete coating, and the chassis was submerged again to coat all copper traces. Initial results indicated a tendency for the copper layer to crack when cooling after removal from the solution, as shown in Fig. 5. Therefore, the minimum copper feature size was increased from 133 μm to 472 μm , providing greater surface area to capture enough solder to "heal" any cracks that form.

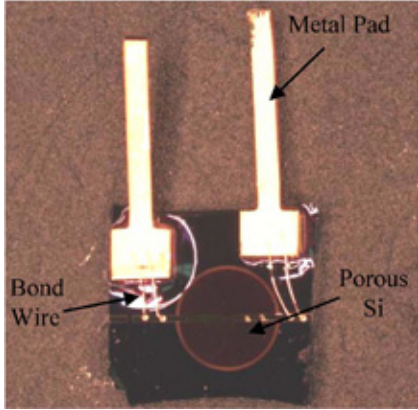


Fig. 6. Metal bond pads fixed to Si allow the energetic to be connected to the control circuit.

C. Assembly

A serial process was used to assemble each of the components. The hexapod and circuit components were separately coated with the low melting temperature alloy. A solder iron was used to manually solder external wires to the capacitors and the MOSFET before the components were assembled onto the hexapod chassis. This allowed electrical leads to be easily attached to charge the capacitor power sources after assembly. The polymer hexapod was then placed on a hotplate at 65 °C to melt the Indalloy, and the circuit components were positioned using tweezers. Moderate pressure was applied manually between the component and the binding site to ensure a robust connection. The hexapod was then removed from the hotplate and allowed to cool. As the polymer substrate cooled, the circuit components were fused to the binding sites.

Attempts to solder directly to the energetic porous silicon chip were unsuccessful because the thin-film initiator was not robust enough to withstand the heat of a soldering iron. The low melting temperature alloy was not attempted because of concern that the dipping process might contaminate the nanoporous silicon. Although it was possible to wirebond to the silicon chip, wirebonding to the polymer chassis was not successful because the polymer was too soft. Therefore, gold-plated metal pads shown in Fig. 6 were glued to the silicon chip, and wirebonds were made between the integrated initiator and the metal pads. Wires were then soldered between the control circuit and these metal pads, and the nanoporous energetic silicon was attached to the underside of the hexapod using a double-adhesive tape. In future iterations, the pads could be eliminated by creating vias in the polymer chassis and the nanoporous silicon substrate and filling them with metal for direct connection using the low-temperature solder.

Once the hexapod was assembled, the circuit and underlying electrical traces were coated with an additional layer of Loctite to prevent delamination of the rigid circuit elements from the flexible polymer skeleton. This robust integration allowed the hexapod legs to be flexed and potentially actuated out of plane, without disturbing the functionality of the circuit. This unique process therefore uses one material as the mechanical structure, electrical substrate, and packaging material for the microrobotic

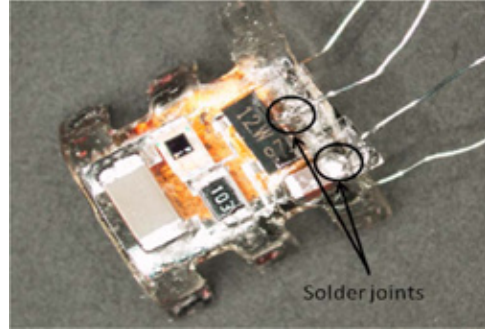


Fig. 7. Metal bond pads soldered to wires coming off of the capacitor and MOSFET.

platform. Fig. 7 shows a circuit that has been fully assembled onto the polymer chassis.

D. Packaging

The sodium perchlorate oxidizer used to make the nanoporous silicon into an energetic material is strongly hygroscopic, and the absorption of water by the oxidizer degrades the efficiency of the energetic reaction and produces stress within the porous layer. The induced stress can also cause the porous material to crack and the hotwire initiator to subsequently break. For this reason, the jumping experiments were all conducted in a dry box plumbed with nitrogen. Even so, the process of opening the door of the enclosure to charge the capacitors prior to ignition allowed enough time for the oxidized sample to absorb water and degrade the efficiency of the reaction.

Three techniques were employed to limit the rate at which moisture was absorbed by the oxidizer. The first technique involved applying one drop of oxidizer solution (3.2 M NaClO_4 in methanol) using a syringe in a dry room controlled to < 1% relative humidity and allowing the sample to dry for 20 min. After the sample was dried, a thin layer of Loctite ($\sim 500 \mu\text{m}$ thick) was carefully applied on top of the porous silicon and UV cured for 5 min. The second technique was to apply the oxidizer and dry in a nitrogen dry box, then seal the porous silicon with an evaporated parylene layer ($\sim 12 \mu\text{m}$ thick). While loading the samples into the parylene system, there was some exposure to environmental moisture. An alternative approach which has not been attempted yet would be to dry the sample under the dry nitrogen inside the parylene coating chamber to avoid transport.

The final (and simplest) humidity exposure minimization approach was to connect leads to the hexapod prior to application of the oxidizer and run these leads outside of the controlled environment chamber. The oxidizer was allowed to dry for 15 min. The door to the chamber was then opened very briefly (less than 30 s) to disconnect the leads and then closed for the experiment.

IV. RESULTS

Experiments were performed in a laboratory, and a moderately dark environment was simulated by turning off all

overhead fluorescent lights, and turning on a small 12-W lamp in the corner of the room to allow some visibility for positioning the device and connecting and disconnecting electrical leads. The resulting ambient light level at the photodetector was ~ 0.3 lux, as mentioned above. Oxidizer was applied to the nanoporous energetic silicon using one of the three different techniques discussed above to minimize moisture exposure. The $100\ \mu\text{F}$ and $10\ \mu\text{F}$ capacitors were charged to 6 V, and the hexapod was positioned approximately 12 inches under a high intensity 3 LED array light source. The light source was turned on, triggering the phototransistor, which closed the MOSFET switch, which in turn triggered ignition of the energetic nanoporous silicon. Each jump was captured by a high-speed camera recording at 1000 frames per second.

The first untethered experiment was performed with the Loctite moisture seal encapsulating the porous silicon. The experiment was done in ambient air; therefore an encapsulation layer was needed to prevent moisture uptake and subsequent degradation of the porous silicon and oxidizer mixture. This hexapod had a total weight of 280 mg, and achieved a vertical height of 1 cm when the light was turned on. The limited height may have been due to packaging the sample with Loctite. Deposition of the Loctite directly on the porous silicon resulted in a thick layer ($\sim 500\ \mu\text{m}$) of the Loctite remaining on the surface. A portion of the output energy being converted into thrust for movement would therefore be lost in breaking the seal created by the Loctite. It was also possible that the Loctite coating may have affected the oxidized porous silicon surface, causing it to be less reactive. Similar results were achieved with the parylene-coated samples. Further work must be done to explore other alternatives to encapsulate the energetic without degrading the performance.

The best jump heights were achieved with the simplest humidity exposure minimization approach, which involved pre-connecting the electrical leads to charge the capacitors before applying and drying the oxidizer, and running the experiment in a nitrogen-filled box. The box was only very briefly opened (less than 30 s) to disconnect the leads. In this case, a 314-mg hexapod jumped approximately 8 cm vertically (Fig. 8).

The authors analyzed approximately 200 frames of the jump trajectory to determine if any significant acceleration sources other than gravity affected the microrobotic platform during flight. Several frames at the end of the trajectory were not captured in the high-speed video, so the landing portion of the trajectory was not shown. The center of the hexapod chassis was chosen as the center of mass, and the height was measured as the center of mass crossed each half centimeter marker on the height scale. The resulting position versus time data is shown in Fig. 9. Given the resolution of the camera, the accuracy with which we were able to pinpoint the robot's center of mass in each frame, and parallax errors involved observation from a fixed viewpoint, we estimated the uncertainty for each data point as approximately 0.25 cm. Using this uncertainty, the potential energy based on the maximum observed height was between $246\ \mu\text{J}$ and $262\ \mu\text{J}$.

The data points were then fitted to the parabolic curve describing the motion of a projectile under constant free-fall acceleration g and negligible air resistance. The parabolic curve

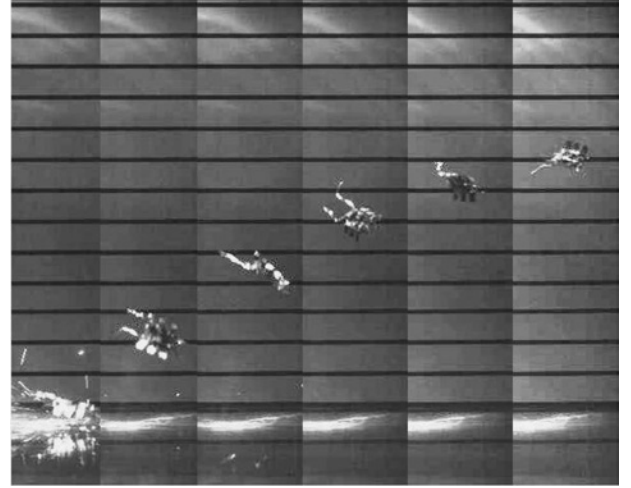


Fig. 8. Propelled hexapod when actuator triggered by light captured at 1000 frames per second. Frames shown above are 20 ms apart. The vertical scale bar shown is spaced 1 cm per division.

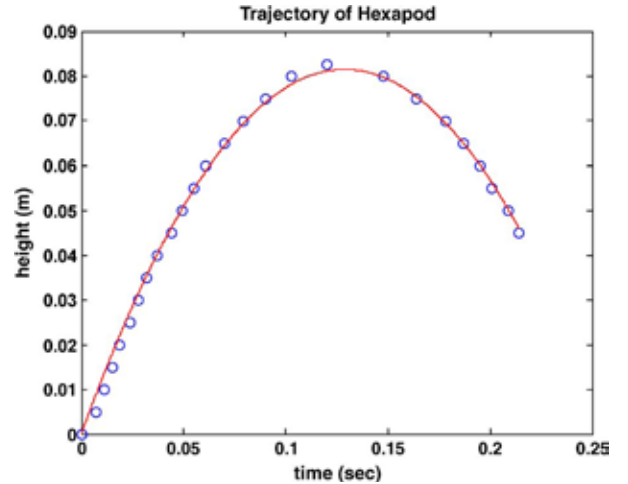


Fig. 9. Trajectory of the hexapod jump. Experimentally determined height shown as blue circles. The parabolic curve fit describes projectile motion under acceleration due to gravity and negligible air resistance.

was then fitted to the data to determine the initial velocity v_i , as shown in Fig. 9. This fit resulted in a calculated take-off velocity of 1.263 m/s. The associated kinetic energy is $250\ \mu\text{J}$, which is within the potential energy uncertainty bounds calculated based on measured maximum height. The quality of the fit to the experimental data also demonstrates that the microrobotic platform followed a drag-free parabolic trajectory under acceleration due to gravity and negligible air resistance.

Although the overall mass of the energetic chip as given in Table I was approximately 25 mg, the mass of the reactive region was estimated at only 0.21 mg. The 2 mm diameter energetic region was able to propel the robot approximately 8 cm into the air, even though the robot was more than 1000 times the mass of the energetic material.

As a point of comparison, to achieve the same height with a conventional actuator would require an actuator stiffness of 2.4 kN/m and a force of at least 9.6 N (assuming the

leg length of 4 mm is the actuator throw). This would be very difficult if not impossible to achieve at this size scale. To ignite the nanoporous energetic silicon, a maximum of 180 μJ of electrical energy was consumed (assuming that the 10 μF capacitor discharged entirely from 6 V to 0 V). Defining an “effective actuation efficiency” as the ratio of mechanical energy produced to electrical energy consumed, the 8 cm jump here represented an effective efficiency of 137%. Based on past measurements of the energy density of the nanoporous energetic silicon reaction, approximately 1.9 J of chemical energy was released [21]. Therefore, the chemical to kinetic conversion efficiency was actually extremely low (0.0127%), indicating that the vast majority of the available energy was wasted.

There is consequently room for improvement, and the authors believe implementation of a nozzle in future designs will increase this efficiency by directing gases in a more effective manner to produce maximum thrust. However, the fact that a respectable height of over $11\times$ the body length was achieved despite the abysmal conversion efficiency underscores the tremendous amount of energy available in the nanoporous energetic silicon. The authors believe that this technology will have many applications in future MEMS systems if the energy can be more efficiently captured and put to use.

V. CONCLUSION

An autonomous jumping microrobot has been demonstrated, achieving a vertical jump of 8 cm, which was over 11 times its longest physical dimension. Autonomy was achieved through on-board integration of a simple circuit constructed of discrete surface mount components. The resulting system has optical sensing, control, power, and mobility. The rudimentary sensing and intelligence allow the hexapod to detect an increase in light intensity and respond by jumping. In addition, the novel use of an energetic material for actuation was shown, allowing significantly more mechanical energy to be produced than the electrical energy needed to initiate the reaction.

A hybrid integration approach has also been presented, which uses a low-temperature solder and metal interconnects patterned directly on the robot’s polymer chassis to integrate various discrete electrical components. One of the unique aspects to the integration approach is that a single UV-curable polymer material was used for the robot chassis, as a substrate for the assembly of the circuit components, and as a packaging material. The authors expect improvements in direction control and development of an array of energetic actuators to allow multiple jumps, leading to future technological leaps for autonomous microrobots.

ACKNOWLEDGMENT

The authors would like to thank the Micro Robotics Laboratory at the University of Maryland for assistance in fabricating the robotic polymer chassis.

REFERENCES

- [1] P. Verschure, B. Krose, and R. Pfeifer, “Distributed adaptive control: The self-organization of structured behavior,” *Robot. Autonom. Syst.*, vol. 9, no. 3, pp. 181–196, 1992.
- [2] R. Pfeifer, “Robots as cognitive tools,” *Int. J. Cognit. Technol.*, vol. 1, no. 1, pp. 125–143, 2002.
- [3] C. Bartneck and J. Forlizzi, “A design-centred framework for social human-robot interaction,” in *Proc. 13th IEEE Int. Workshop Robot Human Interact. Commun. ROMAN*, Sep. 20–22, 2004, pp. 591–594.
- [4] G. Bekey, “Software architectures for autonomous robots,” in *Autonomous Robots: From Biological Inspiration to Implementation and Control*. Cambridge, MA: MIT Press, 2005, pp. 104–107.
- [5] R. Casanova, A. Dieguez, A. Arbat, O. Alonso, A. Sanuy, J. Canals, J. Colomer, and J. Samitier, “Integration of the control electronics for a mm^3 -sized autonomous microrobot into a single chip,” in *Proc. IEEE ICRA*, May 12–17, 2009, pp. 3007–3012.
- [6] A. M. Hoover, E. Steltz, and R. S. Fearing, “RoACH: An autonomous 2.4g crawling hexapod robot,” in *Proc. IEEE/RSJ IROS*, 2008, pp. 26–33.
- [7] G. Caprari and R. Siegwart, “Mobile micro-robots ready to use: Alice,” in *Proc. IEEE/RSJ Int. Conf. IROS*, Aug. 2–6, 2005, pp. 3295–3300.
- [8] B. R. Donald, C. G. Levey, C. D. McGray, I. Paprotny, and D. Rus, “An untethered, electrostatic, globally controllable MEMS micro-robot,” *J. Microelectromech. Syst.*, vol. 15, no. 1, pp. 1–15, Feb. 2006.
- [9] T. Ebefors, T. Mattsson, E. Kalvesten, and G. Stemme, “A walking silicon micro-robot,” in *Proc. 10th Int. Conf. Solid-State Sens. Actuators (Transducers’99)*, Sendai, Japan, Jun. 7–10, 1999, pp. 1202–1205.
- [10] R. J. Wood, “The first takeoff of a biologically inspired at-scale robotic insect,” *IEEE Trans. Robot.*, vol. 24, no. 2, pp. 341–347, Apr. 2008.
- [11] S. Hollar, A. Flynn, C. Bellew, and K. S. J. Pister, “Solar powered 10 mg silicon robot,” in *Proc. IEEE 16th Annu. Int. Conf. MEMS*, Kyoto, Japan, Jan. 19–23, 2003, pp. 706–711.
- [12] H. Masato and T. Tooru, “Development of a humanoid robot ASIMO,” *Honda R&D Tech. Rev.*, vol. 13, no. 1, pp. 1–6, 2001.
- [13] L. J. Currano and W. A. Churaman, “Energetic nanoporous silicon devices,” *J. Microelectromech. Syst.*, vol. v18, no. v4, pp. 799–807, Aug. 2009.
- [14] D. Kovalev, V. Y. Timoshenko, N. Kunzner, E. Gross, and F. Koch, “Strong explosive interaction of hydrogenated porous silicon with oxygen at cryogenic temperatures,” *Phys. Rev. Lett.*, vol. 87, no. 6, p. 068 301, Aug. 2001.
- [15] M. Kovac, M. Fuchs, A. Guignard, J.-C. Zufferey, and D. Floreano, “A miniature 7g jumping robot,” in *Proc. IEEE ICRA*, Pasadena, CA, May 19–23, 2008, pp. 373–378.
- [16] L. J. Currano, W. A. Churaman, J. Rajkowski, C. J. Morris, and S. Bergbreiter, “Nanoenergetic silicon as a thrust actuator for jumping microrobots,” in *Proc. Hilton Head Workshop: A Solid-State Sens., Actuators Microsyst. Workshop*, Hilton Head Island, SC, Jun. 6–10, 2010, pp. 126–129.
- [17] P. Schlyter, Radiometry and Photometry in Astronomy. [Jan. 3, 2011], Mar. 18, 2009. [Online]. Available: <http://stjarnhimlen.se/comp/radfaq.html#10>
- [18] A. Pears, “Chapter 7: Appliance technologies and scope for emission reduction,” in *Strategic Study of Household Energy and Greenhouse Issues*, Australian Greenhouse Office, Australia, Jun. 1998, pp. 61.
- [19] J. Rajkowski, “Rapid polymer prototyping for applications in low cost and robust microrobots,” M.S. thesis, Dept. Mech. Eng., Univ. Maryland, College Park, MD, 2010.
- [20] C. Morris and B. Parviz, “Micro-scale metal contacts for capillary force-driven self-assembly,” *J. Micromech. Microeng.*, vol. 18, no. 1, p. 015 022, Jan. 2008.
- [21] L. J. Currano, W. Churaman, and C. Becker, “Nanoporous silicon as a bulk energetic material,” in *Proc. Int. Solid-State Sens., Actuators Microsyst. Conf. (TRANSDUCERS)*, Denver, CO, Jun. 21–25, 2009, pp. 2172–2175.



Wayne A. Churaman received the B.S. and M.S. degrees in electrical engineering from the University of Maryland, College Park, in 2005 and 2010, respectively, with a specific focus on microelectronics and microrobotic platforms.

He currently works as a MEMS Engineer for the U.S. Army Research Laboratory, Adelphi, MD. His interests include experimental analysis of nanoenergetic materials, integration of nanoenergetic materials with MEMS, and MEMS sensor design and fabrication. He is currently developing novel actuators using nanoenergetic porous silicon.



Luke J. Currano (M'09) received the B.S., M.S., and Ph.D. degrees in mechanical engineering from the University of Maryland, College Park, in 2000, 2002, and 2010, respectively.

He has worked as a MEMS Engineer for the U.S. Army Research Laboratory (ARL), Adelphi, MD, since 2001. He is currently Team Leader of the MEMS and Nanoenergetic Devices team at ARL. His research interests include integration of energetic materials with MEMS, high force/displacement MEMS actuators, acceleration switches, no-power sensors, and biologically inspired MEMS devices.



Christopher J. Morris (S'04–M'07) received the M.S. degree in mechanical engineering and the Ph.D. degree in electrical engineering from the University of Washington, Seattle, in 2000 and 2007, respectively.

Between his graduate studies, he was with Micronics, Inc., developing microfluidic devices. He is currently with the U.S. Army Research Laboratory in the Sensors and Electron Devices Directorate, Adelphi, MD. His current research interests lie in the integration of new materials and technologies with microelectronics and MEMS, including on-chip energetic materials, electronics packaging, and fluidic self-assembly.



Jessica E. Rajkowski received the B.S. and M.S. degrees in mechanical engineering from the University of Maryland, College Park, in 2009 and 2010, respectively, with a focus on microrobotics.

She is currently a Senior Systems Engineer at The MITRE Corporation, McLean, VA, where she works in the Nanosystems Group. Her research interests include the design and fabrication of millimeter-scale robotics and thermal micro-actuators.



Sarah Bergbreiter (S'03–M'07) received the B.S.E. degree in electrical engineering from Princeton University, Princeton, NJ, in 1999, and the M.S. and Ph.D. degrees from the University of California, Berkeley, in 2004 and 2007, respectively.

She is currently an Assistant Professor of Mechanical Engineering, with a joint appointment in the Institute for Systems Research at the University of Maryland, College Park. Her research addresses the challenges necessary to make robotic bugs move, including effective locomotion, efficient actuation, micromechanism design and fabrication, power systems, sensing, and integration.

Dr. Bergbreiter received a DARPA Young Faculty Award for her work toward autonomous millimeter-scale robots in 2008.

Simulations of High-Pressure Phases in RDX

Lynn B. Munday¹, Peter W. Chung¹, Betsy M. Rice¹, and Santiago D. Solares²

¹ U.S. Army Research Laboratory, Aberdeen Proving Ground, MD

² Department of Mechanical Engineering, University of Maryland,
College Park, MD

ABSTRACT

Using a fully flexible molecular potential in equilibrium molecular dynamics simulations, we study the α - and γ -polymorphs of the energetic molecular crystal hexahydro-1,3,5-trinitro-s-triazine (RDX), their respective properties, and the conditions that contribute to the stress-induced $\gamma \rightarrow \alpha$ solid-solid phase transition mechanisms. We find the pressure-dependent atomic structure, mechanical properties, and transition behavior to be described reasonably well. Uniaxial deformation of α -RDX along the crystal axes is shown to result in three different crystal responses where compression of the c -axis results in the $\alpha \rightarrow \gamma$ transition, compression of the b -axis causes a transition with resulting structure similar to stacking faults observed by Cawkwell et al. [J. Appl. Phys. 2010, 107, 063512], and no transitions are observed for compression of the a -axis.

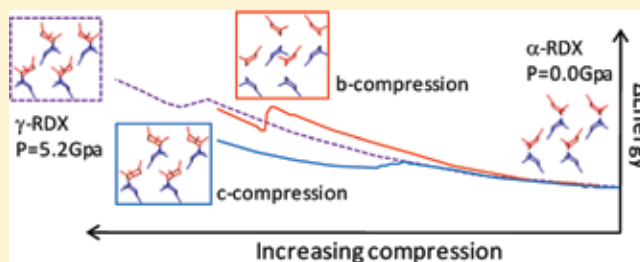
The Journal of Physical Chemistry B, Volume 115, Pages 4378-4386 (2011)

Simulations of High-Pressure Phases in RDX

Lynn B. Munday,^{†,‡} Peter W. Chung,^{*,†} Betsy M. Rice,[†] and Santiago D. Solares[‡][†]U.S. Army Research Laboratory, Aberdeen Proving Ground, Maryland 21005, United States[‡]Department of Mechanical Engineering, University of Maryland, College Park, Maryland 20742, United States

S Supporting Information

ABSTRACT: Using a fully flexible molecular potential in equilibrium molecular dynamics simulations, we study the α - and γ -polymorphs of the energetic molecular crystal hexahydro-1,3,5-trinitro-*s*-triazine (RDX), their respective properties, and the conditions that contribute to the stress-induced $\gamma \rightarrow \alpha$ solid–solid phase transition mechanisms. We find the pressure-dependent atomic structure, mechanical properties, and transition behavior to be described reasonably well. Uniaxial deformation of α -RDX along the crystal axes is shown to result in three different crystal responses where compression of the *c*-axis results in the $\alpha \rightarrow \gamma$ transition, compression of the *b*-axis causes a transition with resulting structure similar to stacking faults observed by Cawkwell et al. [J. Appl. Phys. 2010, 107, 063512], and no transitions are observed for compression of the *a*-axis.



1. INTRODUCTION

The events leading up to initiation of energetic materials is an area of research that continues to draw much interest.¹ The need to assess the sensitivity of explosive materials for the sake of safety and handling has fostered research that has led to better understanding of the mechanisms that convert mechanical stimuli to enable chemical events. Numerous efforts have described potentially relevant initiation mechanisms including up-pumping,² steric hindrance,³ dislocation avalanches,⁴ and electronic effects at extremely high compressions.⁵ Required in the representation of these mechanisms is a presumption of the polymorph at the point of initiation.

One of the more popular systems used to explore initiation mechanisms is the energetic crystal RDX ($C_3H_6N_6O_6$ or hexahydro-1,3,5-trinitro-*s*-triazine), a cyclic nitramine widely used in military applications. At the reference conditions, $T = 300$ K and $P = 1$ atm, RDX is stable in the α -polymorphic form, which is an orthorhombic unit cell occupied by eight molecules in space group 61. The unit cell axes and origin for space group 61 can be chosen in multiple ways and are represented by the symbols $Pbca$ ^{6,7} or its alternative axes setting $Pcab$.⁸ α -RDX material properties are orthotropic in thermal expansion⁹ and elastic tensor.^{8,10} At high pressure, it goes through a phase transition to form the γ -polymorph, which also contains eight molecules but belongs to the orthorhombic $Pca2_1$ space group 29.¹¹ Other observed phases include the β phase¹² and the δ and ϵ phases,¹³ which are summarized by Ciezak and Jenkins¹⁴ in a P – T phase diagram. The experimentally determined crystal phases of RDX^{6,11–14} are distinguishable by the so-called wag angle δ , which is the angle between the N–N bond and the plane created by the C–N–C triple (as shown in Figure 1a). Each RDX molecule has three such wag angles. The wag angle normally falls

into three approximate ranges, less than -10° , -10 to $+10^\circ$, and greater than $+10^\circ$ in the positive sense of the angle shown in Figure 1a. These segments of the molecule are in the so-called equatorial (E), intermediate (I), or axial (A) configurations, respectively. An α -RDX molecule has two N–N bonds in the axial configuration and one bond in the equatorial configuration; thus, the conformation of such a molecule is denoted as AAE. The same conformation is shared by all eight molecules in the unit cell of α -RDX. In contrast, among the eight molecules in the γ -RDX unit cell, four have the AAI configuration and four have the AAE configuration. The molecular conformations and unit cells of α - and γ -RDX are presented in Figure S2 of the Supporting Information. The β -¹² and ϵ -RDX¹³ phases both belong to the $Pca2_1$ space group and contain molecules in the AAA conformation.

Early experiments^{15,16} identified the existence of the γ -polymorph at high pressure. The accompanying discontinuous decrease in volume across the α - to γ -transition and distinct compressibility changes at high pressure^{11,14–16} make knowledge of this nonreactive behavior important for determining its role in initiation. Hydrostatic compression experiments place the critical transition pressure at 3.8 GPa, independent of temperature in the range of 150–375 K.¹⁷ Shock experiments on single crystals have shown the phase transition at approximately 4.5 GPa to be independent of crystal orientation.¹⁸

Atomistic simulations have largely been qualitatively consistent with experiment. Nonreactive flexible molecule models of RDX such as that of Boyd et al.¹⁹ or Smith and Bharadwaj²⁰ (SB)

Received: December 19, 2010

Revised: March 2, 2011

Published: March 24, 2011

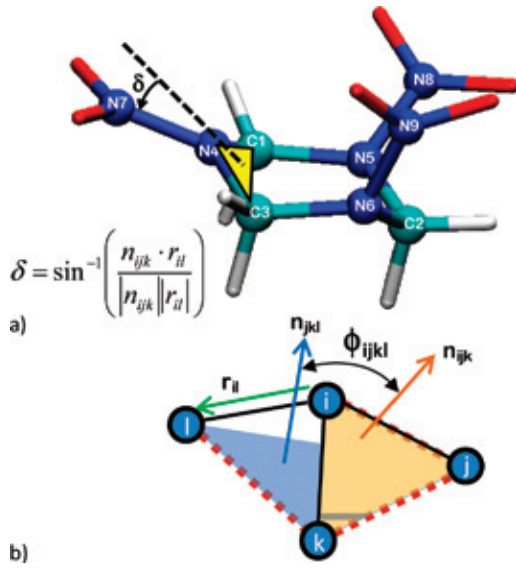


Figure 1. (a) RDX wag angle δ and (b) definition of the improper dihedral angle ϕ_{ijkl} and vectors used to find wag angle δ used in this study. The wag angle, δ , in (a) is related to the indices in (b) by $i = N4$, $j = C1$, $k = C3$, and $l = N7$.

have been shown to reproduce the various experimental conformations of RDX and mechanical properties (see Supporting Information). The SB potential has furthermore been used to simulate the observed dependence of shock strength and orientation on the nonreactive dynamic processes involved in the elastic plastic response of RDX.^{21–24} On the basis of their simulations, Cawkwell et al.²¹ and Ramos et al.²² proposed that partial dislocation loops homogeneously nucleated throughout the material as stacking faults cause an anomalous hardening, changing the elastic plastic response as observed in (111)- and (021)-oriented shock experiments.^{22,25} They also determined these stacking faults to be stabilized by stress applied normal to the (001) plane and nucleated by shear stress in the [010] direction.²¹ However, it was also noted that anomalous hardening may be observed if the stress was sufficient to induce the transition into the γ -polymorph. Owing to the higher experimentally known transition pressure and the fairly isotropic dependence on shock orientation,¹⁸ the involvement of the $\alpha \rightarrow \gamma$ transition was deemed unlikely.^{17,22}

Bedrov et al.²³ performed uniaxial constant stress Hugoniot-stat simulations using the SB potential for [100] compression of α -RDX, resulting in amorphous shear banding for pressures above 9 GPa. Similar calculations of [001] compression of α -RDX produced the $\alpha \rightarrow \gamma$ transition for pressures above 2.0 GPa.²³ Furthermore, Bedrov et al. found differing behavior according to the crystal orientation. Whereas [100] compression yielded amorphization and sudden changes in volume following the initial compression, similar behavior did not occur for [001] compression. Clearly, determining the dependence of this solid–solid phase transition upon compression, stress, and shear of the material requires further exploration.

In this paper, we study the basic equilibrium properties of and transitions to and from the α - and γ -polymorphs in crystalline RDX based on the SB potential.²⁰ Atomic-level effects in preinitiation processes are difficult to discern from measurement, but they likely play significant roles in the mechanisms that lead to initiation. Thus, verified atomistic models may offer useful

insights to complement experiments. While it has been shown that the γ -phase is observable using atomistic simulation approaches, to the best of our knowledge, a definitive lowest possible pressure and properties of the stable γ -structure using the SB potential have not been reported. It would therefore be useful to determine the conditions that foster transition behavior in simple models of RDX (such as that described by the SB potential). To this end, we employ molecular dynamics (MD) with the SB potential to model the quasi-static response of the RDX crystal to hydrostatic and uniaxial compression. We also compute the transitioned structure under uniform deformations at room temperature to study the steric mechanisms. In addition, we consider the roles of crystal anisotropy and load orientation on these steric effects. The paper is organized as follows. In section 2, the details of the simulation method are presented. Results and discussions are presented in section 3 and, the conclusions are given in section 4.

2. SIMULATION APPROACH

2.1. Molecular Potential. The nonreactive potential energy function parametrized by Smith and Bharadwaj²⁰ (SB) is used in this work to describe RDX atomic interactions with fully flexible bonded interactions and nonbonded electrostatic and dispersion repulsion forces. The SB potential was parametrized to quantum mechanical calculations for octahydro-1,3,5,7-tetranitro-1,3,5,7-tetrazocine (HMX) but has been shown to be transferable to use in atomistic simulations of RDX.^{21–24} The form of the SB potential is

$$\begin{aligned}
 U_{\text{Total}} = & \sum_{i=1}^{N-1} \sum_{j>i}^N \left(k_e \frac{q_i q_j}{r_{ij}} + A_{ij} \exp(-B_{ij} r_{ij}) - \frac{C_{ij}}{r_{ij}^6} \right) \\
 & + \sum_{\text{bonds}} \frac{K^S}{2} (r - r^0)^2 + \sum_{\text{angles}} \frac{K^B}{2} (\theta - \theta^0)^2 \\
 & + \sum_{\text{proper dihedrals}} \frac{K^T}{2} [1 - \cos(n\phi)] + \sum_{\text{improper dihedrals}} \frac{K^D}{2} \phi^2
 \end{aligned} \quad (1)$$

with the parameters published by Bedrov et al.²⁶ The intramolecular bonded terms include harmonic bond stretching and angle bending (K^S and K^B), harmonic out-of-plane bending using an improper dihedral (K^D), and cosine series dihedrals (K^T and n). The improper dihedral angle definition used in this study is shown in Figure 1b, where the black lines represent bonds and the dashed red lines represent the improper dihedral. Nonbonded interactions are represented by exponential repulsion (A_{ij} and B_{ij}), r^{-6} dispersion (C_{ij}), and electrostatic interactions (partial charges q_i and q_j), which are calculated between all atoms separated by more than two bonds.

2.2. Simulation Methodology. Molecular dynamics simulations in both the isothermal–isochoric (NVT) and isothermal–isostress (NST) ensembles were performed. The MD package DL-POLY 2.20²⁷ was used to determine the thermalized equilibrium structures of the RDX polymorphs at the reference state, $P = 1$ atm and $T = 300$ K for α -RDX and $P = 5.2$ GPa and $T = 300$ K simulations for γ -RDX. The supercell used in these simulations is a block of $2 \times 3 \times 3$ crystallographic unit cells of RDX and contains 3024 atoms. The small supercell size will help to isolate only those conditions that foster homogeneous phases and are unable to account for seeding through a local defect.

Table 1. RDX Elastic Constants and Third Order BMEOS Parameters

	α -RDX		γ -RDX
	this work ^a	experiment	this work ^b
Orthotropic Elastic Constants			
C_{11} (GPa)	25.0	25.6 ^c	80.3
C_{22} (GPa)	23.8	21.3 ^c	67.0
C_{33} (GPa)	23.4	19.0 ^c	57.9
C_{44} (GPa)	3.1	5.4 ^c	11.9
C_{55} (GPa)	7.7	4.3 ^c	16.3
C_{66} (GPa)	5.2	7.3 ^c	13.4
C_{23} (GPa)	8.8	6.4 ^c	43.9
C_{31} (GPa)	7.6	5.7 ^c	37.0
C_{12} (GPa)	10.6	8.7 ^c	37.8
Third-Order BMEOS			
B_o (GPa)	13.0	12.1 ^d	
B_o'	9.2	8.6 ^d	
V_o (Å ³)	1634	1641 ^d	

^a α -RDX constants at reference condition. ^b γ -RDX constants at $P = 5.2$ GPa and $T = 300$ K. ^c Sun et al. ¹⁰ ^d Olinger et al. $P = 0 - 3.95$ GPa and $T = 293$ K.¹⁵

Crystallographic properties were calculated using *NST*-MD for both the zero-pressure α -RDX phase characterized by Choi and Prince⁶ and the high-pressure γ -RDX phase characterized by Davidson et al.¹¹ for $P = 5.2$ GPa. Both phases belong to orthorhombic space groups ($Pbca$ for α -RDX and $Pca2_1$ for γ -RDX) and contain eight RDX molecules per unit cell. In order to provide a direct comparison of the γ -polymorph with α , γ -RDX in this study is presented in the $Pb2_1a$ space group, an alternative setting to $Pca2_1$ in space group 29, presented in Figure S2c in the Supporting Information. This effectively switches the b - and c -lattice vectors given by Davidson et al.¹¹ to match those used by Choi and Prince.⁶ Nonorthogonal parallelepiped periodic boundary conditions were used to model the bulk material under the least geometrically restrictive conditions. Additionally, thermalized equilibrium structures of these polymorphs were calculated for a variety of pressures and strains. Each new pressure or strain increment used the final configuration from the prior increment as its initial state.

The α -polymorph was subjected to *NST*-MD simulations over the pressure range of 1 atm to 5.2 GPa using 0.5 GPa increments. The γ -polymorph, beginning with the 5.2 GPa structure, was subjected to *NST*-MD simulations over the same pressure range and increment. The shock Hugoniot of α -RDX was also calculated using the method developed by Erpenbeck.²⁸

The cutoff distance for nonbonded van der Waals and electrostatic interactions is 10 Å. The electrostatic forces were evaluated using Ewald sums. The velocity Verlet algorithms for the *NVT* and *NST* ensembles as implemented in DL-POLY 2.20 were used to integrate the equations of motion with a 0.75 fs time step. Both thermostat and barostat coupling times were set to 1.0 ps. Each system underwent a 7.5 ps equilibration trajectory, during which, direct velocity scaling of the temperature was performed at every 5 steps. After equilibration, trajectories were integrated for 75 ps, during which, ensemble averages were obtained.

2.3. Isochoric Uniaxial Deformation Simulations. Uniaxial deformation of the α -RDX structure is simulated by manually

deforming the system and equilibrating it at constant temperature and volume using the *NVT* ensemble. The forces calculated in these simulations can be used to determine the effective stress. Then, assuming an orthotropic elastic form²⁹ for the stress-strain relationship, the effective elastic constants can be computed. In contrast, *NST* calculations described in section 2.2 used the reverse procedure; the resulting strain was determined based on an applied set of forces corresponding to a prescribed stress. We performed two sets of uniaxial calculations, the first using small increments of 0.1% up to a total of 1% and the second using larger increments of 1% up to a total of 10%. These calculations were repeated for each of the three crystallographic axes. An analogous procedure was performed for three unique shear planes. In each set, we started with the thermalized structures of α -RDX at $P = 0$ GPa and of γ -RDX at $P = 5.2$ GPa. At each strain increment, the system was thermalized for 75 ps. The computed elastic constants are given in Table 1.

At each deformation increment, we map all atom coordinates into a scaled volume using the 3×3 deformation gradient, which is given in terms of the lattice vectors by²⁹

$$\mathbf{F} = \mathbf{h}\mathbf{h}_o^{-1} \quad (2)$$

where \mathbf{h}_o and \mathbf{h} are tensors containing columnwise lattice vectors. The reference lattice vectors, \mathbf{h}_o , are from the *NST* α -RDX simulation at $P = 0$ and $T = 300$ K. Then, specifying the deformed lattice vectors \mathbf{h} uniquely determines the nine terms in \mathbf{F} in eq 2. Because RDX is orthorhombic, the Cartesian coordinates, \mathbf{e}_i , align with the crystal axes with $\mathbf{a} = a\mathbf{e}_1$, $\mathbf{b} = b\mathbf{e}_2$, and $\mathbf{c} = c\mathbf{e}_3$. The reference locations of the molecule centers of mass \mathbf{x}_o are mapped to the deformed unit system by $\mathbf{x} = \mathbf{F}\mathbf{x}_o$. This system is then thermalized using the earlier described procedure. The Lagrange strain, E_{ij} , from F_{ij} is given by^{29,30}

$$E = \frac{1}{2}(\mathbf{F}^T\mathbf{F} - \mathbf{I}) = \frac{1}{2}(\mathbf{h}_o^{-T}\mathbf{h}^T\mathbf{h}\mathbf{h}_o^{-1} - \mathbf{I}) \quad (3)$$

where \mathbf{I} is the identity.

Under small strains, RDX single-crystal elasticity has been shown to be sensitive to the direction of loading.^{8,10} In refs 21, 22, and 25, the material response below the phase transition pressure is sensitive to the crystal direction in which the planar shock travels. This is because the elastic material response is anisotropic as a result of the orthorhombic unit cell and intermolecular interactions. The material response to large deformation leads to molecular and lattice distortions that are also dependent on the crystal axis being loaded. By applying varying levels of uniaxial deformation (a nonhydrostatic deformation and state of stress), measurements of the anisotropy and its connection to underlying crystal orientation can be determined.

We next simulate α -RDX under large uniaxial deformation. In simulations of kinetic mechanisms, it is often appropriate to seed the model with a means to disrupt homogeneity and therefore instigate the kinetic response. A seeded lattice defect, for instance, disrupts the otherwise homogeneous crystal by introducing nontrivial amounts of local shear. The resulting simulation is generally insensitive to the magnitude of the stress from the seed, and it is therefore sufficient to perform simulations on a slab geometry (external surfaces) or with finite void volume (internal surfaces).³¹ Experiments such as those in refs 18, 21, 22, and 25 in ostensibly single crystals can still promote the kinetic mechanisms of interest due to significant surface effects or lattice defects that introduce local shear and escape identification or

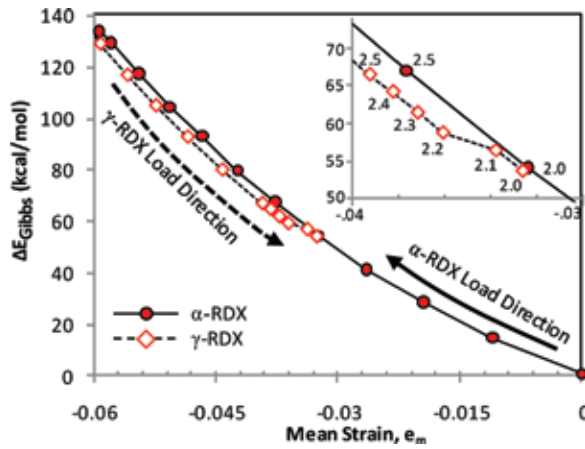


Figure 2. Change in Gibbs energy, $\Delta E_{\text{Gibbs}} = E_{\text{Gibbs}}(P) - E_{\text{Gibbs}}(P=0)$, versus the mean strain relative to the α -RDX configuration at $P = 0$. The inset shows the region near the transition with pressure values labeled in GPa units.

characterization. The direct experimental investigation of shear-induced kinetic structural response of RDX can be accomplished by exploiting such surface effects such as those through indentation.³² Simulations have also investigated RDX in the context of directional loading of the crystal.^{14–21,33} This also produces local crystal shear that can promote bulk kinetic effects such as phase transitions. Common in these approaches are imposed or generated nontrivial components to the deviatoric stress tensor. Because the deviatoric stress tensor is defined as $s = \sigma - 1/3 \text{Tr}(\sigma)$,²⁹ it is possible to load the crystal in a nonhydrostatic but homogeneous sense and produce the simulated effect of a seeded model.

3. RESULTS AND DISCUSSIONS

3.1. NST Pressurization Simulations. We use *NST-MD* simulations to study quasi-static pressurization and depressurization of the bulk crystal. Under these conditions, the Gibbs energy is conserved and used to investigate the crystal phases before and after the transition. The change in Gibbs energy relative to the reference state, $\Delta E_{\text{Gibbs}}(P) = E_{\text{Gibbs}}(P) - E_{\text{Gibbs}}(P=0)$, versus the mean strain is shown in Figure 2 for the α -RDX pressurization (filled circles) and γ -RDX depressurization (open diamonds). The mean strain is the average of the diagonal or volumetric strain components in eq 3, with h_0 given by the undeformed α -lattice vectors at the reference state. A negative mean strain indicates compression from the undeformed α -lattice. Under quasi-static pressurization of α -RDX, the α -structure is maintained up to roughly 10 GPa, the highest pressure value that we tested (see Figure S5 of the Supporting Information for RDF and wag angle distributions reflecting the absence of phase transition). Re-equilibrating the crystal at a higher temperature (350 K) and pressures up to 10 GPa yielded no observable departure from the α -structure. However, starting with the crystal in the γ -polymorph at 5.2 GPa, the γ -phase equilibrates at 300 K and remains stable. Upon release of pressure, the crystal converts to the α -polymorph, as is evident from the Gibbs energy in Figure 2 and structural data (wag angles and RDF) presented in Figure S6 of the Supporting Information. The phase transition occurs at a pressure value of 2.1 GPa and a corresponding mean strain of $e_m = -0.034$ ($V/V_0 = 0.90$). At high pressure, the γ -RDX crystal

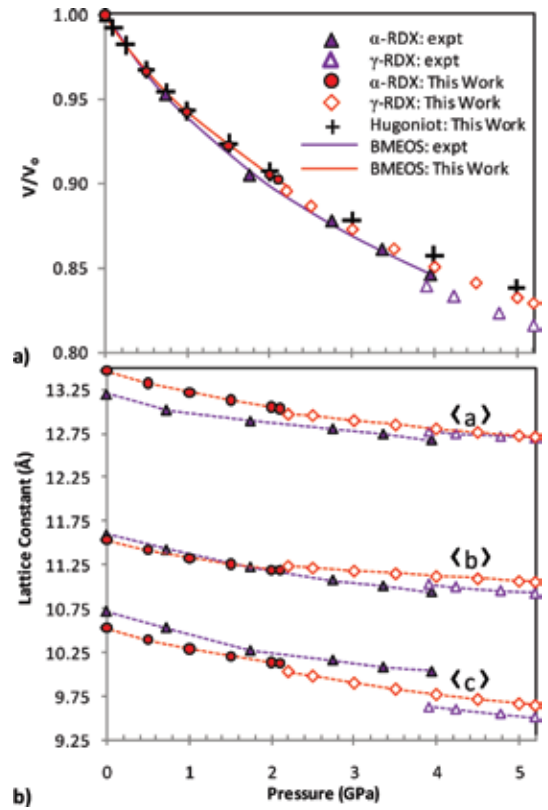


Figure 3. Volume ratio (a) and lattice constants (b) versus pressure. Solid lines in (a) are third-order BMEOS fit. Triangles denote experiments for α -RDX¹⁵ and γ -RDX,¹¹ and circles and diamonds denote the present results. Solid and open symbols denote α - and γ -RDX phases, respectively.

is correctly shown to be lower in Gibb's energy than highly compressed α -RDX (Figure 2 inset).

The computed value of 2.1 GPa is in agreement with the results of Bedrov et al.,²³ where the γ -phase was obtained through a Hugoniotstat approach using a uniaxially applied pressure on the (001) plane of ~ 2.0 GPa. Our results are qualified by the use of a depressurization approach for evoking the reverse $\gamma \rightarrow \alpha$ phase transition. The transition pressure is also in qualitative agreement with the results of Ramos et al.²² and Cawkwell et al.,²¹ where the abrupt changes to the elastic plastic response were computed to occur in the range of 1.0–2.25 GPa. In the present calculations, the appearance of the α -phase from the γ -phase equilibration at discrete pressures was sudden and categorical across the entire simulation domain, though we have not investigated the influence of the small simulation size. However, the sudden change in lattice properties implies changes in the slip plane thickness, dislocation mobility, and shear moduli to which the plastic slip is sensitive. The phase transition that evokes changes in basic lattice parameters is therefore likely to be accompanied by changes in the plastic response of an RDX bulk crystal, particularly one undergoing slip as the transition pressure is reached.

These results indicate the following. First, no γ -structure can be found under equilibration at pressures below a critical value (2.1 GPa), which indicates that the α -phase is indeed the reference state polymorph using the SB potential. Second, the transition is not observable with increasing hydrostatic pressure

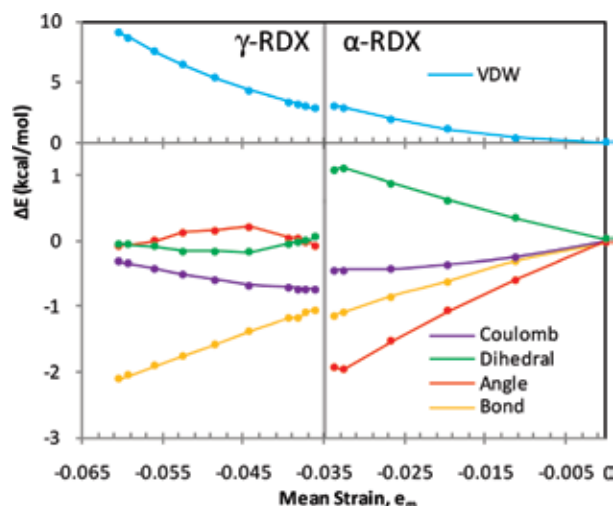


Figure 4. Change in energy components of the SB potential energy given in eq 1, relative to their respective values at $e_m = 0$ versus the mean strain. The van der Waals term is shown on a different scale in the upper frame of the figure.

of pristine α -RDX. Such idealized simulations may preclude the transition to the γ -phase at higher hydrostatic pressures using the SB potential. This is particularly evident in the fact that uniform depressurization of the γ -phase indeed yields the α -phase. To investigate the possibility that simulated hydrostatic compression of an ideal crystal and the smallness of the simulation might artificially preclude the appearance of the γ -polymorph, we explored uniaxial deformation of the RDX model, as will be detailed in a later section.

Basic equilibrium properties were computed using the *NST* ensemble. The pressure-dependent lattice constants and volume for the α - and γ -RDX crystals were found to be in very close agreement with available experimental data,^{6,11} as shown in Figure 3 and presented in Tables S1 and S2 in the Supporting Information. The α -RDX *PV* data for simulation (circles) and experiment (triangles) shown in Figure 3a are fitted to the third-order Birch–Murnaghan equation of state (BMEOS)³⁴ by least-squares fitting of the bulk modulus and its derivative at zero pressure, B_0 and B_0' , respectively. The third-order BMEOS values for V_0 , B_0 , and B_0' fitted to α -RDX data points are given in Table 1; the calculated B_0 underpredicts the available experimental value by 7%. Table 1 also contains values from experiments of ref 10 and the extensive comparisons summarized therein.

Experiments (triangles in Figure 3) have shown that under quasi-static pressurization, the RDX crystal undergoes the $\alpha \rightarrow \gamma$ transition at $P = 3.9$ GPa, evidenced by the abrupt change in volume and lattice constants.^{11,15} The simulation data (circles and diamonds in Figure 3), under depressurization using the SB potential, also show an abrupt change in volume and lattice constants after the transition; however, this occurs at a lower pressure, $P = 2.1$ GPa.

The $\alpha \rightarrow \gamma$ transition involves changes in the molecular conformation as well as abrupt lattice changes. To clarify the potential impact of these conformational changes, it is helpful to detail the variation in each component of the potential energy described by the SB model given in eq 1 before and after the transition; these are shown in Figure 4. Compression of α -RDX leads to increases in the van der Waals and dihedral contributions

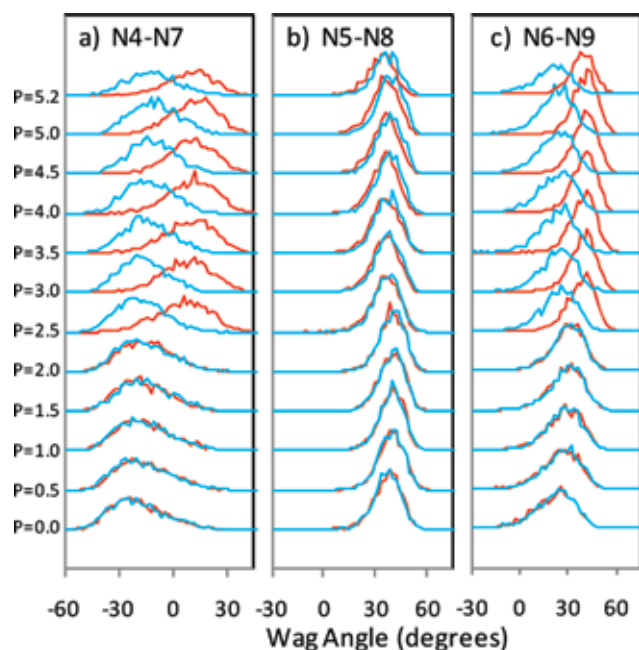


Figure 5. RDX wag angle distributions versus pressure during depressurization of γ -RDX for wag angles (a) N4–N7, (b) N5–N8, and (c) N6–N9 labeled on the molecule in Figure 1a. Red and blue lines indicate those molecules that have AAI and AAE structure in the γ -phase, respectively.

to the potential energy while the other energy components decrease. At the $\alpha \rightarrow \gamma$ transition, the angle energy increases, and the dihedral energy decreases to an almost zero net change from the uncompressed α -RDX crystal. Upon increasing compression of the γ -RDX structure, the angle and dihedral energies remain constant. The Coulomb energy decreases for increasing compression of α -RDX, and after a slight drop across the $\alpha \rightarrow \gamma$ transition, it begins increasing for increasing compression of γ -RDX. These observations show that the pressure-dependent contributions of the SB potential terms in eq 1 are dependent on the crystal phase.

As one of the key molecular structural changes between the two crystalline polymorphs involves the wag angle δ defined in Figure 1a, we have generated relative distributions (shown in Figure 5 and Figures S4 and S6 in the Supporting Information) for values of the three wag angles in crystalline RDX during the depressurization of the γ -polymorph. Each wag angle in the figure identifies the three associated nitro groups individually at each pressure, (a) N4–N7, (b) N5–N8, and (c) N6–N9 as labeled in Figure 1a. The distributions are taken from 30 configurations of the 144 molecules of the supercell recorded during the *NST* simulations. In these figures, the red curves depict distributions of AAI molecules, and the blue curves depict the distributions of AAE molecules. The bimodal distributions in Figure 5a and c for pressures greater than 2.0 GPa (reflecting a mix of AAE and AAI molecules) collapse to single-peaked distributions at lower pressure; these correspond to the AAE conformation of the α -polymorph. The γ -RDX AAE (blue) distribution widths and peak values change very little through the $\gamma \rightarrow \alpha$ transition, suggesting that the transition does not significantly affect the intermolecular interactions between AAE molecules and their neighbors. The AAI molecules (red) exhibit changes in peak location and distribution width for both

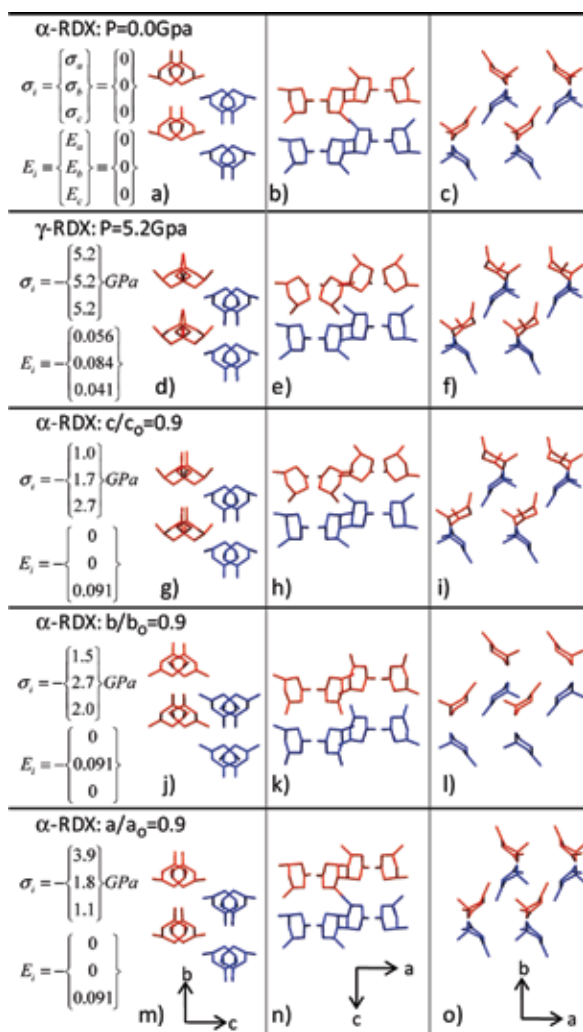


Figure 6. Wireframe depictions of the RDX unit cell for $T = 300$ K at the prescribed axial stress and strain shown to the left of each row. Strain values are found relative to α -RDX at $P = 0$. For ease of viewing, H and O atoms are not shown. α -RDX at $P = 0$ and γ -RDX at $P = 5.2$ GPa from section 3.1 are shown in rows 1 (a–c) and 2 (d–f), respectively. α -RDX uniaxially compressed along either the a -, b -, or c -axis as described in section 3.3 are shown in rows 3 (g–i), 4 (j–l), and 5 (m–o), respectively. Each column represents a view along the indicated crystallographic axis (labeled at the bottom of each column). Molecules that are red are AAI in γ -RDX. Molecules that remain AAE are indicated in blue.

the N4–N7 group, switching from equatorial (E) to intermediate (I), and the axial (A) N6–N9 group, becoming similar to the N5–N8 distribution (see also Figure S4 in the Supporting Information for additional distributions). We find that the symmetry and width of the wag angle distribution are strongly influenced by the dependence on the wag angle of the SB potential in eq 1. A large curvature of the energy leads to narrower distributions. The N4–N7 wag angle is therefore softer and experiences larger vibrational amplitudes than the N6–N9 wag angle on the AAI molecule in the γ -structure. The asymmetry of the distributions is caused mainly by a corresponding asymmetry in the intermolecular dispersion–repulsion interactions. The bonded part of the energy is an order of magnitude smaller and plays a minor role. The behavior of the distributions in Figure 5 with respect to increasing pressure is consistent with

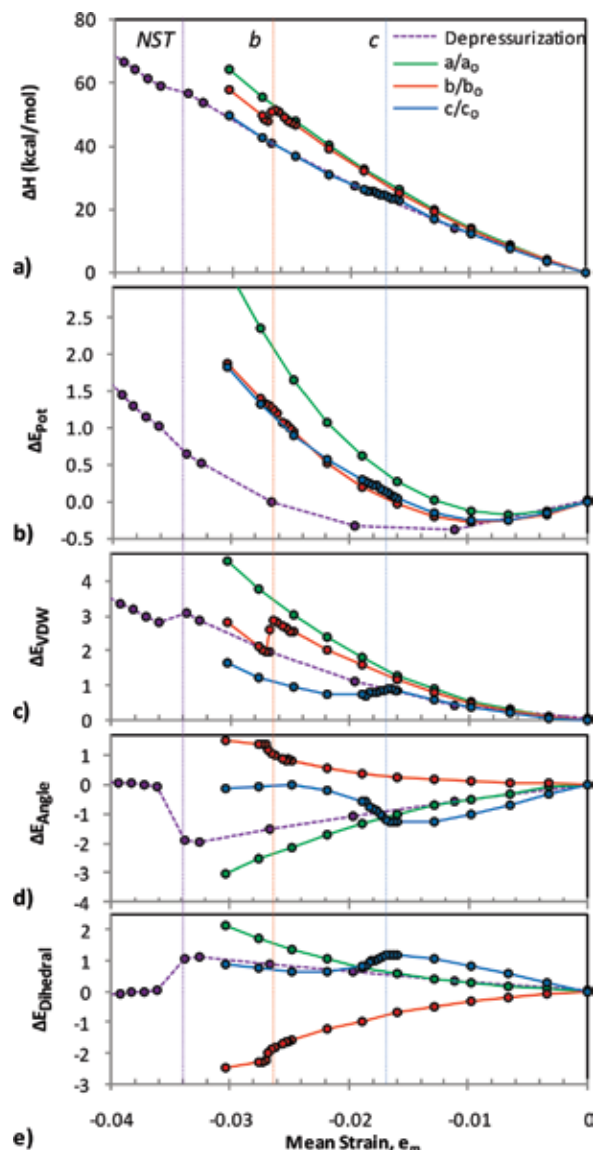


Figure 7. Change in (a) enthalpy, (b) total SB potential energy, (b) van der Waals, (c) angle, and (d) dihedral energy terms of the SB potential for each compression direction and γ -RDX NST depressurization. Zero mean strain signifies the α -RDX reference configuration at reference conditions.

the $\gamma \rightarrow \alpha$ transition at $P = 2.1$ GPa. The locations of the peaks of the wag angle distributions from this work and experiment^{6,11} are presented in Table S3 in the Supporting Information.

Wireframe representations of the eight molecules for the simulated α -RDX unit cells at $P = 0$ GPa are shown in Figure 6a–c, and those of the γ -RDX unit cell at $P = 5.2$ GPa are in Figure 7d–f. The molecules that are AAI in γ -RDX are shown in red, and those that remain AAE are shown in blue; oxygen and hydrogen atoms are not shown for clarity. The γ -RDX molecules in red that undergo the conformation change from AAE to AAI also undergo a rotation about an axis oriented normal to the ring. This rotation may be aided by the effective overall size of the AAI molecule relative to the size of the AAE molecule, which allows them greater freedom to rotate. The molecular centers of mass change little between α - and γ -RDX in Figure 6a–f, and only slight differences are observed in the radial

distribution functions in Figures S3, S5, and S6 of the Supporting Information. The main features of the α - to γ -RDX phase transition are therefore the conformation changes and rotations of the AAI molecules about the axis normal to the ring. Figure 6a–f will be used as reference structures to allow comparison of uniaxial compression results in Figure 6g–o discussed in section 3.3.

3.2. Hugoniot Results. NST-MD simulations were used to explore the α -RDX structure at increasing pressure and temperature for states near the static shock conditions given by the Hugoniot equation, using a method similar to Erpenbeck's.²⁸ To satisfy the conservation of mass, momentum, and energy at the shock front described by the Hugoniot equation, an increase in pressure requires an increase in internal energy (kinetic and potential). This work uses the α -RDX crystal at $P = 0$ and $T = 300$ K as the reference point, and the Hugoniot equation is satisfied at higher pressures by increasing the temperature. At $P = 5$ GPa, the Hugoniot equation results in a Hugoniot temperature of $T_{\text{HG}} = 350$ K, raising the potential and kinetic energy by 11.8 kcal/mol. Isothermal compression from the reference state to $P = 5$ GPa (presented in section 3.1) raised only the potential energy by 6.3 kcal/mol. The Hugoniot simulations do not show the α - to γ -RDX phase transition, despite the increased temperature. Consequently, we note that the computed Hugoniot curve in $P(V)$ space, shown by the + symbols in Figure 3a, is almost identical to the isothermal curve for α -RDX at $T = 300$ K, where the slight deviation is caused by the increased temperature of the Hugoniot simulation. Table S5 in the Supporting Information presents tabulated PVT data for the α -RDX Hugoniot curve.

3.3. NVT Uniaxial Deformation Results. A series of uniaxial deformations were performed first to determine the full set of orthotropic elastic stiffness constants at small strains below 1% from the initial α -RDX equilibrated structure at $P = 0$ GPa and γ -RDX equilibrated structure at $P = 5.2$ GPa. Below 1% strain, the stress–strain response remains linear elastic. The computed coefficients, C_{ij} , are listed in Table 1 and are in reasonable agreement with experiment.⁶ The bulk modulus of α -RDX calculated from C_{ij} is $B = 14.0$ GPa, in close agreement with $B_0 = 13.0$ GPa obtained from the third-order BMEOS fit of hydrostatic compression simulations from section 3.1, listed in Table 1.

Using larger uniaxial deformations, we also investigated the dependence of the loading direction on the appearance of new phases down to an effective compressed volume ratio of $V/V_0 = 0.9$. The uniaxially deformed unit cells along each of the three crystal axes are depicted in Figure 6g–o. The strain-dependent radial distribution functions and wag angle distributions are presented in Figures S7–S9 in the Supporting Information. These three cases of uniaxial deformation lead to three different crystal responses where compression of the c -axis results in the α - to γ - transition, compression of the b -axis results in a phase transition similar to the stacking faults observed in other simulation work,^{21,22} and no transitions are observed for compression of the a -axis.

For compression along the c -axis, the deformed structures are shown in Figure 6g–i for $c/c_0 = 0.9$. They are visually indistinguishable from the γ -RDX structures at $P = 5.2$ GPa in Figure 6d–f. Thus, unlike the hydrostatic pressurization calculations, uniaxial compression evokes the α - to γ -transition. This is consistent with the findings by Bedrov et al.²³ using the SB potential and uniaxial pressure Hugoniotstat applied to the c -axis. Figure 6j–l for b -axis compression at $b/b_0 = 0.9$ shows a large

shift in the location of the two center molecules, most easily observed near the center of Figure 6l. The molecules also change to the AEE conformation, confirmed by the wag angle distributions presented in Figure S8c–e in the Supporting Information. Cawkwell et al.²¹ and Ramos et al.²² observed a similar molecule conformation and stacking change for simulations of weak shock loading at $P = 1.3$ GPa on the (111) and (021) planes. In their simulations, this phase only appeared in partial dislocation loops, which generated stacking faults on the (001) slip plane.²¹

For compression along the a -axis, Figure 6m–o shows the configurations at $a/a_0 = 0.9$. There is no noticeable change in molecular conformation or packing relative to the α -RDX configuration at $P = 0$ (see Figure 6a–c). Uniaxial stress loading along the a -axis or (100) plane of α -RDX is commonly studied in the literature because it leads to no resolved shear stress on experimentally known slip systems,^{24,32} making this direction sensitive to shock loading according to the steric hindrance model.² The steric hindrance model predicts that sensitivity in energetic molecular crystals is related to the absence of available slip systems for dislocation-based deformation and that deformation in these directions leads to large molecular distortions and the breaking of bonds. Experimentally, uniaxial shocks above $P = 3.9$ GPa applied to the a -axis result in the γ -RDX phase after a 100 ns so-called incubation period,¹⁸ but reproducing these experimental conditions would be outside of the spatial and temporal range of atomistic simulations. Simulated shocks on the a -axis by Cawkwell et al.²¹ and Bedrov et al.,²³ both using the SB potential, showed no noticeable conformation changes for weak shocks below 5.9 GPa. For stronger shocks above 9 GPa, they both show the development of amorphous shear bands oriented along planes of maximum shear stress irrespective of the crystal axes.

We next examine the effects of crystal orientation and material anisotropy. Earlier in this section and elsewhere,^{21–24} it was found that RDX response is sensitive to the direction of loading relative to its native crystal axes. We now attempt to clarify the dependence of the transition on the direction of loading through the analysis of steric effects under uniform and uniaxial strain.

Figure 7a–e shows the change in different energy components, ΔE , relative to their corresponding value for α -RDX at reference conditions as functions of mean strain. Depicted are the three uniaxial compression simulations, a (green), b (red), and c (blue), and the NST depressurization simulation of γ -RDX (purple). It is apparent that uniaxial deformation causes phase transitions to occur at smaller effective volumetric strains and therefore lower effective pressures. The effective mean strains at which the transitions occur are indicated by the vertical colored lines traversing all plots. The purple line represents the NST $\gamma \rightarrow \alpha$ transition at $\epsilon_m = -0.034$ ($V/V_0 = 0.90$), the red line is the b -compression transition at $\epsilon_m = -0.026$ ($V/V_0 = 0.92$), and the blue line is the $\alpha \rightarrow \gamma$ transition for c -compression at $\epsilon_m = -0.017$ ($V/V_0 = 0.95$). Once again, no transition is observed for compression along the a -axis. The transition due to uniaxial loading in the c -direction occurs earliest with c -axis stress -1.4 GPa, followed by the transition due to loading in the b -direction at b -axis stress -2.58 GPa. No transition is observed for loading in the a -direction.

The change in enthalpy, ΔH , gives a measure of the system internal energy plus the work put into the system due to the deformation. For a crystalline material at room temperature, the Gibb's energy is approximately equal to the enthalpy. In the NST γ -RDX simulation, the potential energy contributes 69% to the

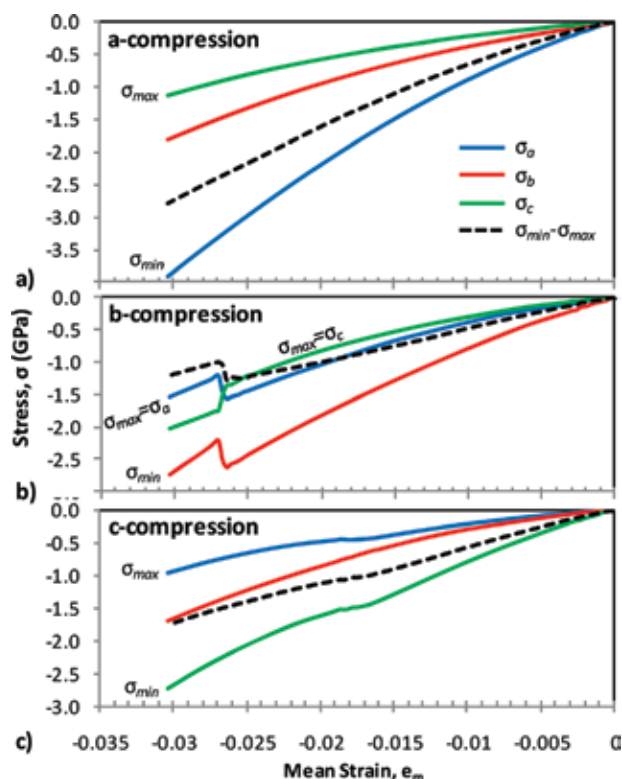


Figure 8. Stress versus mean strain for uniaxial compression along the (a) *a*-axis, (b) *b*-axis, and (c) *c*-axis. Principal stress components are labeled by the crystal axis (e.g., σ_a is the principal stress oriented along the *a*-axis of α -RDX). Maximum shear stress ($\sigma_{\min} - \sigma_{\max}$) is shown by the dashed line.

total system enthalpy at the maximum compression of $P = 5.2$ GPa but only 5% to the change in enthalpy from that state during depressurization. The largest contribution to ΔH is external work (PV). The abrupt change in ΔH for the *NST* simulation is due to the abrupt volume change shown in Figure 3a and the abrupt change in ΔH for *NVT* *b*-compression is due to an abrupt change in stresses, shown in Figure 8b.

The principal noteworthy observation is the sensitivity of molecular deformation, reflected by the angle and dihedral energies in Figure 7d and e, to the crystal axis being compressed. Compressions of the *a*- and *c*-axes of α -RDX result in decreasing angle energy and increasing dihedral energy, as is seen in the *NST* case. A transition is observed for *c*-compression strained beyond $e_m = -0.017$, where the change in angle energy diminishes to zero, as is observed for *NST* compression of γ -RDX. Compression of α -RDX along the *b*-axis follows opposite trends with an increase in angle energy and decrease in dihedral energy.

The stress components that develop along each crystal axis ($\sigma_{a,b,c}$ along *a*, *b*, *c*-axes, respectively) are also the principal stresses and are shown in Figure 8a–c. The maximum shear stress, shown by the dashed line, is equal to the minimum (σ_{\min}) minus the maximum (σ_{\max}) principal stresses. The maximum shear stress is an indicator of plastic material response when its magnitude exceeds the known yield strength of the material and acts on a plane oriented 45° to the directions of σ_{\max} and σ_{\min} .

Remarkably, the *b*- and *c*-compressed transitions occur consistently for ($\sigma_{\min} - \sigma_{\max}$) in the range of -1.0 to -1.25 GPa. For *b*-compression, the principal stresses change abruptly after the transition with σ_c (green line) decreasing and both σ_a (blue

line) and σ_b (red line) increasing. Prior to the phase change, the maximum principal stress is oriented along the *c*-axis ($\sigma_{\max} = \sigma_c$), which becomes oriented along the *a*-axis ($\sigma_{\max} = \sigma_a$) in the new phase. The change in crystal phase leads to a reorientation of σ_{\max} and in effect a reorientation of the plane of maximum shear stress. Thus, new slip systems may become active, resulting in plastic slip on new planes that block the α -RDX slip planes. Similar effects were observed in the simulated plastic response of RDX under oriented shock loading.^{21,22}

4. SUMMARY AND CONCLUSIONS

Details at the atomic level provided by MD simulations are useful in providing additional chemical and physical interpretations to experimental data. In this work, we studied the applicability of the SB potential to model α - and γ -phases of RDX under various load conditions using simulations and comparing to available experimental data. The simulations were used to provide details of the roles of molecular conformation and mechanical deformation on the phase transitions. The small simulation cell and time scale limits the consideration to homogeneous phase transitions under hydrostatic and uniaxially deformed conditions. The uniaxial conditions mimic the effect of local shear that can occur in larger simulations. The non-reactive SB potential was appropriate for this work because simulation conditions were limited to those processes preceding chemical events.

The homogeneous crystal structures obtained were in agreement with experimental α - and γ -RDX structures, and the orientation dependence of the phase transitions agree well with other simulation work using the SB potential.^{21–24} We showed that under increasing hydrostatic loads, the α - to γ -transition could not be observed for the time and space scales of the current simulations. However, the reverse or hydrostatic depressurization transition was found at a critical computed pressure of 2.1 GPa.

Under uniaxial deformation, the transitions were shown to depend on the crystal axis being strained. Two different phase transitions were shown to occur at mean strains equal to $e_m = -0.017$ and -0.026 , both of which are less than the strain $e_m = -0.034$ required to observe the transition under hydrostatic stress. Compressive deformation along the *c*-axis reproduced the γ -RDX configuration for $\sigma_c = -1.5$ GPa. Compression along the *b*-axis did not result in the γ -RDX structure but instead led to a structure similar to that identified in simulations by Cawkwell et al.²¹ and Ramos et al.²² as a stacking fault. Deforming along the different crystal axes had markedly different effects on the molecule conformation, reflected in the bonded SB potential terms where loading on the *b*-axis decreased the dihedral energy, whereas it increased for loading along the *c*-axis. These results suggest that the molecule conformation in RDX crystals plays a significant role in the stability and accessibility of high-pressure phases.

■ ASSOCIATED CONTENT

Supporting Information. Pressure-dependent lattice constants for the α - and γ -RDX simulations are given in Figure S1 and Tables S1 and S2. Figure S2 contains the graphical depictions of the contents of the α - and γ -RDX unit cells with the asymmetric units overlaid on the corresponding space group diagrams. Figure S3 presents a comparison of α - and γ -RDX

radial distribution functions to the experimental data. Figure S4 presents wag angle distributions for each of the eight molecules in the unit cells for the α - and γ -RDX simulations, and Table S3 gives locations of the peak. Figures S5–S9 present RDF and wag angle distributions for each series of NST pressurizations and NVT uniaxial strain simulations. Figures S10 and S11 give temperature-dependent lattice constants and strain used to determine the coefficients of thermal expansion presented in Table S4. Table S5 presents PVT points for the calculated Hugoniot curve. This material is available free of charge via the Internet at <http://pubs.acs.org>.

■ ACKNOWLEDGMENT

Support is gratefully acknowledged from the U.S. Army Research Laboratory STEP program and the DoD Higher Performance Computing Modernization Office through the Multiscale Reactive Modeling of Insensitive Munitions Software Applications Institute. Computing support was provided by the DoD Supercomputing Resource Center located at the Army Research Laboratory.

■ REFERENCES

- (1) For a general overview of current research trends in energetic materials, see: *Proceedings of the Fourteenth International Detonation Symposium*; ONR Report No. ONR-351-10-185; Coeur d'Alene, ID, April 2010.
- (2) Dlott, D. D.; Fayer, M. D. *J. Chem. Phys.* **1990**, *92*, 3798–3812.
- (3) Dick, J. J.; Ritchie, J. P. *J. Appl. Phys.* **1994**, *76*, 2726–2737.
- (4) Armstrong, R. W. *Rev. Adv. Mater. Sci.* **2009**, *19*, 13–40.
- (5) Kuklja, M. M.; Stefanovich, E. V.; Kunz, A. B. *J. Chem. Phys.* **2000**, *112*, 3417–3423.
- (6) Choi, C. S.; Prince, E. *Acta Crystallogr.* **1972**, *B28*, 2857–2862.
- (7) Hakey, P.; Ouellette, W.; Zubieta, J.; Korter, T. *Acta Crystallogr.* **2008**, *E64*, o1428.
- (8) Haussühl, S. Z. *Kristallografiya* **2001**, *216*, 339.
- (9) Cady, H. H. *J. Chem. Eng. Data* **1972**, *17*, 369–371.
- (10) Sun, B.; Winey, J. M.; Hemmi, N.; Dreger, Z. A.; Zimmerman, K. A.; Gupta, Y. M.; Torchinsky, D. H.; Nelson, K. A. *J. Appl. Phys.* **2008**, *104*, 073517.
- (11) Davidson, A. J.; Oswald, I. D. H.; Francis, D. H.; Lennie, A. R.; Marshall, W. G.; Millar, D. I. A.; Pulham, C. R.; Warren, J. E.; Cumming, A. S. *CrystEngComm* **2008**, *10*, 162–165.
- (12) Millar, D. I. A.; Oswald, I. D. H.; Francis, D. J.; Marshall, W. G.; Pulham, C. R.; Cumming, A. S. *Chem. Commun.* **2009**, 562–564.
- (13) Millar, D. I. A.; Oswald, I. D. H.; Barry, C.; Francis, D. J.; Marshall, W. G.; Pulham, C. R.; Cumming, A. S. *Chem. Commun.* **2010**, *46*, 5662–5664.
- (14) Ciezak, J. A.; Jenkins, T. A. *Propellants, Explos., Pyrotech.* **2008**, *33*, 393.
- (15) Olinger, B.; Roof, B.; Cady, H. In *Proceedings of International Symposium on High Dynamic Pressures*; Commissariat à l'Energie Atomique: Paris, France, 1978; p 3.
- (16) Yoo, C.-S.; Cynn, H.; Howard, W. M.; Holmes, N. In *Proceedings of the 11th International Detonation Symposium*; Snowmass, CO, 1998; pp 951–957.
- (17) Baer, B. J.; Oxley, J.; Nicol, M. *High Pressure Res.* **1990**, *2*, 99–108.
- (18) Patterson, J. E.; Dreger, Z. A.; Gupta, Y. M. *J. Phys. Chem. B* **2007**, *111*, 10897–10904.
- (19) Boyd, S.; Gravelle, M.; Politzer, P. *J. Chem. Phys.* **2006**, *124*, 104508.
- (20) Smith, G. D.; Bharadwaj, R. K. *J. Phys. Chem. B* **1999**, *103*, 3570–3575.
- (21) Cawkwell, M. J.; Ramos, K. J.; Hooks, D. E.; Sewell, T. D. *J. Appl. Phys.* **2010**, *107*, 063512.
- (22) Ramos, K. J.; Hooks, D. E.; Sewell, T. D.; Cawkwell, M. J. *J. Appl. Phys.* **2010**, *108*, 066105.
- (23) Bedrov, D.; Hooper, J. B.; Smith, G. D.; Sewell, T. D. *J. Chem. Phys.* **2009**, *131*, 034712.
- (24) Cawkwell, M. J.; Sewell, T. D.; Zheng, L.; Thompson, D. L. *Phys. Rev. B* **2008**, *78*, 014107.
- (25) Hooks, D. E.; Ramos, K. J.; Martinez, A. R. *J. Appl. Phys.* **2006**, *100*, 024908.
- (26) Bedrov, D.; Ayyagari, C.; Smith, G. D.; Sewell, T. D.; Menikoff, R.; Zaug, J. M. *J. Comput.-Aided Mater. Des.* **2001**, *8*, 77–85.
- (27) Smith, W.; Forester, T. R. *J. Molec. Graphics* **1996**, *14*, 136–141.
- (28) Erpenbeck, J. J. *Phys. Rev. A* **1992**, *46*, 6410.
- (29) Bower, A. F. *Applied Mechanics of Solids*; CRC Press: Boca Raton, FL, 2009.
- (30) Parrinello, M.; Rahman, A. *J. Appl. Phys.* **1981**, *52*, 7182–7190.
- (31) Agrawal, P. M.; Rice, B. M.; Thompson, D. L. *J. Chem. Phys.* **2003**, *119*, 9617–9627.
- (32) Ramos, K. J.; Hooks, D. E.; Bahr, D. F. *Philos. Mag.* **2009**, *89*, 2381–2402.
- (33) Conroy, M. W.; Oleynik, I. I.; Zybin, S. V.; White, C. T. *J. Appl. Phys.* **2008**, *104*, 113501.
- (34) Birch, F. *Phys. Rev.* **1947**, *71*, 809–824.

Elastic-Plastic Behavior of Cyclotrimethylene Trinitramine Single Crystals Under Spherical Indentation: Modeling and Simulation

J. D. Clayton and R. Becker

U.S. Army Research Laboratory, Aberdeen Proving Ground, MD

ABSTRACT

A nonlinear anisotropic elastic-plastic model is developed for single crystals of the energetic material cyclotrimethylene trinitramine (RDX). Numerical simulations of spherical indentation on oriented single crystals are performed; predictions are compared with experimental data and observations from the literature. Model predictions for elastic response and initial yield using elastic constants obtained from resonant ultrasound spectroscopy agree with experimental data; predicted forces using constants obtained from Brillouin scattering tend to exceed experimental data. Influences of elastic anisotropy and elastic nonlinearity are significant. Predicted slip system activity is in reasonable agreement with that deduced from experimental surface profiles when a uniform strength of $G/20$ is assigned to all six slip systems, with G an effective elastic shear modulus. Predicted indentation forces in the post-yield regime exceed those observed in experiments, suggesting that surface and possibly subsurface fractures may contribute to a loss of stiffness in experiments at larger indentation depths

Journal of Applied Physics 111, 063512 (2012)

Elastic-plastic behavior of cyclotrimethylene trinitramine single crystals under spherical indentation: Modeling and simulation

J. D. Clayton^{a)} and R. Becker

Impact Physics RDRL-WMP-C, U.S. Army Research Laboratory, Aberdeen Proving Ground, Maryland 21005–5066, USA

(Received 5 January 2012; accepted 13 February 2012; published online 21 March 2012)

A nonlinear anisotropic elastic-plastic model is developed for single crystals of the energetic material cyclotrimethylene trinitramine (RDX). Numerical simulations of spherical indentation on oriented single crystals are performed; predictions are compared with experimental data and observations from the literature. Model predictions for elastic response and initial yield using elastic constants obtained from resonant ultrasound spectroscopy agree with experimental data; predicted forces using constants obtained from Brillouin scattering tend to exceed experimental data. Influences of elastic anisotropy and elastic nonlinearity are significant. Predicted slip system activity is in reasonable agreement with that deduced from experimental surface profiles when a uniform strength of $G/20$ is assigned to all six slip systems, with G an effective elastic shear modulus. Predicted indentation forces in the post-yield regime exceed those observed in experiments, suggesting that surface and possibly subsurface fractures may contribute to a loss of stiffness in experiments at larger indentation depths. [<http://dx.doi.org/10.1063/1.3695392>]

I. INTRODUCTION

Defects in energetic materials are thought to affect their initiation sensitivity. Stresses concentrate in the vicinity of cracks, pores, or lattice defects, which in turn can affect initiation of reactions associated with burning or detonation. In single crystals, availability of slip systems associated with mobile dislocations may lower peak stresses and decrease sensitivity to shock initiation.¹

The focus of the present work is the mechanical behavior of the energetic material cyclotrimethylene trinitramine ($C_3H_6N_6O_6$), referred to as RDX (Research Development eXplosive). Single crystals of RDX belong to an orthorhombic space group with eight molecules per unit cell. Dislocations in RDX have been characterized using etch pit² and x ray topographic^{3,4} techniques. Likely slip systems in RDX have been suggested from analysis of anisotropic hardness profiles⁵ and indentation experiments.^{6,7} The latter experiments^{6,7} also provide an estimate of the critical resolved shear stress associated with slip initiation, thought to be on the order of the theoretical strength (i.e., $\approx G/10$ – $G/20$, with G a representative elastic shear modulus), which corresponds to homogeneous dislocation nucleation. Inelastic behavior of RDX crystals has also been probed using shock experiments^{1,8} and molecular dynamics simulations.^{8,9}

Continuum crystal plasticity theory permits predictive mesoscale modeling of materials' behavior at length scales larger than that feasible using molecular models, but with greater resolution than that afforded by macroscopic elastic-plastic models that omit anisotropy and slip system activity. Grain interactions can be studied in direct numerical simulations via finite element models, wherein each crystal of a polycrystal is resolved geometrically. Crystal plasticity

models have been implemented elsewhere to study shock loading of energetic materials cyclotetramethylene tetranitramine (HMX)¹⁰ and pentaerythritol tetranitrate (PETN).^{11,12} One aim of the present work is development and implementation of a crystal plasticity model for RDX, a particular model which, to the authors' knowledge, has not been published elsewhere.

The single crystal elastic-plastic model developed here extends a previous model¹³ for cubic crystals loaded to possibly high pressures. Here, the model is applied to crystals with orthorhombic symmetry characteristic of RDX. Anisotropic elastic constants and pressure-dependent compressibility are considered from experimental literature.^{14–16} Six slip systems (from four different families of systems) are implemented following analysis of indentation loading profiles and surface impressions.^{5,6} The model is applied to study indentation, with a spherical indenter of (001), (021), and (210) faces of single crystals of RDX.

This paper is organized as follows: Constitutive theory and material properties are described in Sec. II. Indentation simulations are reported in Sec. III. Conclusions follow in Sec. IV. Notation of continuum mechanics is used, e.g., bold-face type for vectors and tensors all referred to fixed Cartesian coordinates. Summation applies over repeated indices.

II. THEORY

A. Single crystal model

Let $\mathbf{x} = \boldsymbol{\chi}(\mathbf{X}, t)$ denote the motion of material points of the body. The deformation gradient is

$$\nabla \boldsymbol{\chi} = \mathbf{F} = \mathbf{F}^E \mathbf{F}^P, \quad (1)$$

where $\nabla(\cdot)$ denotes the material gradient (i.e., $F_{aA} = \nabla_A \chi_a = \partial \chi_a / \partial X_A$), \mathbf{F}^E denotes thermoelastic deformation of the

^{a)}Author to whom correspondence should be addressed. Electronic mail: john.d.clayton1.civ@mail.mil.

crystal lattice, and \mathbf{F}^P represents plastic deformation due to slip. The spatial velocity gradient is

$$\dot{\mathbf{F}}\mathbf{F}^{-1} = \dot{\mathbf{F}}^E\mathbf{F}^{E-1} + \mathbf{F}^E\mathbf{F}^P\mathbf{F}^{E-1}, \quad (2)$$

where the plastic velocity gradient associated with slip rates, $\dot{\gamma}^k$, reference slip directions, \mathbf{s}_0^k , and reference slip plane normals, \mathbf{m}_0^k , on slip systems, k , is

$$\mathbf{L}^P = \dot{\mathbf{F}}^P\mathbf{F}^{P-1} = \sum_k \dot{\gamma}^k \mathbf{s}_0^k \otimes \mathbf{m}_0^k. \quad (3)$$

Slip system geometry is pushed forward to the current configuration via $\mathbf{s}^k = \mathbf{F}^E\mathbf{s}_0^k$ and $\mathbf{m}^k = \mathbf{F}^{E-T}\mathbf{m}_0^k$, where $(\cdot)^T$ denotes the transpose. From orthonormality of slip directions and slip plane normals, plastic deformation is isochoric; thus, $J = \det \mathbf{F} = \det \mathbf{F}^E > 0$. By the polar decomposition theorem, let $\mathbf{F}^E = \mathbf{R}^E\mathbf{U}^E$. A logarithmic thermoelastic strain measure is defined as $\boldsymbol{\varepsilon} = \ln \mathbf{U}^E$ and is split into deviatoric and volumetric parts as

$$\boldsymbol{\varepsilon} = \boldsymbol{\varepsilon}' + (1/3)\bar{\varepsilon}\mathbf{1}, \quad \bar{\varepsilon} = \text{tr} \boldsymbol{\varepsilon} = \ln J, \quad (4)$$

where $\mathbf{1}$ is the second-order unit tensor, and the trace of a second-order tensor is $\text{tr}(\cdot)$. Let $\boldsymbol{\sigma}$ denote the usual Cauchy stress tensor; stress in an unrotated coordinate system is $\mathbf{S} = \mathbf{R}^{E-1}\boldsymbol{\sigma}\mathbf{R}^E$.

Only the isothermal case is considered, an appropriate assumption for applications of the model discussed in Sec. III. Let the unrotated stress be split into deviatoric and hydrostatic parts,

$$\mathbf{S} = \mathbf{S}' + \bar{S}\mathbf{1}, \quad \bar{S} = (1/3)\text{tr} \mathbf{S} = (1/3)\text{tr} \boldsymbol{\sigma} = -p, \quad (5)$$

with p the Cauchy pressure. The following operator extracts the deviatoric part of a second-order tensor,

$$\mathbb{I}' = \mathbb{I} - (1/3)\mathbf{1} \otimes \mathbf{1}, \quad \mathbb{I}'_{ABCD} = \delta_{AC}\delta_{BD} - (1/3)\delta_{AB}\delta_{CD}. \quad (6)$$

Constitutive equations for deviatoric stress and pressure are¹³

$$\mathbf{S}' = \mathbb{I}' : \mathbb{C} : \boldsymbol{\varepsilon}' + (1/3)(\mathbb{I}' : \mathbb{C} : \mathbf{1})\bar{\varepsilon}, \quad (7)$$

$$p = (B_0/B')[\exp(-B'\bar{\varepsilon}) - 1] - (1/3)\boldsymbol{\varepsilon}' : \mathbb{C} : \mathbf{1}. \quad (8)$$

Here, B_0 and B' are the reference bulk modulus and pressure derivative of the bulk modulus and \mathbb{C} is the tensor of second-order elastic constants referred to the (unrotated) crystal frame. The colon denotes contraction over two pairs of indices, e.g., $(\mathbb{C} : \boldsymbol{\varepsilon}')_{AB} = \mathbb{C}_{ABCD}\boldsymbol{\varepsilon}'_{CD}$. Pressure dependence of shear elastic coefficients, implemented elsewhere for cubic crystals,¹³ is omitted in Eq. (8) because of limited experimental data for the material of present interest.

The flow rule for slip is¹³

$$\boldsymbol{\tau}^k = \boldsymbol{\sigma} : (\mathbf{s}^k \otimes \mathbf{m}^k) = \tau_0^k [(|\dot{\gamma}^k| + \xi)/\dot{\gamma}_0]^m \text{sgn}(\dot{\gamma}^k). \quad (9)$$

The resolved shear stress on slip system k is τ^k . Material parameters are initial and constant slip strength, τ_0^k , for each slip system, reference strain rate, $\dot{\gamma}_0$, and rate sensitivity, m . Constant $\xi \ll \dot{\gamma}_0$ provides a finite strength at zero strain rate.

TABLE I. Structural and physical properties of RDX single crystals (ambient).

Property	Value	Ref.
Space group	<i>Pbca</i>	5
Crystal structure	Orthorhombic	
Lattice parameters [nm]	$a = 1.3182$ $b = 1.1574$ $c = 1.0709$	5
Mass density [g/cm ³]	1.806	16

B. RDX

Physical properties of RDX single crystals are listed in Table I. The description applies to the α phase, the stable polymorph for pressures under ≈ 3.8 GPa and temperatures under ≈ 480 K.

Elastic properties are listed in Table II. Isentropic second-order elastic constants^{15,16} and bulk modulus have been converted to isothermal values at 295 K via the usual thermodynamic formulae,¹⁷ incorporating anisotropic thermal expansion¹⁸ and specific heat.¹⁹ Voigt's notation is used: $\mathbb{C}_{ABCD} \leftrightarrow C_{\alpha\beta}$, where Greek indices 1, 2, ..., 6. Voigt (G_V) and Reuss (G_R) bounds¹⁷ on the effective shear modulus are also listed. Differences between Voigt and Reuss bounds for bulk modulus B_0 , on the order 1–3%, are considered insignificant.

As is evident from Table II, reported values of second-order elastic constants can vary substantially. Values obtained using resonant ultrasonic (RUS) methods¹⁵ listed in Table II are in reasonably close agreement with those reported by other researchers using the same method.²⁰ Values obtained using Brillouin scattering¹⁶ listed in Table II are notably different, with particularly larger bulk stiffness and shear stiffness in certain directions. Values obtained using a third technique, impulsive stimulated thermal scattering,²¹ are similar to those obtained using RUS. Possible reasons for differences among measurements of elastic constants of organic molecular crystals are discussed elsewhere.²² Values predicted using empirical atomic models^{23,24} also exhibit differences from those obtained in experiments, though these predicted values tend to align

TABLE II. Isothermal second-order elastic constants of RDX (converted from ambient isentropic values).

Property	Value ¹⁵	Value ¹⁶
C_{11} [GPa]	24.56	36.48
C_{22} [GPa]	18.85	24.49
C_{33} [GPa]	17.33	20.78
C_{12} [GPa]	7.61	0.90
C_{13} [GPa]	5.30	1.26
C_{23} [GPa]	5.24	8.16
C_{44} [GPa]	5.15	11.99
C_{55} [GPa]	4.06	2.72
C_{66} [GPa]	6.90	7.68
B_0 [GPa]	10.5	11.2
G_V [GPa]	6.06	9.26
G_R [GPa]	5.72	6.40

more closely with those from RUS than from Brillouin scattering.

In this work, the two sets of elastic constants^{15,16} are used, because these are the softest and stiffest reported experimental measurements, respectively; results obtained using these two sets might be expected to bound the actual response. Results obtained using these particular RUS constants¹⁵ are very close to those that would be obtained using similar values.^{20,21}

Pressure and temperature dependencies of second-order elastic coefficients have been calculated using molecular dynamics;²³ however, these predicted values have not been validated using experiments, and some discrepancies exist among calculated second-order elastic constants at room temperature and experimental values.¹⁶ For this reason, in the present study, the nonlinear elastic model only incorporates pressure dependence of the compressibility obtained experimentally¹⁴ and not that of all elastic coefficients, specifically, $B' = 6.95$.

Crystal plasticity theories incorporating higher-order elastic constants have also been developed^{12,25} and might offer an improved description of effects of volumetric and shear deformations on tangent elastic moduli; such an approach is not pursued here, because higher-order elastic constants (e.g., 20 independent third-order constants for an orthorhombic crystal¹⁷) are unknown for RDX. In a crystal plasticity model of PETN,¹² a tetragonal crystal, the Cauchy relations were used to estimate unknown third-order elastic constants.

Potential slip systems in RDX—as identified from hardness versus orientation profiles,⁵ indentation force versus depth data,^{6,7} and residual surface impressions from indentation⁶—are listed in Table III. Slip system geometry (Fig. 1) is referred to a Cartesian system with axes (X_1, X_2, X_3) parallel to lattice vectors ($\mathbf{a}, \mathbf{b}, \mathbf{c}$). Listed initial slip system strengths are upper bounds estimated from analysis of load excursion data using the analytical Hertzian solution for frictionless spherical indentation into a semi-infinite, linear elastic, isotropic material.⁶ Other systems may become active (and those listed may become inactive) for loading regimes involving very different pressures, temperatures, and/or strain rates; e.g., molecular dynamics simulations⁸ suggest that partial dislocation loops may glide on (001)[010] during shock loading at pressure in excess of ≈ 1 GPa.

Strengths for various families of systems are varied parametrically between physically reasonable bounds on the order of the theoretical strength,^{6,7} where $G = G_R = 6.4$

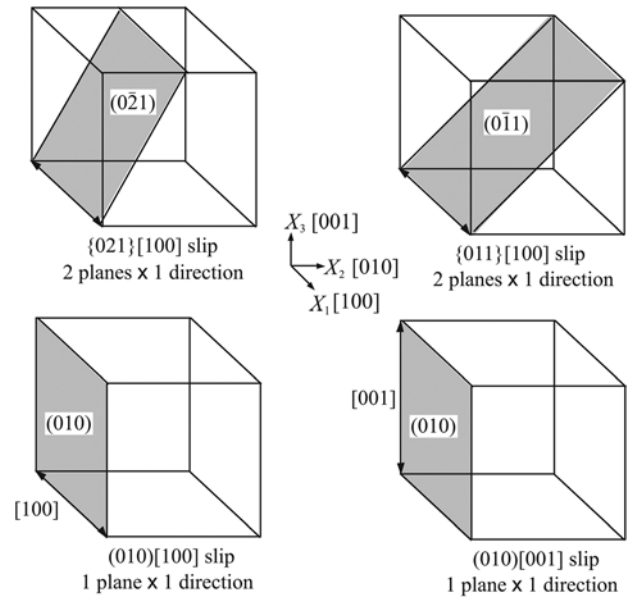


FIG. 1. Slip systems in RDX (unit cell parameters not to scale).

GPa.¹⁶ Because strengths of families of slip systems are not known precisely *a priori* from experiments, shear strengths, τ_0^k , are varied parametrically over the range listed in Table IV. This range is physically descriptive of homogeneous nucleation of glissile dislocation lines and loops.^{6,7,17} Other parameters, which provide a nearly rate-independent response, are also listed in Table IV.

III. INDENTATION

A. Boundary value problem

The constitutive model of Sec. II is implemented in the ALE3D multi-physics code. Simulations of indentation are performed using an implicit solver for static equilibrium.

The problem geometry mimics previous experimental studies.^{6,7} A spherical diamond indenter of radius $R = 1.482 \mu\text{m}$ is used to indent a flat surface of a single crystal of RDX of variable lattice orientation. Diamond is represented as an isotropic nonlinear elastic material with $B_0 = 443$ GPa, $G = 538$ GPa, and $B' = 4.0$.

The substrate is represented by a right circular cylinder.²⁶ The cylinder is assigned a height and radius of $2R$; further increases in dimensions of the cylinder did not affect results of interest. The indenter is modeled as a half-sphere. Each body is discretized using eight-node hexahedral elements with selective reduced integration. The mesh of the substrate is highly refined in the vicinity of contact beneath the indenter, where stress fields are inhomogeneous, and the

TABLE III. Slip systems in RDX single crystals (indentation).

System k	Miller indices	\mathbf{m}_0	\mathbf{s}_0	Max. strength [GPa]	Ref.
1	(021)[100]	(0, 0.880, 0.475)	[1, 0, 0]	0.885	5, 6
2	(0 $\bar{2}$ 1)[100]	(0, -0.880, 0.475)	[1, 0, 0]		
3	(011)[100]	(0, 0.679, 0.734)	[1, 0, 0]	0.645	5, 6
4	(0 $\bar{1}$ 1)[100]	(0, -0.679, 0.734)	[1, 0, 0]		
5	(010)[100]	(0, 1, 0)	[1, 0, 0]	0.885	6
6	(010)[001]	(0, 1, 0)	[0, 0, 1]	0.885	5, 6

TABLE IV. Crystal plasticity model parameters for RDX.

Property	Value
τ_0^k	$G/40 < \tau_0^k < G/10$
m	$\sim 5 \times 10^{-3}$
$\dot{\gamma}_0$	$10^{-2}/\text{s}$
ζ	$10^{-7}/\text{s}$

TABLE V. Elastic stiffness and Young's modulus of RDX oriented for indentation on planes (001), (021), and (210).

Stiffness	Plane [RUS ¹⁵]			Plane [Brillouin ¹⁶]		
	(001)	(021)	(210)	(001)	(021)	(210)
C_{11} [GPa]	24.56	24.56	20.15	36.48	36.48	22.17
C_{22} [GPa]	18.85	16.78	17.33	24.49	24.94	20.78
C_{33} [GPa]	17.33	17.62	23.06	20.78	26.98	28.29
E_{11} [GPa]	20.85	20.85	16.72	36.40	36.40	19.12
E_{22} [GPa]	15.69	14.05	15.40	21.28	22.84	18.04
E_{33} [GPa]	15.40	14.19	19.31	18.04	25.55	23.61

mesh coarsens progressively with distance from the initial contact point. Simulations with smaller elements demonstrated that further increases in mesh refinement did not affect results of interest.

During the loading phase, the upper face of the half-spherical indenter is assigned a constant (downward) velocity of $\dot{D} = 10$ nm/s in the laboratory X_3 -direction, leading to strain rates similar to those of experiments.⁶ The lower face of the cylinder is rigidly fixed, while the lateral sides (circumference) are traction-free. Indentation depth is denoted by D ; actual depth d of the tip of the sphere in contact with the surface is monitored as an outcome of the solution. Only for a rigid indenter would $d = D$. Indentation force P is the sum of nodal forces along the upper face of the half sphere acting in the direction of D , i.e., the sum of forces work conjugate to prescribed nodal velocities.

Contact between the indenter and substrate is assumed frictionless, following previous studies that rely on analytical solutions.^{6,7} Experimental measurements of dynamic friction for RDX single crystals sliding on a glass substrate²⁷ suggest

a friction coefficient on the order of unity for loads under 1 g (≈ 10 mN), wherein contact is characterized as elastic, and a friction coefficient of 0.35 for loads in excess of 10 g, wherein contact is characterized as plastic. The present indentation simulations consider a different geometry, smaller system sizes (loads under 1 g), and slower sliding velocities (on the order of 10 nm/s), so the reported experimental values for friction coefficients²⁷ may not strictly apply here. In additional simulations,²⁸ it was found that differences in indentation force among cases invoking frictionless and sticking contact were insignificant. In some simulations, unloading is also performed, whereby, after a peak depth is attained, the upper face of the indenter is assigned an upward velocity of $\dot{D} = 10$ nm/s until contact is released. If plastic deformation has occurred, then some residual deformation remains in the substrate upon unloading.

The present simulations enable direct quantification of surface and subsurface slip on each system. In contrast, hardness or indentation experiments⁵⁻⁷ require substantial interpretation of data to deduce slip activity and do not provide a quantitative measure of relative contributions of each slip system to the overall strain field. In the aforementioned experiments, visual observations of slip traces are restricted to residual surface profiles, whereas simulations enable visualization of subsurface slip activity.

Simulations of indentation onto (001), (021), and (210) planes are reported in Sec. III B. Let $\mathbb{C}^{(ijk)}$ be the fourth-order matrix of elastic constants of the crystal oriented for indentation into crystallographic plane (ijk) . Let $\mathbf{R}^{(ijk)}$ be the corresponding rotation matrix. Then,

$$\mathbb{C}_{ABCD}^{(ijk)} = R_{AE}^{(ijk)} R_{BF}^{(ijk)} R_{CG}^{(ijk)} R_{DH}^{(ijk)} \mathbb{C}_{EFGH}, \quad (10)$$

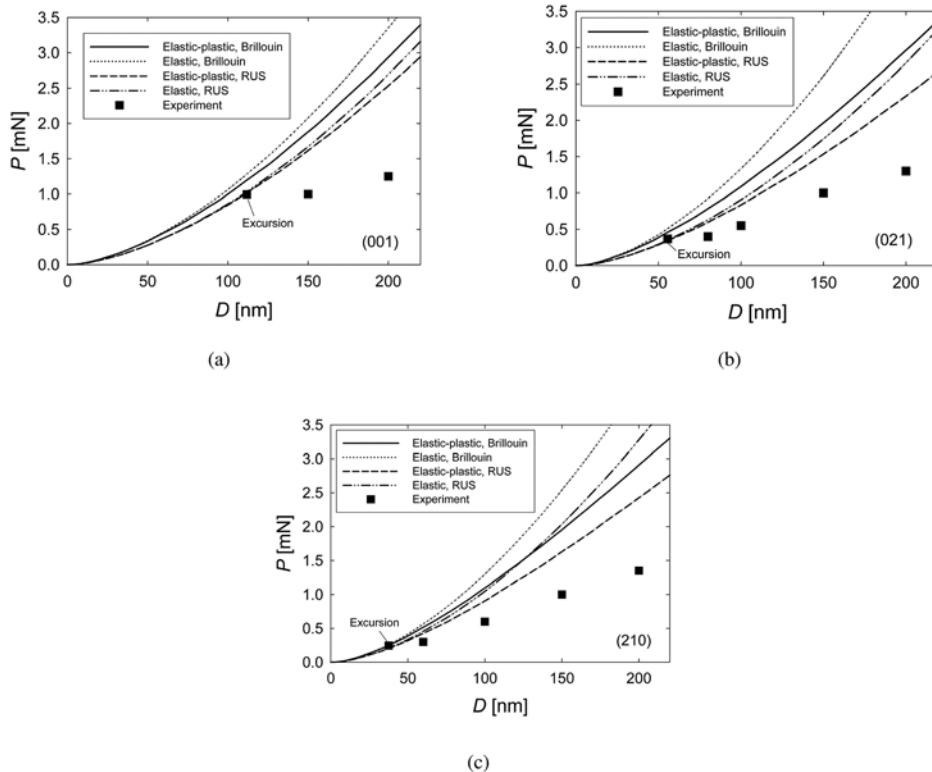


FIG. 2. Indentation force vs applied displacement; model predictions obtained using RUS (Ref. 15) and Brillouin (Ref. 16) elastic constants compared to experiment (Ref. 6): (a) indentation into (001); (b) indentation into (021); (c) indentation into (210).

where \mathbb{C}_{EFGH} corresponds to elastic constants of Table II. Values of elastic stiffness are listed in Table V. Perhaps most pertinent to indentation in the X_3 -direction, $C_{33}^{(210)} > C_{33}^{(021)} > C_{33}^{(001)}$ for either set of constants. Note that $C_{33}^{(ijk)}$ from Brillouin scattering¹⁶ always exceeds the corresponding value from RUS.¹⁵ Components of compliance $S_{\alpha\beta}$ are those of the inverse of $C_{\alpha\beta}$. Young's moduli are $E_{11} = 1/S_{11}$, $E_{22} = 1/S_{22}$, and $E_{33} = 1/S_{33}$. From Table V, $E_{\alpha\alpha}^{(ijk)}$ from Brillouin scattering¹⁶ always exceeds the corresponding value from RUS¹⁵ for $\alpha = 1, 2$, and 3.

B. Model predictions

Predictions obtained using each set of elastic constants^{15,16} are compared directly for substrate orientations (001), (021), and (210) in Fig. 2. In results marked as “elastic”, slip is suppressed to permit assessment of the elasticity model in isolation and to permit deduction of the yield point upon comparison with “elastic-plastic” results, wherein the slip model of Sec. II is enabled. For the latter results shown in Fig. 2, for each set of elastic constants, strength is set to a constant value of $\tau_0^k = G/20$ for all six slip systems.

Significantly closer agreement between model and experiment⁶ is obtained from the elastic constants from RUS¹⁵ for indentation onto (001) and (021) planes. The first experimental data point in each figure corresponds to the maximum depth at which the indentation process remains elastically reversible, i.e., initiation of the first excursion from a smooth force-displacement profile.^{6,7} Comparable accuracy is obtained from either set of elastic constants for indentation on (210) planes. The present simulations strongly suggest that elastic constants obtained from RUS^{15,20} provide a more realistic representation of elastic stiffness during nano-indentation than elastic constants obtained from Brillouin scattering,¹⁶ with the latter appearing too stiff. Results shown in Fig. 2 invoke the geometrically nonlinear elastic model with pressure-dependent bulk modulus; comparison with results of additional calculations²⁸ with $B' = 0$ for RDX demonstrated that the effect of nonlinear compressibility becomes noticeable for $D \gtrsim 50$ nm.

In simulations, the yield point (initiation of slip) can be deduced as the indentation depth beyond which elastic and elastic-plastic model predictions begin to differ. From Fig. 2, the predicted yield point matches the experimental excursion point reasonably well for each orientation when RUS elastic constants¹⁵ are used in the model. In contrast, the indentation depth at which yielding is predicted is premature for (001) and (021) orientations when Brillouin constants¹⁶ are used. This difference is presumably a result of attainment of larger resolved shear stresses at a given depth of indentation when stiffer constants are used.

Predicted forces exceed experimental values at larger indentation depths in each orientation and for both sets of elastic constants. Results corresponding to more compliant elastic constants¹⁵ provide closer agreement to experimental values than results corresponding to stiffer elastic constants.¹⁶ As noted elsewhere,^{26,28} uncertainty in the true tip radius, R , of the indenter could lead to discrepancies between

simulations and experiments. Surface fractures and/or sub-surface fractures could contribute to a loss of stiffness that would be reflected only in the experimental data. RDX is prone to cleavage fracture on planes (001), (010), (001), (241), and ($\bar{2}41$).^{2,4,6} Experimental data demonstrate nearly horizontal steps in force versus displacement corresponding to discrete shear discontinuities and/or fracture events that are not readily resolved by a constant strength continuum crystal plasticity model, such as the one formulated here. In

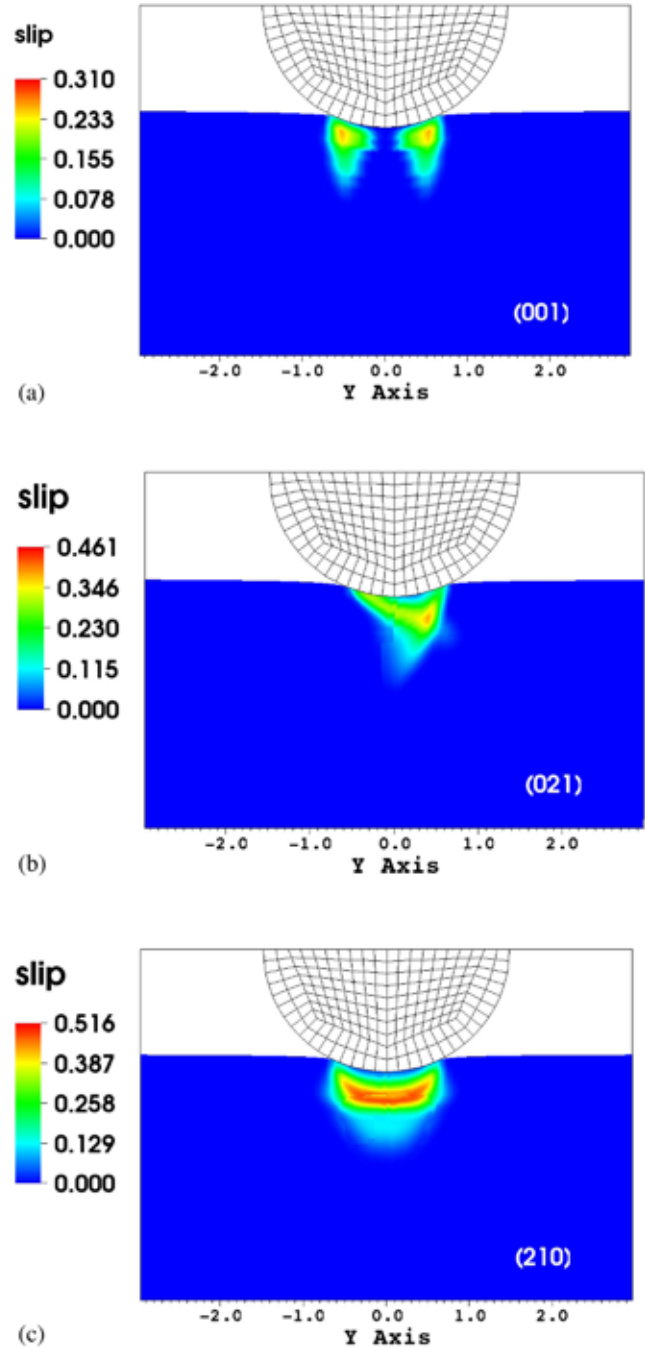


FIG. 3. Cumulative total slip contours for indentation to depth $D = 200$ nm using elastic constants from RUS (Ref. 15) and slip system strength $G/20$; a slice along the centerline of the cylinder normal to the laboratory X_1 axis is shown: (a) indentation into (001)[X-axis normal to (100)]; (b) indentation into (021)[X-axis normal to (100)]; (c) indentation into (210)[X-axis normal to ($\bar{2}30$)].

TABLE VI. Maximum local slip γ^k at indentation depth of 200 nm for indentation on (001), (021), and (210) planes; RUS elastic constants.¹⁵

System k	Plane (001)	Plane (021)	Plane (210)
1	0.01	0.19	0.40
2	0.01	0.00	0.40
3	0.08	0.16	0.29
4	0.08	0.00	0.29
5	0.00	0.10	0.51
6	0.31	0.41	0.16
all (γ)	0.31	0.46	0.52

experiments,⁶ surface fractures are detected only at loads significantly exceeding yield excursion.

Details of slip system interactions and pressure dependence of shear strength are omitted in the present model. Indentation experiments have suggested the importance of cross slip,⁶ and atomic modeling has noted that different slip mechanisms may become important at high pressures.⁸ Incorporation of these effects into a more complex slip model might provide closer agreement with experiment, e.g., if glide resistance were to decrease with pressure, since local pressures under the indenter can achieve several GPa.²⁸ Atomic modeling^{8,24} may provide insight into dependence of slip resistance on pressure (and temperature, etc.) not available from experimental methods.

Model predictions of cumulative slip for indentation to a depth of $D = 200$ nm onto planes (001), (021), and (210) are shown in Fig. 3. In each case, a slice along the centerline of the cylinder normal to the laboratory X_1 axis (i.e., X -axis) is shown. For indentation on (001) and (021) planes, the X_1 axis is normal to a (100) plane; for indentation on (210), the X_1 axis is approximately normal to a $(2\bar{3}0)$ plane. Cumulative total slip, γ , is defined as

$$\gamma = \sum_k \gamma^k = \sum_k \int |\dot{\gamma}^k| dt, \quad (11)$$

with γ^k the monotonically increasing cumulative slip on system k . Slip activity is greater for indentation into (021) and (210) planes than for indentation on (001). For this particular viewing plane, slip contours for indentation on (021) are noticeably asymmetric. The wireframe mesh of the indenter is drawn in each figure; in order to enable clear visualization of heterogeneous slip distributions in the RDX, the mesh of

TABLE VII. Maximum local slip γ^k at indentation depth of 200 nm for indentation on (001), (021), and (210) planes; Brillouin elastic constants.¹⁶

System k	Plane (001)	Plane (021)	Plane (210)
1	0.01	0.19	0.41
2	0.01	0.00	0.41
3	0.06	0.13	0.28
4	0.06	0.00	0.28
5	0.01	0.10	0.52
6	0.35	0.51	0.26
all (γ)	0.35	0.56	0.58

the substrate, which is considerably more refined than that of the indenter, is not shown.

Tables VI and VII list maximum local cumulative slip (i.e., the maximum value of γ^k at any location in the RDX substrate) at an indentation depth $D = 200$ nm when various elastic constants^{15,16} are implemented. Total slip, γ , listed in the bottom row of each table is not necessarily the sum of all γ^k listed in a given column, because the location in the substrate where total slip is maximum does not necessarily correspond to the location where each γ^k is maximum. Orientation (001) exhibits slip primarily on system 6. Significant activity of multiple slip systems is evident for indentation onto (021) and (210) planes. Trends are qualitatively similar, regardless of choice of elastic constants. Cumulative slip magnitudes are generally slightly larger in Table VII than in Table VI, because larger stresses are attained at the same depth of indentation when stiffer elastic constants are prescribed.

Elastic-plastic simulations were also performed, wherein the strength, τ_0^k , of one family of systems was set to $G/20$, with that of all others set to $G/10$. Comparison of force versus depth profiles among these simulations enabled further assessment of the most active slip systems for each crystal orientation.²⁸ Results were consistent with those in Tables VI and VII: slip system 6 is dominant for indentation on (001) and (021), while systems 1–5 are all important for indentation on (210).

Model predictions for uniform slip strengths, τ_0^k , of $G/10$, $G/20$, and $G/40$ are compared with experimental data⁶ in Fig. 4 for indentation on (210). Reduction of slip strength from $G/20$ to $G/40$ enables closer agreement with experiment at larger indentation depths, but also leads to premature initiation of slip and under-prediction of force at smaller depths

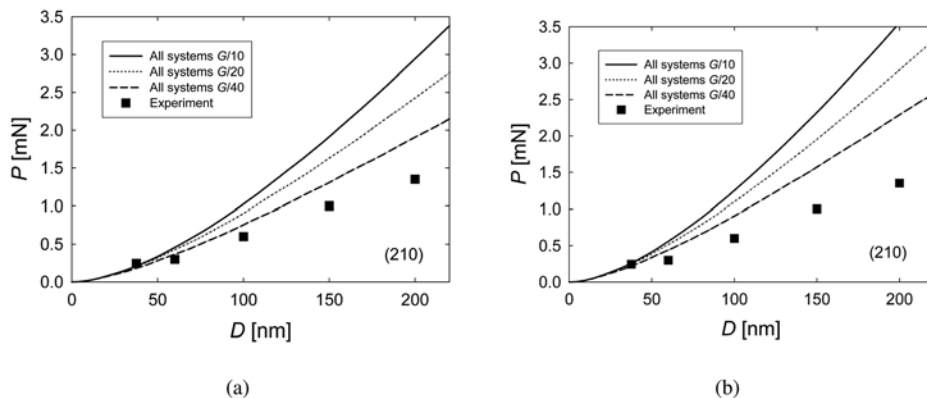


FIG. 4. Indentation force vs applied displacement for elastic-plastic indentation into plane (210) with uniform slip strengths $G/10$, $G/20$, and $G/40$ compared to experiment (Ref. 6); model predictions obtained using (a) RUS (Ref. 15) and (b) Brillouin (Ref. 16) elastic constants.

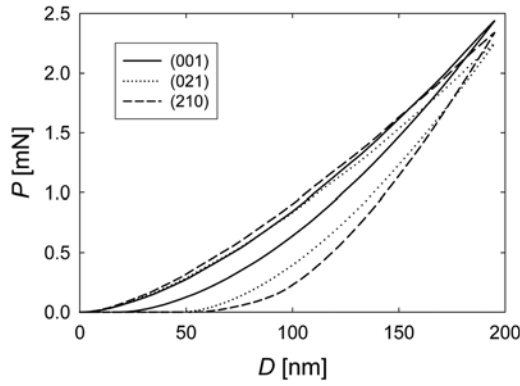


FIG. 5. Indentation force vs applied displacement for a single load-unload cycle on each of (001), (021), and (210) planes; elastic constants from RUS (Ref. 15), uniform slip strength $G/20$.

near experimental excursion points, i.e., near initial yield. Similar trends were predicted²⁸ for indentation onto (001) and (021) planes when strength is increased or decreased uniformly among slip systems.

Loading-unloading simulations of indentation on (001), (021), and (210) planes were performed to enable comparison with experimental observations. Force versus displacement predictions are shown in Fig. 5 for a single load-unload cycle, corresponding to loading to $D \approx 200$ nm and then unloading to $D = 0$. During much of the loading phase, orientation (001) is slightly less stiff than orientations (021) and (210). However, at $D \approx 200$ nm, P is largest for orientation (001). Recall that orientation (001) demonstrates a lower elastic stiffness, but also less slip

activity. Hence, at larger indentation depths, increased slip activity for orientations (021) and (210) lowers their effective tangent stiffness and, hence, P below that of orientation (001). Hysteresis is also substantially greater for indentation on (021) and (210) than for (001), again demonstrating less slip activity in the latter. Orientation (210) demonstrates the most hysteresis (and greatest slip activity) and the largest elastic stiffness for much of the unloading phase.

Figure 6 shows total cumulative slip, γ , on unloaded surfaces of (001), (021), and (210) planes. In each case, the maximum indentation depth prior to unloading is $D \approx 200$ nm. Non-circular contours are consistent with activity of fewer than five geometrically independent systems necessary to accommodate an arbitrary plastic strain field.⁶

Surface slip contours from individual systems were also examined.²⁸ Predicted surface slip activity results primarily from system 6 for indentation on (001). Slight contributions to the circular total slip trace in Fig. 6(a) are due to systems 3 and 4, i.e., $\{011\}[100]$. Surface slip activity is predominantly from system 6, with minor contributions from systems 1 and 3, for indentation on (021). Surface slip activity is predominantly from system 5, with contributions from systems 1, 2, and 6, for indentation on (210). Faint contributions from systems 3 and 4 are also predicted for indentation on (210).

Active slip planes during the loading history at the specimen surface, as predicted here, are compared with those deduced from experimental surface impressions⁶ in Table VIII. It is noted that, in simulations of indentation on (210),

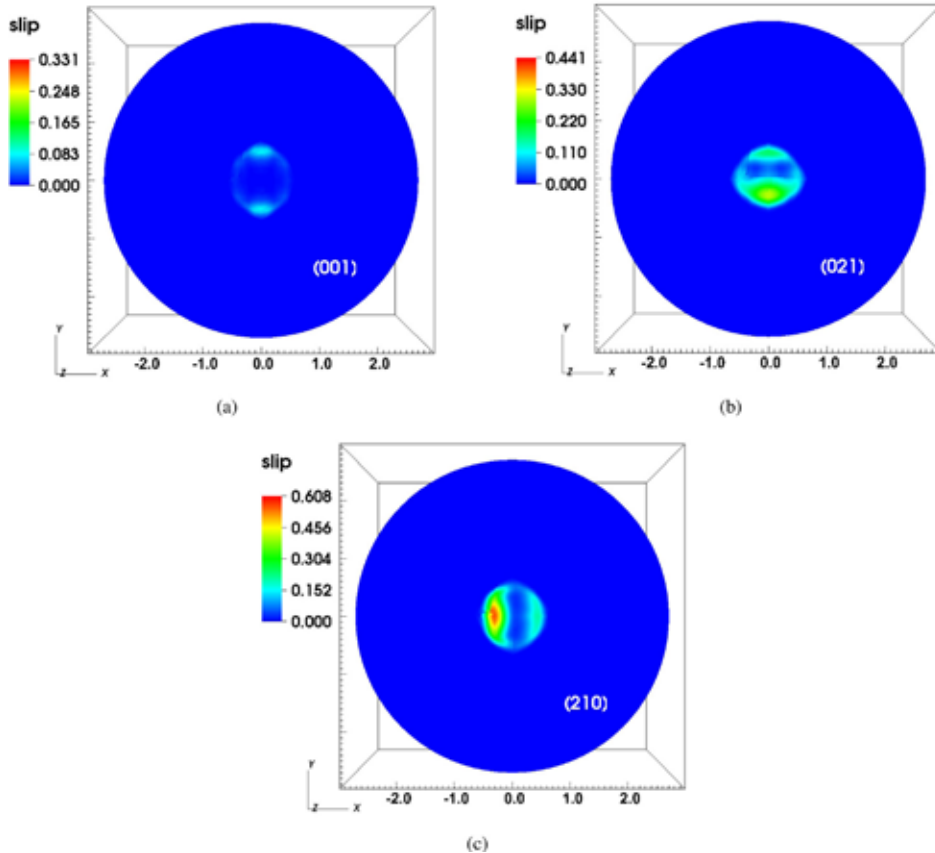


FIG. 6. Residual total slip contours at the surface for indentation to depth $D \approx 200$ nm followed by unloading; results obtained using elastic constants from RUS (Ref. 15) and uniform slip system strength $G/20$: (a) indentation into (001); (b) indentation into (021); (c) indentation into (210).

TABLE VIII. Significantly active slip planes at the specimen surface during indentation of (001), (021), and (210) planes.

Indentation surface	Present results	Experiment ⁶
(001)	(010), {011}	(010), {011}, {021}
(021)	(010), (011), (021)	Not reported
(210)	(010), {011}, {021}	(010), {011}, {021}

systems 3 and 4, i.e., {011}[100], demonstrate substantial activity within the bulk material (i.e., beneath the surface), but little cumulative slip at the surface. Though not presented graphically in this paper, predicted residual bulk and surface slip contours were also obtained using the relatively stiff elastic constants from Brillouin scattering.¹⁶ Predicted slip contours appeared qualitatively similar, regardless of choice of elastic constants from RUS¹⁵ or Brillouin.¹⁶

IV. CONCLUSIONS

A nonlinear anisotropic elastic-plastic model has been developed for RDX. The model accounts for orthorhombic elastic constants, pressure-dependent compressibility, and dislocation glide on up to six distinct slip systems.

Numerical simulations of spherical indentation on (001), (021), and (210) planes of single crystals show significant influences of elastic anisotropy and nonlinearity on force-displacement data. Model predictions for initial elastic response using constants measured with resonant ultrasound spectroscopy agree with experimental force-displacement data for indentation on (001), (021), and (210) planes. Predictions using constants measured with Brillouin scattering are in reasonable agreement with experiments for indentation on (210), but are stiffer than experiments for indentation on (001) and (021). Orientation (001) is elastically most compliant, in agreement with experiments.

Critical shear strengths associated with slip initiation have been estimated as $G/20$, where G is a representative elastic shear modulus. Initial yield points predicted by the model are in close agreement with experimental load excursion data when elastic constants from resonant ultrasound spectroscopy are used. Predictions of force for larger indentation depths, wherein predicted plastic slip is substantial, tend to exceed experimental values, regardless of which set of elastic constants is used. The constant strength (i.e., perfectly plastic) slip model implemented here is unable to replicate nearly horizontal steps in indentation force observed in experiments. Such steps may correspond to discrete slip events of width too fine to be captured by a conventional continuum slip model. Dependencies of shear strength on slip history and pressure have been omitted; incorporation of such physics, for example, as suggested by atomic simulations, might provide improved agreement. Fractures observed in experiments (at the surface) or not observed (subsurface) would also explain the higher stiffness in simulations relative to experiments.

Simulations suggest that slip planes (010) and {011} contain active systems for indentation on (001), with slip on

system (010)[001] dominating the inelastic response; experimental surface observations confirm that these, as well as {021} slip planes, may also be active. Simulations suggest that slip planes (010) and {021}, and to a lesser extent {011}, are active at the specimen surface for indentation on (210); these same planes have also been confirmed as active in experiments. Simulations suggest that planes (010), (011), and (021) contain active systems for indentation on (021); particular slip planes active for this orientation have not been reported from experiments.

The present results suggest that system (010)[001] provides the largest contribution to the inelastic material response (i.e., post-yield force versus displacement curve) for indentation on (001) and (021) planes, while five systems {021}[100], {011}[100], and (010)[100] all contribute to inelastic response for indentation on (210) planes. Plastic deformation and hysteresis are more extensive for indentation on (021) and (210) than for indentation on (001). Since much plastic deformation occurs in the bulk of the material, and since different slip mechanisms may be prominent at the surface and in the bulk, the present results offer new insight into inelastic mechanical behavior of RDX not available from experimental observations of residual surface topography alone.

The model developed here, when used with elastic constants obtained from resonant ultrasonic methods, is thought to provide an accurate representation of the nonlinear anisotropic response of RDX single crystals up to and including the onset of slip. The present model is also thought to provide a qualitatively reasonable depiction of activity of different slip systems when a uniform and constant shear strength on the order of $G/20$ is prescribed. Refinements of the model are needed to address any reduction in stiffness associated with discrete or highly localized shear events or cleavage fractures observed at larger indentation depths.

¹D. E. Hooks, K. J. Ramos, and A. R. Martinez, *J. Appl. Phys.* **100**, 024908 (2006).

²W. Connick and F. G. J. May, *J. Cryst. Growth* **5**, 65 (1969).

³P. J. Halfpenny, K. J. Roberts, and J. N. Sherwood, *J. Cryst. Growth* **65**, 524 (1983).

⁴W. L. Elban, R. W. Armstrong, K. C. Yoo, R. G. Rosemeier, and R. Y. Yee, *J. Mater. Sci.* **24**, 1273 (1989).

⁵H. G. Gallagher, P. J. Halfpenny, J. C. Miller, and J. N. Sherwood, *Philos. Trans. R. Soc. London, Ser. A* **339**, 293 (1992).

⁶K. J. Ramos, D. E. Hooks, and D. F. Bahr, *Philos. Mag.* **89**, 2381 (2009).

⁷K. J. Ramos, D. F. Bahr, and D. E. Hooks, *Philos. Mag.* **91**, 1276 (2011).

⁸M. J. Cawkwell, K. J. Ramos, D. E. Hooks, and T. D. Sewell, *J. Appl. Phys.* **107**, 063512 (2010).

⁹K. J. Ramos, D. E. Hooks, T. D. Sewell, and M. J. Cawkwell, *J. Appl. Phys.* **108**, 066105 (2010).

¹⁰N. R. Barton, N. W. Winter, and J. E. Reaugh, *Modell. Simul. Mater. Sci. Eng.* **17**, 035003 (2009).

¹¹J. J. Rimoli, E. Gurses, and M. Ortiz, *Phys. Rev. B* **81**, 014112 (2010).

¹²J. M. Winey and Y. M. Gupta, *J. Appl. Phys.* **107**, 103505 (2010).

¹³R. Becker, *Int. J. Plast.* **20**, 1983 (2004).

¹⁴B. Olinger, B. Roof, and H. H. Cady, *Proceedings of the International Symposium on High Dynamic Pressures* (Commissariat a l'Energie Atomique, Paris, 1978), pp. 3–8.

¹⁵S. Haussuhl, *Z. Kristallogr.* **216**, 339 (2001).

¹⁶J. J. Haycraft, L. L. Stevens, and C. J. Eckhardt, *J. Chem. Phys.* **124**, 024712 (2006).

¹⁷J. D. Clayton, *Nonlinear Mechanics of Crystals* (Springer, Dordrecht, 2011).

- ¹⁸H. H. Cady, *J. Chem. Eng. Data* **17**, 369 (1972).
- ¹⁹D. Bedrov, J. B. Hooper, G. D. Smith, and T. D. Sewell, *J. Chem. Phys.* **131**, 034712 (2009).
- ²⁰R. B. Schwarz, D. E. Hooks, J. J. Dick, J. I. Archuleta, and A. R. Martinez, *J. Appl. Phys.* **98**, 056106 (2005).
- ²¹B. Sun, J. M. Winey, N. Hemmi, Z. A. Dreger, K. A. Zimmerman, Y. M. Gupta, D. H. Torchinsky, and K. A. Nelson, *J. Appl. Phys.* **104**, 073517 (2008).
- ²²L. L. Stevens, D. E. Hooks, and A. Migliori, *J. Appl. Phys.* **108**, 053512 (2010).
- ²³T. D. Sewell and C. M. Bennett, *J. Appl. Phys.* **88**, 88 (2000).
- ²⁴L. B. Munday, P. W. Chung, B. M. Rice, and S. D. Solares, *J. Phys. Chem. B* **115**, 4378 (2011).
- ²⁵J. D. Clayton, *Proc. R. Soc. Ser. A* **465**, 307 (2009).
- ²⁶R. Nowak, T. Manninen, K. Heiskanen, T. Sekino, A. Hikasa, K. Niihara, and T. Takagi, *Appl. Phys. Lett.* **83**, 5214 (2003).
- ²⁷J. K. A. Amuzu, B. J. Briscoe, and M. M. Chaudhri, *J. Phys. D: Appl. Phys.* **9**, 133 (1976).
- ²⁸J. D. Clayton and R. C. Becker, U.S. Army Res. Lab. Tech. Report ARL-TR-5864, 2012.

Particle-Based Multiscale Coarse Graining with Density-Dependent Potentials: Application to Molecular Crystals (hexahydro-1,3,5-trinitro-s-triazine)

Sergei Izvekov, Peter W. Chung, and Betsy M. Rice

U.S. Army Research Laboratory, Aberdeen Proving Ground, MD

ABSTRACT

We describe the development of isotropic particle-based coarse-grain models for crystalline hexahydro-1,3,5-trinitro-s-triazine (RDX). The coarse graining employs the recently proposed multiscale coarse-graining (MS-CG) method, which is a particle-based force-matching approach for deriving free-energy effective interaction potentials. Though one-site and four-site coarse-grain (CG) models were parameterized from atomistic simulations of non-ordered (molten and ambient temperature amorphous) systems, the focus of the paper is a detailed study of the one-site model with a brief recourse to the four-site model. To improve the ability of the one-site model to be applied to crystalline phases at various pressures, it was found necessary to include explicit dependence on a particle density, and a new theory of local density-dependent MS-CG potentials is subsequently presented. The density-dependency is implemented through interpolation of MS-CG force fields derived at a preselected set of reference densities. The computationally economical procedure for obtaining the reference force fields starting from the interaction at ambient density is also described. The one-site MS-CG model adequately describes the atomistic lattice structure of α -RDX at ambient and high pressures, elastic and vibrational properties, pressure-volume curve up to $P = 10$ GPa, and the melting temperature. In the molten state, the model reproduces the correct pair structure at different pressures as well as higher order correlations. The potential of the MS-CG model is further evaluated in simulations of shocked crystalline RDX.

The Journal of Chemical Physics, Volume 135, Page 044112 (2011)

Particle-based multiscale coarse graining with density-dependent potentials: Application to molecular crystals (hexahydro-1,3,5-trinitro-s-triazine)

Sergei Izvekov,^{a)} Peter W. Chung, and Betsy M. Rice

U.S. Army Research Laboratory, Aberdeen Proving Ground, Maryland 21005, USA

(Received 21 January 2011; accepted 15 June 2011; published online 27 July 2011)

We describe the development of isotropic particle-based coarse-grain models for crystalline hexahydro-1,3,5-trinitro-s-triazine (RDX). The coarse graining employs the recently proposed multiscale coarse-graining (MS-CG) method, which is a particle-based force-matching approach for deriving free-energy effective interaction potentials. Though one-site and four-site coarse-grain (CG) models were parameterized from atomistic simulations of non-ordered (molten and ambient temperature amorphous) systems, the focus of the paper is a detailed study of the one-site model with a brief recourse to the four-site model. To improve the ability of the one-site model to be applied to crystalline phases at various pressures, it was found necessary to include explicit dependence on a particle density, and a new theory of local density-dependent MS-CG potentials is subsequently presented. The density-dependency is implemented through interpolation of MS-CG force fields derived at a preselected set of reference densities. The computationally economical procedure for obtaining the reference force fields starting from the interaction at ambient density is also described. The one-site MS-CG model adequately describes the atomistic lattice structure of α -RDX at ambient and high pressures, elastic and vibrational properties, pressure-volume curve up to $P = 10$ GPa, and the melting temperature. In the molten state, the model reproduces the correct pair structure at different pressures as well as higher order correlations. The potential of the MS-CG model is further evaluated in simulations of shocked crystalline RDX. [doi:10.1063/1.3607603]

I. INTRODUCTION

Modeling of molecular crystals is becoming an important tool to aid materials design in numerous applications ranging from drugs, electronic devices, and energetic materials. Computer simulations using the molecular dynamics (MD) simulation method based on sophisticated atomistic force fields have greatly advanced our understanding of dynamics in molecular solids on time and length scales difficult to readily access through experimental techniques. However, the MD modeling of molecular crystalline materials at the atomistic level encounters difficulties due to a significant disparity between characteristic time scales for intramolecular and lattice movements as the former are governed by strong intramolecular chemical bonds while the latter rely on the weak interactions between molecules, which are typically uncharged and non-polar. The presence of fast intramolecular modes in the molecular solids makes it nearly impossible to extend atomistic computer simulations to mesoscale using presently available computer power. Understanding behavior at such a scale is necessary in many areas such as study of microstructured and heterogeneous crystals, crystals with extended defects, or response of materials to external mechanical stimuli (shock, shear, etc.). The difficulties have prompted development of new approaches for computer simulations at the mesoscale. In recent years, particle-based coarse-graining approaches,

where groups of atoms are replaced with structureless interaction centers that interact through effective (coarse-grain) potentials, have grown increasingly popular. A large variety of schemes for constructing such potentials has been reported in the literature (for recent reviews see Ref. 1).

The development of coarse-grain (CG) potentials for condensed-phase systems presents additional challenges beyond the accuracy and validity of the underlying atomistic potentials.^{1,2} The first difficulty is a so-called “representability paradigm” as a general impossibility to design a CG potential which is able to reproduce every property of the atomistic ensemble even at a single thermodynamic state.³ For example, the thermodynamics of a CG ensemble of N particles matches that of the reference atomistic ensemble if the CG potential accurately approximates the atomistic free energy $W(\mathbf{R}^N)$ in CG coordinates $\mathbf{R}^N = (\mathbf{R}_1, \dots, \mathbf{R}_N)$. However, at non-zero temperature T , the $W(\mathbf{R}^N)$ potential, which can be referred to as the free-energy based CG potential, cannot reproduce the total average internal potential energy of the system, $U(\mathbf{R}^N)$, as the $W(\mathbf{R}^N)$ contains both the potential energy and the entropic contributions associated with averaged out atomistic coordinates as $W(\mathbf{R}^N) = U(\mathbf{R}^N) - TS(\mathbf{R}^N)$. This feature is one prominent manifestation of the representability problem. CG potentials derived to match the atomistic free-energy $W(\mathbf{R}^N)$ are preferable as they can correctly reproduce the density correlations in the CG ensemble, and therefore the correct thermodynamics. Another difficulty associated with the use of CG potentials is due to poor state-point transferability as the potentials naturally

^{a)} Author to whom correspondence should be addressed. Electronic mail: sergiy.izvekov@us.army.mil.

depend on the thermodynamic state at which they were parametrized.^{4,5} The CG modeling of molecular compounds is further complicated by the fact that there is no “universal” functional form to describe CG interactions as, for example, a Lennard-Jones form to represent short-ranged dispersion interactions between atoms. Moreover, the functional form suitable to parameterize the CG interactions could not be even determined *a priori* from physical principles and in most cases a numerical representation is the only way to fit CG potentials accurately. Furthermore, CG potentials are essentially many-body functions and must be pairwise decomposable for ease of implementation and low computational expense.

Recently, an efficient *bottom-up* force-matching (FM) based approach was developed which properly addresses the above challenges. This method, the multiscale coarse-graining (MS-CG) method,⁵⁻⁹ is similar to conventional structure inversion methods (e.g., Boltzmann inversion, Schommers inversion,¹⁰ or Inverse Monte Carlo¹¹ approaches) which are all based on Henderson’s uniqueness theorem,¹² in that it yields a pairwise decomposition of the *all-particle* CG potential of mean force (PMF), but better captures higher order correlations of the reference ensemble. The MS-CG method can be naturally extended to include dependence on thermodynamic state variables such as density. Importantly, the MS-CG method yields a force field which can be implemented directly into MD codes, as the MD method does not require knowledge of the potential to integrate the dynamics. This becomes an advantage if the density dependency is introduced.

Thus far, the MS-CG method has been extensively applied to soft-matter systems.⁹ Because the quality of numerical MS-CG models depend on how well the intermolecular separations are sampled, the MS-CG approach would be difficult to apply directly to crystals. The goal of this research is to explore to what extent a FM model from the disordered phase (e.g., liquid) is transferable to crystalline structures. We discuss application of the MS-CG method to coarse-grain intermolecular interactions in hexahydro-1,3,5-trinitro-s-triazine (RDX), which is an important energetic crystal widely used as a secondary explosive and in propellants. The primary model we investigate is a one-site model in which every molecule of RDX in the crystal is represented using a coarse-grained particle with a single interaction site. However, on several occasions it is useful to also discuss and compare the one-site results with those of a four-site model. One of the major applications we sought for our one-site MS-CG model is studying crystalline RDX under a shock load. Therefore, to improve transferability to high pressures, we introduce a computationally economical procedure for constructing a density-dependent potential, which follows the recipe outlined in Ref. 5. We also present a new theory for local density dependent MS-CG potentials, which were previously introduced in our recent work⁵ at a rather *ad hoc* level.

We proceed as follows: In Sec. II, we describe the computational method and present new theory for local-density dependent potentials. In Sec. III, we describe details of application of the developed formalism to coarse graining of crystalline RDX. We discuss the derivation of MS-CG potentials, their validation, and then report applications of the

MS-CG model to study shocked RDX. Conclusions are given in Sec. IV.

II. METHOD

A. MS-CG method

The MS-CG method is described elsewhere^{5,8,9} as a FM-based approach for constructing free-energy based CG potentials (e.g., Gibbs potential for *NPT* or Helmholtz potential for *NVT* ensembles). The MS-CG approach uses the configurations and associated forces sampled from the atomistic (we assume here canonical, *NVT*) ensemble of n atoms partitioned into N groups to construct a pairwise additive approximation to the free-energy (Helmholtz) potential,

$$W^{atm}(\mathbf{R}^N, N, V, T) = -kT \ln \langle \delta(\mathbf{r}^n - \mathbf{R}^N) \rangle, \quad (1)$$

in the CG coordinates $\mathbf{R}^N = (\mathbf{R}_I, I = 1, N)$, which describe translational degrees of freedom (dof) of the groups. In Eq. (1) $\mathbf{r}^n = (\mathbf{R}^N, \mathbf{x}^P)$ are canonical atomistic coordinates, where \mathbf{x}^P denotes integrated out (intragroup) dof. The brackets $\langle \dots \rangle$ denote the canonical average. In terms of coordinates \mathbf{x}^P and their conjugated momenta \mathbf{p}_x^P , we can write $\langle \delta(\mathbf{r}^n - \mathbf{R}^N) \rangle$ as an ensemble average over \mathbf{x}^P ,

$$\langle \delta(\mathbf{r}^n - \mathbf{R}^N) \rangle \equiv \langle 1 \rangle_{\mathbf{x}^P} = \frac{1}{Z_n} \int d\mathbf{x}^P \exp[-\beta U^{atm}(\mathbf{R}^N, \mathbf{x}^P)], \quad (2)$$

where $U^{atm}(\mathbf{R}^N, \mathbf{x}^P)$ is the atomistic potential energy function; Z_n is the system partition function excluding the kinetic contribution; and $\beta = 1/kT$. The $N! \langle \delta(\mathbf{r}^n - \mathbf{R}^N) \rangle = \Delta(\mathbf{R}^N)$ is an N -particle distribution function. The \mathbf{R}_I coordinate can be any weighted average $\mathbf{R}_I = \sum_{i=1, s_I} c_{Ii} \mathbf{r}_i$, where $\sum_{i=1, s_I} c_{Ii} = 1$ and s_I is the number of atoms in the I th group. Commonly, the \mathbf{R}_I coordinate is associated with the group’s center-of-mass (c.m.); i.e., $c_{Ii} = m_i/M_I$, where m_i , M_I are atom and group masses. The dependence of W^{atm} on the number of intraparticle dof P and the volume V_P in \mathbf{x}^P space develops due to the ensemble average over \mathbf{x}^P in Eq. (2). For a fixed number of intraparticle dof per CG particle, the P and V_P variables can be replaced with the number of CG particles N and the volume of the CG system V . Furthermore, the CG coordinates \mathbf{R}^N may be viewed as thermodynamic state variables for the thermodynamic potential W^{atm} . Finally, the CG Hamiltonian which governs the dynamics in CG system becomes

$$H^{CG}(\mathbf{P}^N, \mathbf{R}^N, N, V, T) = \sum_{I=1, N} \frac{\mathbf{P}_I^2}{2M_I} + W^{atm}(\mathbf{R}^N, N, V, T), \quad (3)$$

where \mathbf{P}_I is the momentum of the CG particle conjugated to \mathbf{R}_I .

The MS-CG interaction is constructed through force-matching of the thermodynamic force field,

$$\mathbf{F}_I^{\text{PMF}}(\mathbf{R}^N, N, V, T) = -[\nabla_{\mathbf{R}_I} W^{atm}(\mathbf{R}^N, N, V, T)]_{N, V, T}. \quad (4)$$

The \mathbf{F}^{PMF} field is an ensemble average over the \mathbf{x}^P dof,

$$\mathbf{F}_I^{\text{PMF}}(\mathbf{R}^N, N, V, T) = \frac{\langle \mathbf{F}_I^{\text{CG}}(\mathbf{R}^N, \mathbf{x}^P) \rangle_{\mathbf{x}^P}}{\langle 1 \rangle_{\mathbf{x}^P}}, \quad (5)$$

of the atomistic instantaneous c.m. force field

$$\mathbf{F}_I^{\text{CG}}(\mathbf{R}^N, \mathbf{x}^P) = \sum_{i=1, s_I} \mathbf{f}_i, \quad (6)$$

where \mathbf{f}_i are instantaneous atomistic forces. Therefore, the MS-CG interaction potential W^{atm} [Eqs. (1) and (2)] can be interpreted as an N -particle PMF. Now, define a function $\mathbf{G}_I^{\text{MSCG}}(\mathbf{R}^N, \Omega)$ that has an additive decomposition into pairwise and central force fields

$$\mathbf{G}_I^{\text{MSCG}}(\mathbf{R}^N, \Omega) = \sum_{J \neq I} g^{\text{MSCG}}(R_{IJ}, \Omega) \mathbf{n}_{IJ}, \quad (7)$$

where $\mathbf{R}_{IJ} = \mathbf{R}_I - \mathbf{R}_J$, $R_{IJ} = |\mathbf{R}_{IJ}|$, $\mathbf{n}_{IJ} = \mathbf{R}_{IJ}/R_{IJ}$, and Ω is a set of adjustable parameters. A least-squares approximation of $\mathbf{F}_I^{\text{PMF}}$ can be obtained from $\mathbf{G}_I^{\text{MSCG}}(\mathbf{R}^N, \Omega_0)$ by finding the optimal set $\Omega_0 \in \Omega$ that minimizes⁵

$$\chi(\Omega) = \left\langle \sum_{I=1, N} |\mathbf{F}_I^{\text{CG}}(\mathbf{R}^N, \mathbf{x}^P) - \mathbf{G}_I^{\text{MSCG}}(\mathbf{R}^N, \Omega)|^2 \right\rangle. \quad (8)$$

Then, the potential

$$W^{\text{MSCG}}(\mathbf{R}^N, \Omega) = \sum_{I < J} w^{\text{MSCG}}(R_{IJ}, \Omega), \quad (9)$$

where

$$w^{\text{MSCG}}(R, \Omega) = \int_R^\infty dR' g^{\text{MSCG}}(R', \Omega), \quad (10)$$

implements a pairwise decomposition of the $W^{\text{atm}}(\mathbf{R}^N, N, V, T)$. In a practical implementation of the MS-CG method, the $g^{\text{MSCG}}(R, \Omega)$ function in Eq. (7) can be a cubic spline function defined on a mesh $\{R_k\}$ up to a preselected cut-off distance R_{cut} . The problem of minimizing $\chi(\Omega)$ is then reduced to an overdetermined system of linear equations, which is solved using a block-averaging scheme.^{5,6} As shown in Ref. 5, the MS-CG procedure eliminates part of the atomistic free energy associated with the integrated-out dof, resulting in a pressure deficiency in the CG ensemble. This deficiency can be corrected using a virial constraint^{5,6} in Eq. (8).

It is worthwhile to comment on the difference between the MS-CG methodology and the RDF inversion methods, which are based on the Henderson's uniqueness theorem.¹² The Henderson's theorem postulates the existence of a unique isotropic pairwise effective potential in a system of same-type particles with an arbitrary interaction which reproduces the RDF of the ensemble. Such an effective potential, $w^H(R) = w^H(R, N, V, T)$, can be found using the target RDF $g(R)$ as an input through an iterative scheme.¹⁰ The $g(R)$ is related to the two-particle PMF as

$$W^{\text{atm}}(\mathbf{R}^2) = -kT \ln[\Delta(\mathbf{R}^2)] = -kT \ln[\rho^2 g(R_{12})], \quad (11)$$

where $\Delta(\mathbf{R}^2) = \int_{V_{N-2}} d\mathbf{R}^{N-2} \Delta(\mathbf{R}^N)/(N-2)!$ is a two-particle distribution function and ρ is the particle's density. Similar to the MS-CG potential, the $w^H(R)$ represents an approximate *pairwise* decomposition of the *all(N)-particle* PMF

as $W^{\text{atm}}(\mathbf{R}^N) \approx \sum_{I < J} w^H(R_{IJ}) = W^H(\mathbf{R}^N)$ [cf. Eq. (9)]. It can be shown that in the N -particle ensemble with the interactions described by the $w^H(R)$, the $W^{\text{atm}}(\mathbf{R}^2)$ and therefore two-particle correlations are reproduced exactly. On the other hand, the MS-CG approximation $w^{\text{MSCG}}(R)$ is not necessary to reproduce the *exact* two-particle PMF and corresponding RDF. Rather, the $w^{\text{MSCG}}(R)$ is biased to approximate the entire spectrum of the k -particle PMFs ($k = 2, N$), resulting in better capturing of the many-particle correlations.

B. Density-dependent MS-CG potentials

As the $W^{\text{MSCG}}(\mathbf{R}^N, \Omega)$ represents a pairwise approximation to the system free energy $W^{\text{atm}}(\mathbf{R}^N, N, V, T)$, it is explicitly dependent on the ensemble thermodynamic state variables N , V , and T , thus limiting the state-point transferability^{3,4,13} of the model. In the homogeneous equilibrium system, such as bulk crystal or liquid, the W^{atm} is a function of the global density $\rho_G = N/V$ as $W^{\text{atm}}(\mathbf{R}^N, \rho_G, V, T)$ or $W^{\text{atm}}(\mathbf{R}^N, N, \rho_G, T)$, depending on whether N or V is chosen as an independent thermodynamic variable.

Strictly speaking, as briefly discussed in Sec. II A, since the canonical average in Eq. (2) is over \mathbf{x}^P , the W^{atm} depends on the total number of intraparticle dof P and volume V_P of the phase subspace \mathbf{x}^P sampled by the system and therefore on the global density $\rho_{P,G} = P/V_P$. The $\rho_{P,G}$ can be replaced with the density of CG particles ρ_G under the assumption of a fixed number of intraparticle dof per CG particle and if $V_P \propto V$. For the density-dependent potentials, it is convenient and correct to assume that the $\rho_{P,G}$ (or equivalently ρ_G) is not determined by either the dimension of CG coordinate phase space N or the CG particle coordinates \mathbf{R}^N , and is actually an independent thermodynamic variable. For similar reasons, we can regard V_P (or equivalently V) as a state variable independent of $\rho_{P,G}$ (ρ_G) and \mathbf{R}^N . We will assume $\rho_{P,G} = \rho_G$, $V_P = V$, and use $N_G = \rho_G V$ to distinguish the dimension of intraparticle phase space from the dimension N of CG configuration \mathbf{R}^N .

The CG interaction can be viewed as an effective interaction between particles immersed into a “sea” of intraparticle dof density that may vary. In such a picture, the “intraparticle” chemical potential,

$$\mu(\mathbf{R}^N) = \left(\frac{\partial W^{\text{atm}}}{\partial N_G} \right)_{\mathbf{R}^N, V, T} = \frac{1}{V} \left(\frac{\partial W^{\text{atm}}}{\partial \rho_G} \right)_{\mathbf{R}^N, V, T}, \quad (12)$$

determines a response of the effective interaction in an ensemble of N CG particles due to a change in density of intraparticle dof under constant configuration of CG particles (\mathbf{R}^N), V , and T . Within this formalism, all thermodynamic equations relating the Helmholtz free energy potential and other thermodynamic potentials, which are functions of state variables \mathbf{R}^N , N , V , T , remain valid. The above picture is analogous to the effective electron mediated ion-ion interactions in a nuclei-electron plasma, with electrons considered as “intraparticle” dof, if the latter are well localized at the nuclei.

C. Global density dependency

Improved transferability with regard to both density and temperature conditions can be achieved directly by incorporating dependence on a global density $\rho = \rho_G$ in the MS-CG potential.⁵ Following Ref. 5, the global density potential can be implemented using a linear interpolation of the MS-CG forces parameterized at several reference densities ρ_i as

$$\begin{aligned} g^{\text{MSCG}}(R, \rho) &= a_\rho \times g^{\text{MSCG}}(R, \rho_{i+1}) \\ &\quad + (1 - a_\rho) \times g^{\text{MSCG}}(R, \rho_i), \\ a_\rho &= \frac{\rho - \rho_i}{\rho_{i+1} - \rho_i}, \quad \rho \in [\rho_i, \rho_{i+1}], \end{aligned} \quad (13)$$

where i is an index over a finite number of states selected for the parameterization. The forces $g^{\text{MSCG}}(R, \rho)$ in Eq. (13) can then be used directly in MD simulations. In contrast, Eqs. (9) and (10) cannot be used to calculate the total potential energy of the CG system with respect to any other reference state of a different density (including a vacuum), as an assumption of a density change along system trajectories leads to

$$\begin{aligned} \mathbf{G}_I^{\text{MSCG}}(\mathbf{R}^N, \rho) &= -\nabla_{\mathbf{R}_I} W^{\text{MSCG}}(\mathbf{R}^N, \rho) \\ &\quad - [W^{\text{MSCG}}(\mathbf{R}^N, \rho)]'_\rho \nabla_{\mathbf{R}_I} \rho. \end{aligned} \quad (14)$$

However, if we assume that the force field $\mathbf{G}_I^{\text{MSCG}}(\mathbf{R}^N, \rho)$ can be uniquely integrated to a potential function (which is a reasonable assumption even for the local density approximation¹⁴), then the total energy is pairwise and can still be determined using Eq. (9) with

$$w^{\text{MSCG}}(R, \rho) = \int_R^\infty dR' g^{\text{MSCG}}(R', \rho(R')), \quad (15)$$

where $\rho(R') = \frac{R'^3}{R^3} \rho$. Therefore, the total potential energy using Eqs. (9) and (15) is obtained by calculating the work by the $\mathbf{G}_I^{\text{MSCG}}(\mathbf{R}^N, \rho)$ force field as the system uniformly expands from the initial state with the density ρ , and thus represents the interparticle potential energy with respect to infinite separation of the particles.

Importantly, for a piecewise interpolation of Eq. (13), the potential Eq. (15) is continuously differentiable with respect to density, and therefore the chemical potential μ [Eq. (12)] is a continuous function of the density. This can be seen by transforming the potential to an integral over $\rho' = R'^3/R^3 \rho$ as

$$\begin{aligned} w^{\text{MSCG}}(R, \rho) &= \frac{R}{3\rho^{2/3}} \left[\int_\rho^{\rho_1} + \sum_{i=1, i_{\max}-1} \int_{\rho_i}^{\rho_{i+1}} + \int_{\rho_{i_{\max}}}^0 \right] \\ &\quad \times d\rho' \rho'^{-1/3} g^{\text{MSCG}}(\rho'^{1/3} \rho^{-1/3} R, \rho'), \end{aligned} \quad (16)$$

and then easily verifying that for the linear interpolation Eq. (13) $[w^{\text{MSCG}}(R, \rho_i + 0)]'_\rho = [w^{\text{MSCG}}(R, \rho_i - 0)]'_\rho$, and therefore $w^{\text{MSCG}}(R, \rho)$ is continuously differentiable with respect to ρ .

D. Local density dependency

For simulations of macroscopically structured systems such as those with multiple phases, under external fixed potential, or quasiequilibrium states such as within a shock front, the potentials need to be dependent on local density $\rho = \rho(\mathbf{R}^N)$. Under constant NVT conditions, the local density refers to the number of particles within the elemental volume in the configurational phase space. Since the number of particles within this elemental volume defined by the local density is not a constant, the local density potential refers rather to the grand-canonical (constant chemical potential-volume, μVT) ensemble instead of NVT . This observation can be used to find a representation of a local density potential for the NVT ensemble, which is consistent with the existence of global density variable. Recall that $W^{\text{atm}}(\mathbf{R}^N, \rho_G, V, T)$ is considered to be a function of the global density of *intraparticle* dof ρ_G and corresponding volume as introduced in Sec. II A with a respective interpretation of the chemical potential $\mu(\mathbf{R}^N)$ Eq. (12). We will derive this relation for a homogeneous system that can be characterized by a spatially uniform $\mu(\mathbf{R}^N)$, meaning that μ is *not* a function of \mathbf{x}^P .

Using the Legendre transformation, the constant μVT potential [see Eq. (12)] is introduced as

$$W^{\text{atm}}(\mathbf{R}^N, \mu, V, T) = W^{\text{atm}}(\mathbf{R}^N, \rho_G, V, T) - \mu \rho_G V. \quad (17)$$

The corresponding equation for the MS-CG pairwise approximation Eqs. (9) and (10) is

$$\begin{aligned} W^{\text{MSCG}}(\mathbf{R}^N, \mu, V, T) &= \sum_{I=1, N} \left(W_I^{\text{MSCG}}(\mathbf{R}^N, \rho_G, V, T) - \frac{\mu}{N} \rho_G V \right) \\ &= \sum_{I=1, N} \left(W_I^{\text{MSCG}}(\mathbf{R}^N, \frac{\mu}{N}, V, T) \right), \end{aligned} \quad (18)$$

where

$$W_I^{\text{MSCG}}(\mathbf{R}^N, \rho, V, T) = \frac{1}{2} \sum_{J \neq I} w^{\text{MSCG}}(R_{IJ}, \rho, V, T). \quad (19)$$

At this step, in order to proceed with defining a local density, we have to make an assumption on the nature of the dependence of $W_I^{\text{MSCG}}(\mathbf{R}^N, \rho, V, T)$ on ρ . Because $w^{\text{MSCG}}(R_{IJ}, \rho, V, T) = 0$ for $R_{IJ} > R_{\text{cut}}$, and therefore the sum in Eq. (19) is over only those particles which are within R_{cut} of the I th site, we may postulate that

$$W_I^{\text{MSCG}}(\mathbf{R}^N, \rho, V, T) = W_I^{\text{MSCG}}(\mathbf{R}^N, \rho_I, V, T), \quad (20)$$

where we introduce the “local” density

$$\rho_I = N_I / V^{R_{\text{cut}}}, \quad (21)$$

and where $V^{R_{\text{cut}}} = V_I$ is the volume of sphere of radius R_{cut} centered at the I th particle, and N_I is a number of intraparticle dof within the sphere. In other words, Eq. (20) assumes that the effective potential W_I^{MSCG} experienced by the I th CG particle is sensitive to changes in its local density of only those intraparticle dof which are associated with the CG

particles with which the I th particle interacts. Note, that V in the r.h.s. of Eq. (20) should not be replaced with V_I because the W_I^{MSCG} is an *extensive* function of V . Otherwise, if $W_I^{\text{MSCG}}(\mathbf{R}^N, \rho_I, V, T) = W_I^{\text{MSCG}}(\mathbf{R}^N, \rho_I, V_I, T)$, the chemical potential $\mu(\mathbf{R}^N)$ [Eq. (12)] will be a spatially varying function of intraparticle coordinates \mathbf{x}^P , thus contradicting the assumption that the system is homogeneous. Next, in applying the Legendre transformation [Eq. (17)] to terms W_I^{MSCG} in the last sum in Eq. (18), we obtain

$$W^{\text{MSCG}}(\mathbf{R}^N, \mu, V, T) = \sum_{I=1, N} W_I^{\text{MSCG}}(\mathbf{R}^N, \rho_I, V, T) - \frac{\mu}{N} \sum_{I=1, N} \rho_I V. \quad (22)$$

Now, we can introduce the “global” density variable as

$$\rho_G = \frac{1}{N} \sum_{I=1, N} \rho_I, \quad (23)$$

and again using the transformation in Eq. (17), we derive a relation between the global and local density MS-CG potentials as

$$W^{\text{MSCG}}(\mathbf{R}^N, \rho_G, V, T) = W^{\text{MSCG}}(\mathbf{R}^N, \mu, V, T) + \mu \rho_G V = \sum_{I=1, N} W_I^{\text{MSCG}}(\mathbf{R}^N, \rho_I, V, T). \quad (24)$$

It is easily seen that in the thermodynamic limit ($N \rightarrow \infty$, $N/V = \text{const}$), the definition in Eq. (23) is equivalent to $\rho_G = N/V$.

Next, Eq. (24), with only the density dependence shown, can be written explicitly in a pairwise form as

$$W^{\text{MSCG}}(\mathbf{R}^N, \rho_G) = \sum_{I < J} w^{\text{MSCG}}(R_{IJ}, \rho_I, \rho_J), \quad (25)$$

whereupon using Eq. (15) we may write

$$w^{\text{MSCG}}(R_{IJ}, \rho_I, \rho_J) = \frac{1}{2} (w^{\text{MSCG}}(R_{IJ}, \rho_I) + w^{\text{MSCG}}(R_{IJ}, \rho_J)). \quad (26)$$

Note that similar to W^{MSCG} and W_I^{MSCG} , the $w^{\text{MSCG}}(R, \rho, V)$ should be considered as extensive functions of V . Eqs. (25) and (26) represent a pairwise implementation of the local density potential.

If we assume that the spatial variation of the density is small,

$$\rho_I = \rho_G + \delta\rho_I, \delta\rho_I/\rho_G \ll 1, \quad (27)$$

then the potential in Eq. (26) can be approximated as

$$w^{\text{MSCG}}(R_{IJ}, \rho_I, \rho_J) \cong w^{\text{MSCG}}\left(R_{IJ}, \rho_G + \frac{1}{2}(\delta\rho_I + \delta\rho_J)\right) = w^{\text{MSCG}}(R_{IJ}, \rho_{IJ}), \quad (28)$$

where

$$\rho_{IJ} = \frac{1}{2}(\rho_I + \rho_J). \quad (29)$$

Equation (28) results in a computationally more efficient scheme, as the potential $w^{\text{MSCG}}(R, \rho)$ requires the knowledge of the density at a single point instead of two as in Eq. (26) and can be used in simulations if the spatial variation of density on length scales $l \sim R_{\text{cut}}$ is relatively small. In our derivations, the \mathbf{R}^N are considered as independent thermodynamic state variables, and therefore $w^{\text{MSCG}}(R_{IJ}, \rho_I)$ and $g^{\text{MSCG}}(R_{IJ}, \rho_I)$ are related by Eq. (10); then Eqs. (26) and (28) can be written for forces. In particular, in the limit Eq. (27), we introduce the density dependent pairwise force as

$$g^{\text{MSCG}}(R_{IJ}, \rho_I, \rho_J) = g^{\text{MSCG}}(R_{IJ}, \rho_{IJ}) \quad (30)$$

which was introduced in our previous work in Ref. 5 on an *ad hoc* level. An alternative to Eq. (29) could be

$$\rho_{IJ} = \max(\rho_I, \rho_J), \quad (31)$$

which agrees with Eq. (29) to within $O(\delta\rho_I/\rho_G)$. To obtain the potential with respect to a gas of non-interacting CG particles, the force in Eq. (30) should be integrated in accordance to Eq. (15). Such a potential should be also utilized to calculate the system total energy in the simulations of inhomogeneous systems.

In closing, we would like to make several important conclusions on the applicability of the local density potentials presented in Eqs. (21) and (25), and (26): (I) The local density can be introduced if the free energy W^{atm} is separable into a sum of “local” terms W_I^{atm} associated with each CG site. The pairwise approximation gives a natural way [see Eqs. (10), (15) and (19)] to construct such a separable representation. In principle, under certain circumstances, the partitioning of the free-energy potential into local terms (i.e., constructing the local density approximation) could be accomplished for systems with many-body interactions; (II) The notion of local density involves *all* particles within the range of interaction. Therefore, the local density becomes poorly defined for systems with long-ranged interactions; (III) It is generally incorrect to use the definition of local density as in Eq. (21) with an arbitrarily small $V^{R_{\text{cut}}}$.

It is instructive to compare the above formalism with the formalism for many-body conservative potentials which are free-energy based and density dependent, as developed by Pagonabarraga and Frenkel.^{14,15} Their postulates of the notion of local and global densities and their relation are similar to those which we have derived more rigorously.

Within the approach developed by Allen and Rutledge,^{13,16} the local density potentials are derived by inverting the RDFs [or two-particle PMFs, see Eq. (11)] at local densities, which are related to the RDF at the global density through consistency equations. Because the MS-CG potentials represent a similar inversion of the N -particle PMF, the method by Allen and Rutledge can be readily generalized to the MS-CG potentials. Unfortunately, the consistency equations of Allen and Rutledge are formulated in terms of energy, whereas the present MS-CG method requires forces. Therefore, the application of this technique to MS-CG potentials has not been attempted.

E. Parameterization of density dependency

Ideally, $g^{\text{MSCG}}(R, \rho_i)$ in Eq. (13) should be obtained from separate atomistic simulations at the appropriate thermodynamic conditions at each reference density ρ_i . For RDX however, the slow intermolecular dynamics in dense states precludes a sufficiently large sampling of atomistic configurations for the purpose of FM at $P \geq 2$ GPa. For this reason, we developed a less direct but computationally more efficient scheme to construct a reference potential set $\{g^{\text{MSCG}}(R, \rho_i)\}$ than that used in our earlier study for liquid nitromethane (NM).⁵ The scheme is based on the difference between two MS-CG potentials calculated for NM in accordance with Eq. (10), one of which corresponds to $g^{\text{MSCG}}(R, \rho_i)$ derived without a virial constraint and the other derived with a virial constraint. The former MS-CG potential is pressure deficient while the latter produces the correct pressure. In that study, we showed that the difference between the two potentials is close to a linearly decaying function. In the same study, we observed that the density contribution can be described in the CG potential by a linear term over a fairly broad range of densities. This suggests that for $\rho_i > \rho_0$, where ρ_0 is the ambient density, the force term $g^{\text{MSCG}}(R, \rho_i)$ can be constructed as a sum of ambient $g^{\text{MSCG}}(R, \rho_0)$ and a constant term, where the latter has the linearly decaying potential. We used the form

$$g^{\text{MSCG}}(R, \rho_i) = g^{\text{MSCG}}(R, \rho_0) + g_i^{\text{MSCG}}(R), \quad (32)$$

where $g^{\text{MSCG}}(R, \rho_0)$ was force-matched to the atomistic simulation at the ambient density and the $g_i^{\text{MSCG}}(R)$ is approximated as

$$g_i^{\text{MSCG}}(R) = \begin{cases} g_i, & R \leq R_{\text{cut}} - \delta_R \\ g_i \sin\left(\frac{(R_{\text{cut}} - R)\pi}{\delta_R}\right), & R_{\text{cut}} - \delta_R < R \leq R_{\text{cut}} \\ 0, & R > R_{\text{cut}} \end{cases} \quad (33)$$

In order to improve energy conservation in the dynamics simulations, the $g_i^{\text{MSCG}}(R)$ force is smoothly attenuated to zero within a δ_R distance to R_{cut} [second line in Eq. (33)]. In the past, a linear correction similar to Eq. (33) has been used to improve pressure properties in structure-based coarse-graining frameworks.¹⁷

For each $\rho_i > \rho_0$, the parameter g_i was adjusted to reproduce the atomistic $V - P$ isotherm of the atomistic α -RDX bulk crystal as discussed below. As discussed later, varying only the parameter g_i at higher pressures is not always sufficient to obtain the target density while preserving the correct lattice symmetry. To improve the match in the density, the $g_i^{\text{MSCG}}(R)$ term was subjected to additional rescaling modification as

$$g_i^{\text{MSCG}}(R, a) = \frac{1}{a} g_i^{\text{MSCG}}\left(\frac{1}{a} R\right) \quad (34)$$

with regard to an adjustable parameter, a .

Similar to Ref. 5, we will refer to the $g^{\text{MSCG}}(R, \rho_i)$ interactions as MS-CG/ P_i , where P_i is the pressure which corresponds to ρ_i , while the corresponding density dependent model introduced in accordance to Eq. (13) is referred to as the MS-CG-D model. Within the MS-CG-D model, for

systems with a macroscopically inhomogeneous particle density, the local density Eqs. (21) and (26) should be used. This scheme was used to evaluate the local density dependence of the interactions in systems with strong density gradients such as in shock fronts. In the systems in which the density gradients are deemed to be relatively small (e.g., simulations of melting), we used the computationally simpler scheme from Eqs. (21), (28), and (31). In equilibrium homogeneous simulations such as bulk phases, the density in the latter scheme was replaced with the $\rho_G = N/V$ as discussed in Secs. II B and II C.

Practically, in the CG simulations, the $g^{\text{MSCG}}(R, \rho_i)$ were stored as two-dimensional data arrays. In simulations with local density dependent potentials, the local density for each particle was evaluated at each time step of a MD simulation by counting the particles within a sphere of radius R_{cut} centered at the particle. All local densities were then rescaled uniformly to satisfy the consistency equation Eq. (23) with the instant global density $\rho_G = N/V$ as estimated from a current system volume. For the system sizes used in the study, Eq. (23) is well satisfied, so that the rescaling of local densities is not necessary. The pairwise forces were then evaluated through the interpolation scheme in Eq. (13) and the total system energy was updated using Eq. (15) if necessary. Therefore, in the simulations of inhomogeneous systems, the interaction between the CG particles changes at each step of the dynamics following the density changes.

III. RESULTS AND DISCUSSION

A. Reference atomistic simulations and details of coarse graining

Atomistic MD simulations of the RDX systems were performed using the all-atom flexible force field developed by Smith and Bharadwaj (SB model).^{18,19} The SB model accurately predicts many physical properties of crystalline RDX, including its crystal structure, elastic properties, and thermal expansion.²⁰ This model was also employed to simulate RDX under shock conditions.²⁰ We will also use data from all-atom simulations using the Sorescu-Rice-Thompson (SRT) force field,^{21,22} which is rigid body, and also the force field by Boyd *et al.*²³ for comparison with the MS-CG-D results.

The coarsening of the RDX molecule into one- and four-site models is depicted in Fig. 1. As discussed in the Introduction, the present version of the MS-CG method cannot use reference data sampled from simulations of ordered (e.g. crystalline) systems due to the piecewise functional form of the pairwise terms $g^{\text{MSCG}}(R_{IJ}, \Omega)$ [Eq. (7)]. Therefore, two noncrystalline systems were used to obtain reference trajectory and force data. The first was molten RDX at $T = 550$ K, and the second was disordered RDX obtained by annealing the molten RDX to $T = 350$ K. Electrostatic interactions were treated with the Ewald method²⁴ and the short-ranged interactions were cut off at 1.0 nm. The simulations were carried out at $P = 0$ GPa and a cubic supercell containing 144 molecules was used. Periodic boundary conditions were imposed in all directions. The constant isobaric-isothermal (NPT) conditions were simulated using Melchionna's modification of the Hoover algorithm, in which

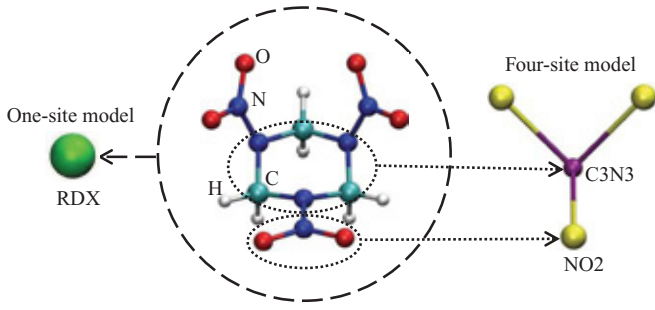


FIG. 1. Coarse graining of the RDX molecule into one-site and four-site representations.

the equations of motion couple a Nosé-Hoover thermostat and a barostat,²⁵ with relaxation times of 0.5 and 3 ps, respectively.²⁵

First, the two systems were equilibrated under constant NPT conditions for 10 and 30 ns, respectively. The configurations, velocities, and forces were then sampled from constant NVT simulations and these data were then used in the subsequent CG FM procedure. The value of the instantaneous virial was recorded for each configuration during the NVT stage and later imposed through the virial constraint during the force-matching.⁵ The 550 K system was simulated for 30 ns with configurations recorded at 2 ps intervals; the 350 K system was simulated for 60 ns with configurations recorded at 4 ps intervals, thus providing a total of 15 000 configurations for each system to be used in the FM procedure. The sampled data were then transformed into the CG coordinates of interest (either molecular or group c.m.) and merged such that each high temperature configuration was followed by the lower temperature one.

The merged 350 K and 550 K state point data (350/550 K sampling) were used to parameterize the one-site MS-CG force field at $P = 0$ GPa (MS-CG/0 model). The MS-CG/0 was served as a base interaction in the procedure outlined in Sec. II E to build the MS-CG/ $P_i, P_i > 0$, force fields and then the MS-CG-D model as described in details in Sec. III B and III C. For a comparison, we also force-matched the one-site model from only “pure” state point 550 K data. Two four-site models, which are non-density dependent, were developed from the 350K/550 K and only 550 K data, respectively. The MS-CG forces were determined using the block averaging scheme^{5,6} with the block size of 10 on a radial mesh with bin size of 0.1 a.u. The cutoff $R_{cut} = 29$ a.u. (15.35 Å) for one-site models and $R_{cut} = 23$ a.u. (12.17 Å) for four-site models were used.

The atomistic and CG MD simulations were performed using the DL_POLY 2.20 simulation package,²⁶ which was modified to enable density dependency of the interactions in accordance with Eqs. (13) and (15).

B. MS-CG potentials without density dependency

The one-site effective force as yielded by the force-matching to mixed 350/550 K and pure (molten) 550 K state points at ambient pressure are displayed in Fig. 2(a). The corresponding one-site MS-CG/0 potentials are shown in Fig. 2(b). The MS-CG potential cannot be determined at short

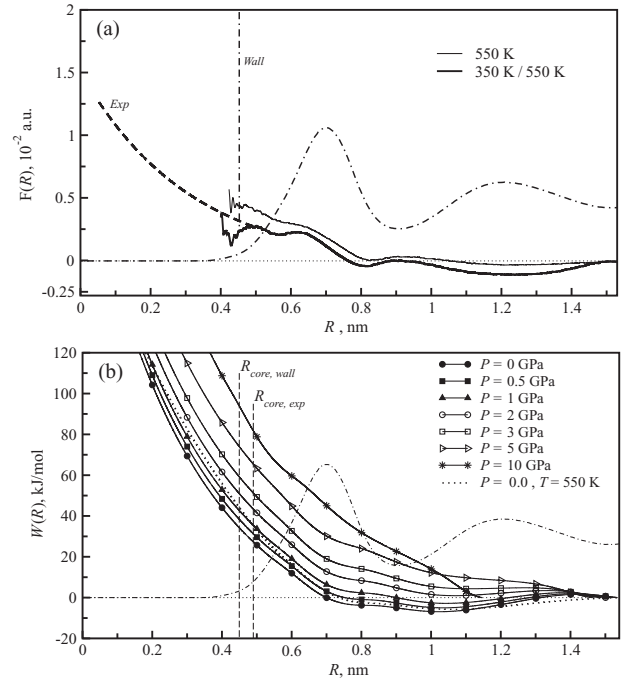


FIG. 2. Panel (a): One-site MS-CG force profiles as obtained from force-matching to 550 K (thin solid) and 350/550 K (thick solid) samplings. For 350/550 K force (MS-CG/0 model), possible choices of core interactions corresponding to core distances outlined in panel (b) in vertical lines are shown in dash-dash-dotted (hard-wall core) and dashed (exponential core). Panel (b): One-site MS-CG potentials at different pressures and $T = 300$ K. Vertical dashed lines mark possible selections of the core distance. Shown are potentials at P (GPa): 0 (filled circles), 0.5 (filled squares), 1 (filled triangles), 2 (empty circles), 3 (empty squares), 5 (empty triangles), 10 (stars). The $P = 0$ GPa potential corresponds to 350 K/550 K force in panel (a). Dotted line shows the potential corresponding to 550 K force in panel (a). On both panels dot-dashed line outlines the atomistic c.m.-c.m. RDF in arbitrary units.

distances $R < R_{core}$ (referred to as the core region), since this region is not sampled in the reference simulation; therefore, the MS-CG potential must be extrapolated in this region. The exponential core (shown in Fig. 2) typically produces slightly better results (e.g. RDFs) at ambient conditions. However, at shocked states the hard-wall potential (also shown in Fig. 2) performed slightly better and, therefore, was chosen for the calculations presented here.

A more portable representation of the 350/550 K MS-CG/0 force can be obtained through a least-squares fit of the tabulated spline data by powers of $1/R$

$$g(R) = \sum_{n=2}^{n_{max}} A_n / R^n. \quad (35)$$

A better fit can be obtained with the more rapidly convergent Chebyshev series

$$g(R) = A_0/2 + \sum_{n=1}^{n_{max}} A_n T^n(\bar{R}), \quad (36)$$

where $T^n(\bar{R})$ is the Chebyshev polynomial of degree n and

$$\bar{R} = (2/R - 1/R_{core} - 1/R_{cut}) / (1/R_{core} - 1/R_{cut}). \quad (37)$$

TABLE I. Coefficients A_n of the least-squares fit of the one-site MS-CG force at $P = 0$ GPa using the polynomial equation (35) (second column) and Chebyshev series equations (36) and (37) (third column), with power of the term n shown in the first column. Atomic units for force and distance were used. For the Chebyshev series, the following radii were used in Eq. (37): $R_{core} = 8.5$ a.u., $R_{cut} = 29.011$ a.u. The expansions were switched to zero using the linear switching function as in Eq. (33) with $\delta_R = 4.0$ a.u. for a polynomial expansion and with $\delta_R = 2.0$ a.u. for a Chebyshev expansion. The fourth column shows the values of parameters for the density dependent contribution Eq. (33). At $R < R_{core} = 8.5$ a.u., the force extrapolated as discussed in Sec. III B. A cutoff of 1.535 nm must be applied to the expansions.

n	A_n, Pol (a.u.)	$A_n, Cheb$ (a.u.)	g_i, a (a.u.)
0	0.0	$0.295090311504 \times 10^{-02}$	$P = 0.5$ GPa:
1	0.0	$0.187126981336 \times 10^{-02}$	$0.7745 \times 10^{-4}, 1.0$
2	-164.77839357004	$-0.249111348590 \times 10^{-04}$	$P = 1$ GPa:
3	39914.936788713	$-0.620876162674 \times 10^{-03}$	$1.8 \times 10^{-4}, 1.0$
4	-3312200.9193869	$0.143777893709 \times 10^{-03}$	$P = 2$ GPa:
5	140675713.66804	$-0.445005999642 \times 10^{-04}$	$3.6 \times 10^{-4}, 0.9784$
6	-3525421465.5670	$0.429487649160 \times 10^{-04}$	$P = 3$ GPa:
7	55168999115.916	$-0.212373560733 \times 10^{-03}$	$5.4 \times 10^{-4}, 0.9679$
8	-543866611821.71	$0.257218649672 \times 10^{-04}$	$P = 5$ GPa:
9	3253068550427.9	$0.244979561419 \times 10^{-03}$	$8.6 \times 10^{-4}, 0.9534$
10	-10456759286650	$-0.761237529621 \times 10^{-04}$	$P = 10$ GPa:
11	11504453156792	$-0.952354112853 \times 10^{-04}$	$1.88 \times 10^{-3}, 0.7468$
12	10486861064266	$0.163080035111 \times 10^{-04}$	
13	4483868093300.0	$0.389889598497 \times 10^{-04}$	
14	1370873909039.2	$-0.605523294055 \times 10^{-04}$	

The $n_{max} = 14$ was selected for both expansions Eqs. (35) and (36). The summary of polynomial representations is given in Table I. To improve energy conservation in the MD simulation, the polynomials were smoothed at R_{cut} as described in the caption to the table. In both cases, slight differences in properties may result from simulations using these analytical representations when compared to results using the tabulated MS-CG potentials and forces.

C. Density dependent one-site MS-CG model

Next, the global density dependency to the MS-CG/0 model was added in accordance with the procedure outlined in Sec. II E. The density dependence was introduced by parameterizing the set $\{g_i^{MSCG}(R, \rho_i)\}$ to reproduce the $V - P$ isotherm for the reference atomistic system at preselected pressures. Because $P(V) = -\partial W / \partial V$, where W is the total free energy of the system, the ability of the MS-CG potentials to reproduce the atomistic $P(V)$ ensures a correct change of the free energy W under a change in pressure (and, therefore, density) as well as the system's compressibility. The latter determines the magnitude of particle density fluctuations, and therefore thermodynamics of the particle ensembles including those under constant volume conditions. To reproduce the atomistic ensemble thermodynamics, the density fluctuations in the CG ensemble must match those in the atomistic system. Conclusively, the correct compressibility and, thus, density dependency of the CG interactions is important to have even in *constant volume* simulations. The compressibility can be viewed as a measure of the model transferability to different density states in the vicinity of the reference state.

Furthermore, because MS-CG/ P_i potentials represent a pairwise decomposition of the free energy of reference atomistic system in the CG coordinates, the correspondingly parameterized MS-CG-D model should yield the correct free energetics of the CG ensemble. The reference system was chosen to be the ambient crystal.

Under ambient thermodynamic conditions the most stable crystalline phase of RDX is the α -polymorph, in which RDX adopts an orthorhombic unit cell containing eight molecules in the space group $Pbca$.²⁷ The parameters g_i and a in Eqs. (33) and (34) were optimized to reproduce the density of the bulk α -RDX from constant stress-temperature (NsT) simulations at pressures 0.5, 1, 2, 3, 5, 10 GPa and at $T = 300$ K. Because of the large cutoff of the MS-CG interactions (15.35 Å), the CG simulations used a supercell composed of $4 \times 6 \times 6$ unit cells of α -RDX. At $P \geq 2$ GPa, the target ρ_i could not be achieved by merely varying the repulsion parameter g_i . At small g_i , the crystal collapses into a structure of a different symmetry than that of the experimental crystal. At sufficiently large g_i , the target crystal structure is stable but its density is too low. For this reason, fitting was done in two steps. In the first step, the repulsion g_i was decreased to the value for which the structure is still stable but would undergo change with a further decrease of g_i . Next, the $g_i^{MSCG}(R)$ [Eq. (33)] was rescaled according to Eq. (34) with the factor a being adjusted to achieve the target ρ_i . The corresponding potentials from the resulting forces $g_i^{MSCG}(R, \rho_i)$ [Eq. (10)] are depicted in Fig. 2(b). The MS-CG potentials and forces used in all simulations reported herein are in tabular form and can be obtained upon request. The simulations with local density potentials were performed as described at the end of Sec. II E. Because the calculation of the system total energy using Eq. (15) is computationally expensive, it was performed only when the total energy was required (e.g., to calculate thermodynamic quantities).

D. Crystal structure

We compared the lattice structure of the molecular c.m. of bulk α -RDX with the crystal structure by the MS-CG-D model at $T = 4.5$ K. The atomistic MD supercell was a $2 \times 3 \times 3$ block of crystallographic unit cells (144 molecules) of α -RDX. The MS-CG-D simulations were performed using a $4 \times 6 \times 6$ supercell and under constant NsT ensemble conditions and using global density dependent potentials as discussed in Sec. II E. Remarkably, the relaxed MS-CG-D supercell maintained orthorhombic symmetry with the CG site positions being close to the molecular c.m. within the corresponding atomistic supercell. The striking similarity can be seen from Fig. 3, in which the atomistic unit cell and the corresponding rectangular block from the MS-CG-D supercell are superimposed. For purposes of comparison, we will denote this latter rectangular block of eight sites as the MS-CG "unit cell". The unit cell geometries and corresponding densities from the atomistic and MS-CG-D models are compared in Table II. The differences between the atomistic and MS-CG-D lattices can be better seen in Fig. 4, and can be characterized as small shifts of certain crystallographic

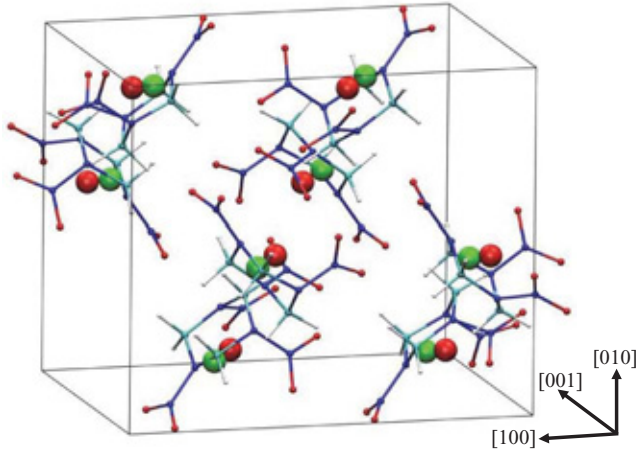


FIG. 3. Comparison of RDX unit cells calculated at $T = 4.5$ K using atomistic and MS-CG-D models. For the atomistic model unit cell, red balls denote the molecular c.m. locations superimposed upon the ball-and-stick representations of the molecules, whereas green balls denote the CG interaction sites.

planes. An analysis of the MS-CG lattice indicates that it is of a higher symmetry, that of hexagonal close-packed (hcp) A3-type (Pearson symbol hP2, space group $P6_3/mmc$). The hP2 lattice has two sites in the unit cell and coordination number of 12 [see Fig. 5(c)]. The highest packing efficiencies are found in hcp and fcc lattices. However, the observed hP2 lattice is not a structure of highest density for the MS-CG/0 potential (without density dependency). In computer experiments exploring the compressibility of this crystal, we found that under external stimuli (e.g., stress), the hP2 lattice described by the MS-CG/0 potential irreversibly transforms into a higher density structure with crystalline domains that differ from hP2 symmetry as shown in the insert to Fig. 4(a). The new packing has a higher density by 3% as compared to the hP2 lattice. This is one artifact of the MS-CG model. Similar domains appear at the solid-liquid interface in the MS-CG-D simulations as discussed below [Sec. III H and Fig. 7(a)].

Unfortunately, the four-site model is unable to produce a correct crystal symmetry beyond approximately 30 K. The CG crystal configuration evolves into a state with significant orientational disorder regardless of the initial configuration. However, the density remains close to the atomistic value. A strong anisotropy of the site-site interactions within the crys-

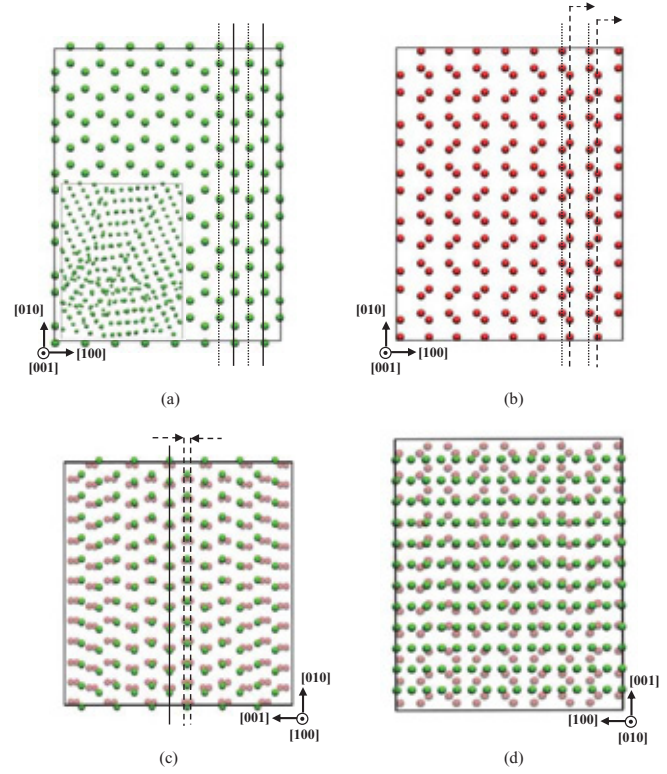


FIG. 4. Comparison of the α -RDX crystal lattice structure from simulations using the atomistic (red balls denote molecular c.m.) and MS-CG-D (green balls) models. Panel (a): [001]-view of lattice from the MS-CG-D simulation; Panel (b): Same view as in panel (a) for the atomistic model; Panel (c): [100]-view of superimposed lattices; Panel (d): [010]-view. In panels (a), (b), and (c) dotted and dashed lines outline location of planes in the atomistic lattice, which correspond to planes shown in dotted and solid lines for MS-CG-D lattice. In panel (b), atomistic planes (dashed) move to new locations in MS-CG-D lattice (solid) in panel (a). In panel (c), the two distinct planes in the atomistic representation (dashed) collapse into a single plane in the MS-CG representation (solid line).

tal arrangement, likely between the ring (C3N3) and NO₂ sites (see Fig. 1), which cannot be represented adequately by spherically isotropic interactions within the four-site description, is probably one reason for the non-transferability of the four-site model to the crystalline structures. In this sense, the one-site RDX model is advantageous as it lacks orientational dof and, thus, does not suffer from orientational melting due to an anisotropy of molecular-molecular interactions being averaged within the one-site description. As a remedy, a finer coarse graining, possibly of the ring group, may be exercised to build the CG models having orientational dof, which are capable of reproducing the atomistic crystal symmetry of the RDX.

E. Pairwise structure in molten phase

Radial distribution functions (RDFs), which map out pair correlations, is an important test for the quality of the free-energy based CG model. As shown in Fig. 5(a), all MS-CG/0 models produce liquid RDFs in satisfactory agreement with the respective atomistic c.m. RDF. The one-site MS-CG/0 model matched to 550 K sampling naturally gave a better RDF as compared to the 350/550 K potential. For $P > 0$ GPa,

TABLE II. Lattice parameters a , b , c and density ρ of the RDX crystal at different T and $P = 0$ GPa from atomistic and MS-CG-D models.

	$a(\text{nm})$	$b(\text{nm})$	$c(\text{nm})$	$\rho(\text{kg/m}^3)$
$T = 4.7$ K:				
atm (SB)	13.36	11.33	10.34	1885
MS-CG-D	13.93	12.06	10.10	1739
$T = 298$ K:				
atm (SB)	13.46	11.53	10.53	1805
atm (SRT) ^a	13.40	11.80	10.73	1740
MS-CG-D	13.96	12.09	10.13	1726
Expt ^b	13.18	11.57	10.71	1806

^a $T = 300$ K (Refs. 22 and 34).

^b $T = 300$ K (Ref. 27).

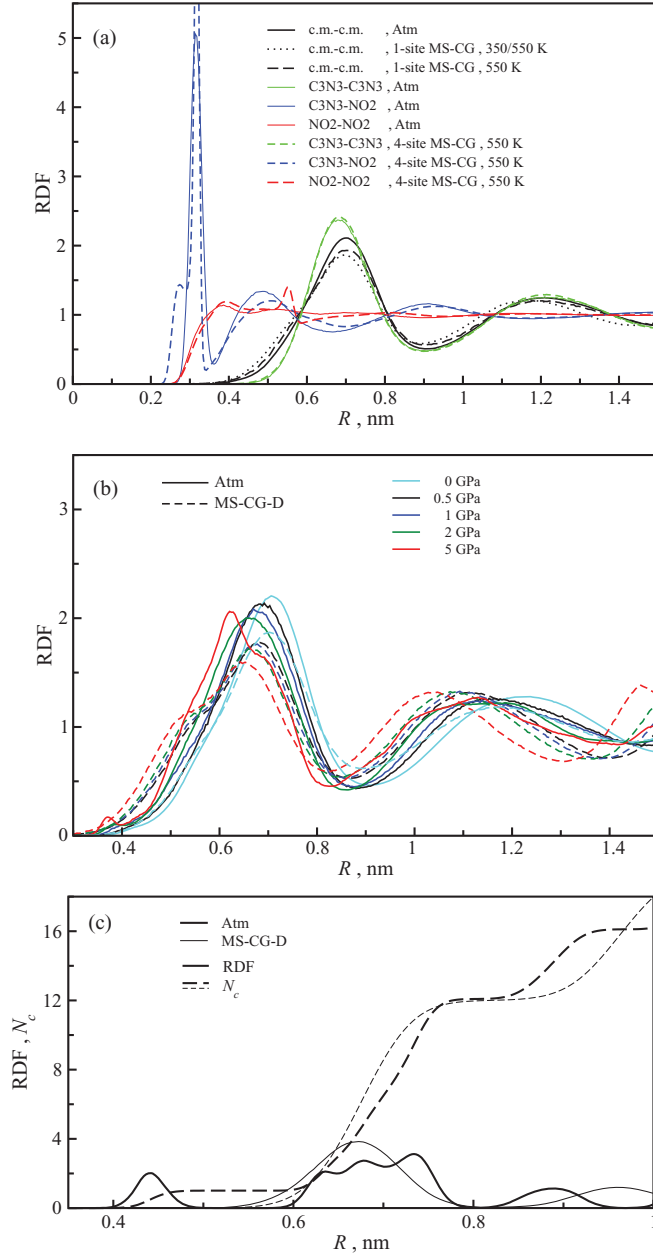


FIG. 5. Panel (a): c.m. RDFs from atomistic (solid), MS-CG 350/550 K (dotted), and 550 K (dashed) simulations of liquid RDX at $T = 550$ K using one-site (black) and four-site (color) MS-CG models. Panel (b): c.m. RDFs from atomistic (solid) and one-site MS-CG-D (dashed) simulations at different P . Shown are P (GPa): 0 (cyan), 0.5 (black), 1 (blue), 2 (green), and 5 (red). Panel (c): c.m. RDFs from atomistic (thick solid) and MS-CG-D (thin solid) simulations of crystalline RDX at $T = 300$ K. The corresponding running coordination number N_c shown in dashed lines.

we employed the *ad hoc* procedure of Eq. (33) to construct the reference $g^{MSCG}(R, \rho_i)$ [Eq. (13)] and thus, the results may not yield the same result as that produced by direct application of the force-matching. Therefore, we have tested the validity of the MS-CG-D model produced using Eqs. (8), (33), and (34) by comparing the predicted liquid RDFs under different pressures with the atomistic simulations [both shown in Fig. 5(b)]. As is evident, the MS-CG-D model describes adequately the pressure dependence of the liquid structure. For example, the first maximum in the atomistic RDF decreases

in intensity by 0.18 and shifts by 0.041 nm to shorter separations as the pressure increases from ambient to 2 GPa, in satisfactory agreement with the respective values of 0.17 and 0.040 nm from the MS-CG-D model. At $P = 5$ GPa, structure appears in the first peak in the atomistic RDF reflecting an increased molecular order in the first coordination shell. For liquid NM, the one-site MS-CG model, which was force-matched explicitly to a liquid phase under 5 GPa, was able to reproduce accurately similar increases in structure in the first coordination shell under high pressures.⁵ The MS-CG-D model using the *ad hoc* density dependency is not able to capture such changes in the effective interaction. However, the MS-CG-D RDF exhibits a step-like structure in the front slope, which gradually develops as more pressure is applied. This structure vaguely resembles the shape of the front slope of the atomistic RDF and the similarity becomes more pronounced with increasing pressure. These observations suggest that the g_i used in Eq. (33) may reflect relevant pressure effects in the effective intermolecular interactions. Finally, in Fig. 5(c), we present the RDFs from crystal simulations. The features in the crystal MS-CG RDF are consistent with those of close-packed structure. In particular, the coordination is 12. The atomistic lattice has 12 molecules within a shell of the size of the MS-CG first coordination shell (0.8 nm), however, the density is structured within this shell.

In Fig. 5(a), we also present a comparison of RDFs for the four-site model [Fig. 1] force-matched to the 550 K data. As seen, the four-site model yields the structure, which is in very good agreement with its atomistic counterpart.

F. Many-body effects

The RDFs provide a measure of the correlation between pairs of particles only, whereas an orientational order parameter can provide a measure of many-body correlations in a system. Therefore, the ability of the MS-CG-D model to capture the many-body correlations can be determined by comparing the distributions of an orientational order parameter with those generated from an atomistic model. While several forms of orientational order parameters are available,²⁸ we have chosen a form similar to that introduced to study tetrahedral close-range ordering in liquid water.²⁹ For the I th site, we introduce the instantaneous order parameter as

$$\psi_I = 1 - \frac{1}{N_c} \frac{3}{8} \sum_{K=1, N_c} (\cos \theta_{IK} - 1)^2, \quad (38)$$

where the θ_{IK} is the smallest angle formed by the vector R_{IK} joining the I th site and the K th closest site from the preselected coordination shell of N_c sites in the liquid configuration and the analogous vector in the reference (crystal) configuration. In the perfect (i.e., reference crystal) alignment, $\langle \psi_I \rangle = 1$ where $\langle \dots \rangle$ denotes ensemble averaging. If the arrangement is random, as in an ideal gas, then $\langle \psi_I \rangle = 0$. The averaging ψ_I among the I site and the J sites in its coordination shell yields an averaged local order parameter

$$\bar{\psi}_I = \frac{1}{N_c + 1} \left(\psi_I + \sum_J \psi_J \right). \quad (39)$$

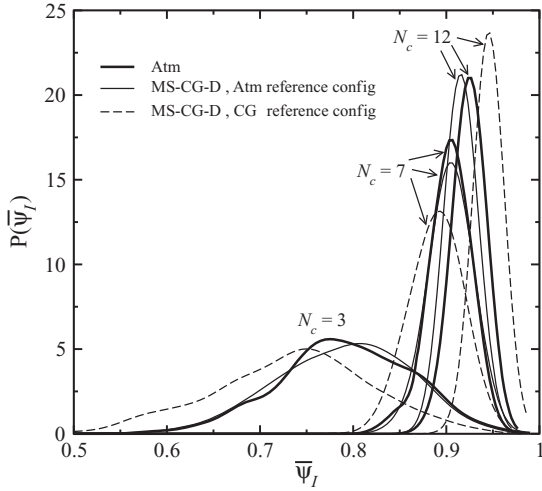


FIG. 6. Distributions of the order parameter Eqs. (38) and (39) with different coordination number N_c for atomistic (thick) and MS-CG-D (thin) models. The MS-CG-D results shown for reference crystal structure $\{R_{IK}\}$ from atomistic (solid) and MS-CG-D (dashed) models.

The order parameter $\langle \tilde{\psi}_I \rangle$ is a convenient parameter for monitoring (orientational) amorphization of the crystal. The global order parameter $\tilde{\psi}$ is the average of $\tilde{\psi}_I$ over all sites in the system. The level of agreement between the atomistic and MS-CG-D distributions $P(\tilde{\psi}_I)$ is a measure of how well the local N_c -body correlations are captured by the MS-CG models. In partially ordered phases such as in a liquid, the exact shape of the $P(\tilde{\psi}_I)$ is determined by the set of reference vectors $\{R_{IK}\}$ as well by the size of the coordination shell N_c . Fig. 6 shows the atomistic and MS-CG-D $P(\tilde{\psi}_I)$ for different N_c and different reference structures. The atomistic distributions were calculated with the $\{R_{IK}\}$ for the optimized atomistic lattice, while the MS-CG-D $P(\tilde{\psi}_I)$ were calculated for both the atomistic and MS-CG-D $\{R_{IK}\}$. The atomistic and MS-CG-D distributions agree remarkably well if the same (atomistic) reference structure is used, thus affirming the ability of MS-CG-D model to capture the higher-than-pairwise correlations in liquid state.

G. Melting

We determined the melting temperature T_{melt} of the CG crystal from the solid-liquid coexistence (two-phase) method.³⁰ The melting point of the MS-CG crystal was estimated from a solid-liquid mixture with a planar interface as shown in Fig. 7(a) and using local density dependent potentials as elaborated in Sec. II E. The interface was prepared by joining liquid and solid slabs of material simulated at 480 K. The sample contained 9206 sites. The interface moves into the solid phase if $T > T_{melt}$ and moves in the opposite direction or remains stationary if $T < T_{melt}$. The dynamics of the liquid-solid interface was monitored using temporal profiles of $\tilde{\psi}(z)$, which is calculated by averaging $\tilde{\psi}_I$ within a slab of a preselected width centered at z (see Fig. 11, where similar profiles shown for the shocked sample). The T_{melt} was determined from a series of NsT simulations at different temperatures starting with $T = 480$ K, and increasing the

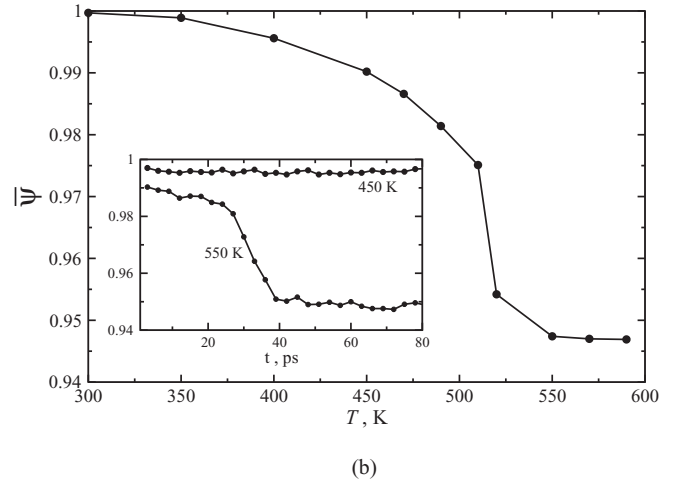
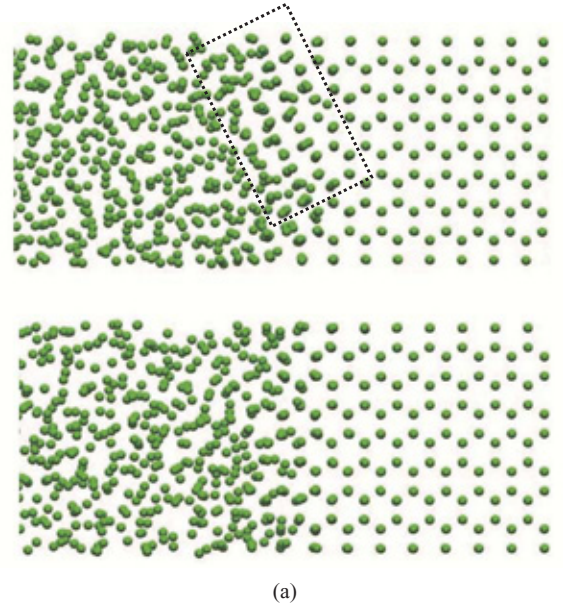


FIG. 7. Panel (a): Snapshots of the liquid-solid interface from simulation of slab melting at $T = 490$ K, at which close-packed structure formed at the interface (upper), and more common configuration (bottom). In the upper snapshot, the closed-packed domains of different hP2 structure are contoured by dotted line. Such domains are artifact of the model reflecting limited transferability of the model to heterogeneous structures such as interfaces. These domains are similar to those shown in inset to Fig. 4(a) and discussed in the text. Panel (b): Equilibrium global order parameter, $\tilde{\Psi}$, Eq. (39) with $N_c = 12$ as a function of T for crystal. Inset shows $\tilde{\Psi}(t)$ for crystal at $T = 450$ and 550 K.

temperature in increments of 5 K. The melting temperature was obtained ($T_{melt} = 490$ K) and is in reasonable agreement with the experimental value of 462 K. The atomistic SRT model used with a flexible intramolecular potential energy function predicts $T_{melt} = 439$ K.³¹

The $\tilde{\psi}(T)$ curve for the bulk crystal is shown in Fig. 7(b). As seen the crystal needs to be superheated to $T = 510 - 520$ K before it starts melting. Above this range, it takes about 40 ps for the sample to melt [Fig. 7(b) inset]. In atomistic simulations of α -RDX, the crystal was superheated to $T = 510$ K before melting was observed.³² Full orientational disorder was reached at $T = 540$ K and translational freedom at $T = 580$ K. In the MS-CG-D simulation of the perfect crystal, domains of closed packed symmetry different from

hP2, which are similar to those shown in Fig. 4(a), first appear. The occurrence of such domains is responsible for the finite slope in the $\bar{\psi}(T)$ curve in the 510 – 520 K interval. Such domains were occasionally observed at the liquid-solid interface at $T > T_{melt}$ as contoured in Fig. 7(a). This is an artifact of the model.

H. Elastic properties

The isothermal Young's moduli $E_{1,2,3}$ and shear moduli G_{23}, G_{31}, G_{12} were evaluated for the MS-CG-D model at several thermodynamic state points using the direct strain-stress method. For orthorhombic symmetry as in our case, there are six independent elements of the strain tensor ($\varepsilon_k, k = 1, 6$). Within the direct strain-stress approach, we first derive the stress-strain curve from the *NVT* MD simulations for each ε_k . The stress-strain curve was determined by uniformly deforming the simulation cell initially in a stress-free state, which has basis vectors $h_0 = (a_i^0)$, to a new geometry $h = (a_i)$. The new h is selected to have a strain tensor $[\varepsilon_{ij}] = \frac{1}{2}([hh_0^{-1}]^T hh_0 - I)$, where I is a unity matrix, with only one preselected $\varepsilon_k \neq 0$ [$\varepsilon_1, \varepsilon_2, \varepsilon_3 = \varepsilon_{11}, \varepsilon_{22}, \varepsilon_{33}, \varepsilon_4, \varepsilon_5, \varepsilon_6 = 2\varepsilon_{23}, 2\varepsilon_{31}, 2\varepsilon_{12}$ in Voigt notation]. The stress σ for the deformed structure is then measured from the *NVT* simulation. The residual stress $\sigma - \sigma^0$, where σ^0 is the *NVT* equilibrium value for the h_0 cell, represents a point on the stress-strain curve. For each ε_k , five strain increments from 0.0 to 0.015 were applied. The elements of the stiffness matrix (elastic constants) were then evaluated from the slope at zero of a quadratic least-squares fit of the stress-strain points. The elastic moduli and Poisson ratios were then determined from the elastic constants using the Voigt average, which gives an upper bound estimate for shear moduli.

The calculated elastic moduli are reported in Table III. The experimental data were obtained from acoustic measurements by Haussuhl *et al.*³³ The atomistic simulation data are compiled from the SRT and SB models.^{34,35} At all state points, the MS-CG-D results are in reasonable agreement with the atomistic data, with overall better agreement with the SB model (from which the MS-CG-D potential was derived). One of the most prominent differences between the MS-CG-D and atomistic results is the degree of anisotropy among Young's moduli. The MS-CG-D results at $T = 298$ K are almost isotropic, whereas both SB and SRT models demonstrate anisotropy in the moduli. There are two major reasons for this discrepancy. The first is due to the use of virial data⁵ ($\sum_{i=1,3} \sigma_{ii}$ vs. V) to match the MS-CG-D model, resulting in a more "isotropic" σ for the MS-CG-D crystal. Indeed, at ambient conditions, the MS-CG/0 model (without a density dependency) yields a very low $E_3 = 0.7$ GPa, while the MS-CG-D model predicts the E_3 as a largest component (10-15% larger than the E_1 and E_2). Interestingly, the SB and SRT models yield different ordering of Young's moduli. For the SRT model, $E_2 > E_3$ is in agreement with experiment, while the SB model yields an inverted ordering, which is carried over to the MS-CG-D model. We note that the SRT model only describes intermolecular interactions, and the simulations were performed within the rigid-molecule

TABLE III. Young's (E) and shear (G) moduli at different T (K) and P (GPa). Units are GPa.

	E_1	E_2	E_3	G_{23}	G_{31}	G_{12}
$T = 218, P = 0$:						
atm (SRT) ^a	27.3	27.0	17.4	9.6	6.0	9.1
MS-CG-D	24.2	20.5	22.9	8.1	8.0	4.7
$T = 298, P = 0$:						
atm (SB)	19.3	16.2	18.5	7.6	4.9	3.0
atm (SRT) ^a	24.2	21.1	15.4	8.4	5.3	7.6
MS-CG-D	19.7	19.4	21.9	7.2	7.1	4.1
Expt	20.9	16.0	15.6	5.2	4.1	6.9
$T = 304, P = 1$:						
atm (SRT) ^a	29.8	32.1	26.6	12.7	8.0	11.6
MS-CG-D	25.5	26.8	28.5	8.1	8.0	4.9

^aReference 34.

approximation. The second reason, which in part relates to the first one, is due to a different structure of atomistic and MS-CG-D lattices as discussed in Sec. III D. The MS-CG-D lattice belongs to a more symmetrical crystalline space group that in turn contributes to the absence of a significant anisotropy. The isothermal bulk modulus $B_T = 13.0$ GPa was obtained from a fit to the $P - V$ curve [see Fig. 8(a)] using the Murnaghan equation.³⁶ The SB³⁵ and MS-CG-D values of B_T are identical. If the isotropic relation $B_T = E/3(1 - 2\nu)$ is assumed, where E is the arithmetic average of Young's moduli, the MS-CG-D model yields the average Poisson ratio $\nu = 0.24$, which compares well with the SB model prediction ($\nu = 0.27$). Importantly, the MS-CG-D model predicts the shear moduli in reasonable agreement with the reference atomistic data. With regard to the shear moduli, the most noticeable qualitative difference is the degree of anisotropy. The MS-CG-D G_{23} and G_{31} moduli have similar values, while the atomistic models predict more anisotropy for these shears. Most likely, this feature is due to the same reasons as the behavior of Young's moduli discussed above. With regard to comparison with experiment, the SRT model results correlate with directional response, while the SB and MS-CG-models differ. Finally, it is notable that the MS-CG-D model exhibits the expected decrease in moduli with increasing temperature and increase in moduli with increased pressure.

I. Thermal properties

The MS-CG-D model accurately reconstructs the ambient $V - P$ isotherm of crystalline RDX as displayed in Fig. 8(a), and is most certainly a consequence of the way the model was parameterized as described in Sec. II E. For the molten state, the MS-CG-D $V - P$ isotherm is noticeably stiffer at $P > 0.5$ GPa. This discrepancy could be due to the behavior of the $\Delta U^{conf} - P$ isotherm [shown in Fig. 8(b)]. For the molten phase, the MS-CG-D model predicts an increase in ΔU^{conf} with increasing pressure for $P < 1$ GPa, whereas the atomistic model shows a decrease. However, at higher pressures the shapes of the MS-CG-D and atomistic $\Delta U^{conf} - P$ curves visually are similar. The poorly predicted $V - P$ and $\Delta U^{conf} - P$ isotherms in the molten phase by the MS-CG-D model suggest the importance

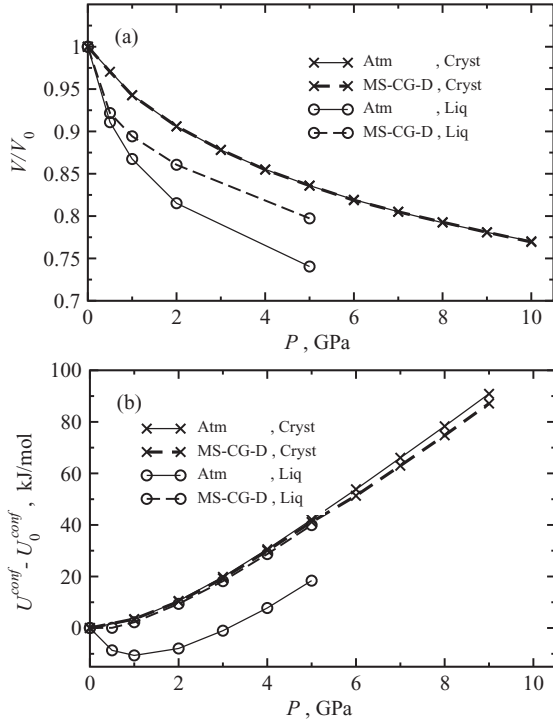


FIG. 8. Comparison of isotherms for crystalline RDX at $T = 300$ K (crosses) and molten RDX at $T = 550$ K (circles) from atomistic (solid) and MS-CG-D (dashed) models. Panel (a): $V/V_0 - P$ isotherm, where V_0 is ambient volume; Panel (b) $\Delta U^{conf} - P$ isotherm, where $\Delta U^{conf} = U^{conf} - U_0^{conf}$ is the change in the total internal potential energy with respect to the ambient value U_0^{conf} .

of structural rearrangements of the molecules as pressure increases, which cannot be captured by a MS-CG-D model derived from crystal $P - V$ data.

The significantly degraded thermal expansion properties of the MS-CG crystal could be attributed to the use of $P - V$ data at a single temperature (300 K) to parameterize the density dependency. At $T = 300$ K and $P = 0$ GPa, the MS-CG-D model yields a coefficient of constant stress thermal expansion $\alpha_V = 22.3 \times 10^{-6}$ 1/K, 7.3 times lower than the atomistic value of 163.8×10^{-6} 1/K³⁵ and the experimental value of 193.4×10^{-6} 1/K.³⁷ The lower α_V from the MS-CG-D model is a direct consequence of the fact that the temperature transferability of the MS-CG-D model is inherited from its density dependency, while in reality the T enters the effective interactions as an independent thermodynamic parameter. We calculated a constant volume specific heat capacity for the MS-CG-D model using the fluctuation formula³⁸ as $c_V = 97$ J/kg · K, which is about an order of magnitude lower than the experimental value of 1088 J/kg · K. The ratio $(c_P - c_V)/c_V = \alpha_V^2 B_T T / \rho c_V$ is about 0.01. In the atomistic model c_V is dominated by the excitations of the vibrational modes of the RDX molecules; removing them in the CG description results in c_V being severely underestimated. The ambient value of the Grüneisen coefficient $\Gamma = B_T \alpha_V / \rho c_V$, which is a measure of overall anharmonicity of the crystal, is estimated for the MS-CG-D crystal as $\Gamma = 1.726$. For the atomistic model assuming the experimental c_V , $\Gamma = 1.084$ and the experimental value is $\Gamma = 1.103$.

The similar values of Grüneisen parameter obtained by the atomistic and MS-CG-D descriptions indicate roughly the same level of anharmonicity. The inclusion of molecular structure to the MS-CG model, such as in the four-site representation, will improve the heat capacity of the system, and therefore the equation of state which governs quasiequilibrium phenomena such as shock propagation [see Sec. III K].

J. Vibrational spectrum

In Fig. 9 the vibrational density of states (VDOS) for the bulk crystal at $T = 300$ K calculated with the MS-CG-D and atomistic models are compared. The VDOS was determined using the power spectrum of the velocity autocorrelation function (VACF) $VACF(t) = \langle \mathbf{v}(t) \mathbf{v}(0) \rangle$. For the atomistic system, the VDOS was obtained from the all-atom and c.m. VACFs. The lattice part of the atomistic c.m. VDOS is expected to be dominated by the optical modes. For a better comparison, the atomistic VDOSs in Fig. 9 are normalized on the integral intensity up to 50 cm^{-1} , and the MS-CG-D VDOS rescaled. The part of the experimental spectrum³⁹ of α -RDX, which is due mainly to optical lattice vibrations, extends to about 150 cm^{-1} [regions (I) and (II) in Fig. 9]. The

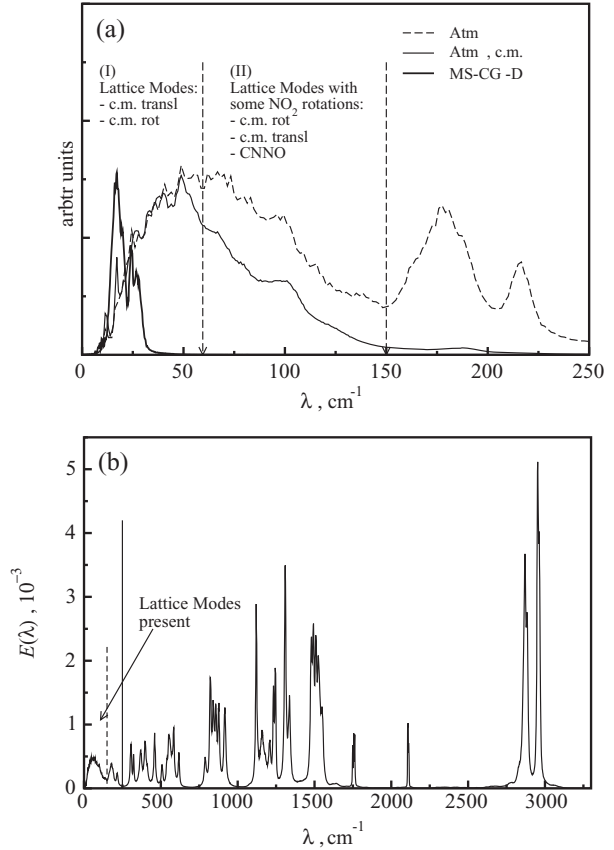


FIG. 9. Panel (a): All-atom VDOS (dashed), atomistic VDOS of c.m. (thin solid), and MS-CG-D (thick solid) in arbitrary units. The vertical dashed lines mark the parts of spectrum: (I) Only lattice modes associated with movements and rotations of molecular c.m.; (II) Mix of c.m. lattice modes with wagging and torsional modes of nitro groups. Panel (b): All-atom VDOS with portion of spectrum shown in panel (a) marked with a vertical solid line. The vertical dashed line (150 cm^{-1}) marks the low frequency region in which lattice modes are present.

major contributor to the c.m. lattice modes are translations and rotations of the molecules; however, low-frequency intramolecular vibrations may contribute.²³ The low-frequency boundary of the spectrum is determined by the size of the supercell. The atomistic c.m. VDOS is nearly all confined to the $< 150 \text{ cm}^{-1}$ region, indicating that the SB model captures adequately the lattice part of the spectrum. In the VDOS region (I), which in the experimental spectrum extends to about 60 cm^{-1} , all vibrations can be assigned to the lattice modes. In region (II) ($60\text{--}150 \text{ cm}^{-1}$ according to experimental data), the lattice modes are mixed with the wagging and torsional motions of the nitro groups.²³ Outside the regions (I), (II), all modes originate from intramolecular vibrations. As seen from Fig. 9(a), the all-atom and c.m. VDOSs start deviating at approximately 50 cm^{-1} due to the contribution of intramolecular modes in the all-atom VDOS. Outside region (II) of the c.m. VDOS, there is a weak tail stretching to about 200 cm^{-1} , which may correspond in part to a cluster of vibrational modes centered at 180 cm^{-1} in which (according to other studies) significant motion of nitro groups is accompanied with c.m. movements. In the atomistic model of RDX by Boyd *et al.*,⁴⁰ the upper boundary of the lattice spectrum is aligned at 190 cm^{-1} . The VDOS from the MS-CG-D model occupies the frequency region below 35 cm^{-1} and is composed of three well defined peaks³⁹ at 18, 24, and 27 cm^{-1} . The first major peak exhibits splitting into three levels. The MS-CG-D VDOS possibly corresponds to a cluster of five lowest laying normal modes, which occupy the $18 - 29.2 \text{ cm}^{-1}$ range in the experimental spectrum. The modes from region (I), which are not reproduced by the MS-CG-D model, can be attributed to the lattice vibrations due to the molecular rotational dof, which are projected out in the CG description.

K. Shocked RDX

As a first step in the evaluation of the performance of the MS-CG-D model in simulating shocked RDX, we calculated thermodynamic properties of the explosive on its Rankine-Hugoniot curve,

$$H_g(T, V) = 0 = E - E_0 - \frac{1}{2}(P + P_0)(V_0 - V), \quad (40)$$

which describes the locus of thermodynamic states with the specific volume, internal energy, and pressure ($V = 1/\rho$, E , P) accessible by shock loading from an initial thermodynamic state ($V_0 = 1/\rho_0$, E_0 , P_0). The Rankine-Hugoniot states under hydrostatic compression were calculated using the procedure described by Erpenbeck⁴¹ from multiple NsT simulations integrated for 50 ps. We used the $4 \times 6 \times 6$ supercell and $T_0 = 300 \text{ K}$, $P_0 = 1 \text{ bar}$. The E was calculated using Eqs. (9) and (15). The Hugoniot in the $P - V/V_0$ plane is shown in Fig. 10(a) along with shock data by Olinger *et al.*,⁴² and in the $P - T$ plane in Fig. 10(b). The MS-CG-D $P - T$ locus is much steeper than its atomistic counterpart due to the smaller number of dof (by a factor 21) and low c_V (referred to in Sec. III I). On the Hugoniot locus, the MS-CG-D model goes into the inelastic regime at about $P_{melt} = 0.45 \text{ GPa}$ as it partially melts.

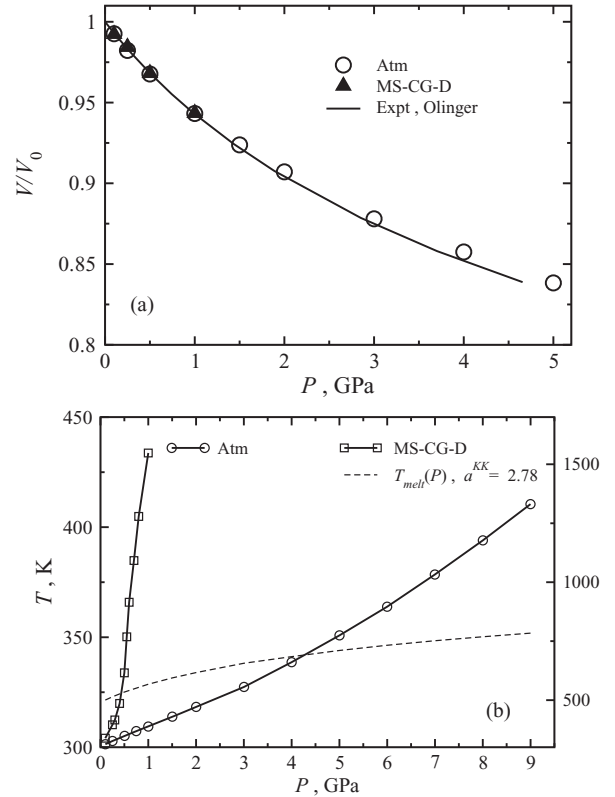


FIG. 10. Panel (a): Hugoniot curves of RDX from the atomistic model (circles), the MG-CG-D model (triangles), and experiment (solid line). Panel (b): Pressure vs. temperature for the calculated shock Hugoniot of RDX from atomistic (circles) and MS-CG-D (squares) models. Dashed line depicts the MS-CG-D melting curve using the Kraut-Kennedy relation as discussed in the text. Right T -axis is for the atomistic model and left T -axis is for the MS-CG-D model.

The melting temperature can be related linearly to a volume change ΔV using the Kraut-Kennedy relation⁴³ $T_{melt} = T_{melt}^0(1 + a^{KK} \Delta V/V_0)$, with the constant $a^{KK} = 2(\Gamma - \frac{1}{3})$. For the MS-CG-D model, $a^{KK} = 2.78$ and the resulting melting curve $T_{melt}(P)$ is depicted by the dashed line in Fig. 10(b). The values of a^{KK} estimated from experimental data are typically $a^{KK} = 1.54 - 1.66$.⁴⁴ The MS-CG-D estimate of a^{KK} suggests that the CG crystal will melt at fairly moderate shock loads above $P_{melt} = 0.44 \text{ GPa}$, which is close to the observations from the Hugoniot calculations. For the SB model, the elastic limit in uniaxial compression along the [100] direction is reached at about 8 GPa .³⁵ For a shock along the [001] direction, elastic behavior was observed to 12 GPa .¹⁹ The temperature can be related to the specific internal energy E and V as $T(V, E) = T_0(\frac{V_0}{V})^\Gamma + \frac{(E - E_S(V))}{c_V}$. The first term describes isentropic compression and contributes to a temperature increase of about 25 K/GPa for the MS-CG-D model and 15 K/GPa for the atomistic model. Because the MS-CG-D model underestimates the atomistic $E - E_S(V)$ by the specific rotational and vibrational kinetic energies [Fig. 8(b)], the low c_V (as discussed in Sec. III I) is a reason for superheating of the shocked CG crystal. The superheated shocked states caused by the abnormally low c_V is an artifact generic to the mesoparticle modeling and in principal can be eliminated by extending the model to include the energy exchange between the CG particles and their internal dof. Such a formalism requires the modeling of the intraparticle

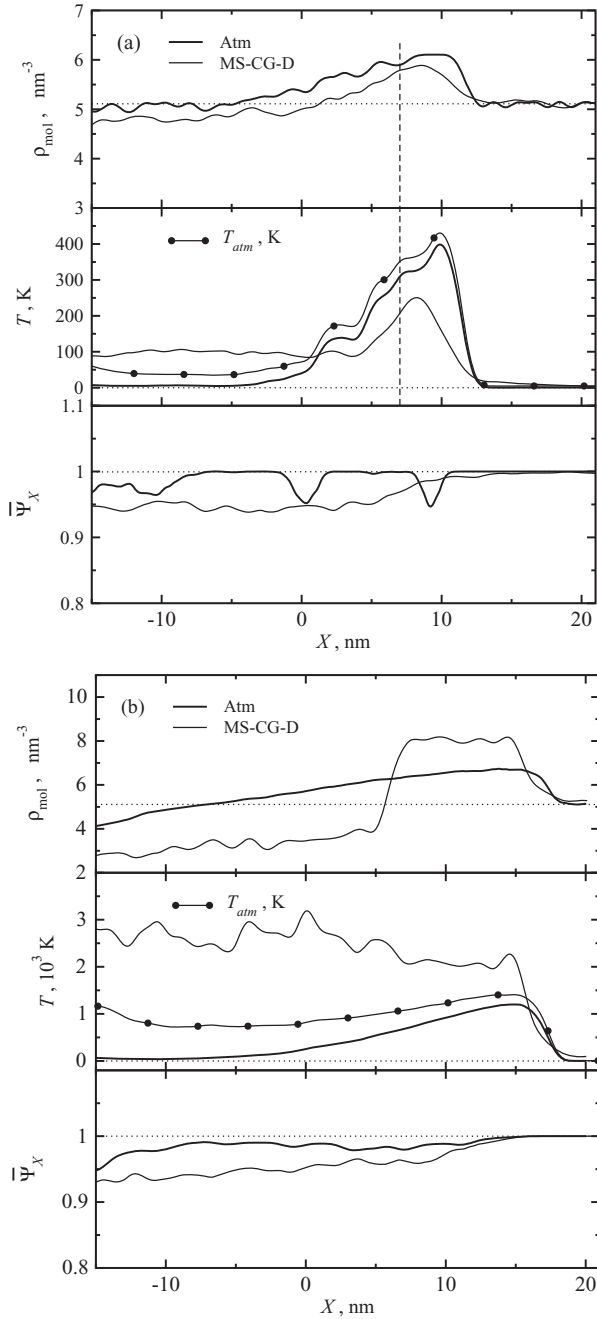


FIG. 11. The profiles of (top frame) molecular density ρ_{mol} , (middle frame) effective translational temperature T_{eff} , atomistic temperature T_{atm} (filled circles), and (bottom frame) global order parameter $\bar{\psi}_X$ [Eq. (39)] in shocked RDX from atomistic (thick) and MS-CG-D (thin) simulations. Panel (a): $V_p = 1$ km/s; Panel (b): $V_p = 3$ km/s. The MS-CG-D ρ_{mol} curve is shifted up by difference $\Delta\rho_0 = 0.215$ in the values of atomistic and MS-CG-D molecular density of crystal at $T = 4.5$ K for a better comparison.

specific heat capacity $c_i(T, P)$ as a function of temperature and pressure. The $c_i(T, P)$ function has to be chosen to restore correct atomistic Hugoniot locus in $P - T$ plane. Several models for such mesoparticle modeling have been proposed in the past, which include the constant energy DPD method⁴⁵ and mesodynamics with an internal thermostat.⁴⁶

In Fig. 11 the wave profiles for a planar shock along the [100] direction for two particle velocities $V_p = 1$ and 3 km/s are presented. The shock wave was generated by impacting a flyer plate and its target as described elsewhere.⁴⁷

The initial velocities of the flyer and the target were $\frac{5}{3}V_p$ and $-\frac{1}{3}V_p$. The atomistic translational and CG temperature T_{transl} is shown as an effective temperature $T_{eff} = T_{transl}/N_{atm}$, where $N_{atm} = 21$ is the number of atoms in the RDX molecule. For the CG model, the T_{transl} is a physical temperature. We have also plotted the atomistic temperature T_{atm} to illustrate the degree of energy transfer from the shock load into the molecular dof. For the atomistic system, we have calculated stress profiles P and $P_{[100]}$ using the scheme of Lindahl *et al.*⁴⁸ The P at the shock front estimated from the stress profile is 7.5 GPa for $V_p = 1$ km/s, with about 20% due to intramolecular contributions and 35 GPa for $V_p = 3$ km/s with about 50% due to intramolecular stresses. The sufficiently close agreement of the atomistic and MS-CG-D T_{eff} profiles for $V_p = 1$ km/s suggests that the atomistic Hugoniot with T considered as T_{eff} is adequately reproduced by the MS-CG-D model for shock strengths up to 7-8 GPa. For example, if we assume that the final equilibrium state of the shock wave is that denoted by the vertical dashed line in Fig. 11(a), then the slopes for the Hugoniot $T - P$ with $T = T_{eff}$ are estimated as 1555 K/GPa for the atomistic model and 1558 K/GPa for the MS-CG-D model. A comparison between the T_{atm} and T_{eff} for the atomistic models in Fig. 11(a) and 11(b) provides insight into the degree of energy transfer from molecular translational dof excited upon shock impact into intramolecular vibrational modes as a function of impact energy. For $V_p = 1$ km/s, such energy transfer is small, whereas energy transfer from the molecular translational dof to the intramolecular vibrational modes behind the shock front is more efficient for the higher velocity impact. The atomistic profile $\bar{\psi}_X$ for $V_p = 1$ km/s indicates an absence of orientational melting: the molecules for the most part relax to their original orientations upon shock wave passage, while for $V_p = 3$ km/s melting is evident with significant kinetic energy imparted to the intramolecular vibrations. Increased numbers of molecular collisions in the liquid state could explain the larger degree of vibrational heating seen for the $V_p = 3$ km/s impact. Finally, we have also carried out a simulation in which the shock load is 0.3 km/s; no melting was observed in the MS-CG-D system.

IV. CONCLUSIONS

We discussed the application of the MS-CG approach, which is based on force-matching of the atomistic ensemble, to develop particle-based CG models of molecular crystals. The particular application was the development of a transferable one-site CG model for RDX suitable for simulating shocked crystals. The imposed requirements on the model transferability in a broad range of thermodynamic conditions and across the phases was accomplished by introducing a density-dependent potential. The density-dependent model was constructed in two steps. In the first step, the MS-CG potential was derived explicitly through force-matching of data sampled from simulations of molten and amorphous RDX states at ambient pressure. The derived potential predicted an orthorhombic (hP2-A3) symmetry of the crystal lattice, which was very close to the native geometry of the

atomistic lattice, and within 5% of the density predicted by the atomistic model. In the next step, the density-dependency of the MS-CG potential was implemented through interpolation of potentials parameterized at several reference pressures up to 10 GPa. In contrast to our earlier work on nitromethane, the reference potentials were constructed using an empirical force term fitted to the crystalline $V - P$ isotherm. The form of the density dependent force contribution was close to the distance-independent term as suggested by our earlier works on MS-CG modeling of nitromethane. This new procedure requires much less computational efforts than the direct application of the force-matching. The resultant model was able to reproduce a wide range of the structural and thermodynamic properties of crystalline and liquid states of RDX, including pair (RDF) and many-body (orientational ordering) correlations, elastic and vibrational properties, and isotherms. As a result of coarse graining of the intramolecular dof, the MS-CG model predicts a specific heat that is more than 10 times lower than that of the atomistic value. This deficiency in the model is manifested in a significant deviation from the atomistic result in the Hugoniot $P - T$ locus. The Hugoniot data indicate that the MS-CG RDX crystal may melt under unrealistically low (< 0.5 GPa) shock loads, reflecting the importance of the intramolecular dof in the shock event. We can conclude that the application of the MS-CG model to perform realistic simulations of a shocked RDX crystal would require the introduction of an intraparticle equation-of-state and explicit heat exchange between particles and intraparticle heat reservoirs, such as that in the constant energy DPD method.⁴⁵

To date, numerous types of CG models exist.² All classes of coarsening approaches, including structure-based and *top-down* techniques, may result in different coarse-grain representations of the same system, each potentially yielding different properties. Such observations exemplify the nonuniqueness of coarse graining and the problems surrounding the representability paradigm. The advantage of *bottom-up* approaches, such as MS-CG or structure-based methods, is the greater thermodynamic consistency with the atomistic models as these methods systematically project the atomistic microscopic statistical information to mesoscales. If the properties of interest are primarily dependent on pairwise correlations (e.g., RDFs) the structure-based methods are quite useful. On the other hand, the MS-CG models by design are capable of better capturing the many-body correlations as compared to structure-based models. This makes them more amenable to high ordered systems such as crystals. Therefore the MS-CG models would be advantageous in simulations of those properties in which many-body effects are important.

The reported isotropic one-site model of RDX opens up several possibilities to extend quasimolecular modeling of crystalline explosives to mesoscales, which are still not accessible with existing all-atomistic models. For instance, a knowledge of detailed molecular dynamics at the mesoscale is of crucial importance for understanding how the sensitivity of solid explosives is affected by the presence of extended defects such as voids which, when shocked, lead to hotspots via void collapse.⁴⁹ Due to the low computational cost of the one-site model of RDX, its prospective application may include simulations of the hydrodynamic regime of void

collapse. Namely, under conditions of large voids, when the void collapse takes much longer than the shock to traverse the void, the void collapse dynamics evolves into the hydrodynamic regime, which is characterized by the formation of a molecular jet that emerges from upstream wall. The jetting may lead to a hot spot formation through enhanced focusing of kinetic energy onto the downstream side. The detailed dynamics of the jetting mechanism for realistic crystalline systems is still poorly understood and in the past was studied using highly idealized or unrealistically small systems.⁵⁰ Thus, computational approaches that make the mesoscale representation of materials tractable are needed. This effort is a significant step towards realistic modeling at mesoscales.

ACKNOWLEDGMENTS

The authors wish to thank Dr. John Brennan and Ms. Sarah Hamdan for helpful comments. This research was supported by the DoD High Performance Computing Modernization Program Software Application Institute for Multi-scale Reactive Modeling of Insensitive Munitions. Computing support was provided by the DoD Supercomputer Resource Center.

- ¹C. Peter and K. Kremer, *Faraday Discuss.* **144**, 9 (2010).
- ²V. Ruhle, C. Junghans, A. Lukyanov, K. Kremer, and D. Andrienko, *J. Chem. Theory Comput.* **5**, 3211 (2009).
- ³A. A. Louis, *J. Phys.: Condens. Matter* **14**, 9187 (2002).
- ⁴M. E. Johnson, T. Head-Gordon, and A. A. Louis, *J. Chem. Phys.* **126**, 144509 (2007).
- ⁵S. Izvekov, P. W. Chung, and B. M. Rice, *J. Chem. Phys.* **133**, 064109 (2010).
- ⁶S. Izvekov and G. A. Voth, *J. Chem. Phys.* **123**, 134105 (2005).
- ⁷S. Izvekov and G. A. Voth, *J. Phys. Chem. B* **109**, 2469 (2005).
- ⁸W. G. Noid, J. W. Chu, G. S. Ayton, V. Krishna, S. Izvekov, G. A. Voth, A. Das, and H. C. Andersen, *J. Chem. Phys.* **128**, 244114 (2008); W. G. Noid, P. Liu, Y. Wang, J. W. Chu, G. S. Ayton, S. Izvekov, H. C. Andersen, and G. A. Voth, *J. Chem. Phys.* **128**, 244115 (2008); A. Das and H. C. Andersen, *J. Chem. Phys.* **131**, 034102 (2009); V. Krishna, W. G. Noid, and G. A. Voth, *J. Chem. Phys.* **131**, 024103 (2009); A. Das and H. C. Andersen, *J. Chem. Phys.* **132**, 164106 (2010); L. Larini, L. Y. Lu, and G. A. Voth, *J. Chem. Phys.* **132**, 164107 (2010); S. Izvekov, *J. Chem. Phys.* **134**, 034104 (2011).
- ⁹W. G. Noid, G. S. Ayton, S. Izvekov, and G. A. Voth, in *Coarse-Graining of Condensed Phase and Biomolecular Systems*, edited by G. A. Voth (Taylor and Francis, Boca Raton, 2008), p. 21.
- ¹⁰W. Schommers, *Phys. Lett. A* **43**, 157 (1973).
- ¹¹A. P. Lyubartsev and A. Laaksonen, *Phys. Rev. E* **52**, 3730 (1995).
- ¹²R. L. Henderson, *Phys. Lett. A* **49**, 197 (1974).
- ¹³E. C. Allen and G. C. Rutledge, *J. Chem. Phys.* **130**, 034904 (2009).
- ¹⁴I. Pagonabarraga and D. Frenkel, *J. Chem. Phys.* **115**, 5015 (2001).
- ¹⁵S. Y. Trofimov, E. L. F. Nies, and M. A. J. Michels, *J. Chem. Phys.* **117**, 9383 (2002).
- ¹⁶E. C. Allen and G. C. Rutledge, *J. Chem. Phys.* **128**, 154115 (2008); E. C. Allen and G. C. Rutledge, *J. Chem. Phys.* **130**, 204903 (2009).
- ¹⁷H. Wang, C. Junghans, and K. Kremer, *Eur. Phys. J. E* **28**, 221 (2009).
- ¹⁸G. D. Smith, R. K. Bharadwaj, D. Bedrov, and C. Ayyagari, *J. Phys. Chem. B* **103**, 705 (1999); G. D. Smith and R. K. Bharadwaj, *J. Chem. Phys.* **103**, 3570 (1999); T. D. Sewell, R. Menikoff, D. Bedrov, and G. D. Smith, *J. Chem. Phys.* **119**, 7417 (2003).
- ¹⁹D. Bedrov, J. B. Hooper, G. D. Smith, and T. D. Sewell, *J. Chem. Phys.* **131**, 034712 (2009).
- ²⁰M. J. Cawkwell, T. D. Sewell, L. Q. Zheng, and D. L. Thompson, *Phys. Rev. B* **78**, 014107 (2008).
- ²¹D. C. Sorescu, B. M. Rice, and D. L. Thompson, *J. Phys. Chem. B* **104**, 8406 (2000); D. C. Sorescu, B. M. Rice, and D. L. Thompson, *J. Phys. Chem. A* **105**, 9336 (2001); P. M. Agrawal, B. M. Rice, and D. L. Thompson, *J. Chem. Phys.* **119**, 9617 (2003).

- ²²P. M. Agrawal, B. M. Rice, L. Q. Zheng, and D. L. Thompson, *J. Phys. Chem. B* **110**, 26185 (2006).
- ²³S. G. Boyd and K. J. Boyd, *J. Chem. Phys.* **129**, 134502 (2008).
- ²⁴T. Darden, D. York, and L. Pedersen, *J. Chem. Phys.* **98**, 10089 (1993).
- ²⁵S. Melchionna, G. Ciccotti, and B. L. Holian, *Mol. Phys.* **78**, 533 (1993).
- ²⁶W. Smith and T. R. Forester, *J. Mol. Graphics* **14**, 136 (1996); W. Smith, C. W. Yong, and P. M. Rodger, *Mol. Simulat.* **28**, 385 (2002).
- ²⁷C. S. Choi and E. Prince, *Acta Crystallogr., Sect. B: Struct. Sci.* **28**, 2857 (1972).
- ²⁸J. R. Morris and X. Song, *J. Chem. Phys.* **116**, 9352 (2002); L. Zheng, Q. An, Y. Xie, Z. Sun, and S.-N. Luo, *J. Chem. Phys.* **127**, 164503 (2007).
- ²⁹J. R. Errington and P. G. Debenedetti, *Nature (London)* **409**, 318 (2001); S. Matysiak, C. Clementi, M. Praprotnik, K. Kremer, and L. D. Site, *J. Chem. Phys.* **128**, 024503 (2008).
- ³⁰S.-N. Luo, A. Strachan, and D. C. Swift, *J. Chem. Phys.* **120**, 11640 (2004).
- ³¹P. M. Agrawal, B. M. Rice, L. Q. Zheng, G. F. Velardez, and D. L. Thompson, *J. Phys. Chem. B* **110**, 5721 (2006).
- ³²L. Q. Zheng and D. L. Thompson, *J. Chem. Phys.* **125**, 084505 (2006).
- ³³S. Haussuhl, *Z. Kristallogr.* **216**, 339 (2001).
- ³⁴T. D. Sewell and C. M. Bennett, *J. Appl. Phys.* **88**, 88 (2000).
- ³⁵L. Munday, P. Chung, B. Rice, and S. Solares, *Proceedings of the 14th International Detonation Symposium* (Coeur d'Arleone Resort, Idaho, 2010); L. B. Munday, P. W. Chung, B. M. Rice, and S. D. Solares, *J. Phys. Chem. B* **115**, 4378 (2011).
- ³⁶F. D. Murnaghan, *Proc. Natl. Acad. Sci. U.S.A.* **30**, 244 (1944).
- ³⁷B. M. Dobratz and P. C. Crawford, *LLNL Explosives Handbook, Properties of Chemical Explosives and Explosive Simulants, Report UCRL 52997, Rev. 2* (LLNL, Livermore, CA, 1985).
- ³⁸M. P. Allen and D. J. Tildesley, *Computer Simulation of Liquids* (Oxford University Press, New York, 1987).
- ³⁹J. J. Haycraft, L. L. Stevens, and C. J. Eckhardt, *J. Appl. Phys.* **100**, 053508 (2006).
- ⁴⁰S. Boyd, M. Gravelle, and P. Politzer, *J. Chem. Phys.* **124**, 104508 (2006).
- ⁴¹J. J. Erpenbeck, *Phys. Rev. A* **46**, 6406 (1992).
- ⁴²B. Olinger, B. Roof, and H. H. Cady, *Symposium International Sur Le Comportement Des Milieux Denses Sous Hautes Pressions Dynamiques* (Commissariat a l'Energie Atomique Centre d'Etudes de Vajours, Paris, France, 1978), p. 3.
- ⁴³E. A. Kraut and G. C. Kennedy, *Phys. Rev.* **151**, 668 (1966).
- ⁴⁴R. Menikoff and T. D. Sewell, *Combust. Theory Model.* **6**, 103 (2002).
- ⁴⁵P. Espanol, *Europhys. Lett.* **40**, 631 (1997).
- ⁴⁶A. Strachan and B. L. Holian, *Phys. Rev. Lett.* **94**, 014301 (2005).
- ⁴⁷B. L. Holian and P. S. Lomdahl, *Science* **280**, 2085 (1998).
- ⁴⁸E. Lindahl and O. Edholm, *J. Chem. Phys.* **113**, 3882 (2000).
- ⁴⁹J. E. Field, *Acc. Chem. Res.* **25**, 489 (1992).
- ⁵⁰Y. Shi and D. W. Brenner, *J. Phys. Chem. C* **112**, 6263 (2008); K.-i. Nomura, R. K. Kalia, A. Nakano, and P. Vashishta, *Appl. Phys. Lett.* **91**, 183109 (2007).

Laser-Induced Plasma Chemistry of the Explosive RDX with Various Metallic Nanoparticles

Jennifer L. Gottfried

U.S. Army Research Laboratory, Aberdeen Proving Ground, MD

ABSTRACT

The feasibility of exploiting plasma chemistry to study the chemical reactions between metallic nanoparticles and molecular explosives such as cyclotrimethylenetrinitramine (RDX) has been demonstrated. This method, based on laser-induced breakdown spectroscopy, involves the production of nanoparticles in a laser-induced plasma and the simultaneous observation of time-resolved atomic and molecular emission characteristic of the species involved in the intermediate chemical reactions of the nanoenergetic material in the plasma. Using this method, it has been confirmed that the presence of aluminum promotes the ejection process of carbon from the intermediate products of RDX. The time evolution of species formation, the effects of laser pulse energy, and the effects of trace metal content on the chemical reactions were also studied.

Applied Optics, Volume 51, Number 7, pages B13-B21 (2012)

Laser-induced plasma chemistry of the explosive RDX with various metallic nanoparticles

Jennifer L. Gottfried

U.S. Army Research Laboratory, RDRL-WML-B, Aberdeen Proving Ground,
Maryland, 21005, USA (jennifer.gottfried@us.army.mil)

Received 27 September 2011; revised 10 January 2012; accepted 13 January 2012;
posted 13 January 2012 (Doc. ID 155400); published 26 January 2012

The feasibility of exploiting plasma chemistry to study the chemical reactions between metallic nanoparticles and molecular explosives such as cyclotrimethylenetrinitramine (RDX) has been demonstrated. This method, based on laser-induced breakdown spectroscopy, involves the production of nanoparticles in a laser-induced plasma and the simultaneous observation of time-resolved atomic and molecular emission characteristic of the species involved in the intermediate chemical reactions of the nanoenergetic material in the plasma. Using this method, it has been confirmed that the presence of aluminum promotes the ejection process of carbon from the intermediate products of RDX. The time evolution of species formation, the effects of laser pulse energy, and the effects of trace metal content on the chemical reactions were also studied.

OCIS codes: 140.3450, 300.6365.

1. Introduction

It is well known that two-component explosives consisting of metal particle fuels and oxidizers can produce more than twice the energy of high performance molecular explosives alone. Aluminum powder (typically $\sim 50\ \mu\text{m}$ average diameter) is frequently added to explosives and propellants to improve their performance. The addition of metallic aluminum results in a considerable increase in the heat of explosion and higher temperatures since alumina (Al_2O_3) has a high heat of formation [1]. Other fuels used in heat-producing pyrotechnics include Ti, Mg, Ni, Zr, and Be [2]. Recently there has been considerable interest in using nanoparticle fuels, which offer the possibility of faster energy release, more efficient combustion, and controllable explosive performance (via particle size or passivation layer properties) [3,4]. The development of nanoenergetic materials has been limited by the lack of fundamental understanding regarding the chemical dynamics involved.

The need to understand the chemical mechanisms of combustion, thermal explosion, and detonation is essential in order to develop more efficient explosives and propellants. In addition, the chemical products produced during detonation can negatively affect

device performance, so an understanding of the chemical reactions involved during the decomposition of component mixtures is crucial. In a recent study, Song *et al.* investigated the formation of C and AlO in an aluminized-cyclotrimethylenetrinitramine (RDX) shock tube explosion [5]. Both unreacted carbon (C, C_2) and AlO decrease rocket performance. By monitoring the C_2 and AlO emission, they observed that increasing the quantity of Al particles ($\sim 4.5\ \mu\text{m}$ diameter) added to the RDX resulted in increased C_2 emission. They subsequently studied the effect of nanoaluminum on the detonation of RDX in a similar experimental setup [6].

Here, we demonstrate an alternate approach for studying the chemical reactions of molecular explosives and metallic nanoparticles. This approach, based on laser-induced breakdown spectroscopy (LIBS), involves generating the metallic nanoparticles via laser ablation and studying the chemical reactions that occur in the laser-induced plasma by monitoring the time-resolved emission spectra. In the past decade, laser ablation has increasingly been used to produce metallic nanoparticles. The size and distribution of the nanoparticles can be controlled by using sequential laser pulses, varying repetition rates, laser fluence, wavelength, and pulse width,

and choice of carrier gas (air, argon, nitrogen, etc.) [7–10]. LIBS is an analytical technique that has been widely investigated over the past several decades for both qualitative and quantitative material analysis [11]; previous applications include the detection of explosives [12]. It is only recently that a few groups have started investigating the chemical reactions involving explosive materials that occur during the lifetime of the laser-induced plasma (tens to hundreds of microseconds) and the subsequent effect on the LIBS signature [13–18].

The potential advantages to this approach to studying nanoenergetic materials include (1) little or no sample preparation is needed (the laser directly ablates the explosive and substrate material), (2) the intermediate chemical reactions of the nanoenergetic material can be studied on a small scale (microgram quantities), eliminating the need for a shock tube or other explosive containment apparatus, (3) the properties of the laser (pulse energy, wavelength, pulse duration) can be tuned to control the size and distribution of the particles formed, and (4) time-resolved relative concentrations of a large number of atomic and molecular species can be tracked simultaneously. With this approach, any type of material can be ablated with the laser and its plasma chemistry studied as long as the laser energy exceeds the breakdown threshold.

In this work, the laser ablation of thin film residues of RDX on various metal substrates (generating nanoenergetic particles) has been combined with the observation of time-resolved optical emission from the resulting high-temperature plasma. The relative concentrations of C, C₂, CN, H, N, and O (as well as any other metal substrate-related atomic, molecular, or ionic species emitting from 200–940 nm) were tracked during the lifetime of the plasma (typically <1 ms). Several experiments designed to understand the time dependence of species formation in the plasma, to determine the effect of bulk and trace metals on the chemistry of RDX, and to study the effects of laser pulse energy were performed.

2. Experimental Methods

Colleagues at the U.S. Army Research Laboratory provided Class 1 (<850 μm particle diameter), military-grade RDX. Double pulse LIBS spectra of a thin layer of RDX crushed on the surface of a 1-mm-thick Al substrate (Sigma-Aldrich, 99.999%) were obtained using two Big Sky CFR400 lasers (1064 nm, 225 mJ per laser) focused on the sample surface with a 10 cm focal length convex lens. The interpulse delay between the two laser pulses ($\Delta t = 2 \mu\text{s}$) was selected to minimize the amount of atmospheric contribution to the O, N, and H emission signals. A pierced mirror was used to collect the spatially integrated plasma emission in a 600 μm fiber optic. The fiber was inserted into a Catalina Scientific echelle spectrometer (SE200) through a 25 μm pinhole (200–1000 nm). An Apogee (AP2Ep) ICCD (gain = 600) served as the detector. The gate delay (t_{delay}) was varied from 0

to 10 μs while the integration time ($t_{\text{int}} = 1 \mu\text{s}$) was held constant at the minimum value for the detector. Ten single-shot spectra at each gate delay were recorded.

To study the laser-induced plasma chemistry, a second double pulse LIBS setup was employed. For this experiment, two Nd:YAG lasers (Continuum Surelite, 1064 nm, maximum ≈ 420 mJ per laser) were focused onto the sample surface with a 10 cm lens. The plasma emission was directed into a 400 μm fiber optic using a pierced mirror setup. An echelle spectrometer (Catalina Scientific EMU-65) was paired with an electron multiplying CCD (EMCCD) detector (Andor iXon, gain = 2) to collect the LIBS spectra (200–1000 nm) under an argon flow with the following timing parameters: $\Delta t = 2 \mu\text{s}$, $t_{\text{int}} = 50 \mu\text{s}$, and $t_{\text{delay}} = 1 \mu\text{s}$. Both detectors [intensified CCD (ICCD) and EMCCD] were corrected for their spectral responses using a calibrated deuterium tungsten-halogen light source. For the samples used to study the plasma chemistry, the RDX was suspended in acetonitrile, which enables fairly reproducible, semiquantitative sample deposition. Typical RDX concentrations of ~ 10 mg/ml were applied to the substrate surfaces with multiple deposits from a 10 μl syringe, resulting in residue concentrations of $\sim 2.5 \mu\text{g}/\text{mm}^2$; approximately 13 μg of RDX was sampled with each laser shot. The substrates used for this experiment were high-purity metals (≥ 1 mm thick) obtained from Sigma-Aldrich: Al (99.999%), Cu (99.999%), Ni (99.98%), Sn (99.998%), and Ti (99.998%). Fifty single-shot spectra of RDX residue on each of the pure metal substrates were obtained. Spectra of RDX residue on an Al₂O₃ sample from our laboratory and Al alloy standard reference material (SRM) purchased from the National Institutes of Standards and Technology (NIST SRM 1256b, alloy 380; NIST SRM 1259, alloy 7075; NIST SRM 1715, alloy 5182) were also acquired.

Additional experiments performed using the Continuum double pulse laser setup include the sampling of mixtures of RDX with <75 μm diameter Al powder (Sigma-Aldrich). The Al powder was added to 8 mg of RDX in several weight ratios (0:1, 1:1, 2:1, and 4:1). The mixtures were then spread onto a 6.5 cm^2 area on the surfaces of the pure metal substrates Al, Cu, Ni, Sn, and Ti. Fifteen single-shot spectra were acquired under argon for each sample. Unlike the pure RDX residue, which tends to stick easily to substrate surfaces, a significant portion of the RDX/Al mixtures was blown off the substrate by the shock wave from each laser shot. An exhaust port was placed near the point of laser ablation to ensure none of the explosive mixtures were inhaled or otherwise dispersed into the laboratory.

The dependence of the emission spectra on laser pulse energy was studied using the Continuum double pulse laser with the echelle/EMCCD spectrometer. As before, the RDX was suspended in acetonitrile and deposited on the pure Al substrate

($\sim 2.5 \mu\text{g}/\text{mm}^2$). Twenty spectra of both the pure substrate and the RDX residue were acquired under argon using a single 210 mJ laser pulse, a double 210 mJ pulse (total energy 420 mJ), a single 420 mJ pulse, and a double 420 mJ pulse (total energy 840 mJ).

3. Results and Discussion

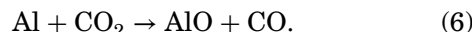
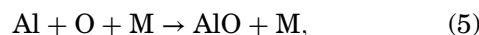
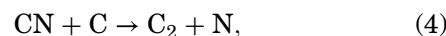
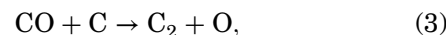
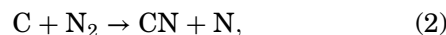
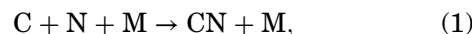
A. Time-Resolved Emission Spectroscopy

Background-corrected peak emission intensities for the atomic and molecular species relevant to RDX were tracked over the first 10 μs of the laser-induced plasma lifetime (Fig. 1). Although the emission spectra collected with a 0 μs gate delay (and a 1 μs gate width) contain the background continuum characteristic of *bremstrahlung* emission (which persists for the first several hundred nanoseconds), discrete emission lines were also observed. After subtracting the average background signal near the relevant emission line, the peak intensities for the C (247.856 nm), H (656.285 nm), N (746.831 nm), and O (777.194/777.417 nm) lines were normalized to the total emission intensities of selected atomic and molecular species, including CN (388.340 nm), C_2 (516.520 nm), and AlO (484.220 nm). Because the RDX residue was applied to an aluminum substrate, Al I and Al II emission features were observed in addition to AlO (formed by the reaction of the Al from the substrate and O liberated from the RDX).

The cause of the initial increase in the normalized O intensity over the first several microseconds is unclear, but may be the result of slower dissociation reactions involving the release of atomic O. The O (after 2 μs), N, and H emission from the RDX slowly decays over time, while the C emission is relatively constant for the first 10 μs of the plasma lifetime. The energy required to promote C into the excited state (which subsequently emits radiation at 247.856 nm as the electron relaxes to a lower energy level) is much lower than that for the O, N, and H lines (7.68 eV compared to 10.7, 12.0, and 12.1 eV, respectively) [19] and is therefore less affected by the decreasing thermal energy in the plasma at later

times. Because the double pulse LIBS technique [20] was used to collect the data, only a minimal amount of air was entrained into the plasma and most of the O, N, and H signals were from the RDX residue (and potentially contaminants on the aluminum surface).

As previously reported for other materials with much lower laser energies [21–23], the molecular species exhibit very different time-dependent behavior in the laser-induced plasma. Of the three molecules observed in the LIBS spectra of RDX on aluminum, only the CN is present at very early times in the plasma lifetime since some CN fragments are formed by the initial laser ablation of the RDX molecule (Figure 2). These initial CN fragments are dissociated into atomic C and N atoms by collisions in the high-temperature plasma [13]. The ratio of singly ionized Al (466 nm) to neutral Al (309 nm) is also shown in Fig. 2. The excitation temperatures calculated based on the Boltzmann two-line method using the Al I lines (309 and 394 nm) follow the same trend as the ionization ratio—both decrease as the plasma cools. The calculated temperatures drop from $\sim 11,000$ K at a gate delay of 0 μs to around 3700 K at a gate delay of 10 μs . As the plasma begins to cool, CN, C_2 and AlO form from chemical reactions, e.g., Eqs. (1–4) [13], Eq. (5) [24], and Eq. (6) [25], resulting in an increase in molecular emission at times $> 2 \mu\text{s}$:



The formation of molecular species during the lifetime of the laser-induced plasma is clear evidence

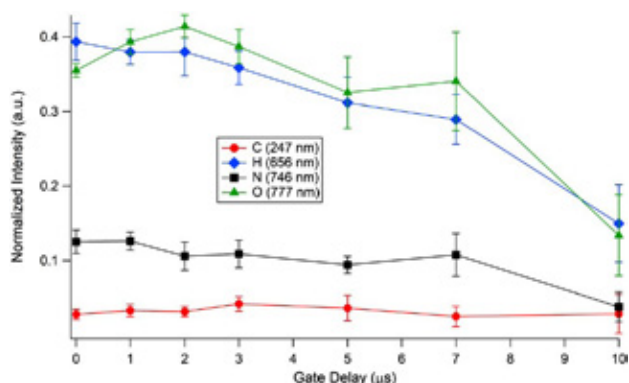


Fig. 1. (Color online) Peak atomic emission intensities as a function of gate delay (gate width 1 μs). Error bars represent 95% confidence intervals.

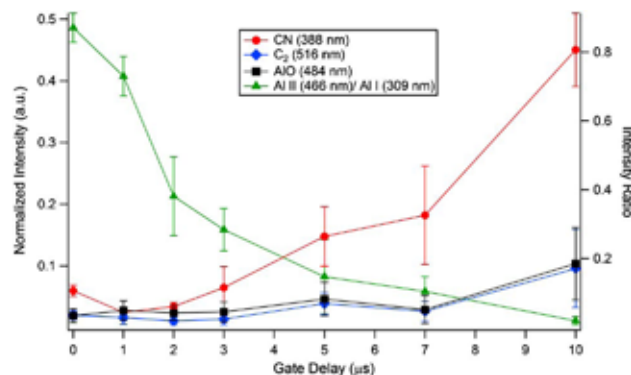


Fig. 2. (Color online) CN, C_2 , and AlO emission (shown as a function of gate delay with a gate width = 1 μs) increases as the plasma cools and becomes less ionized. Error bars represent 95% confidence intervals.

that chemistry is occurring in the highly excited, nonequilibrium environment. While most LIBS practitioners therefore limit the detector gate width in order to minimize changes in the emission intensities (at the expense of sensitivity), our goal was to determine if useful information about the species involved in the plasma chemistry can be obtained using longer gate widths. While using longer gate widths results in stronger overall emission intensities, changes in emission intensities resulting from chemical reactions in the plasma (as well as changes in the plasma temperature) also affect the relative emission intensities for the different species in the plasma over the integrated plasma lifetime.

B. Plasma Chemistry

Selected regions of spectra (double pulse LIBS under argon) from the five high-purity substrates with and without RDX are shown in Figure 3. The increase in the C, H, N, O, and CN emission with the presence of RDX (dotted red traces) is clearly visible. In this experiment very little air was entrained in the laser-induced plasma, so most of the nitrogen used in the formation of CN originates from the RDX. The highest excitation temperatures for the RDX/metal plasmas (calculated using the Ar I lines at 750.387 and 751.465 nm) correspond to $\text{Ti} > \text{Al} > \text{Cu} > \text{Sn} > \text{Ni}$ (Table 1). The Ti substrate plasma had the greatest increase in temperature with the addition of RDX, while the plasma for the Sn substrate remained essentially unchanged. The higher plasma temperature for the blank Sn implies less laser energy coupled to the sample and more energy went into heating the plasma. In this case, there would be fewer ablated Sn atoms in the plasma to affect the chemistry.

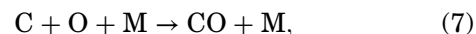
The extent of ionization for each RDX/metal plasma (represented by the ion/neutral ratio) followed almost the same trend as the temperature, $\text{Ti} > \text{Al} > \text{Cu} > \text{Ni} > \text{Sn}$ (Fig. 4). The ion/neutral ratios are drastically different among the substrates. Al and Ti have the lowest ionization potentials of the five substrates (5.986 and 6.828 eV, respectively, compared to 7.726 eV for Cu, 7.640 eV for Ni, and 7.344 eV for Sn) [26], and their plasmas have the highest ion/

Table 1. Calculated Excitation Temperatures for Metal Substrates With and Without RDX Residue

Substrate	Temperature (K)		% Change
	Blank	RDX Residue	
Al	9594 ± 251	12195 ± 796	27%
Cu	9369 ± 142	11802 ± 611	26%
Ni	9839 ± 177	11335 ± 488	15%
Sn	11639 ± 398	11434 ± 585	-1.8%
Ti	9123 ± 176	16834 ± 1295	85%

neutral ratios. The ionization of the Al plasma is substantially decreased when RDX residue is added to the substrate, while the ionization in the Ti and Cu plasmas increased. The ionization of the Ni and Sn substrate plasmas showed little change with the addition of RDX residue. These properties of the substrate will significantly affect the chemical reactions occurring in the laser-induced plasma.

Figure 5 shows three contour plots created by plotting the relative emission intensities of species within the laser-induced plasma (normalized to the Ar line at 763.511 nm) generated by ablation of RDX residue on the five substrates. These plots illustrate the variations in the plasma chemistry caused by the different substrates. Figure 5(a) shows that, as the C intensity in the plasma increases, the CN intensity increases, as well. The CN intensity is essentially independent of the atomic N content, however, which indicates that Eq. (2) is the dominant mechanism for formation of CN in the plasma, rather than Eq. (1). This observation is consistent with previous results (e.g., [23]). The O intensity increases as the N increases, while increasing C content results in decreasing O [Fig. 5(b)]. This result can be explained by the formation of CO and CO_2 in the plasma via the reactions



Equations (7) and (8) are important reactions in the decomposition of RDX, since the formation of gaseous

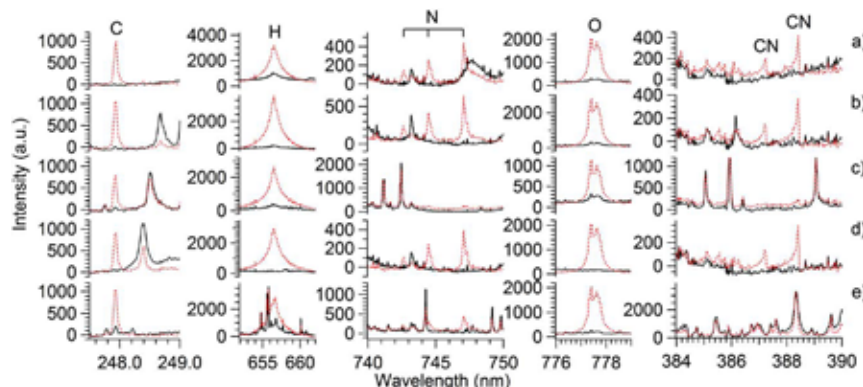


Fig. 3. (Color online) Selected regions of LIBS spectra for (a) Al, (b) Cu, (c) Ni, (d) Sn, and (e) Ti with (dotted red) and without (solid black) RDX residue.

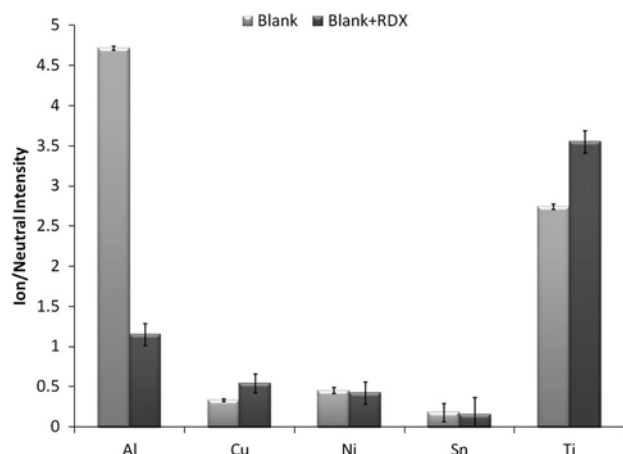


Fig. 4. Ion/neutral intensity ratios for the five high-purity substrates with and without RDX residue. The Al I 669.867 nm and Al II 466.306 nm lines were used to calculate ion/neutral ratios for Al since the 309.271 nm line was saturated. Other emission lines used for calculating ion/neutral ratios included: Cu I 296.116 nm and Cu II 227.626 nm, Ni I 343.356 nm and Ni II 243.789 nm, Sn I 333.062 nm and Sn II 533.236 nm, Ti I 373.890 nm and Ti II 462.928 nm. Error bars represent 95% confidence intervals.

products such as CO and CO₂ is highly exothermic and results in the liberation of large quantities of energy upon detonation [27]. Figure 5(c) shows that, as the CN intensity increases, the O intensity decreases. This decrease in O content in the presence of CN can be explained by the reaction



The concentration of atomic O in the laser-induced plasma is, therefore, highest in conditions of low C and low CN.

The assumption for the preceding analysis is that the minor differences in plasma temperature between substrates with RDX residue on them (with the exception of Ti, see Table 1) are less important than the effects of the ablated metal on the plasma chemistry. Since the subsequent analysis agrees with previous studies, we believe this assumption is reasonable. For a more quantitative approach to this analysis, inclusion of the temperature and ground state populations would need to be considered. In addition, the plasma chemistry is extremely complex, and there may be further complications not considered in this simplified approach.

To further understand the effect of metals on the chemical reactions of RDX in the laser-induced plasma, Al powder was mixed with the RDX in varying concentrations (0:1, 1:1, 2:1, and 4:1) and applied to the five substrates. Al is rapidly oxidized by oxygen (O, O₂), CO₂, H₂O, and possibly other species, such as NO, N₂O, and NO₂, to form AlO before reaching its final equilibrium state, alumina (Al₂O₃) [28]. Because of the high heat of formation for Al₂O₃, the addition of Al to explosive formulations results in a considerable increase in the heat of explosion. In

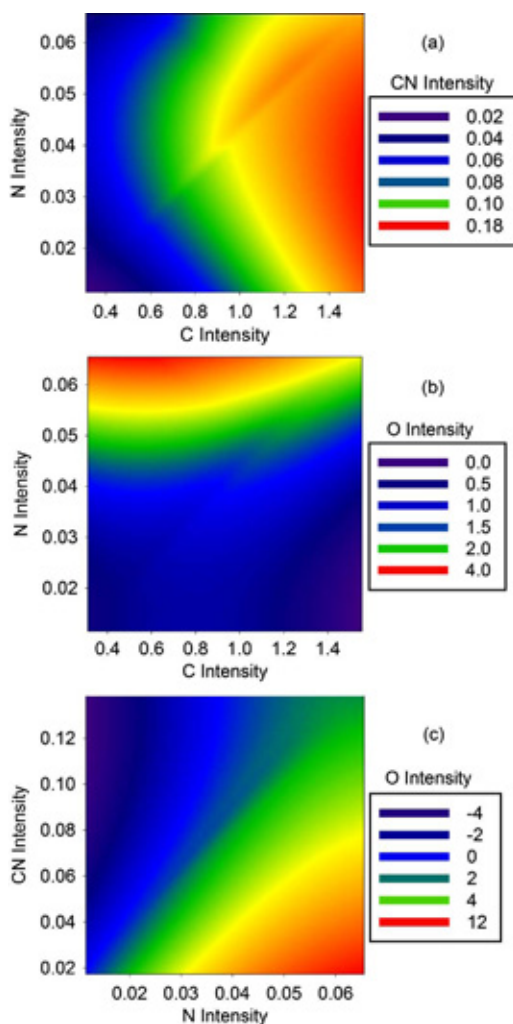


Fig. 5. (Color online) Contour plots for the (a) N, C, CN, (b) N, C, O, and (c) CN, N, O emission intensities of RDX on five different metal substrates (Al, Cu, Ni, Sn, and Ti).

these experiments, the laser-induced plasma temperature for each substrate increased by as much as 55% with the addition of Al powder to the RDX (Fig. 6). The Ti was the only substrate that showed an initial decrease in plasma temperature with Al (compared to the pure RDX residue).

As the concentration of Al powder was increased, the substrate emission lines decreased (due to increased residue surface coverage) and the Al emission lines increased. While the C, H, N, H, and CN emission lines decreased with increasing Al (possibly because less RDX was being sampled in the plasma), the C₂ and AlO increased on all substrates (Fig. 7). This result is confirmed by the conclusions of Song *et al.* [5], who observed the increase in C₂ and AlO emission with increasing Al content during an aluminized-RDX explosion in a shock tube. The higher the concentration of Al in the laser-induced plasma, the more O the Al scavenges to form AlO, and the less O available to react with the C to form CO. This results in an increase in condensed phase C aggregate (soot) and C₂. Although the increase in

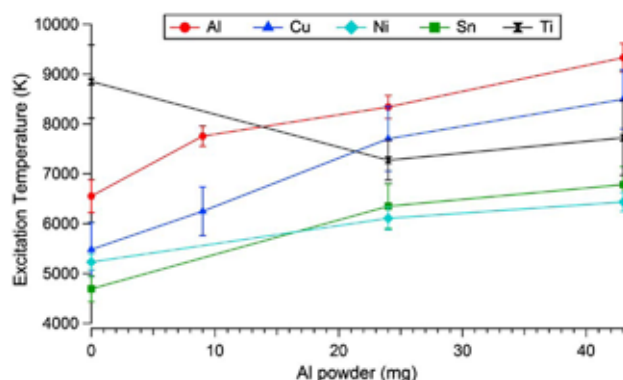


Fig. 6. (Color online) Excitation temperatures for RDX/Al mixture residues on Al, Cu, Ni, Sn, and Ti substrates calculated using Al I lines at 308.215 and 396.152 nm. Error bars represent 95% confidence intervals.

plasma temperature is more significant in this set of experiments, the accumulation of soot with increasing Al content has been observed in the previous experiment [5], substantiating our assumption that the increase in C_2 emission results from chemical reactions in the plasma.

C. Laser Pulse Energy Dependence

Conventional formulations of energetic materials containing Al particles to improve the performance of explosives and propellants use particles with a mean diameter of $\sim 50 \mu\text{m}$, but the reactivity of Al nanoparticles has been shown to increase with decreasing size [29]. Previous experiments have demonstrated that ablation of an Al target with a pulsed laser produces Al nanoparticles with a mean primary particle size of 5–500 nm (depending on laser pulse duration and fluence as well as carrier gas type and pressure) [7,9,30]. It has also been demonstrated that using higher laser pulse energies increases the number of smaller nanoparticles produced [10].

A comparison of the LIBS spectra of RDX on Al obtained using different pulse energy schemes (ranging from 210 to 840 mJ) showed that higher laser pulse energy results in both increased overall spectral emission and relative AlO emission (Fig. 8); the smaller Al particle sizes produced by the high laser pulse energy are more reactive (due to the higher relative surface area) and, therefore, are oxidized more quickly. While the slight increase in plasma temperature observed with increasing laser pulse energy affects the observed emission intensities, the standard deviation for the calculated temperatures was only 505 K, so we would expect this effect to be minimal.

The double laser pulses result in stronger RDX spectra (compared to single pulse spectra of the same total pulse energy), but weaker AlO emission, since less O is entrained in the laser-induced plasma (as seen by comparing the O intensity from the blank Al at 420 mJ versus 2×210 mJ in Fig. 8). The relative C intensity increases with increasing laser pulse energy. Unlike with the AlO, there is no decrease in C emission between a single 420 mJ pulse and a double

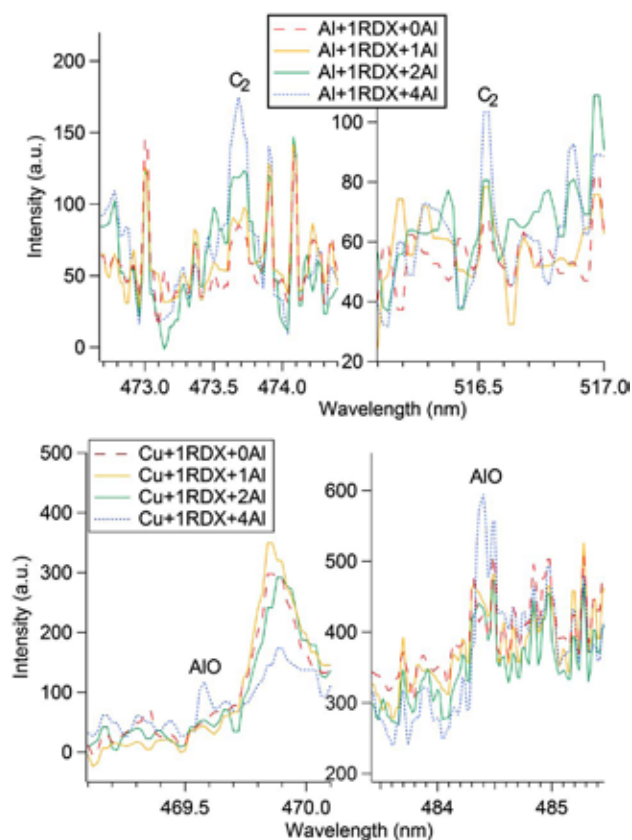


Fig. 7. (Color online) As the concentration of Al in the RDX/Al mixture was increased, the C_2 (top) and AlO (bottom) emission from the laser-induced plasma increased on all five metal substrates, including the Al and Cu substrates.

2×210 mJ pulse. Despite the strong C signal, no C_2 was observed at any laser pulse energy. RDX does not contain any C–C bonds, so no C_2 fragments are formed by the initial laser ablation (Fig. 2). Without the presence of additional Al to scavenge the O, the O in the plasma reacts with C (Eq. 7), preventing the formation of significant amounts of C_2 [15].

D. Effect of Trace Elements on RDX Chemistry

In addition to studying the interaction of pure metal substrates and Al additive with RDX, we also investigated the effect of minor impurities or trace elements on the chemical reactions occurring in the laser-induced plasma. LIBS spectra of a series of primarily aluminum samples were obtained, including an Al_2O_3 substrate and three NIST standard reference material Al alloys. Table 2 lists the concentrations of the trace elements for each sample (when known), divided into two categories: those observed in the double pulse LIBS spectra in argon, and those that were not observed. Only the Al_2O_3 substrate spectra contained significant O emission lines, indicating that the atmospheric contributions to the LIBS signal were negligible (none of the blank substrates had measurable N lines). All five substrates have C and H lines, even after multiple cleaning shots to remove surface contamination.

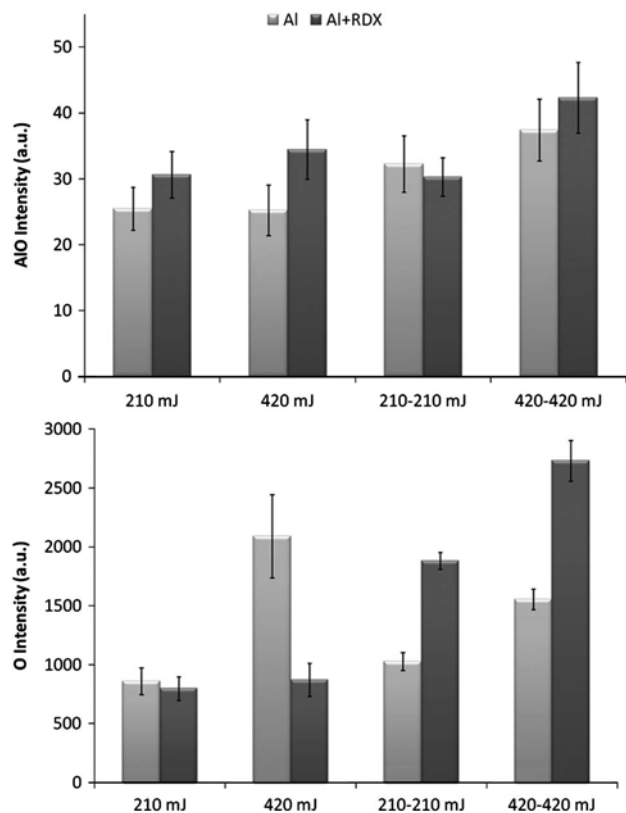


Fig. 8. Emission intensity for AIO (top) and O (bottom) obtained from RDX residue on Al with a single 210 mJ pulse, a 420 mJ pulse, and double pulse excitation (2×210 and 2×420 mJ). Error bars represent 95% confidence intervals.

RDX residue was applied to the five aluminum substrates and Fig. 9 shows the C emission intensities (normalized to the Ar line at 763.511 nm) observed in the LIBS spectra. The high-purity aluminum substrate, with the fewest trace elements, gave the strongest C signal from the RDX residue. The presence of more Al in the plasma increases the C signal by reducing the amount of free O available to react with C via Eq. (7). However, much of this increase in C emission intensity can be attributed to the higher plasma temperature with the pure Al substrate ($12,086 \pm 356$ K). The four Al alloys, on the other hand, produce nearly identical plasma temperatures when the RDX residue is present (within

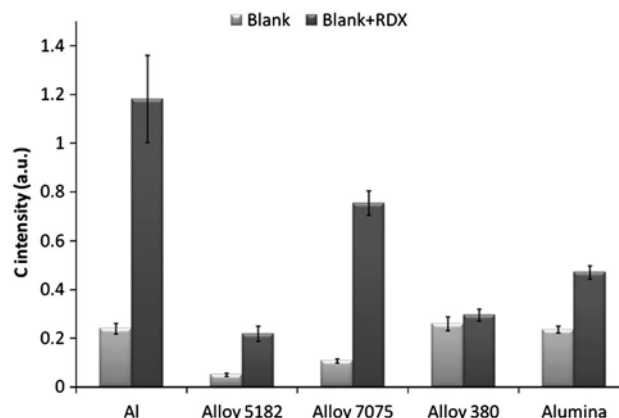


Fig. 9. Emission intensities for the C line from the LIBS spectra of RDX residue on five different Al samples. Error bars represent 95% confidence intervals.

the standard deviation of the shot-to-shot variation). For example, alloy 5182 (with RDX) results in a plasma temperature of $10,565 \pm 145$ K, compared to $10,608 \pm 243$ K for alloy 7075—yet the increase in C emission signal is nearly fourfold for alloy 7075. Differences in the plasma chemistry resulting from the trace elements present in the aluminum alloys are clearly evident. Alloy 7075 has the highest Zn concentration, and the highest C signal of the three alloys. Alloy 5182, despite having the highest Al concentration of the three alloys, has the highest Mg concentration. Since Zn has a significantly lower oxidation potential (0.76 V) than Mg (2.37 V) [26], it makes sense that alloy 7075 would have the highest C signal among the alloys and alloy 5182 would have the lowest—the presence of easily oxidizable species will decrease the amount of O available to react with the C. Alloy 380 also contains a significant amount of Si, which also has a low oxidation potential (0.91 V) [26]. Alumina has the highest O content, which would typically favor the formation of CO/CO₂ (i.e. less C emission); however, this effect may be offset by its higher aluminum content than the other three alloy substrates.

4. Conclusions

Although, at first glance, an explosive detonation and a laser-induced plasma may not seem to have much in

Table 2. Trace Metal Content (Including Elements Observed in LIBS Spectra) for Five Different Aluminum Samples

Sample	% Al	Minor Components	
		Observed	Not Observed
Alumina (Al ₂ O ₃)	unknown	Si, Mg, Fe, Ti, Sr, Cr, Pb, Cu	Mn, Zn, Ni, Sn, Be
Alloy 380	82.99	9.362% Si, 3.478% Cu, 1.011% Zn, 0.865% Fe, 0.3857% Mn, 0.4135% Ni, 0.0188% Sr, 0.877% Ti, 0.0572% Cr, 0.0637% Mg, 0.1075% Pb, 0.0212% V	0.35% Sn
Alloy 7075	89.76	5.44% Zn, 2.48% Mg, 1.60% Cu, 0.025% Be, 0.173% Cr, 0.18% Si, 0.205% Fe, 0.079% Mn, 0.063% Ni	
Alloy 5182	94.58	4.474% Mg, 0.3753% Mn, 0.1553% Si, 0.0494% Cu, 0.199% Fe	0.034% Cr, 0.015% Pb, 0.0195% Ni, 0.0002% Sr, 0.0335% Ti, 0.0174% V, 0.0505% Zn
Aluminum	99.999	Si, Cu, Fe	Mn, Zn, Sn, Pb, Ni, Sr, Ti, Cr, V, Be

common, they are both very high-temperature (thousands of Kelvin), high pressure (up to $\sim 10^5$ atm) environments subjected to a shock wave resulting in the rapid decomposition of the explosive into atomic constituents and subsequent exothermic formation of gaseous products. Understanding the chemistry that occurs in the reaction front of an explosive detonation is extremely difficult due to the short time scale and violent release of energy in the form of heat, sound, light, and blast. In addition, full-scale detonation testing is quite expensive. The ability to study the chemical reactions of explosives in a small-scale laboratory environment that does not require extensive safety precautions would greatly benefit the development of improved explosive formulations. The use of optical emission spectroscopy to study the chemical reactions of laser-generated nanoenergetic materials in laser-induced plasmas is extremely promising. By monitoring the emission intensity of different reactant species as a function of time, a better understanding of the chemistry of metallic nanoparticles and molecular explosives at high temperatures can be achieved, eventually enabling the development of explosive formulations with higher explosive power and fewer harmful byproducts.

Time-resolved, broadband emission of chemical species involved in the reaction of RDX and metallic nanoparticles in a laser-induced plasma has been observed. Using the methodology presented here for investigating the chemical processes involved in nanoenergetic material reactions, we observed the increase in C_2 emission resulting from an increase in Al powder additive, as confirmed by the observations of Song *et al.* [5] in a shock tube explosion. The time evolution of species formation, the effects of laser pulse energy, and the effects of trace metal content on chemical reactions were also studied. In addition to matrix effects induced by the interaction of the laser with the metal substrate (affecting the amount of material ablated, plasma temperatures, electron densities, etc.), we have shown that differences in the plasma chemistry of RDX with ablated metals significantly alters the LIBS spectra of RDX.

In a recent kinetic modeling study by Ma and Dagdigian [23], the effect of Al particles ablated from the substrate surface on the plasma chemistry was neglected based on assumptions as to the entrainment of the ablated Al in the laser-induced plasma [16]. Their initial experimental results [16], which formed the basis for this assumption, were obtained under very different experimental conditions than the present study (a single laser pulse of 20 mJ at 355 nm on a thin Al foil was used). In addition, the effect of the presence of organic residue on the laser–material interaction was not considered. Their resulting kinetic model significantly underestimated the molecular emission of C_2 (and CN) from the plasma [23]. Our current experimental results showing that increasing the Al content in the plasma results in increased C_2 emission as a result of the preferential oxidation of Al over C suggest that including the

effects of Al in the kinetic model may improve the results.

Future improvements to the current experimental setup should include the incorporation of on-line monitoring of particle size distribution [10] in order to directly correlate the plasma chemistry to particle size effects, and the monitoring of mid-IR emission from the plasma to obtain information on the concentration of important species such as CO, CO_2 , NO, and NO_2 in the plasma [31]. Experiments are underway to study the particle sizes produced by laser ablation of RDX. Additional experiments to be performed include tuning the laser properties, such as pulse duration and wavelength, to adjust the size and size distribution of the ablated particles, and exploring other explosive formulations, such as TNT/Al and Al/Teflon.

The author thanks Dr. Frank C. De Lucia, Jr. for numerous thoughtful discussions relating to this work.

References

1. P. Politzer, P. Lane, and M. E. Grice, "Energetics of aluminum combustion," *J. Phys. Chem. A* **105**, 7473–7480 (2001).
2. P. W. Cooper and S. R. Kurowski, *Introduction to the Technology of Explosives* (Wiley-VCH, 1996).
3. P. Brousseau and C. J. Anderson, "Nanometric aluminum in explosives," *Propellants Explos. Pyrotech.* **27**, 300–306 (2002).
4. D. D. Dlott, "Thinking big (and small) about energetic materials," *Mater. Sci. Technol.* **22**, 463–473 (2006).
5. Y. Song, J.-H. Wu, Y.-P. Wang, G.-D. Wu, and X.-D. Yang, "Optical investigation of shock-produced chemical products in pseudo-aluminized explosive powders explosion," *J. Phys. D* **40**, 3541–3544 (2007).
6. Y. Song, J.-H. Wu, M.-A. Xue, Y.-P. Wang, D. Hu, and X.-D. Yang, "Spectral investigations of the combustion of pseudo-nanoaluminized micro-cyclic- $[CH_2N(NO_2)]_3$ in a shock wave," *J. Phys. D* **41**, 235501 (2008).
7. M. Ullmann, S. K. Friedlander, and A. Schmidt-Ott, "Nanoparticle formation by laser ablation," *J. Nanopart. Res.* **4**, 499–509 (2002).
8. S. Eliezer, N. Eliaz, E. Grossman, D. Fisher, I. Gouzman, Z. Henis, S. Pecker, Y. Horovitz, M. Fraenkel, S. Maman, and Y. Lereah, "Synthesis of nanoparticles with femtosecond laser pulses," *Phys. Rev. B* **69**, 144119 (2004).
9. S. Amoroso, R. Bruzzese, M. Vitiello, N. N. Nedialkov, and P. A. Atanasov, "Experimental and theoretical investigations of femtosecond laser ablation of aluminum in vacuum," *J. Appl. Phys.* **98**, 044907 (2005).
10. R. Sattari, C. Dieling, S. Barcikowski, and B. Chichkov, "Laser-based fragmentation of microparticles for nanoparticle generation," *J. Laser Micro/Nanoeng.* **3**, 100–105 (2008).
11. D. A. Cremers and L. J. Radziemski, *Handbook of Laser-Induced Breakdown Spectroscopy* (Wiley, 2006).
12. J. L. Gottfried, F. C. De Lucia Jr., C. A. Munson, and A. W. Miziolek, "Laser-induced breakdown spectroscopy for detection of explosives residues: a review of recent advances, challenges, and future prospects," *Anal. Bioanal. Chem.* **395**, 283–300 (2009).
13. V. I. Babushok, F. C. De Lucia, P. J. Dagdigian, J. L. Gottfried, C. A. Munson, M. J. Nusca, and A. W. Miziolek, "Kinetic modeling study of the laser-induced plasma plume of cyclotrimethylenetrinitramine (RDX)," *Spectrochim. Acta Part B* **62**, 1321–1328 (2007).
14. V. Lazić, A. Palucci, S. Jovicevic, C. Poggi, and E. Buono, "Analysis of explosive and other organic residues by laser

- induced breakdown spectroscopy," *Spectrochim. Acta Part B* **64**, 1028–1039 (2009).
15. F. C. De Lucia, Jr. and J. L. Gottfried, "Characterization of a series of nitrogen-rich molecules using laser-induced breakdown spectroscopy," *Propellants Explos. Pyrotech.* **35**, 268–277 (2010).
 16. P. J. Dagdigian, A. Khachatryan, and V. I. Babushok, "Kinetic model of C/H/N/O emissions in laser-induced breakdown spectroscopy of organic compounds," *Appl. Opt.* **49**, C58–C66 (2010).
 17. P. Lucena, A. Dona, L. M. Tobaria, and J. J. Laserna, "New challenges and insights in the detection and spectral identification of organic explosives by laser induced breakdown spectroscopy," *Spectrochim. Acta Part B* **66**, 12–20 (2011).
 18. M. Civiš, S. Civiš, K. Sovová, K. Dryahina, P. Španěl, and M. Kyncl, "Laser ablation of FOX-7: proposed mechanism of decomposition," *Anal. Chem.* **83**, 1069–1077 (2011).
 19. Y. Ralchenko, A. E. Kramida, J. Reader, and N. A. Team, "NIST atomic spectra database (version 4.1)" (National Institute of Standards and Technology, 2010), retrieved 6 Sept. 2011, <http://physics.nist.gov/asd>.
 20. V. I. Babushok, F. C. De Lucia Jr., J. L. Gottfried, C. A. Munson, and A. W. Miziolek, "Double pulse laser ablation and plasma: laser induced breakdown spectroscopy signal enhancement," *Spectrochim. Acta Part B* **61**, 999–1014 (2006).
 21. M. Baudelet, M. Boueri, J. Yu, S. S. Mao, V. Piscitelli, X. Mao, and R. E. Russo, "Time-resolved ultraviolet laser-induced breakdown spectroscopy for organic material analysis," *Spectrochim. Acta Part B* **62B**, 1329–1334 (2007).
 22. M. Boueri, M. Baudelet, J. Yu, X. L. Mao, S. S. Mao, and R. Russo, "Early stage expansion and time-resolved spectral emission of laser-induced plasma from polymer," *Appl. Surf. Sci.* **255**, 9566–9571 (2009).
 23. Q. Ma and P. Dagdigian, "Kinetic model of atomic and molecular emissions in laser-induced breakdown spectroscopy of organic compounds," *Anal. Bioanal. Chem.* **400**, 3193–3205 (2011).
 24. S. Yuasa, Y. Zhu, and S. Sogo, "Ignition and combustion of aluminum in oxygen/nitrogen mixture streams," *Combust. Flame* **108**, 387–390 (1997).
 25. A. Fontijn and W. Felder, "HTFFR kinetics studies of $\text{Al} + \text{CO}_2 \rightarrow \text{AlO} + \text{CO}$ from 300 to 1900 K, a non-Arrhenius reaction," *J. Chem. Phys.* **67**, 1561–1569 (1977).
 26. D. R. Lide, ed., *Handbook of Chemistry and Physics*, 75th ed. (CRC Press, 1994).
 27. J. Akhavan, *The Chemistry of Explosives*, 2nd ed. (The Royal Society of Chemistry, 2004).
 28. Z. Ji and L. Shufen, "Aluminum oxidation in nitramine propellant," *Propellants Explos. Pyrotech.* **24**, 224–226 (1999).
 29. K. Park, D. Lee, A. Rai, D. Mukherjee, and M. R. Zachariah, "Size-resolved kinetic measurements of aluminum nanoparticle oxidation with single particle mass spectrometry," *J. Phys. Chem. B* **109**, 7290–7299 (2005).
 30. I. Balchev, N. Minkovski, T. Marinova, M. Shipchka, and N. Sabotinov, "Composition and structure characterization of aluminum after laser ablation," *Mater. Sci. Eng. B* **135**, 108–112 (2006).
 31. C. S.-C. Yang, E. E. Brown, U. H. Hommerich, S. B. Trivedi, A. C. Samuels, and A. P. Snyder, "Mid-infrared emission from laser-induced breakdown spectroscopy," *Appl. Spectrosc.* **61**, 321–326 (2007).

Biographies of ARL Authors

Jan L. Allen is a chemist with expertise in materials and solid state chemistry. Dr. Allen's interest is focused on Li-ion battery materials, with particular emphasis on electrode and electrolyte materials. He received his B.S. in chemistry from Truman State University in Missouri in 1989. He continued his education at Northwestern University and earned a Ph.D. in inorganic chemistry in 1993, under the direction of Professor Ken Poeppelmeier. Following postdoctoral research at the University of Caen in Caen, France, with Professor Bernard Raveau, and at the University of Kentucky with Professor Peter Eklund, Allen worked at the Gillette Research Institute, the corporate laboratory of the Gillette Company in Gaithersburg, Maryland. In 2000, Allen joined ARL. Dr. Allen received the Department of the Army Research & Development Achievement Award for Technical Excellence in 2002 and 2011.

Radhakrishnan Balu is a researcher in computational material science, with a research focus on energetic materials and nanomaterials used in electronics and optical devices. He has been working at ARL since 2007 and uses state-of-the-art quantum mechanics-based calculations leveraging the high performance computing infrastructure for research. He has over 20 publications, including peer-reviewed journal papers. He has five degrees in science and engineering, with a Ph.D. in computational chemistry from the University of Maryland Baltimore County, an M.S. in biotechnology from Johns Hopkins University, and a B.S. in computer science from the Indian Institute of Science Bangalore.

Richard Becker received a B.S. and M.S. in mechanical engineering from the University of Pittsburgh. His M.S. thesis work on micromechanical modeling of ductile void growth was continued at Brown University, where he received his Ph.D. in engineering. Dr. Becker accepted a position at Alcoa, pursuing modeling of crystallographic texture evolution and anisotropy, thermo-mechanical process modeling, and constitutive model development. In 1999, he went to Lawrence Livermore National Laboratory, where he worked on algorithm and code development, and multi-scale model development and validation for strength and fracture models under the Advanced Supercomputing Initiative. Dr. Becker joined ARL in 2009, where he has been focusing on multi-scale modeling, material model development, and model implementation in large-scale hydrocodes. Dr. Becker is on the editorial board of several journals and is a member of the American Academy of Mechanics, the American Society of Mechanical Engineers, and the Sigma Xi Scientific Research Society.

Jennifer Ciezak-Jenkins is a research physicist within the Energetic Materials Science Branch. Her research examines the properties of materials under thermomechanical extremes using optical spectroscopy, x-ray and neutron probes, and diamond anvil cell techniques. Dr. Ciezak-Jenkins began her research career in molecular spectroscopy and electronic structure theory and obtained an NRC postdoctoral fellowship with ARL and Dr. Betsy Rice in 2004. Dr. Ciezak-Jenkins attended St. Bonaventure University, where she studied chemistry and physics (B.S., 2001). She did her graduate work in chemical physics at Syracuse University (Ph.D. 2004). After an NRC post-doctoral fellowship with Drs. Betsy Rice and Samuel Trevino (2004-2006), she joined ARL as a research physicist in 2006. She is the recipient of five ARL Director's Research Initiative (DRI) grants concerning polymeric nitrogen, structural bond energy release, ultrahard phases of carbon, and low energy nuclear reactions, and is a member of the American Physical Society, the American Chemical Society, and the Neutron Scattering Society of America.

Peter Chung is a Team Leader in the Simulation Sciences Branch, Computational Sciences Division of CISD. He holds a Ph.D. in mechanical engineering from the University of Minnesota and a B.S. in aerospace engineering from the University of Virginia. After a one-year NRC Post-doc, he joined the civil service at ARL in 2001. He is the recipient of the 2010 Army Science Conference Best Paper Co-Award, 2008 ICCES Outstanding Young Investigator Award in Computation, 2004 US RDECOM Outstanding Young Scientist, and 2003 Army Superior Civilian Service Award. He has served as mentor for 15 current and former post-docs and students, and has participated on eight Ph.D. and M.S. degree committees. He currently leads a research team in areas related to computational basic research of multiscale science, materials, physics, chemistry, and mechanics. He has published 38 archival journal papers and 42 conference papers and presentations, and has given nine invited talks.

Wayne A. Churaman received B.S. and M.S. degrees in electrical engineering from the University of Maryland, College Park, in 2005 and 2010, respectively, with a specific focus on microelectronics and microrobotic platforms. He has been working as a MEMS Engineer for the ARL since 2005. His interests include experimental analysis of nanoenergetic materials, integration of nanoenergetic materials with MEMS, and MEMS sensor design and fabrication. He is currently pursuing a Ph.D. in mechanical engineering at the University of Maryland, College Park, developing nanoenergetic porous silicon as a novel actuator to enhance mobility of microrobotic platforms.

John D. Clayton has been on ARL's Technical Staff at APG, Maryland, since 2003. Dr. Clayton served at APG as a NRC Postdoctoral Fellow; he was previously a Visiting Scientist, performing graduate research at Sandia National Laboratories in Livermore, California (2000), and he performed undergraduate research at Worcester Polytechnic Institute, Massachusetts (1997). Dr. Clayton is a member of several professional associations, including the American Ceramic Society, the American Academy of Mechanics, the American Physical Society, the American Society of Mechanical Engineers, the Society of Engineering Science, and the U.S. Association for Computational Mechanics. His work has garnered him the ARL Award for Publication (2011), as well as multiple DRI Awards, one of which ("Phase Field Modeling") was rated as one of the Top 3 DRI projects in 2010.

Arthur von Cresce holds a Ph.D. in materials science and engineering from the University of Maryland, College Park, and joined ARL in January 2012 as a materials engineer. His primary research focus is on polymer science, the synthesis of organic polymers, and their manipulation and characterization. He currently performs organic synthesis as it relates to Li-ion batteries, and making additive and solvent compounds. He also performs a variety of electrochemical characterizations of Li-ion battery systems, as well as materials characterizations such as FTIR, XPS, and mass spectrometry.

Luke J. Currano received B.S., M.S., and Ph.D. degrees in mechanical engineering from the University of Maryland, College Park, in 2000, 2002, and 2010, respectively. He has worked as a MEMS Engineer for ARL since 2001. He is currently Team Leader of the MEMS and Nanoenergetic Devices team at ARL. His research interests include integration of energetic materials with MEMS, high force/displacement MEMS actuators, acceleration switches, no-power sensors, and biologically inspired MEMS devices.

Jennifer L. Gottfried received a B.S. in chemistry from Ohio Northern University in May 2000, an M.S. in physical chemistry from the University of Chicago in August 2001, and a Ph.D. in physical chemistry from the University of Chicago in August 2005. She joined ARL in September 2005 as a postdoctoral fellow and was hired as a Physical Scientist in May 2008. In 2009, Dr. Gottfried was the Gold medal winner for Rookie Employee of the Year—Technical Scientific and Program Support (Excellence in Federal Career Award). She was a co-recipient of a 2009 Research and Development Award for "Stand-off Detection of Explosives," co-investigator on one of the top three FY07 DRI projects, and principal investigator for one of the top four FY09 DRI projects. Dr. Gottfried has contributed to a double-pulse LIBS review paper and a book chapter on explosives detection, and has written more than 29 additional peer-reviewed papers.

Sergiy Izvyekov is a Physical Scientist who joined the Weapons and Materials Research Directorate at ARL in April 2009. Dr. Izvyekov received a Ph.D. in Physics from National University of Kiev (Kiev, Ukraine) in 1992. He has authored 62 articles in peer-reviewed journals (over 1700 citations), four book chapters, and numerous presentations at national and international conferences. Additionally, he received the 27th Army Science Conference Best Paper Award in "Advanced High Performance Computing in Physical Sciences and Engineering." Dr. Izvyekov is a member of the American Chemical Society.

T. Richard Jow currently leads the ARL team developing advanced energy storage materials for high power density and high energy density electrochemical and electrostatic energy storage devices. Dr. Jow has been the technical lead of the DOE-ARL Interagency Agreements on Li-ion electrolytes and batteries project since 2000. He also managed Army Capacitor ManTech Development Program for pulsed power applications (2004-2008). Dr. Jow received his B.S. and M.S. in physics from Tsing Hua University, Taiwan, China, and received his Ph.D. in materials science and engineering from Northwestern University in 1977. Dr. Jow joined ARL in 1989. He received the Allied-Signal Inventors Award in 1987, the ARL Technical Achievement Award in Science in 1996, and the Army R&D Achievement Award in 1996, 1999, 2001, 2002 and 2011. Dr. Jow has also authored and co-authored over 130 journal publications and received 27 U.S. patents.

William D. Mattson is a Research Physicist in the Weapons and Materials Research Directorate at ARL. Dr. Mattson obtained his B. S. in physics and computer science at the University of Maryland Baltimore County in 1996. He further obtained his Ph.D. in physics at the University of Illinois at Urbana-Champaign in 2003, under the direction of Professor Richard Martin. Dr. Mattson has worked for the ARL since 1993, and on his current work in the simulation of energetic materials since 1994. Dr. Mattson has more than 30 publications, and more than 70 presentations. Dr. Mattson developed and serves as the PI for theory of the Disruptive Energetics ARL Mission program. Dr. Mattson has also participated in developing scalable software for classical atomistic molecular dynamics simulations under several DoD HPCMP programs, and currently serves as the Computational Technology Lead for Computational Chemistry and Material Science.

Christopher Morris joined ARL in 2007 as a DARPA-sponsored fellow under the S.M.A.R.T. fellowship program, and was hired a government employee in 2009. He earned a Ph.D. in electrical engineering from the University of Washington in 2007, following a two-year stint at a biotechnology startup company, and an M.S. in mechanical engineering in 2000, also from the University of Washington. Current research interests include the use of stored chemical or mechanical energy for novel high-force and large-displacement actuators; fuze and initiation technologies; and new packaging and assembly methods to enable complete, functional, and self-contained microsystems. He has authored or co-authored over 45 peer-reviewed journal and conference papers, with a recent paper on RFID-integrated battery-free MEMS actuators highlighted as being in the top 0.5% of all IEEE publications for that month.

Lynn B. Munday works in ARL's Simulation Sciences Branch, Computational Sciences Division. He holds a Ph.D. from the University of Maryland, an M.S. from the University of New Mexico, and a B.S. from Montana State University, all in mechanical engineering. He joined the staff of ARL in late 2011 after working an intern. His research is in computational solid mechanics. He has published three archival journal papers, and four conference papers and presentations.

Jeffrey A. Read received his Ph.D. in chemistry from the University of Michigan in 1996, under Dr. Anthony Francis, where he studied the spectroscopy of metal chalcogenides and their intercalates. From 1993 to 1997, he conducted applied research on new materials and electrolytes for Li-ion polymer batteries at Ultralife Batteries, with emphasis on cycle life and storage at elevated temperatures. From 1997 to 1998 he worked on advanced development of rechargeable Zn-Air batteries at AER Energy Resources, with particular focus on cycle life and failure analysis. Dr. Read began at ARL in 1999 and has focused on primary battery research for Soldier applications. Chemistries studied include Li/MnO₂, Li/CF_x, and Li/Air batteries. Dr. Read is Team Leader on the group looking to the next generation of primary and rechargeable batteries, including Li/S and rechargeable batteries using ceramic conducting membranes.

Betsy M. Rice is a research chemist and Leader of the Multiscale Reactive Modeling Team in the Energetic Materials Science Branch, Weapons and Materials Research Directorate of ARL. She is responsible for initiating, planning, and personally performing research investigations to determine microscopic details of the physical and chemical processes of materials of interest to the Army, including energetic materials and materials related to armor/armaments. Dr. Rice's expertise lies in the theoretical chemistry areas of classical molecular simulation and quantum mechanical molecular characterization directed toward advanced modeling of materials that are critical components of several DoD weapons and S&T mission areas. Dr. Rice began her tenure with the Army as a National Research Council Postdoctoral Fellow at the Ballistic Research Laboratory in 1989, and was hired in 1990. Dr. Rice received a B.S. Degree in chemistry from Cameron University, Lawton, Oklahoma, in 1984, and was awarded a Ph.D. in chemistry at Oklahoma State University in 1987. Dr. Rice also holds the position of Senior Scientist at the High Performance Computing Software Application Institute for Multiscale Reactive Modeling of Insensitive Munitions. Dr. Rice was named as an ARL Fellow in 2000.

Xiaoming Ren is a Senior Research Chemist, focusing on alkaline fuel cell technology for portable and stationary applications, and developing a lithium air battery. He came to ARL in 2010, after experience as a Post-Doctoral Research Fellow at the University of Texas at Dallas and the Los Alamos National Laboratory, as well years of experience in private industry. Dr. Ren received a B.S. from Chengdu University of Science and Technology in 1984, and a Ph.D. from the Memorial University of Newfoundland in 1993.

Dat T. Tran obtained his B.S. and Ph.D., both with honors, in chemistry from SUNY Binghamton in 1998 and 2005, respectively. He pursued postdoctoral studies in the area of bio-inspired materials synthesis at Cornell University during 2006-2007. He joined ARL in June 2008 as a research chemist. His areas of research include synthesis and characterization of inorganic materials for liquid phase desulfurization of logistic JP-8 fuel and catalysts materials for Army fuel cell/battery applications. In his research areas, Dr. Tran has authored 20 peer-reviewed journal papers and several proceedings papers and technical reports. His research work has often been cited by other research workers in the field. Dr. Tran is an active member of the American Chemical Society.

Jeffrey Wolfenstine is currently working at ARL in the area of Li-ion batteries for both Soldier and vehicle applications. Prior to joining ARL, he was a professor of mechanical engineering at the University of California Irvine investigating the high temperature mechanical behavior of composites, intermetallics, and ceramic materials. He is an internationally recognized scientist in the field of materials science, with main emphasis on processing, characterization, and properties of structural and energy storage materials. He has published over 100 journal papers with a citation index over 1,000, and his research is referenced in textbooks. He received outstanding paper of the year for one journal, two Army R&D awards, and one best paper at an Army science conference, and has two patents and five patent disclosures.

Kang Xu is a Research Chemist whose areas of interest include energy storage materials, interface chemistry in electrochemical devices, and bio-inspired synthesis of materials. Dr. Xu received a B.S. in organic chemistry from Southwest University, an M.S. in polymer chemistry from Institute of Chemical Physics, Academy of Sciences, and a Ph.D. from Arizona State University. He joined ARL in 1997, and has been cited since then for his technical excellence with Department of Army R&D Awards (1999, 2001, 2002 and 2011), Best Paper Award at Army Science Conference (2008), the Citation for Leadership Excellence in DDR&E Wearable Power Prize Competition (2008), ARL Publication (2005) and Science Awards (2011), respectively. He serves as a frequent panelist for industry, DOE, Electrochemical Society, and other international academic communities. He has 114 publications in peer-reviewed journals, and has edited/co-authored three books and book chapters. His work has over 3,800 citations in literature with an h-index of 34.

Sheng S. Zhang is a research chemist in Electrochemistry Branch of ARL's Sensors and Electron Devices Directorate. He received a Ph.D. in physical chemistry from the University of Science and Technology Beijing, China, in 1993. After experience in academy and industry, he joined ARL as a postdoctoral associate in 1997, and became an employee in 2002. His research activities focus on advanced materials for electrochemical energy storage and conversion devices, including rechargeable Li-ion batteries, lithium batteries, metal-air batteries, and electrochemical capacitors. He investigates high energy density batteries beyond Li-ion, including Li/CF_x battery, Li-air battery, and lithium-sulfur batteries. Dr. Zhang has authored 117 peer-referred journal papers, published 21 patents/applications, and edited a review book. His publications have received an h-index of 34 with over 3200 citations. He received two Army R&D Achievement Awards in 2000 and 2001, and serves as an editorial board member for International Journal Electrochemistry, Journal of Energy Storage and Conversion, The Open Electrochemistry Journal, and Dataset Papers in Materials Science.

